X-ray study of structural intermediates during nanomaterials synthesis

Kilian Frank

Munich 2025

X-ray study of structural intermediates during nanomaterials synthesis

Kilian Frank

Dissertation
an der Fakultät für Physik
der Ludwig-Maximilians-Universität München

vorgelegt von
Kilian Frank
aus München

München, den 12.08.2025

Erstgutachter: PD Dr. Bert Nickel

Zweitgutachter: Prof. Dr. Alexander S. Urban

Tag der mündlichen Prüfung: 17. Oktober 2025

Zusammenfassung

Kolloidale Nanokristalle haben faszinierende größen- und formabhängige Eigenschaften. Ein großes Oberfläche-zu-Volumen-Verhältnis, starke Quanteneinschlusseffekte und plasmonische Effekte machen sie für Anwendungen in der Energieumwandlung und der Katalyse interessant. Trotz rapider experimenteller Fortschritte bleibt eine rationale Kontrolle der Partikelgröße und -form bei der Synthese von Halbleiter-, Metall- und Metalloxid-Nanokristallen eine Herausforderung. Die zeitliche Entwicklung von atomarer Struktur und Partikelform während der Synthese ist Gegenstand aktueller Forschung, mit dem Ziel, Wachstumsmechanismen zu erklären und zu optimieren. In situ-Studien können im Falle nicht-klassischer Nukleation Zwischenzustände sichtbar machen, deren Einfluss auf die Partikeleigenschaften oft ungeklärt ist.

In dieser Dissertation werden verschiedene kolloidale Nanokristallsynthesen mit Röntgenstreuung untersucht. Die Kombination labor- und speicherringbasierter Quellen für hochenergetische Röntgenstrahlung (17.4 bis 104 keV) mit neuen Probenumgebungen ermöglicht eine gleichzeitige Aufnahme von Klein- und Weitwinkelröntgenstreuung (SAXS und WAXS), Total Scattering (TS), und eine Analyse der Paarverteilungsfunktion (PDF). Die untersuchten Materialien umfassen anisotrope (stäbchen- oder plättchenförmige) Bleihalid-Perovskit-Nanokristalle, Kupfer-Nanokugeln, Kupfer-Palladium-Superkristalle und Kobaltoxid-Nanoassemblate.

SAXS, WAXS und TS mit simultaner Photolumineszenzspektroskopie zeigen, dass die Synthese von Bleihalid-Perovskit-Nanokristallen mizellare Strukturen der Ausgangssubstanzen und Liganden sowie stäbchenförmige Nanocluster als Zwischenzustände hat. Durch die Zugabe eines Anti-Lösungsmittels verschmelzen die Nanocluster entweder in einer dichten, hexagonalen Mesophase zu Stäbchen oder lösen sich auf, wachsen langsam zu Plättchen, und assemblieren später. Die Keimbildung von Kupfer-Nanokugeln findet in einer dichten Subphase aus Metall-Phosphonat-Lamellen statt. Kupfer-Palladium-Superkristalle bestehen aus ikosaederförmigen Nanokristallen, die aus einer kurzreichweitig geordneten Phase heraus eine fcc-Struktur bilden. Im Fall von Kobaltoxid fügen sich polyhedrale Kristallite unter gleichzeitigem Wachstum zu porösen Partikeln zusammen. Für Halbleiter-, Metall- und Metalloxid-Nanokristalle werden also häufig nichtklassische Nukleations-, Wachstums- und Selbstassemblierungsphänomene beobachtet. In manchen Systemen sorgt kontrollierte Selbstassemblierung für eine definierte Partikelform und eine enge Größenverteilung. Dabei spielen Wechselwirkungen zwischen Nanokristallen, Liganden und Lösungsmitteln eine Schlüsselrolle. Das Lösungsmittel ist dabei nicht nur homogenes und inertes Medium, sondern kann sich selbst ordnen, Selbstassemblierung initiieren oder die Ligandenhülle gezielt destabilisieren. So beeinflussen beispielsweise das Dipolmoment der Lösungsmittelmischung und ihr Hansen-Löslichkeitsparameter für Wasserstoffbrückenbindungen die Anisotropie der Bleihalid-Perovskit-Nanokristalle.

Diese Ergebnisse zeigen das Potential von in situ-Röntgenstreuexperimenten für die gezielte Optimierung nicht-klassischer Nanokristallsynthesen durch quantitative Analyse. Die automatisierte und miniaturisierte in situ-Probenkammer, die in dieser Dissertation entwickelt wurde, kann für eine schnelle Erkundung des Reaktionsparameterraums verwendet werden. Die Analyse des TS und der PDF eignen sich besonders für kleine atomare Cluster in der frühen Nukleationsphase. SAXS unterstützt die Detektion der Anisotropie der Nanokristalle. Die Strukturierung des Lösungsmittels und seine Wechselwirkung mit den Nanokristallen können als weitere Kontrollmechanismen für die Partikelgröße und -form dienen. Durch gezielte Veränderung der hier identifizierten Zwischenzustände, Liganden und Lösungsmittel lassen sich Materialeigenschaften grundlegend beeinflussen, was neue Synthesewege ermöglicht.

Abstract

Colloidal nanocrystals have fascinating size- and shape-dependent properties. A large surface-to-volume ratio, strong quantum confinement and plasmonic effects make them promising candidates for applications in energy conversion and catalysis. Despite rapid experimental progress, rational size- and shape-controlled synthesis of semiconductor, metal, and metal oxide nanocrystals remains a challenge. The temporal evolution of atomic structure and particle shape during synthesis is a subject of current research, with the goal of explaining and optimizing the growth mechanisms. In case of non-classical nucleation, in situ studies can reveal intermediate structures, whose influence on the properties of particles is often unknown.

In this thesis, different colloidal nanocrystal syntheses are studied by X-ray scattering. A combination of laboratory- and storage ring-based sources for high energy X-rays (17.4 to 104 keV) with new experimental setups allows a simultaneous recording of small- and wide-angle X-ray scattering (SAXS and WAXS), total scattering (TS), and analysis of the pair distribution function (PDF). The materials under investigation include anisotropic (rod- or platelet-shaped) lead halide perovskite nanocrystals, copper nanospheres, copper palladium supercrystals, and cobalt oxide nanoassemblies.

SAXS, WAXS and TS with simultaneous photoluminescence spectroscopy show that the synthesis of lead halide perovskite nanocrystals involves micellar structures of the precursors with ligands, and rod-like nanoclusters as intermediates. Initiated by addition of an antisolvent, these nanoclusters either fuse to nanorods in a dense, hexagonal mesophase, or dissolve in favor of slowly growing nanoplatelets, which only later assemble. Copper nanospheres are found to nucleate within a dense subphase consisting of metal-phosphonate lamellae. Copper palladium supercrystals are composed of icosahedral nanocrystals, which assemble into an fcc structure from a short-range-ordered intermediate phase. In case of cobalt oxide, it is shown that polyhedral crystallites arrange into porous particles while growing simultaneously. In summary, for semiconductor, metal, and metal oxide nanocrystals non-classical nucleation, growth, and self-assembly phenomena are frequently observed. For selected systems a defined particle shape anisotropy and a narrow size distribution are achieved by controlled self-assembly. Interactions between nanocrystals, ligands, and solvents play a key role in this process. Here, the solvent is not just a homogeneous and inert medium, but can order on its own, initiate self-assembly, or specifically destabilize the ligand shell. The tunable nanocrystal anisotropy realized in the lead halide perovskite synthesis in particular depends on the dipole moment and the Hansen hydrogen bonding parameter of the solvent-antisolvent mixture.

These results show the potential of in situ X-ray scattering for the rational optimization of non-classical nanocrystal syntheses through quantitative analysis. The automated and miniaturized in situ sample cell developed in this thesis can be used for rapid screening of reaction parameter space. TS and the PDF are especially beneficial for the analysis of small atomic clusters in the early nucleation stage. SAXS helps the detection of nanocrystal anisotropy. The structuring of the solvent and its interaction with the nanocrystals can serve as additional control mechanisms for particle size and shape. A targeted manipulation of the reaction intermediates, ligands, and solvents identified here can fundamentally change material properties and enable new synthesis strategies.

Table of Contents

1 Introduction

At the nanometer scale (1 nanometer = 1 nm = 10^{-9} m) the properties of materials are governed by the laws of quantum mechanics. The wave function of a charge carrier inside a few-nanometer-sized crystal – a nanocrystal – experiences quantum confinement, which only allows it to have certain discrete energies, depending on the nanocrystal size [1]. This gives rise to peculiar effects, such as the tunable color of colloidal solutions of semiconductor nanocrystals all across the visible range [2]. The light-induced collective oscillation of electrons in noble metal nanocrystals, the surface plasmon resonance, leads to a characteristic light absorption, which depends on the nanocrystal size and shape [3]. Nanocrystals in general have a large surface-to-volume ratio and their surface plays a dominant role in their properties, such as solubility, luminescence, and catalytic activity [4]. Research on the synthesis and device integration of nanocrystals has led to improved performance and stability of nanomaterials and has enabled their use in fields such as photonics and electronics, lighting and displays, sensing, and biomedical imaging [5–10].

Achieving a precise composition, size, and shape of nanocrystals via synthetic methods continues to be a central goal of modern nanoscience [11–13]. The experimental efforts culminated in the Nobel prize in chemistry 2023, awarded to Bawendi, Brus, and Yekimov for the discovery and synthesis of quantum dots, i.e., colloidal semiconductor nanocrystals with optical absorption and emission tunable by size [14]. The award recognized not only the scientific and technological importance of these materials, but also the synthetic challenge of nanocrystal quality and homogeneity. Separating burst nucleation and controlled growth of particles, e.g., through injection of reagents into a boiling solvent, has been a key principle for achieving monodisperse nanocrystals [15–17]. A wide variety of size- and shape-controlled nanocrystal syntheses has since been reported [18].

Lead halide perovskite (LHP) nanocrystals in particular are an emerging class of materials with favorable optoelectronic properties such as bright and narrow-banded light emission and relatively simple and rapid syntheses [19, 20]. Additional research efforts have been dedicated to the use of earth-abundant, sustainably sourced, and less toxic substances in nanomaterials [10]. This includes lead free perovskites, non-noble metal nanocrystals, and the combination of noble and non-noble metals in alloys and intermetallics [21–23]. An improved control of the shape of semiconductor nanocrystals towards highly anisotropic structures such as rods or platelets has led to the development of luminescent devices with directional and polarized light emission [24–26].

Regular assemblies, i.e., superlattices or mesocrystals from nanocrystals as building blocks, can show new emergent properties due to electronic coupling, such as superfluorescence [27–29]. The combination of semiconducting, metallic, and insulating nanocrystals may allow to fabricate complex electronic devices from the bottom up [30, 31]. The forces governing nanocrystal self-assembly need to be well understood to produce the hierarchically structured materials for such devices [32].

The challenges of facile synthesis, novel compositions, tunable shape and controllable assembly all benefit from a better understanding of synthetic pathways [33]. While transmission and scanning electron microscopy (TEM/SEM) and powder X-ray diffraction (PXRD) are established tools to characterize nanostructured materials with high resolution, they are typically used on separated and/or purified aliquots instead of the ongoing synthesis

reaction. Optical spectroscopy in the ultraviolet and visible range (UV/vis) is a valuable method to characterize absorption and emission in situ, i.e., during synthesis, to obtain the nanocrystal size and reaction kinetics [34–36]. X-ray spectroscopy, in particular X-ray absorption near-edge structure (XANES), is sensitive to the oxidation state and chemical environment of the probed atoms [37], yet larger structures such as the particle morphology on the nanometer scale remain undetected.

Therefore, in this thesis in situ X-ray scattering is used as a structural probe to study four exemplary nanocrystal syntheses. Small-angle X-ray scattering (SAXS) is sensitive to electron density fluctuations between approx. 1 and 100 nm while wide-angle X-ray scattering (WAXS) reveals crystallinity on the atomic (Ångstrom, 10^{-10} m) scale [38]. Total scattering (TS) and the atomic pair distribution function (PDF) are advanced X-ray scattering methods used to characterize the interatomic distances occurring during the initial nucleation [39, 40]. By using high energy X-ray radiation, ranging from 17.4 keV in the laboratory to 104 keV at a 3$^{\text{rd}}$ generation synchrotron source, reactions can be probed inside large volumes, representative of the bulk synthesis. Through a combination with simultaneous UV/vis spectroscopy structure and emission properties are correlated.

Classical theories describe the pathway from a precursor solution to a nanocrystal via burst nucleation and growth by monomer diffusion [15, 41]. Nonclassical crystallization involves more complex processes, including the formation of intermediate structures and the assembly of primary nanoparticles into regular superstructures [42, 43]. Several examples, studied in more detail throughout this work, show that nonclassical pathways are the rule rather than the exception in syntheses of novel nanocrystalline materials. In situ experiments and a combination of structural and optical techniques are essential to identify and characterize the intermediates [33]. Ligands stabilize the growing nanocrystals inside nonpolar solvents [44]. Their structure and their effect on growth and supercrystalline assembly is less commonly probed with X-ray methods. Solvent properties can be classified with several parameters describing the molecular interactions [45, 46]. A changing solvent environment can induce structural transformations of growing nanocrystals by affecting their colloidal stability, ligand coverage, and surface structure, as well as by inducing self-assembly [27, 47]. Furthermore, structure formation inside the solvent, such as emulsification of multicomponent mixtures, can play a role in the reaction pathway [48–50].

Ultimately, the tuning of size and shape of nanocrystals can be further improved through an increased control of the synthesis, which involves a better understanding of the role of precursors, ligands, and solvents. To achieve this goal, this thesis presents and discusses in situ X-ray studies on semiconductor, metal, and metal oxide nanocrystals. The objective of this thesis is to find structural intermediates in the different syntheses, provide a quantitative description of their structure, deduce their role in the reaction pathway, and (where possible) exploit this role to optimize the nanocrystal properties. The chapters are structured as follows:

Chapter 2 briefly summarizes the basic concepts of synthesis and assembly of nanocrystals and their properties. In particular, the fundamentals of classical and non-classical nucleation, anisotropy, ligands and solvents, interparticle interactions, and assembly strategies are presented. LHP nanocrystals, Cu and CuPd alloy nanocrystals, and CoO nanoassemblies serve as examples for the different material classes, each with their own characteristics and synthetic challenges. The main experimental techniques (SAXS, WAXS, TS/PDF and UV/vis spectroscopy) are introduced in detail, while also covering the other methods of characterization (TEM, SEM, XANES and Fourier transform infrared spectroscopy). In

this introductory chapter, ten subdivided research topics are introduced and motivated (Q1–Q10, as shown in Figure 1.1). These topics can be summarized into three focus areas: experimental control through in situ observation, improvement of analytic methods, and the study of structural intermediates and their function.

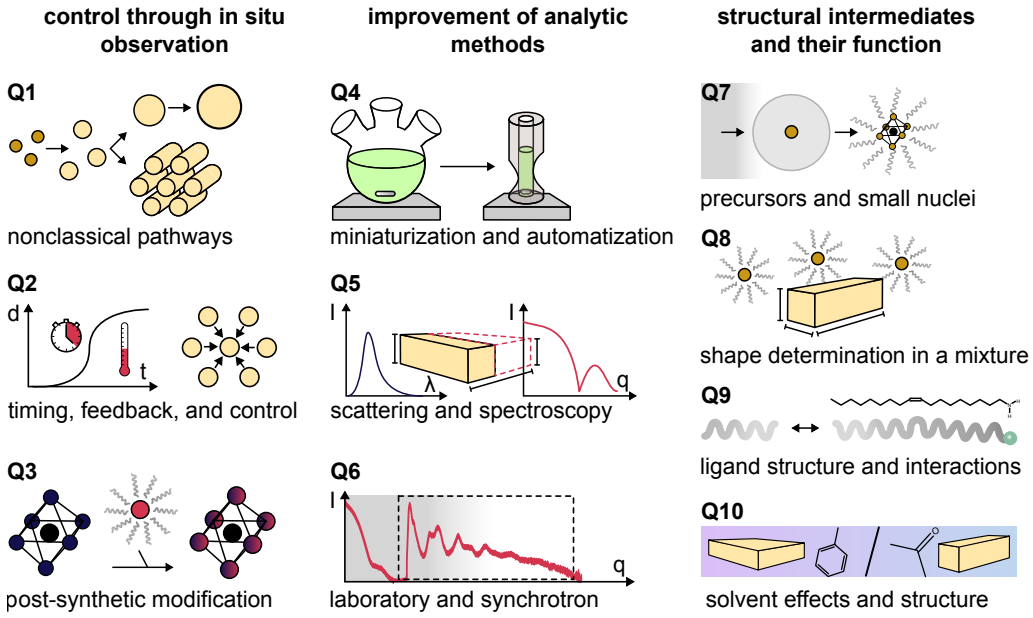

Figure 1.1: Illustrations of the three focus areas and the ten subdivided topics of this thesis.

Chapter 3 describes the experimental methods of nanocrystal synthesis and characterization. In particular, the in situ reaction cell for X-ray scattering and photoluminescence (PL) spectroscopy developed as part of this thesis is presented. The beamline setups used for the experiments at the PETRA III storage ring at the Deutsches Elektronen-Synchrotron (DESY), Hamburg are described. Model equations and analysis sequences for the X-ray scattering patterns and tabulated material properties are included.

Chapter 4 contains the results of this work. The four sections are summarized by short abstracts. Bold text in the abstracts highlights my contribution. Section 4.1 covers the shape control of LHP nanorods and nanoplatelets, and their post-synthetic modification by halide salts. Section 4.2 presents the role of a lamellar intermediate in the nucleation of Cu nanospheres. Section 4.3 follows the one-pot synthesis of supercrystals via icosahedral CuPd nanocrystals. Section 4.4 investigates the synthesis of porous CoO nanoassemblies.

Chapter 5 provides a comprehensive discussion. The common structural intermediates, i.e., nanoclusters, intermediate nanocrystals, assemblies and mesophases, and structured solvents, are compared and further experiments are suggested. An additional discussion is dedicated to the experimental and computational challenges of X-ray scattering-based characterization, including complementary techniques and current technical developments.

A summary of the experimental results and of the overarching discussion is given in Chapter 6, along with an outlook. The Appendix includes additional figures and tables for a more in-depth analysis.

2 Fundamentals

The following section introduces the basic concepts and strategies for synthesizing, assembling, and characterizing size- and shape-controlled nanocrystals. It provides an overview of the relevant equations and current literature and serves as a motivation for the ten subdivided topics addressed by this thesis (Q1 to Q10, illustrated in Figure 1.1).

2.1 Nanocrystal synthesis

Colloidal nanocrystals are produced in a controlled chemical reaction involving one or several precursors, a solvent, and often capping ligand molecules for colloidal stability [51]. In contrast to single crystal growth, which leads to few, macroscopically large crystals, nanocrystal synthesis aims at billions of identical, small copies, which deviate by less than 5% in size [1]. The crystalline domain size is typically on the order of 1 to 10 nm with sizes sometimes ranging up to 100 nm [1, 52]. Termination of crystal growth at a desired size and shape requires a tuning of the nucleation and growth rates and of the precursor and ligand ratios [11, 51]. The complex energy landscape of the process often involves several stable minima [43].

2.1.1 Classical and nonclassical nucleation and growth

Classical nucleation theory describes the formation of a colloidal dispersion from a supersaturated solution [15, 41]: If the solubility is continuously reduced and no nucleation seeds are present, the solution reaches a metastable regime of supersaturation (phase I in Figure 2.1 a). Above a critical concentration C_{min} spontaneous nucleation occurs by random collision of monomers (phase II). The appearance of nuclei relieves the supersaturation below the critical value, which drastically reduces the nucleation rate. In phase III, stable nuclei grow to discrete particles by diffusion of monomers, and an equilibrium concentration C_{sat} is reached. A short "burst" nucleation phase results in monodisperse particles. For a prolonged nucleation phase non-uniform sizes are obtained, since the final size then depends on the time when the nucleus is formed.

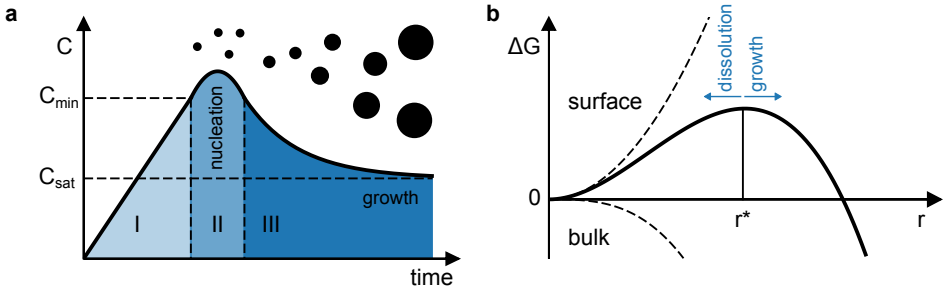

Figure 2.1: Classical nucleation theory. **a**, Schematic sequence of nucleation and growth in the LaMer model [15]. **b**, Gibbs free energy as a function of particle radius. Below a critical radius r^* nuclei tend to dissolve. Above, further growth is energetically favorable.

The critical radius r^* of a nucleus is found by the maximum of the Gibbs free energy $\Delta G_{\mathrm{nuc}}(r) = -\frac{4}{3}\pi r^3\,\Delta G_V + 4\pi r^2\,\gamma$, shown in Figure 2.1 b. ΔG_V is the free energy per unit

volume of the nucleus and γ is its surface energy per unit area. Nuclei with $r < r^*$ redissolve, whereas larger nuclei grow further. At later reaction stages, the size polydispersity can decrease or increase (size focusing or defocusing), e.g., by redissolution or ripening [53]. Ostwald ripening describes the dissolution of smaller particles in a solution and the redeposition of the material onto larger particles [54]. Nucleation and growth phases are well separated in classical models and there are no intermediate minima in the free energy landscape.

Nonclassical nucleation and growth (or nonclassical crystallization) describes multi-step processes (Figure 2.2 a) which involve droplets, clusters, complexes, or oligomers as building blocks instead of atoms, ions, or molecules [42, 55]. Intermediate structures exist in between monomer and crystal and in between molecule and solid. These correspond to local minima in the free energy landscape (Figure 2.2 b) [33, 43].

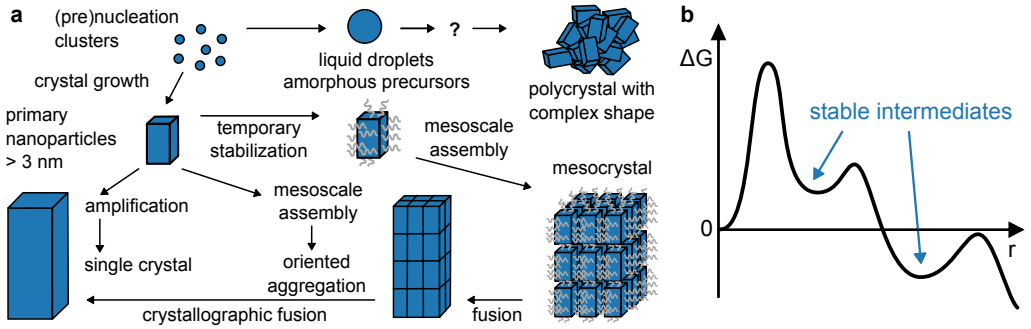

Figure 2.2: Nonclassical crystallization pathways. a, Possible ways of crystallization by a sequence of intermediates. Note the distinction between the growth of a polycrystal and of a mesocrystal or single crystal via primary nanoparticles. Adapted with permission from [42]. Copyright 2019, American Chemical Society. **b**, Schematic free energy landscape as a function of particle radius for nonclassical nucleation, including multiple stable intermediates.

Liquid or amorphous droplets may crystallize to *polycrystalline nanoparticles* [42]. Classical growth can lead to primary nanoparticles, which can be permanently or temporarily stabilized by ligands [43]. Subsequent oriented assembly of these primary particles can lead to the formation of a *mesocrystal* [42]. This term refers to a colloidal crystal of mutually oriented monodisperse nanocrystals, which reaches the microscopic size regime [56]. The terms *supercrystal* or *superlattice* are often used for long-range ordered colloidal crystals with random orientation of the nanocrystalline units [27, 57]. Oriented attachment may transform primary particles to a larger single crystal by crystallographic fusion [55, 58]. Also unoriented aggregation to polycrystalline particles may be followed by recrystallization [59]. Oriented attachment and superlattice assembly have advanced to complex materials design strategies [56, 58]. Liquid-to-crystal transitions are common in protein crystallization [60, 61] and have recently also been realized in the assembly of nanocrystals [62, 63].

Small clusters with a defined number of atoms can exist as transient, i.e., short-lived, intermediates in various syntheses [64, 65]. They can nucleate below the level of supersaturation predicted by classical nucleation theory and thereby affect the kinetics [65, 66]. Also stable magic-sized clusters with a defined number of atoms exist for several metals and semiconductors as locally stable minima in the reaction energy landscape [67–69]. Shape control of nanocrystals via discrete, step-wise transformations of nanoclusters can be achieved if the relevant processes and rates are understood [33, 36, 70].

Organic-inorganic coordination polymers and *mesophases* have also been established as reaction intermediates [69, 71, 72]. These spatially extended intermediate structures consist

of precursor or crystalline material, alternating with organic ligands and/or solvent. They can stabilize embedded clusters [69], act as reservoirs for monomers or as soft templates for low-dimensional nanocrystal growth [73, 74]. Mesophases are liquid crystalline assemblies and show peculiar symmetry and mechanical properties, as detailed below.

Both classical and non-classical nucleation describe the formation of particles from a homogeneous solution, and thus resemble a phase separation, differing mainly in the height of energy barriers [43]. During phase separation a homogeneous mixture transforms into several distinct phases [75, chapter 3]. In the phase diagram (Figure 2.3 a) this means going from a single-phase region into the miscibility gap (shaded area), e.g., by a change of temperature. The spinodal curve describes the composition at which the second derivative of the free energy with composition vanishes [75, pp. 33 ff.]. It encloses a metastable region, in which small fluctuations in composition lead to a spontaneous separation without an energy barrier (Figure 2.3 b), i.e., *spinodal decomposition* [76], and a characteristic pattern of composition fluctuations. In the process of *coalescence* two domains of the same phase come together to form one larger domain [54]. Phase separation in nanocrystal synthesis can occur both in a precursor mixture and in a nanocrystal dispersion before colloidal crystallization [55, 77].

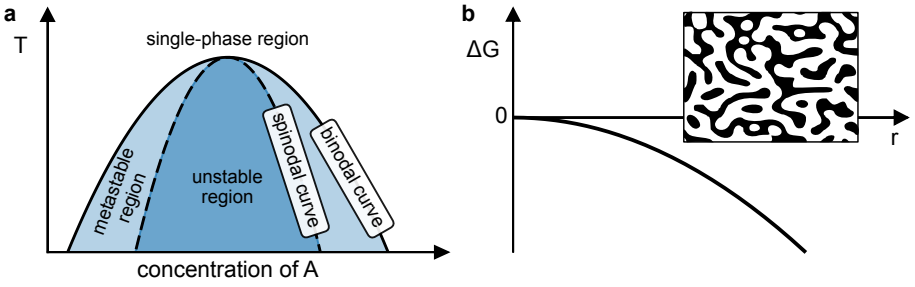

Figure 2.3: Phase separation of a binary mixture. **a**, Phase diagram as a function of an external control parameter, e.g., temperature, showing a miscibility gap, a spinodal curve and a binodal curve. **b**, Schematic free energy as a function of radius for spinodal decomposition. Inset: exemplary structure of a phase-separated mixture.

While detailed theories exist for the individual processes of non-classical crystallization, their interplay still needs to be established for new nanocrystal syntheses of technologically promising materials (see Section 2.3.1 to Section 2.3.3). Preparation of isolable intermediates, where possible, helps to map and optimize the reaction landscapes. Nevertheless, important intermediate structures may go undetected without dedicated in situ experiments, which observe the reaction as it progresses [33]. With in situ X-ray scattering as the tool at hand, the experiments presented in this thesis make nonclassical synthesis pathways visible for different classes of nanomaterials (Q1). Detailed analysis shows when and how fast the structural transformations occur and how they can be controlled to improve the product (Q2).

2.1.2 Nanocrystal shapes

As shown above, the balance of bulk and surface free energy influences the critical size of the nucleus. Similarly, a facet-dependent surface energy determines the growth rate in the respective direction and thus the shape of a nanocrystal [11]. In this thermodynamic picture, particles with isotropic surface energy, such as liquid or amorphous droplets, minimize the surface by a spherical shape. In metals with face-centered cubic (fcc) structure low-

index planes with close atomic packing ({1 0 0}, {1 1 0}, {1 1 1}) are exposed to minimize the free energy. This results in characteristic polyhedral shapes (Figure 2.4 a). Several typical shapes consist of twinned domains, separated by twin planes and connected by special symmetry operations [78, vol. C, chapter 1.3] (Figure 2.4 b). Decahedral and icosahedral particles show a five-fold symmetry of the twin domains around the center, and {1 1 1} outer facets. Also colloidal crystals can grow in an icosahedral shape, which is an optimal packing in spherical confinement [79].

The polyhedron with the lowest surface energy for a given crystalline structure is obtained by the Wulff construction [80, 81]. The surface free energy $\gamma_{[hkl]}$ for a surface normal to a vector $[h\,k\,l]$ is drawn as a plane at a distance proportional to $\gamma_{[hkl]}$ from the origin for all $[h\,k\,l]$. The tangent planes enclose the equilibrium crystal shape. Shapes deviating from the global energy minimum are kinetically controlled. They are metastable forms trapped in a local minimum. Transformation to the equilibrium shape can be arbitrarily slow, depending on the activation barrier [82].

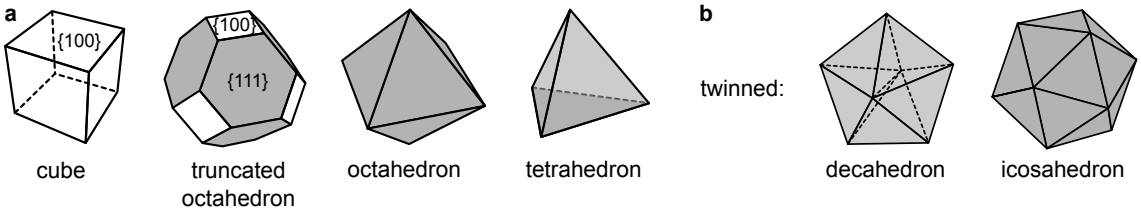

Figure 2.4: Nanocrystal shapes. a, Typical shapes of single crystalline fcc nanocrystals with different facets. **b**, Twinned nanocrystals.

Thermodynamic and kinetic factors influence the shape evolution, and intermediates of different shape may be present simultaneously. This thesis studies how to determine shape in such a complex reaction mixture via model-based analysis of X-ray scattering patterns (Q8) across reaction time and parameter space.

2.1.3 Ligands

Ligands bound to nanocrystals strongly affect their surface energies [82]. Ligands also influence the kinetics of nucleation by affecting the diffusion of monomers to the surface. Furthermore, they regulate precursor availability, impart colloidal stability, prevent fusion of nanocrystals, passivate surface defects such as undercoordinated atoms, and can add functionality such as biocompatibility to nanocrystals [44, 83]. This makes them an essential component of nanocrystal synthesis.

Organic ligands act as a surfactant, binding to the nanocrystal with a (polar) head group and exposing the (unpolar) tail to the solvent. The head group affects facet binding, crystal growth temperature, and electronic properties through its interaction with the nanocrystal core. The tail group mainly controls solubility and colloidal stability, steric hindrance, and monomer diffusion [44]. Typical head groups are carboxylates, amines, phosphonates, thiols, and halides [44]. The oleylamine/oleic acid (OlAm/OlAc) pair, shown in Figure 2.5, is a very common combination [84]. With binary ligand systems, different binding strengths and binding modes to different facets can be used for shape control. Amines often favor a platelet shape of the nanocrystal [25] and have an additional reducing function [84]. OlAm and OlAc are viscous liquids with dynamic viscosities of approx. 5 and 39 mPas, respectively. Using standard bond lengths and angles, the length of an oleate molecule

is approx. 1.9 to 2 nm [85, 86]. A length of 2.05 nm is reported for OlAm [87], and a general length formula is given in reference [88]. Phosphonic acid ligands, e.g., tetradecylphosphonic acid shown in Figure 2.5 are often used for non-noble metal and metal oxide nanocrystals [83, 89].

Taking into account the importance of ligands during synthesis this thesis addresses the question how the ligand structure and the ligand-mediated interactions should be modeled to describe the X-ray scattering patterns (Q9).

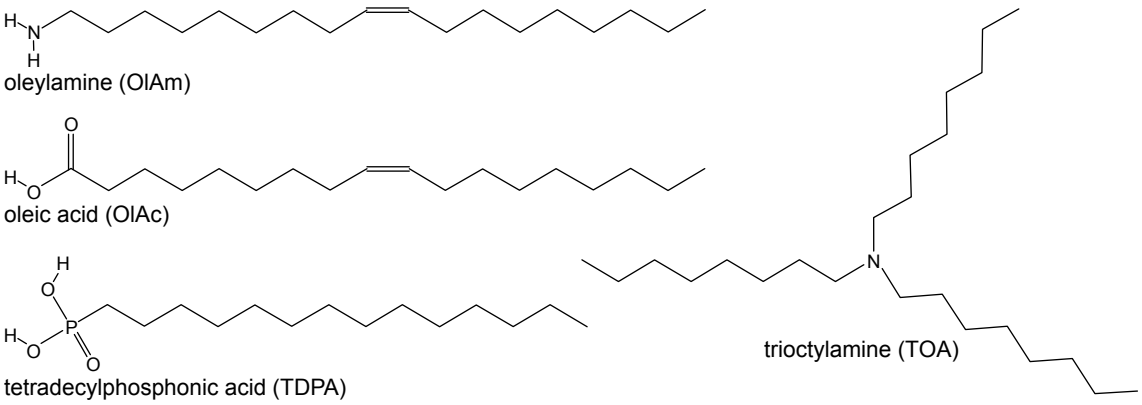

Figure 2.5: Structures of the ligand molecules used in this work.

2.1.4 Solvents

Nanocrystal synthesis is often carried out in organic solvents due to their wide compatible temperature range [52]. Water, ionic liquids, supercritical fluids or biphasic mixtures can also be used [46, 48, 50]. The main task of the solvent is to solubilize and disperse the reactants and the growing nanocrystals. Reaction rates can be strongly affected by the choice of solvent through precursor solubility [90]. After synthesis, nanocrystals can be transferred to a different solvent for storage, characterization, or deposition. Solvents for assembly or device processing require appropriate vapor pressures, wetting characteristics, and compatibility with other deposited materials [27, 45]. The chemical structure of the most important solvents used in this work is shown in Figure 2.6.

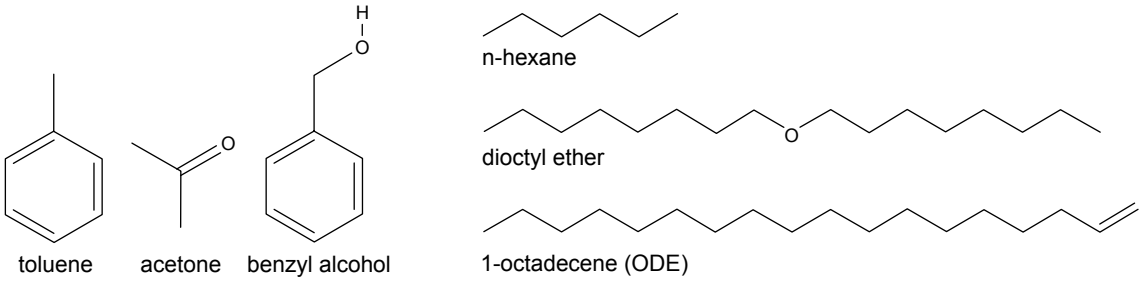

Figure 2.6: Structures of the most important solvent molecules used in this work.

The use of an *antisolvent*, i.e., a poor solvent for either the precursors [91] or the as-formed nanocrystals [20], is particularly common in LHP synthesis and thin film formation: In nanocrystal synthesis antisolvents are used for purification or controlled precipitation of the product from solution [20]. Antisolvents added during spin-coating in solar cell processing lead to a faster and more uniform thin film formation [91, 92].

Several physicochemical concepts are used for solvent classification: *Polarity*, related to the distribution of charges within a molecule, is an essential solvent property. Charge distribution mainly results from the differences in electronegativity of the constituent atoms. A more uneven distribution corresponds to a more polar molecule. Polarity is therefore closely related to the *dielectric constant* ϵ, a measure of the ability to insulate charges [93, chapter 1.7]. ϵ is commonly expressed via the unitless relative permittivity ϵ_r compared to the vacuum value ϵ_0. Polarity is also linked to the *dipole moment* μ, the vector sum of all the bond dipoles of a molecule, with unit Debye (D) [93, chapter 1.8.3]. The polarizability α is the ability to acquire a dipole moment in response to an electric field. Relative permittivity ϵ_r, dipole moment μ, and polarizability α are related by a single equation, which allows to measure the dipole moment experimentally [94, 95].

Empirical polarity scales have been developed for practical use. The $E_T(30)$ polarity scale is based on the solvatochromism, i.e., the solvent-dependent shift of the visible/near infrared absorption band of a particular pyridinium-N-phenolate-betaine dye [96]. Tetramethylsilane and water have the lowest (least polar) and highest $E_T(30)$ values of 0 and 1, respectively.

Solubility for other substances is a key property of a solvent. Solubility theories predict whether a substance dissolves in another based on mutual interaction energies between molecules [97]. Hydrogen bonds are weak ($<$ 20 to 25 $\mathrm{kJmol^{-1}}$ [54]), but important attractive interactions in this context. A hydrogen bond can form between a hydrogen atom from a molecule or a molecular fragment X–H (the donor), in which X is more electronegative than H, and an electron-rich region of an atom or a group of atoms Y–Z (the acceptor), such as a lone pair. *Hansen solubility parameters* assign three energies to a molecule: The energy from dispersive London interactions δ_d (see also Section 2.2.1), the energy from dipolar interactions δ_p, and the energy from hydrogen bonds δ_h, all given in units of $\mathrm{MPa^{1/2}}$. A distance R_a in parameter space can be calculated for a solute-solvent combination:

$$R_a^2 = 4(\delta_{d1} - \delta_{d2})^2 + (\delta_{p1} - \delta_{p2})^2 + (\delta_{h1} - \delta_{h2})^2 \tag{2.1}$$

A radius of solubility R_0 can be determined experimentally and $\frac{R_a}{R_0}$ gives the relative energy difference of the system. Mixtures with a fraction < 1, i.e., within a sphere in the parameter space, dissolve. This thesis uses δ_h for the characterization of solvents, since dispersive and electrostatic interactions are captured by $E_T(30)$ polarity and dipole moment μ.

The *donor number* D_N with unit kcal/mol is a measure of Lewis basicity [98]. It measures the ability of a solvent to solvate cations or Lewis acids. A Lewis acid is a chemical species with an empty orbital, able to accept an electron pair from a Lewis base [54]. In a Lewis base the highest occupied molecular orbital is strongly localized, allowing to form such an adduct. D_N is defined as the negative enthalpy for adduct formation with $SbCl_5$ in the non-coordinating solvent 1,2-dichloroethane. In device processing for photovoltaic applications, D_N indicates the coordinating ability with the Pb^{2+} ion in lead halide precursors [99].

X-ray scattering and diffraction are tools for characterizing structure formation in nanocrystals as well as in solvents. This thesis therefore investigates which level of detail is needed to describe solvent structure in the X-ray scattering patterns of nanocrystal syntheses and which solvent properties affect nanocrystal size and shape the most (Q10).

2.2 Nanocrystal assembly

Assembly of nanocrystals into larger, regular structures like mesocrystals or superlattices is usually done separately from the synthesis reaction [27]. Optimized and purified building blocks with high uniformity, i.e., low size and shape polydispersity, help the formation of long-range symmetry [100, pp. 11721 ff.]. Colloidal crystallization can be used for purification of nanocrystals through size segregation [101].

One-pot syntheses, going from molecular precursors to assemblies via non-assembled nanocrystals and without purification, may provide a simple route towards materials structured on multiple length scales. As an alternative to separate synthesis and assembly experiments, this work investigates assemblies occurring as intermediates as an aspect of non-classical crystallization (see Section 2.1 and Q1). Although the structural quality of such assemblies may not be suitable for further use, the interactions between growing nanocrystals inside them can influence nanocrystal properties (see Q2). The most important interactions, assembly methods, and notable in situ X-ray scattering studies are summarized here.

2.2.1 Interparticle interactions

Besides the dominant van der Waals (vdW) forces between inorganic nanocrystal cores, interactions between surface ligands, electrostatic, and osmotic forces act on colloidal nanocrystals [27], [102, chapters 15 and 16]. The DLVO theory (named after Derjaguin, Landau, Verwey, and Overbeek) combines vdW forces with the electrostatic interactions in an ionic solution [102, pp. 326–331]. The pairwise interaction energy as a sum of vdW attraction, electrostatic repulsion, and steric repulsion, e.g., from non-interpenetrating ligands, is shown in Figure 2.7 a.

In a solution of charged colloids with ions (number density n_i, charge z_i), the electrostatic interaction is screened by a distribution of ions around a colloid. This is described by the Debye screening length $\lambda_D = \sqrt{\frac{\epsilon_0 \epsilon_r k_B T}{e^2 \sum_i n_i z_i^2}}$. ϵ_0 is the vacuum permittivity, ϵ_r is the relative permittivity, $k_B T$ is the thermal energy, and e is the elementary charge. The interaction energy in Figure 2.7 a is shown on a normalized distance scale $\frac{d}{\lambda_D}$. In this work, the ionic strength was not explicitly varied. Therefore, here only vdW and steric interactions are described in more detail.

The attractive *vdW interaction* originates from fluctuations in the charge distributions of two colloids. It includes Keesom interactions between permanent multipoles, Debye interactions between one permanent and one induced multipole, and London dispersion interactions, which arise from instantaneous multipoles. For nanocrystals of identical radius r and surface-to-surface separation d_i the vdW energy is [103]

$$U_{vdW} = -\frac{A}{3}\left[\frac{r^2}{4rd_i + d_i^2} + \frac{r^2}{(2r + d_i)^2} + \frac{1}{2}\ln\left(\frac{4rd_i + d_i^2}{(2r + d_i)^2}\right)\right] \tag{2.2}$$

A is the Hamaker constant, which is calculated in Section 3.4.5. Common interaction geometries and values of A are tabulated in [102, chapter 13].

Ligand shells stabilize colloidal solutions of attracting nanocrystals by repulsion due to *steric interaction* [27]. The elastic compression of ligand chains in contact can be described

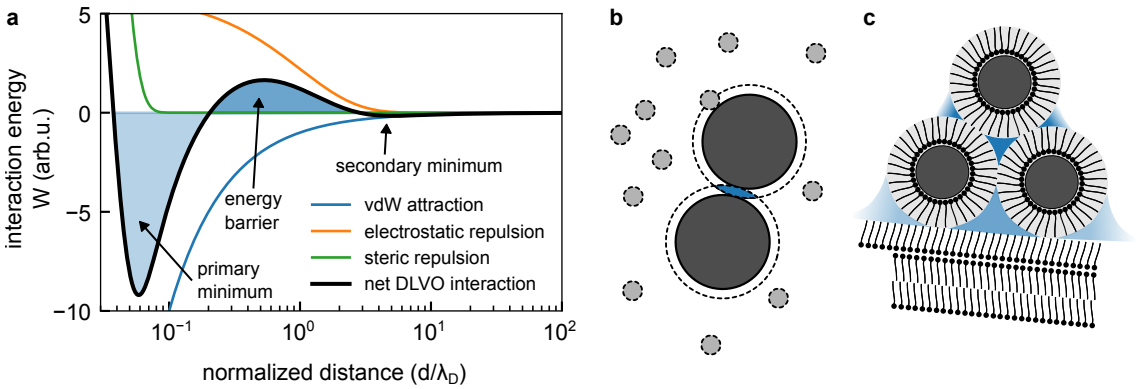

Figure 2.7: Interactions between colloids. **a**, Pairwise colloidal interactions (colors in legend). Shaded areas indicate the deep primary energy minimum, the shallow secondary minimum and an energy barrier in between. **b**, Illustration of depletion interactions. **c**, Illustration of geometric frustration between ligand-coated colloidal particles and ligand lamellae.

as flexible polymer brushes in the Derjaguin approximation [104]. The interaction energy is

$$U_{steric} = k_B T \frac{\pi^3 \sigma r L_0^3}{120 R_e^2} \left(-45 - 40 \ln u + 54u - 10u^3 + u^6\right), \qquad u = \frac{d_i}{2L_0} \tag{2.3}$$

σ is the ligand grafting density. L_0 is the full length of the ligand layer and R_e^2 is the entropic repulsion parameter. Depending on the respective amplitudes, the combination of attractive and repulsive interactions can result in a deep primary (several k_BT) and a shallow secondary potential minimum ($< k_BT$), separated by an energy barrier. Rapid destabilization of a colloidal solution into the primary minimum often results in disordered aggregates. Slow assembly in near-equilibrium conditions favors regular assemblies, since colloids can explore several configurations by thermal motion [27], [100, p. 11723].

Depletion forces with entropic origin result from small, non-interacting cosolutes (depletants, gray circles in Figure 2.7 b) [102, pp. 398 ff.]. The centers of the depletants cannot enter the excluded volume around the colloids (dashed circles). When colloids come into close contact the excluded volumes overlap (blue area), which increases the total volume available for depletant diffusion. The increase of the translational entropy of the depletants leads to an effective osmotic pressure and can induce precipitation of the colloids [27, pp. 11261 f.].

Ligand chains belonging to different nanocrystals in close contact can interdigitate [86], leading to mutual attraction [105]. In the presence of solvent, ligand shells can be swollen by intercalation of solvent molecules [44]. In dense assemblies ligands fill the space between the nanocrystals (blue shaded areas in Figure 2.7 c), which leads to alternating compression and expansion within the Wigner-Seitz cell and an elastic energy penalty [106]. A similar packing frustration occurs at the interface of curved nanocrystal surfaces with planar surfaces, such as flat ligand multilayers.

The weak, cooperative ordering of molecules or colloids can result in the formation of a liquid crystal. This state of matter has properties in between liquids (e.g., the ability to flow) and solids (e.g., defined orientational order) [75, chapter 7]. Some typical liquid crystal mesophases are depicted in Figure 2.8. In a nematic phase, rod-like particles align with their long axes in parallel, but without positional order. In smectic phases, rods arrange inside planes with or without a collective tilt (smectic A and smectic C). Disk-like particles can form nematic, columnar/discotic, or lamellar phases. Thermotropic liquid

crystalline phases form at different temperatures. In lyotropic phases solvent molecules surround the particles, which allows phase transitions as a function of concentration.

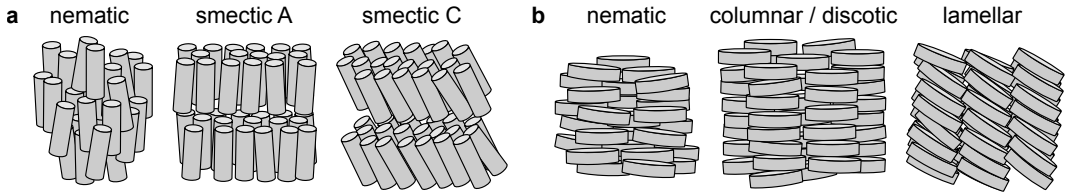

Figure 2.8: Liquid crystalline phases of rods and disks. **a**, In addition to the isotropic liquid and the crystalline solid there are nematic and smectic phases of rod-shaped particles. **b**, For disk-shaped particles nematic, columnar/discotic and lamellar phases exist [27, p. 11240 f.].

2.2.2 Assembly methods

Colloidal self-assembly makes use of fundamental interparticle interactions and controlled reaction conditions. Solubility is reduced so that nanocrystals arrange into an ordered structure to minimize the free energy [27, p. 11226]. The most common techniques, shown in Figure 2.9, are solvent evaporation, addition of salt or depletant, diffusion or enrichment of a nonsolvent, and variation of temperature [27, pp. 11222–11225]. Other strategies include sequence-programmable linkers, auxiliary surfaces, external fields, or geometric confinement [27, pp. 11258 ff.].

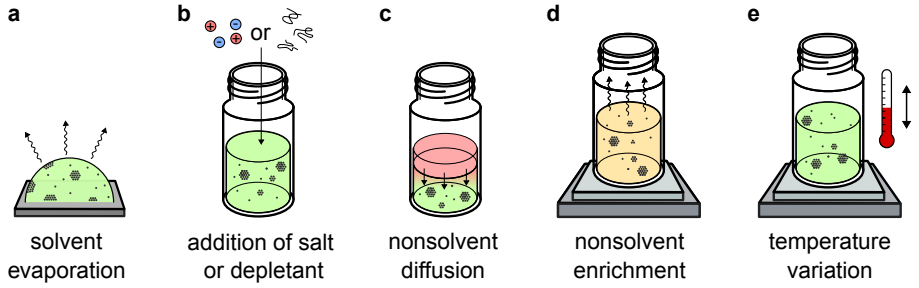

Figure 2.9: Methods for colloidal self-assembly. **a**, Solvent evaporation of a droplet on a substrate. **b**, Destabilization of a colloidal solution via addition of salt or depletant. **c**, Diffusion of a non-solvent (red) into the solvent (green). **d**, Increase of the volume fraction of a nonsolvent with a higher vapor pressure by evaporation of the solvent. **e**, Assembly by adapting the temperature.

When letting a drop of nanocrystal solution evaporate on a substrate, *evaporation-based assembly* can lead to the formation of superlattices. They can nucleate from nanocrystal monomers not only at the solid-liquid interface as a film, but also at the liquid-air interface, confined in a meniscus in a capillary experiment, or in the bulk solvent [107–109]. The choice of solvent can affect the orientation of the nanocrystals on the substrate [110]. Evaporation-based assembly can result in high structural quality and a defined substrate orientation, as visible in electron microscopy or X-ray diffraction [111], but may require many hours or days [56, 112].

Addition of salt to a nanocrystal solution increases the screening of electrostatic interactions, resulting in a more attractive interparticle potential. Depending on the depth and range of the potential either long-range ordered superlattices or short-range ordered aggregates are formed [77, 113]. *Depletion-based self-assembly* is achieved by adding small, non-interacting cosolutes, i.e., polymers or excess ligands, to the nanocrystal suspension [27, pp. 11261 f.], [114].

In *nonsolvent diffusion* a layer of nonsolvent is carefully placed on top of the nanocrystal solution [115]. The slow intermixing of the liquids leads to a gradual decrease of colloidal stability so that the nanocrystals assemble and sediment. In *nonsolvent enrichment* the lower boiling point solvent in a mixture is slowly evaporated, leaving behind a destabilized mixture [116]. Destabilization can also be achieved by simple addition of a non-solvent [117].

Self-assembly by *temperature variation* is typically induced by cooling the nanocrystal solution [103, 118]. Conversely, increasing order upon heating has been reported as a consequence of a melting transition of the ligand shell [119]. Heating or cooling cycles can induce symmetry changes in superlattice structure [120]. Self-assembly at a constant temperature can result from size-dependent vdW interactions if nanocrystal growth and assembly coincide in time [121]. Temperature variation is rather easily applicable to one-pot approaches, where assembly follows nucleation and growth in a single reaction [69, 103, 121–123].

2.2.3 Reaction environments for in situ experiments

In situ X-ray scattering is commonly used to study both nucleation and growth and assembly of nanocrystals [38, pp. 11156 ff.]. In this section several notable studies are categorized by the type of reaction environment (aliquots, flow, miniaturized or shape-adapted reaction vessel) and by the reaction phase (nucleation, assembly, or both). In situ X-ray spectroscopy studies, which often complement scattering experiments, are reviewed in reference [37].

Firstly, nanocrystal synthesis can be studied by *extracting aliquots* from a reaction vessel (Figure 2.10 a), and stopping the reaction in the aliquot, e.g. by cooling in an ice bath [124–126]. Assembly experiments can be carried out under different conditions in separate capillaries [127]. The aliquot as a solution is investigated by ex situ techniques, such as SAXS, WAXS, or TS, or further prepared for, e.g., PXRD or electron microscopy. The measurement conditions and data quality can be optimized for each technique, but the course of the reaction may be altered by aliquotation, cooling, or sample deposition, and time resolution is limited by the extraction.

Secondly, the reactor can be integrated into a measurement setup by continuously pumping the solution through a capillary for *flow-through characterization* (Figure 2.10 b). A conventional large reaction environment with temperature control, stirring, reagent injection, etc., can be used [129]. The reaction conditions are probed closely to the bulk, but may be altered due to pumping or temperature inhomogeneity. Assembly can be induced, e.g., by confinement of nanocrystals in emulsion droplets, which stay intact under flow [85, 130, 131]. The extracted part of the solution can be returned to the bulk volume or collected as aliquots [132].

Nanocrystal syntheses can be carried out entirely in flow by using (micro)fluidic reactors or stopped-flow systems [133, 134]. In situ X-ray or optical probes can be integrated in such reactors as shown in Figure 2.10 b [135]. Automated screening of reaction conditions is feasible with this approach.

Thirdly, the reaction vessel can be *miniaturized* to allow for in situ measurement through the bulk (Figure 2.10 c). In situ X-ray scattering requires an X-ray path length across the reaction volume in the millimeter range (to reduce absorption) and a reactor window

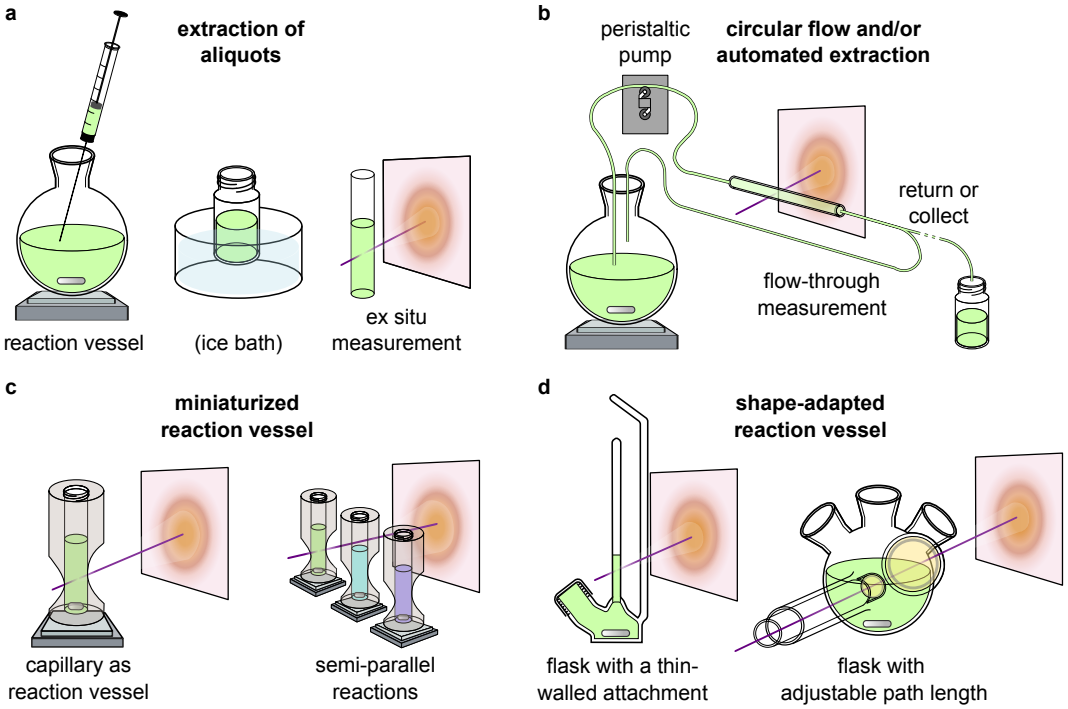

Figure 2.10: Sample environments for X-ray scattering studies of nanocrystal synthesis and assembly. **a**, Extraction of aliquots from a reaction mixture for ex situ characterization. **b**, Automated extraction of the reaction mixture using a pump. Material can be returned to the reactor in a circular flow or collected as aliquots. **c**, Miniaturized reactor for probing the bulk of the reaction mixture. Different reactions can run in parallel, and one at a time is probed. **d**, Shape-adapted glassware can fulfill the shape requirements for different in situ techniques. **d** (left panel) is adapted with permission from [128], Copyright 2022, Royal Society of Chemistry.

thickness in the $\approx 100\,\mu m$ range (to reduce background), as discussed in Section 2.4.5. Miniaturization has been achieved by using a nuclear magnetic resonance (NMR) tube [124, 136], a cuvette with thin glass windows [113], a custom flat-bottom glass capillary [137], a free-standing horizontal capillary [138] or a sandwich of X-ray transparent foils [69]. Several miniaturized reactors can be probed one at a time in a semi-parallel experiment [139]. Temperature control, stirring, reagent injection, etc., need to be remote controlled due to radiation protection. Nucleation, growth, and assembly may be influenced by the increased surface-to-volume ratio of smaller reactors or an inefficient stirring at small capillary diameters. In situ TEM sample environments, with sub-microliter volumes placed in high vacuum, can be considered extreme examples of such a miniaturization.

Fourthly, more complex requirements, e.g., for addition of powders [140], can be fulfilled by *shaping the reaction vessel* via glassblowing (Figure 2.10 d). A thin-walled attachment [128] or an inward recess [103, 113, 141] as an X-ray window is molten to a glass flask. Alternatively, X-ray transparent foils [142, 143], or a length-adjustable insert are added [144, 145]. The volume can be identical to laboratory conditions while allowing X-ray measurements as close as possible to the bulk.

In this work miniaturized and shape-adapted reactors are used for in situ X-ray scattering due to the rather simple reaction conditions and the use of highly penetrating high energy X-rays. Considering the limited reaction volume and space constraints inside the X-ray setups, the question is addressed how to mimic and automate the laboratory syntheses (Q4).

2.2.4 Quantification of nucleation, growth and assembly pathways

In addition to the choice of a sample environment the modeling of in situ X-ray data regarding structure and kinetics deserves particular attention. Finding the rate-limiting phenomena in *nucleation and growth processes* is crucial for size- and shape-controlled synthesis. Different in situ X-ray scattering studies have identified precursor reactivity, thermal activation, diffusion, and reactions at the nanocrystal surface as limiting factors for the reaction rate [72, 141, 146, 147]. Different ligands can change the reaction rate by orders of magnitude [34, 123, 148].

The duration and temporal correlation of nucleation and growth phases can be analyzed via kinetic laws. In addition to the LaMer model for burst nucleation and three-dimensional growth shown above, Finke and Watzky have proposed a model of continuous nucleation and autocatalytic surface growth to describe the sigmoidal kinetics of the transformed material fraction [149]. Furthermore, the JMAK equation (named after Johnson, Mehl, Avrami, and Kolmogorov) describes isothermal phase transformations in the solid state, assuming homogeneous nucleation and isotropic growth [150]. Here, the transformed material fraction as a function of time t is

$$x(t) = 1 - \mathrm{e}^{-(k_g\, t)^n} \tag{2.4}$$

where k_g is the growth rate constant. The exponent n can range between 1 and 4, where lower values represent lower-dimensional growth. The Gualtieri model combines a nucleation and a growth term and has been applied to nanocrystals as well as supercrystals [143, 151, 152]:

$$x(t) = \frac{1}{1 + \mathrm{e}^{-\frac{t-a}{b}}} \left[1 - \mathrm{e}^{-(k_g\, t)^n}\right] \tag{2.5}$$

a and b are the mean and standard deviation of a Gaussian distribution of nucleation time and $\frac{1}{a}$ is the nucleation rate constant.

In situ SAXS experiments have been used to study shape evolution, e.g., to investigate if two-dimensional nanocrystals grow via templating [71, 74, 153]. Model based SAXS analysis has revealed particle anisotropy [142, 154] and seeded growth through multicomponent models [155]. Also the transformation of primary particles to agglomerates has been quantified by SAXS [156], including complex models involving nonclassical intermediates [157]. SAXS analysis is often complemented by refinement of WAXS or PDF data to analyze the evolution of crystallinity and strain, or precursor complex and cluster formation [158–161]. PDF analysis in particular has been used for alloy and intermetallic nanocrystals [162].

In situ scattering studies of *assembly* often focus on the details of the underlying mechanism, such as the ligands, solvents, forces, or intermediates involved [113, 117, 130, 131]. Here, quantitative SAXS analysis can reveal the fractions of free and assembled nanocrystals [103, 107] and the interparticle spacing [86, 117, 123, 131]. Via scanning of the sample the sedimentation of larger assemblies, phase segregation, or the propagation of an assembly front can be probed [77, 163]. Transformations of superlattice symmetry, strain, and defects have been investigated [85, 109, 118, 120, 152, 164] to optimize crystallinity or conductivity [77, 116].

In in situ X-ray studies of *one-pot nucleation, growth, and assembly* regular superlattices are typically found after nanocrystal growth is completed [122, 123]. Sometimes both processes coincide [74, 103, 121] or partly overlap [143]. Attractive vdW forces, which

become dominant above a certain nanocrystal size, are typically identified as the driving mechanism for assembly [103, 121, 123]. Low size polydispersity of the nanocrystals leads to high assembly quality and long-range order [100, 121]. Conversely, the dense and regular packing inside an assembly can affect the size distribution of growing nanocrystals (see Q2): The close interparticle distance can increase the growth rate by enhanced ripening [143], slow it down by inhibiting monomer diffusion [69], or leave it unaltered [103].

Ligands play a crucial role inside nanocrystal assemblies. They make nanocrystals act as soft rather than hard spheres, which lowers the density required for assembly [44]. Longer ligands lead to a larger surface-to-surface separation [85], with subtle deviations due to interdigitation or a partly folded surface conformation [86]. Excess ligands are often found to be beneficial for superlattice formation [44, 103]: In addition to a depletion effect [114], a swelling of the bound ligand shell by free ligands enhances nanocrystal ordering and can be used to tune the lattice symmetry [86, 165].

Self-assembly is affected by the choice of solvent, mainly through solvent-ligand interactions [117]. A change of solvent can affect the solubility of the ligand shell and thus the colloidal stability of the nanocrystals, or strip ligands from nanocrystal surfaces [47]. In mixtures, solvent molecules can be extracted from the swollen ligand shell due to a miscibility gradient [117]. Freezing of the solvent expels the nanocrystal solutes and accumulates them at a propagating crystallization front, which leads to complex interactions [166].

A thorough understanding of nanocrystal synthesis and assembly needs knowledge of intermolecular interactions, a grasp of the combinatorics of multicomponent mixtures and reaction conditions, and quantitative experiments. Having summarized these aspects, the following section introduces the properties of semiconductor, metal, and metal oxide nanocrystals and their assemblies, which motivate their ongoing study and optimization.

2.3 Properties of nanocrystals and assemblies

2.3.1 Semiconductors and perovskite nanocrystals

Semiconductor nanocrystals from lead halide perovskite (LHP) have favorable optoelectronic properties, are obtained from relatively facile syntheses, and have therefore attracted considerable attention in research and technology [19, 20]. The term perovskite originally referred to the mineral $CaTiO_3$, discovered in the Ural mountains in 1839 [167]. Now perovskite denotes a class of materials of composition ABX_3, which share a particular *crystal structure*, shown in Figure 2.11 a and b. A is a monovalent cation, B a divalent cation and X a monovalent anion [20]. In the perovskite structure, corner-sharing BX_6 octahedra are placed on a cubic, tetragonal or orthorhombic lattice. A cations occupy the void between the neighboring eight octahedra.

LHPs were first described in 1893 as $CsPbX_3$ (X = Cl, Br, I) [170]. They returned into the spotlight in 2009, when the organic-inorganic hybrid methylammonium lead halides, $MAPbX_3$, were used in dye-sensitized solar cells [171]. After the optoelectronic properties of LHPs such as long charge carrier lifetimes and high photoluminescence quantum yield (PLQY) were discovered, a rapid increase of solar cell efficiencies followed, now exceeding 26% power conversion efficiency [92]. Light-emitting diodes (LEDs) based on LHPs with external quantum efficiencies over 26% [172–174] as well as perovskite-based lasers have been developed [175]. X-ray detection is a further emerging field of application for LHPs

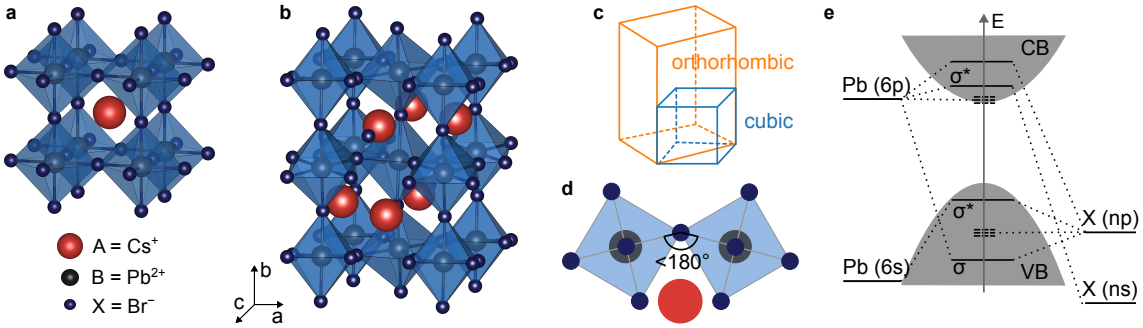

Figure 2.11: Perovskite crystal structure. **a**, Unit cell of a perovskite ABX_3, e.g., $CsPbBr_3$, with cubic structure ($Pm\bar{3}m$, 221). **b**, Unit cell of a perovskite with orthorhombic structure (Pnma, 62) [168]. Note the slight tilt of the octahedral $PbBr_6^{4-}$ units, which requires an enlargement of the unit cell compared to the cubic type (**c**). **d**, Reduction of the Pb–Br–Pb angle as a result of the tilt. **e**, Contributions of the lead and halide orbitals to the conduction (CB) and valence band (VB) edges. σ and σ^* denote bonding and antibonding contributions. Dashed lines indicate shallow defect states. **e** is based on reference [169].

[176]. $CsPbBr_3$ with its small inorganic cation has received particular attention, especially in the form of nanocrystals [20]. LHP nanocrystals can be used for fundamental studies of their excitonic fine structure [177] with potential applications in quantum information processing [178], the coupling of excitons and phonons [179, 180], and optical nonlinearity such as multiphoton absorption [181].

Whether an ABX_3 compound can crystallize in the perovskite structure depends on the ionic radii r_A, r_B, r_X via the *Goldschmidt tolerance factor* $t = \frac{r_A + r_X}{\sqrt{2}(r_B + r_X)}$ [182]. t must be between 0.8 and 1, with a value of 1 indicating a cubic structure ($Pm\bar{3}m$, space group 221). Smaller values lead to a tilt or a distortion of the octahedral units and a lower symmetry structure with a larger primitive unit cell (see Figure 2.11 c) [183]. Bulk $CsPbBr_3$ ($t = 0.92$ [183]) is orthorhombic (Pbnm or Pnma, 62) at room temperature, tetragonal (P4/mbm, 127) above 360 K, and cubic ($Pm\bar{3}m$, 221, lattice constant $a \approx 5.8$ Å to 5.9 Å) above 410 K [184, 185]. $CsPbBr_3$ nanocrystals and nanoclusters also have orthorhombic structure [186–188]. Twinned, locally orthorhombic domains can result in a cubic long-range order with an extended Pb sublattice [189]. For $CsPbI_3$ ($t = 0.89$ [183]) both orthorhombic (Pnma, 62) and cubic structures ($Pm\bar{3}m$, 221, $a \approx 5.8$ Å) at room temperature have been reported [2, 186, 190, 191].

The *octahedral tilt* is described by 23 tilt systems, e.g., $a^+b^-b^-$ for Pnma [192]. They indicate along which axis (a, b) the octahedral units are tilted and whether neighboring units inside a large, non-primitive supercell tilt in phase (+) or out of phase (–) [193]. As a result of tilt the Pb–Br bond angles on a Br atom are smaller than 180°, as shown in Figure 2.11 d. 165.5° and 157.42° have been reported for axial and equatorial Br in bulk orthorhombic $CsPbBr_3$ [194]. The tilt system of LHP nanocrystals can be controlled by reaction kinetics [195]. The layered, Cs-deficient $CsPb_2Br_5$ and the Pb-deficient Cs_4PbBr_6 with its isolated $PbBr_6$ octahedra are not strictly perovskites [196]. They can form as synthesis byproducts or through transformations from $CsPbBr_3$ [143, 197].

Unlike their classical semiconductor counterparts (Si, Ge, GaAs, CdSe, InP, etc.) LHP nanocrystals form at room temperature and under ambient conditions simply by a mixing of precursors, due to their ionic nature [20, p. 10776]. The band structure of LHPs near the conduction and valence band edges can be approximated as shown in Figure 2.11 d. Defect states arising from lead vacancies are located at the energy levels of the halides, which are within the valence band. Dangling lead bonds from halide vacancies lie close to

or within the conduction band [169]. The shallow nature of the defect states and a self-healing property through ion migration in the lattice make LHP "defect tolerant" [198]. This means that (opto)electronic properties are not strongly deteriorated by defects. Post-synthetic treatment with halide salts has been used to passivate surface vacancies and to increase the PLQY to near unity [199, 200].

Due to the valence band maximum involving a halide p orbital the bandgap of LHPs can be changed by the halide composition, with a substantial decrease going from X=Cl (3.0 eV) via Br (2.3 eV) to I (1.7 eV) in $CsPbX_3$ [168, 169]. This is due to the increasing halide ionic radii from Cl^- (1.67 Å) via Br^- (1.82 Å) to I^- (2.06 Å) [201]. Halide anions can be mixed for tuning the optoelectronic properties [199, pp. 316 f.]. Optimized formulations with mixed cations are used for photovoltaics [92]. Halide anions are rather mobile in the perovskite lattice and can be exchanged completely by supply of an excess salt and diffusion [202, 203]. *Vegard's law* is a heuristic structure relationship for such mixed compounds. It states that the lattice parameter of a solid solution with a unique phase is approximately the weighted mean of the lattice parameters of the components [204]:

$$a(A_{1-x}B_x) = (1-x)\,a_A + x\,a_B \tag{2.6}$$

a_A and a_B are the lattice parameters of the components and x is the molar fraction of B in the solution. This assumes that the components have the same crystal structure. Considering the different ionic radii of halide ions and the possible octahedral tilts in LHPs this thesis investigates which structural changes accompany a post-synthetic ion exchange (Q3).

The size of perovskite nanocrystals, especially anisotropic nanorods and nanoplatelets, is usually given as the number of monolayers (ML) of PbX_6 octahedra [25]. Compared to the bulk, the optical absorption and emission of nanocrystals are strongly modified by their finite size through quantum and dielectric *confinement effects*: When a semiconductor absorbs a photon with an energy exceeding the bandgap E_g, an electron is excited to the conduction band and a hole results in the valence band [205, chapter 4]. Through Coulomb interaction, electron and hole form a bound pair, the exciton. Wannier-Mott excitons are spatially delocalized with an exciton Bohr diameter $d_n \approx 7\,\text{nm}$ for $CsPbBr_3$ [2], [20, p. 10790]. Electron and hole in a nanocrystal with size d comparable to d_n can only occupy discrete energy states within the potential well of the crystal [205, chapter 6], which gives rise to the quantum confinement effect. Dielectric confinement refers to the fact that the nanocrystal has a larger dielectric constant than the surrounding [206]. In the limit of strong quantum confinement ($d < d_n$) in all three dimensions (a quantum dot) the electronic density of states is peaked at discrete levels, resembling an "artificial atom" [207], [205, chapter 6]. The energy states $E_c(n)$ can be described by an infinite potential well model

$$E_c(n) = \frac{\pi^2\hbar^2}{2m^*d^2}\,n^2 \tag{2.7}$$

d is the width of the well, m^* is the effective electron or hole mass, $\hbar$ is the reduced Planck constant, and n is an integer. The rod- and platelet-shaped LHP nanocrystals studied here are confined in all dimensions, but some sizes are outside of the strong confinement regime. For such rectangular nanoprisms with d_x, d_y, d_z the energy levels are

$$E_c(n_x, n_y, n_z) = \frac{\pi^2\hbar^2}{2m^*}\left(\frac{n_x^2}{d_x^2} + \frac{n_y^2}{d_y^2} + \frac{n_z^2}{d_z^2}\right) \tag{2.8}$$

with integer n_x, n_y, n_z. The smallest dimension has a dominant influence on the confinement energy via the inverse square dependence in the sum.

Optical absorption and emission spectra of semiconductor nanocrystals are strongly affected by confinement. In a direct bandgap semiconductor (see Figure 2.12 a) excitons can be generated by a transition at $\boldsymbol{k} = 0$ when the incident photon energy $\hbar\omega_1$ equals $E_g - |E_e(n)|$. $E_e(n) = -\frac{\mu}{m_0}\frac{1}{\epsilon_r^2}\frac{R_H}{n^2}$ are the discrete "hydrogen-like" bound exciton energy levels. μ is the reduced electron-hole mass and m_e^*, m_h^* are the effective electron and hole masses, related by $\frac{1}{\mu} = \frac{1}{m_e^*} + \frac{1}{m_h^*}$. m_0 is the mass of the electron, ϵ_r is the relative permittivity, and $R_H = 13.6\,\text{eV}$. The discrete energy states lead to peaks in the absorption spectrum within the fundamental bandgap, as shown in Figure 2.12 b.

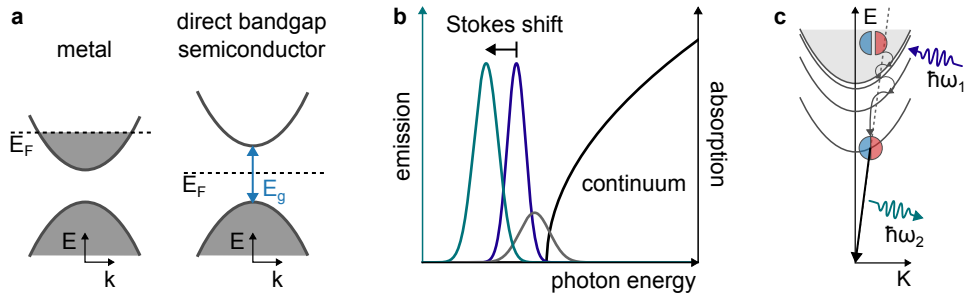

Figure 2.12: Band structure, light emission and absorption. **a**, Band structure of a metal and a direct bandgap semiconductor. $\boldsymbol{k}$ is the crystal wave vector of electrons or holes. E_F indicates the Fermi level, E_g the bandgap. **b**, Contributions to the absorption and emission spectra. Black: absorption into the continuum, peaks: absorption into excitonic states. Teal peak: Energy of an emitted photon, separated from the absorption maximum by the Stokes shift. **c**, Illustration of light absorption and emission [205, p. 119]. Incident light with energy $\hbar\omega_1$ creates an electron-hole pair, which relaxes into the 1s exciton state by phonon emission, followed by emission of a photon with lower energy $\hbar\omega_2$. K is the exciton wave vector.

An excited state can decay by emission of a photon (photoluminescence, PL) with an energy $\hbar\omega_2$ and a radiative lifetime τ_R, as shown in Figure 2.12 c [205, chapter 5.3]. Alternatively, the excited state can decay non-radiatively with a lifetime τ_{NR}, e.g. by emitting phonons or losing energy to impurities or defects. This limits the luminescent efficiency $\eta_R = \frac{1}{1+\frac{\tau_R}{\tau_{NR}}}$. For efficient light emission radiative lifetimes are short ($\tau_R << \tau_{NR}$, $\eta_R \to 1$). Radiative lifetimes of $CsPbBr_3$ nanocrystals reach below the nanosecond range [2, 29, 34].

For nanocrystals, the absorption threshold for a photon gets raised with respect to the bulk bandgap due to the discrete states $E_c(n)$ allowed by quantum confinement. The corresponding PL emission peak is shifted to higher energy, the smaller the nanocrystal [34, 208, 209]. Size control thus tunes absorption and emission without changing the composition. Conversely, nanocrystal size can be inferred from spectroscopic measurements [35]. Considering that anisotropy of a nanoprism is not evident from the value of the confinement energy (see Equation 2.8), this work combines optical spectroscopy with solution X-ray scattering for shape determination (Q5).

Long-term stability and the susceptibility to environmental factors are the main limitations for the application of LHP nanocrystals in a commercial setting [20, 210]. Moisture, heat, oxygen and UV radiation accelerate the degradation of LHPs [211]. Halide segregation is an additional degradation pathway of mixed halide perovskites under illumination or current injection [212]. The contained lead poses an additional risk due to its toxicity [20, pp. 10832 f.], yet lead-free perovskite derivatives show rather limited performance [20,

pp. 10840 f.]. Encapsulation of LHPs is explored as a strategy to mitigate both stability and toxicity concerns [20, pp. 10825 ff.].

Regarding stability and an increased PLQY, surface termination and ligand passivation of LHP nanocrystals have been widely investigated [213]. For $CsPbBr_3$ nanoplatelets a termination by CsBr with Cs and Br vacancies has been determined by X-ray diffraction [187]. For the typically used OlAm/OlAc ligand pair, shown in Figure 2.5, alkylammonium ligands occupy the positions of Cs^+ cations and carboxylate ligands replace Br^- anions [213]. Size- and shape-uniform LHP nanocrystals can serve as building blocks for assembled materials [214, 215], making further use of the concept of an "artificial atom" [1]. Such assemblies can show cooperative effects such as superfluorescence, as summarized in Section 2.3.4.

Going from confinement in all dimensions (i.e., "zero-dimensional" quantum dots) to a nanorod shape (one-dimensional, 1D [24, 209]) or a nanoplatelet shape (two-dimensional, 2D [25, 216]) opens up further possibilities for fundamental studies. Exemplary optical spectra and a visual impression are shown in Figure 2.13. In addition to a tunable emission into the deep blue part of the spectrum [20] *anisotropic LHP nanocrystals* can show directional and polarized light emission [217, 218]. This is due to the oriented transition dipole moment of an anisotropic structure, which can be detected in solution [219] or by regular assembly (face-down or edge-up) on a substrate [26, 220].

As a consequence, many research groups have investigated strategies for fine-tuning the anisotropy of LHP nanocrystals during synthesis [24, 25]. Conventional anisotropic semiconductor nanocrystals such as CdSe have been studied and optimized similarly [221], but their syntheses proceed rather slowly during minutes to hours. This allows to take aliquots at different reaction times and facilitates structure determination by in situ methods [74, 153]. LHPs, due to their ionic character, react quickly during milliseconds to seconds, which complicates time-resolved analysis [13]. Insights into the nucleation and growth kinetics of spheroidal or cuboidal LHP nanocrystals have been gained by slowing down the synthesis through the use of different ligands [34, 123].

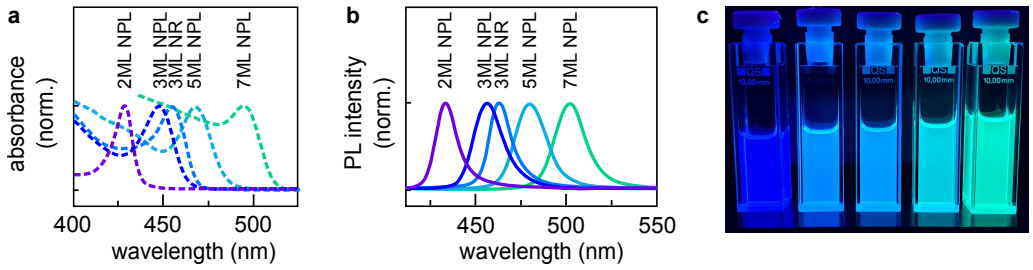

Figure 2.13: Absorption and emission of $CsPbBr_3$ nanocrystals. **a** Absorption spectra of strongly confined $CsPbBr_3$ nanoplatelets (NPL) and nanorods (NR). **b** Corresponding photoluminescence spectra. **c** Photograph of diluted colloidal nanocrystals in **a, b** under 365 nm UV illumination. Data provided by Nina A. Henke.

Various *colloidal syntheses* exist for LHP nanocrystals [199, pp. 3299 ff.]. The hot injection approach consists of the injection of a precursor into a boiling solvent-precursor-ligand mixture [2, 143, 216]. The ligand-assisted reprecipitation process (LARP) brings a precursor solution into the non-equilibrium of supersaturation (see Section 2.1) by, e.g., cooling, solvent evaporation, or injection into a poor solvent [222–224]. Emulsion-based approaches combine non-miscible solvent-precursor-ligand combinations, which form a biphasic mixture, and initiate the LHP crystallization process at the interface [48], from precursor clusters [225], or by demulsifiers such as acetone [49].

Highly anisotropic LHP nanorods or nanoplatelets have been synthesized using different ligands [223], a variation of the ligand to precursor ratio [226], and by controlling the precursor availability [195, 197]. A nanorod morphology has been found to result from different binding preferences of amine and acid ligands [227], small amounts of polar solvent [228], different reaction temperature [229], cluster assembly [230], oriented attachment [231], or a cutting of longer nanowires [24]. Anisotropy can also be achieved by shape transformations from lead or LHP seeds to larger structures at different temperatures [232, 233] or in different solvents [125].

In this thesis a room temperature synthesis of $CsPbBr_3$ nanorods and nanoplatelets by precursor mixing is investigated. The addition of acetone as an antisolvent (see Section 2.1.4) after the mixing phase produces a turbid solution and allows to purify the nanocrystals by centrifugation. The synthesis has previously been optimized to yield a wide range of sizes in the quantum confined regime with a defined anisotropy [200, 234, 235]. Yet, the fast reaction scheme, taking between tens of seconds and several minutes until purification, has precluded a detailed analysis of the underlying mechanisms. The conversion from precursor to LHP (see Q7), the reason for a 1D or 2D particle anisotropy (Q8), and the effect of different antisolvents (Q10) have so far remained elusive. Therefore, this work uses fast in situ SAXS and WAXS experiments with storage ring-based X-ray sources to characterize the full synthesis, and simultaneous PL spectroscopy as an optical readout. Post-synthetic defect passivation and halide ion exchange are investigated by separate in situ experiments (Q3).

2.3.2 Metals and alloy nanocrystals

Dating back to long before the age of semiconductors, metal nanocrystals can be considered the first realization of nanotechnology. The Lycurgus cup from the fourth century AD is a famous example, which owes the distinct color change of its glass (red in transmission and green in reflection) to the surface plasmon resonance of the embedded colloidal gold/silver alloy particles [1].

For metals, the Fermi level lies within the conduction band (see Figure 2.12). In noble metal nanoparticles a collective oscillation of the conduction electrons, induced by incident photons, gives rise to the surface plasmon resonance. It leads to a strongly enhanced light absorption and scattering cross section in the visible range [3]. The resonance condition depends on the size and shape of the particle, and the dielectric constants of particle and medium. Thus, metal nanocrystals like their semiconductor counterparts, have optical characteristics defined by their composition, size and shape.

Optically excited noble metal nanocrystals strongly enhance the electrical field around them. This makes them useful for the detection of nearby analytes and Raman spectroscopy on single molecules, circumventing the inherently small Raman scattering cross sections [236, p. 2759 ff.]. Light trapping in photovoltaics [237] and catalysis [238] are further important applications of metal nanocrystals, which benefit from plasmonic effects.

Also in the absence of optical excitation, noble metal nanocrystals can act as catalysts for a wide range of reactions from organic synthesis to electrochemical water splitting [18, pp. 697 ff.]. This is due to their ability to donate or accept electrons to catalyze reduction or oxidation, depending on the reaction environment. For an optimal catalyst according to the Sabatier principle, the interaction with the reactants should be neither too strong nor too weak so that neither adsorption nor desorption limit the reaction rate [18, pp. 651 f.],

[239]. This principle guides the choice of elemental composition and surface structure. Besides fundamental studies, metal nanocrystals are already widely used as catalysts in an industrial setting [240].

A variation of nanocrystal size affects catalytic activity and selectivity, due to the change in specific surface area, the different contributions of bulk and surface atoms to the electronic structure, and the changing importance of edges and vertices [18, p. 655], [241]. Differently shaped nanocrystals show a distinct coordination of atoms on their facets (see Section 2.1.2). The possible shapes for metal nanocrystals are abundant, ranging from simple convex polyhedra such as cubes, tetrahedra and octahedra, via singly or multiply twinned structures such as bipyramids, decahedra and icosahedra, to concave polyhedra and multipods [18, p. 664]. Density functional theory (DFT) allows to simulate and compare the adsorption modes of molecules to different facets [18, 242]. Infrared spectroscopy and electrochemical characterization are used to investigate structure-property relationships [18, pp. 656 f.].

Increasing research efforts are aimed at earth-abundant and inexpensive metals to replace rare and costly noble metal catalysts [22]. Copper nanocrystals in particular are a promising class of materials for the conversion of climate-damaging CO_2 to useful hydrocarbon products. Several chemicals can be selectively produced on the surface of a copper electrocatalyst depending on the facet and size [241, 243]. While Cu {1 0 0} increases selectivity for ethylene, methane is the main product on Cu {1 1 1} facets [244]. Different shapes such as nanowires, fivefold twins, octahedra, and cubes have been used to steer the CO_2 reduction towards, e.g., ethylene, n-propanol, ethane, and ethanol [244–246].

To produce more selective nanocrystal catalysts the field of shape-controlled synthesis has advanced rapidly, reaching near-atomically precise size and shape control [12, 89]. A separation of the nucleation and growth phases, the use of micellar templates and well-defined seeds are common synthesis strategies [16, 247, 248]. The choice of the ligands and the reductant for the metal salt precursor can steer the growth along defined directions (see Section 2.1.2) [249, 250]. In the earliest reaction phases nanoclusters with an atomically precise composition can be observed, which bridge the regimes of molecular and nanocrystal chemistry [251]. In the cluster regime (below 1 to 2 nm) molecule-like properties such as discrete energy levels dominate [18, p. 655]. The cluster structure is different from the bulk, showing twinned, polyhedral arrangements, which can rearrange to a bulk-like fcc structure [251, 252].

The synthesis of copper-based nanocrystals with advanced shape control has been extensively studied by the group of Prof. Dr. Raffaella Buonsanti, École Polytechnique Fédérale de Lausanne (EPFL), and others [244, 249], [22, pp. 3724 ff.]. This thesis investigates a synthesis of copper nanospheres with a low size polydispersity to further clarify the role of intermediates, such as clusters and organometal heterostructures. A subsequent study on the fine-tuning of the intermediate structures is found in reference [145].

Pairing noble with non-noble metals combines economic and environmental benefits with a high performance and can favor catalytic selectivity through electronic and geometric effects [253, 254]. Nanocrystalline alloys and intermetallics can be realized by a combination and variation of the metal precursors. Alloys are solid solutions, i.e., random mixtures on a crystalline lattice while intermetallics have specific atoms assigned to the sites [255]. Exemplary structures are illustrated in Figure 2.14 a and b.

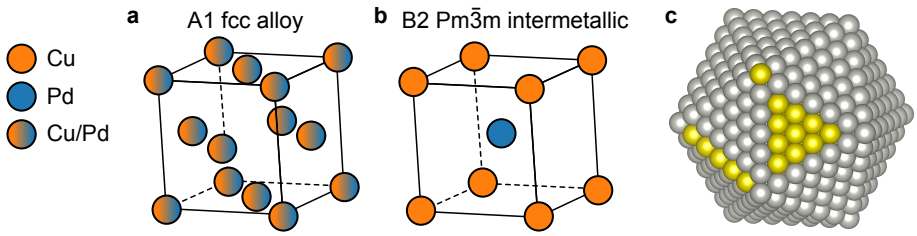

Figure 2.14: Structure of alloys and intermetallics and atomic coordination. **a**, Structure of the A1 fcc alloy of CuPd with random occupation of lattice sites by Cu and Pd. **b**, Structure of the B2 intermetallic of CuPd [162]. **c**, Different coordination of the vertex, edge, and facet atoms of an icosahedral nanocrystal.

In small nanocrystals, vertex, edge and facet atoms all contribute to the surface structure to a similar extent [18, pp. 655 f.] (see Figure 2.14 c), which makes catalytic properties depend on the mixing pattern. Random alloys, intermetallics, and phase-separated bimetallics have shown different selectivity for C_2 chemicals and methane due to electronic as well as structural effects [254, 256]. Fundamental studies of bimetallic catalysts under operating conditions can use dilute or doped mixtures to separate the influence of simultaneously occurring reactions [254].

Synthesis of bimetallics typically proceeds via the coreduction of metal salts in the presence of ligands with a reduction pathway depending on the local environment [23, 162]. Bimetallic catalysts of copper and palladium in particular have been found suitable for CO_2 reduction [256–258].

This thesis follows the synthesis of CuPd supercrystals with a metal ratio close to 1:1, focusing on the aspects of nanocrystal growth and assembly. Supercrystals are produced in a one-pot approach, starting from the molecular precursors. In situ SAXS and TS are recorded simultaneously to circumvent batch-to-batch variation. In the initial phase of the reaction, precursors and small metal nanoclusters are present. Therefore, analysis methods for such small constituents are investigated (see Q7). Typical of a one-pot synthesis, later the signals from several components (nanocrystals, assemblies, ligands, and solvents) superimpose, raising the question how to separate them (see Q8-Q10).

2.3.3 Metal oxides and porous nanomaterials

In addition to metal and metal halide nanocrystals there is a plethora of metal oxide compounds, which can show metallic, semiconducting, or insulating character [259]. Oxides nanostructured with top-down methods are used in electronic devices, e.g., as the gate dielectric [260, pp. 537 f.]. Oxide nanocrystals have also been used in research on all-colloidal field effect transistors [30]. In industrial catalysts oxides can form the active phase or the support [261, p. 6]. Undercoordinated corner and vertex atoms (see Figure 2.14 d) in oxide nanocrystals result in occupied electronic states above the bulk valence band, and an enhanced catalytic activity compared to the bulk [259, p. 3].

Porous electrodes are an essential component of lithium-ion and lithium-air batteries and proton exchange fuel cells for the oxygen evolution reaction [262]. The structure of porous materials is dominated by internal voids, micropores ($< 2\,\text{nm}$), mesopores (2 to 50 nm), or macropores ($> 50\,\text{nm}$), separated by ligaments [263]. In electrochemical applications the large specific surface area due to the porous morphology can compensate for a low reaction rate at the interface and reactants can be stored close to the electrode surface

[264]. Charge carrier transport inside the material towards the active sites is enabled by the electrical connectivity of the matrix [262]. Bicontinuous interpenetrating networks and fractal structures have been realized for this purpose [265, 266]. Besides electrochemical energy storage, porous networks of metal oxides also facilitate the sensing of chemicals due to their sorption characteristics [267].

Porous nanomaterials can be synthesized from the bottom up, e.g., via an assembly of intermediate crystallites, with or without templates [268]. Unoriented assembly leaves part of the volume unoccupied, leading to meso- or microporosity, similar to biominerals [55]. Nanoscale voids can be additionally introduced, e.g., by the outward diffusion of oxygen generated during the synthesis [269, 270].

Cobalt oxide, the material studied in this thesis, is used in electrochemical applications in the stable forms of rock salt CoO, wurtzite CoO, and spinel Co_3O_4 [271]. This work investigates rock salt ($Fm\bar{3}m$) CoO, which is a direct bandgap semiconductor with $E_g \approx 2.2$ to 2.8 eV [272], in the form of nanoparticles. Nanocrystalline CoO can act as a catalyst for electrochemical and solar water splitting [273, 274]. In porous electrodes it can serve as a network support for noble metal catalysts or as the catalyst itself [271, 275, 276]. Structural phase transitions between the different polymorphs have been investigated by computational methods and TEM under operating conditions [277, 278].

Rock salt CoO nanoparticles are often reported to be polycrystalline [279, 280] and therefore hold promise for showing a rich nonclassical reaction pathway during their colloidal synthesis [42, 59] (see Q1). Syntheses of cobalt-based nanocrystals and oxides from acetylacetonate precursors have been extensively optimized in the group of Prof. Dr. Dorota Koziej, University of Hamburg (UHH) and others [281–285]. Yet, the specific mechanisms at play, such as the transformation of precursors to the crystalline phase and the assembly to polycrystals, are not fully understood. This thesis studies the temporal evolution of the morphology on the nanometer scale with SAXS (see Q8).

2.3.4 Assembled materials

Besides the use of nanocrystals suspended in solution or in random arrangements in solids there is a range of applications of their assemblies in superlattices or mesocrystals. Such materials, composed of nanocrystalline building blocks, have been used for photonics [26, 29], electronics [30, 286], and catalysis [287, 288]. In this section, optical, electronic, catalytic, and mechanical aspects are summarized. Additional effects are reviewed in reference [27, pp. 11267 f.].

Self-assembly as a bottom-up approach draws from a vast library of nanocrystal building blocks with various shapes, sizes, and characteristics [5, 289]. This allows to assemble semiconductor or metal nanocrystals, combinations thereof, and bi- or multicomponent structures.

Collective or "emergent" functional properties have been postulated to arise from a coupling of the electronic states of adjacent nanocrystals inside superlattices [28, 290]. Analogous to the formation of energy bands by the overlap of atomic wave functions or the linear combination of atomic orbitals, in closely and regularly packed nanocrystals extended electronic states can occur, as shown in Figure 2.15 a [291].

In practice however, most nanocrystal assemblies show a weak coupling and a temperature-activated hopping transport of charge carriers [28, pp. 7003 f. and pp. 1008 f.]. Hydrocarbon

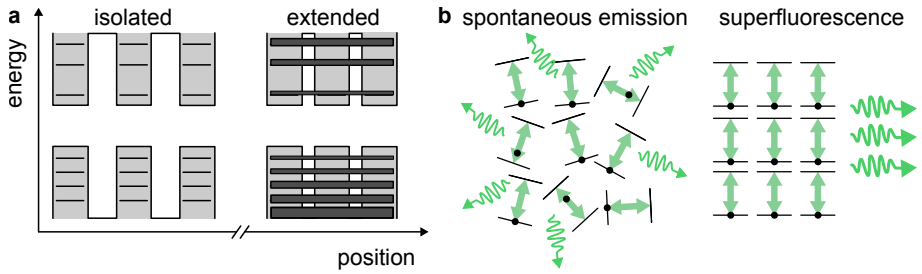

Figure 2.15: Properties of assembled materials. **a**, Coupling of electronic states of closely packed nanocrystals. Extended states form from the energy levels (horizontal lines) in the isolated potential wells (gray) at close interparticle separations [291]. **b**, Illustration of superfluorescence. Spontaneously emitting dipoles are not aligned and emit incoherently at different times. Superfluorescent dipoles are aligned and emit coherently and at a similar time [292].

ligands in between the nanocrystals have a very low conductivity ($< 10^{-11}$ S/cm), which inhibits strong collective effects. Ligand exchange can increase conductivity of an assembly to between 10^{-6} and 10^{-1} S/cm [27, p. 11268 f.], [293]. Increased coupling can also be achieved by closer interparticle spacings (< 1 nm) or epitaxial connections. The superior monodispersity of atomic clusters over nanocrystals as building blocks may likewise lead to improved collective properties [28, p. 6999 f.].

Superfluorescence is a quantum optical phenomenon by which initially uncorrelated fluorescent dipoles spontaneously align to create a collective photon emission with a much faster lifetime, as illustrated in Figure 2.15 b [292]. Superfluorescence has been observed in highly ordered 3D superlattices of LHP nanocubes, whose dipoles, confined in a volume smaller than the emission wavelength, couple above a threshold excitation fluence [29]. The coherent emission could be used for increasing the performance of optoelectronic devices or as a source of entangled photons for quantum communication [178]. Strongly linearly polarized light can be generated by electroluminescence of LHP nanoplatelets arranged in ordered films [26]. Nanorod emitters can be similarly aligned [294]. Compared to conventional generation of polarized light by passing unpolarized light through a polarizer, directly polarized emission reduces losses, which can drive further progress in liquid crystal displays or optical communication [26], [27, p. 11267].

Concerning surface plasmon resonances, superlattices can show a tunable collective plasmonic response in addition to the resonances of individual nanocrystals [295, 296]. Assembled gold nanorods can be used for electric field enhancement in surface-enhanced Raman scattering, e.g., to improve the detection of infectious molecules [112]. Plasmonic circuits, which perform logic operations using the propagation and interaction of electrical charge oscillations, could be realized through colloidal self-assembly [297]. Superlattices could also act as electro-optical modulators via the Kerr effect, harnessing both their optical and electronic properties [28, p. 7012].

In multicomponent assemblies close interparticle separations and intricate superlattice symmetries can be achieved through shape-complementarity [289, 298]. Fluorescence resonance energy transfer (FRET) is possible, with different nanocrystals taking the roles of donors and acceptors. In semiconductor-metal assemblies in particular, exciton and plasmon modes can interact [31]. This can result either in a strong enhancement or a quenching of fluorescence, or add nonradiative decay channels. Such hybrid assemblies can be used for molecular or stress sensing, light harvesting in photovoltaics, and photocatalysis [28, 31]. Binary superlattices of gold and metal oxides have shown increased stability in catalytic processes compared to individual nanocrystals, due to the oxide nanocrystals preventing

sintering and coalescence [299]. Partial erosion or fusion, e.g., by laser irradiation, can transform an assembly into hollow frames with large surface area [300]. Pores in a membrane assembled from nanocrystals can show selective permeability for ions, used in filters or battery anodes [301, 302].

Structuring of a material on a length scale between 2 and 20 nm is challenging to achieve with top-down approaches [27, pp. 11269 f.]. Assembly of nanocrystalline building blocks from solution can be combined with patterning techniques to address this range with a resolution comparable to photolithography [303]. Hierarchical assemblies making use of patterning can span several orders of magnitude in length, up to the macroscopic regime [32]. The mechanical properties of assemblies are influenced by nanocrystal core size, ligand length, solvent, and defects, and generally comparable to nanocrystal-filled polymers or plastics [304]. Peculiar effects include coherent vibrations [305] and a high bending modulus achievable by thermal crosslinking [306]. Mechanical flexibility and robustness allow the integration of nanocrystal assemblies into flexible devices, e.g., as wearable sensors for human health [307].

The diverse applications of materials assembled from nanocrystals evidently inspire ongoing research into their assembly mechanisms and an optimization of their function (see Q2). This thesis focuses on the structural aspects of assembly during synthesis using X-ray methods. Optical characterization provides complementary information. The fundamentals of these experimental techniques are summarized in the following section.

2.4 Characterization by X-ray scattering and diffraction

2.4.1 X-rays, diffraction and scattering

X-rays are part of the electromagnetic spectrum of light and have a wavelength in the Ångstrom range. Following the definitions in reference [308, p. 5], this introduction considers only X-ray radiation with wavelengths between 0.1 and 2 Å (energy 120 to 6 keV), for simplicity. These are the so-called hard (above approx. 6 to 10 keV) and high-energy (above approx. 30 to 50 keV) X-rays [309, 310], for which relativistic effects can be neglected and absorption by air is relatively low compared to absorption by the sample. A detailed introduction to X-ray diffraction is given in references [308] and [311], on which this section is based.

X-rays can interact with matter via absorption, refraction, and scattering. They have a high probability of being scattered by electrons, a process during which the light wave changes propagation direction and/or energy. Constructive interference of scattered waves leads to characteristic patterns, which is the underlying process of an X-ray diffraction experiment. Nobel prizes were awarded to Wilhelm Conrad Röntgen in 1901 for the discovery of X-rays, and to Max von Laue in 1914 and William and Lawrence Bragg in 1915 for their groundbreaking diffraction studies [312].

Thomson scattering of X-rays by a single electron can be summarized as

$$\frac{d\sigma}{d\Omega} = \frac{I_{sc}}{\Phi_0 \Delta\Omega} = r_0^2 \left|\hat{\boldsymbol{\epsilon}} \cdot \hat{\boldsymbol{\epsilon}}'\right|^2, \qquad r_0 = \frac{e^2}{4\pi\epsilon_0 m_e c^2} \approx 2.82 \cdot 10^{-5}\,\text{Å} \tag{2.9}$$

$\frac{d\sigma}{d\Omega}$ is the differential scattering cross section. This term denotes the ratio of scattered to incident photons per unit area and unit time (I_{sc} and Φ_0, respectively), normalized by the

solid angle $\Delta\Omega$ subtended by the detector. $\hat{\boldsymbol{\epsilon}}$ and $\hat{\boldsymbol{\epsilon}}'$ are the polarization vectors of the incident and scattered beam, respectively. e is the elementary charge, ϵ_0 is the vacuum permittivity, m_e is the electron mass and c is the speed of light. r_0 is the Thomson scattering length, also called classical electron radius [308, pp. 8 f.].

Bragg's law, illustrated in Figure 2.16 a, describes constructive interference in a diffraction experiment. An intensity maximum ("Bragg peak") is observed if

$$2d\sin(\theta) = n\lambda \tag{2.10}$$

d is the distance of lattice planes of a crystal, defined in detail below (e.g., Equation 2.14). 2θ is the scattering angle, n is the diffraction order, and λ is the X-ray wavelength. In a general scattering event the radiation changes momentum from $\boldsymbol{k}$ to $\boldsymbol{k}'$, where $|\boldsymbol{k}| = \frac{2\pi}{\lambda}$ (Figure 2.16 b). If $|\boldsymbol{k}'| = |\boldsymbol{k}|$, this describes elastic scattering. $\boldsymbol{q} = \boldsymbol{k} - \boldsymbol{k}'$ is called the momentum transfer or scattering vector [308, p. 11]. Here

$$|\boldsymbol{q}| = q = \frac{4\pi}{\lambda}\sin(\theta) \tag{2.11}$$

where, again, 2θ is the scattering angle.

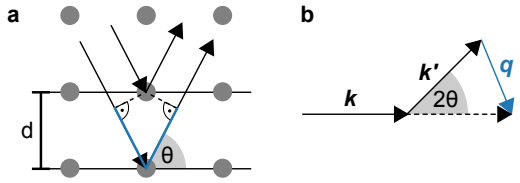

Figure 2.16: Principles of X-ray diffraction. **a**, Illustration of Bragg's law. **b**, Definition of the scattering vector $\boldsymbol{q}$ for elastic scattering.

The electron distribution around an atom with several electrons is approximated as a cloud of number density $\rho(\boldsymbol{r})$. The amplitudes of waves scattered therefrom add up with their respective phases, leading to the atomic form factor

$$f^0(\boldsymbol{q}) = -r_0 \int \rho(\boldsymbol{r})\, \mathrm{e}^{\mathrm{i}\boldsymbol{q}\cdot\boldsymbol{r}}\, d\boldsymbol{r} \tag{2.12}$$

As $q \to 0$, $f^0(q) \to Z$, the total number of electrons of the atom, i.e., the atomic number. For $q > 0$ the atomic form factor is commonly approximated using tabulated values [313]. X-ray energy (E) dependent (resonant or anomalous) terms result from the fact that electrons are bound to the nucleus, $f(\boldsymbol{q}, E) = f^0(\boldsymbol{q}) + f'(E) + if''(E)$. For large q, the atomic form factor $f^0(\boldsymbol{q})$ goes to zero. There, the inelastic Compton scattering dominates over Thomson scattering [308, pp. 21 f.]. *Compton scattering* is only weakly angle-dependent and incoherent, i.e., X-rays scattered in this way do not show defined interference. As detailed in Section 2.4.4, it can often be treated as a background, and subtracted from experimental data.

Simplified equations exist to describe diffraction from an infinite crystal due to its periodicity [308, pp. 148 f.]. A crystalline lattice is spanned by a set of primitive vectors $\boldsymbol{a}_i$ and integer n_i:

$$\boldsymbol{R}_n = n_1\boldsymbol{a}_1 + n_2\boldsymbol{a}_2 + n_3\boldsymbol{a}_3 \tag{2.13}$$

The basis, which can contain several atoms or molecules, is associated with each lattice point and repeated indefinitely along the lattice vectors. The $\boldsymbol{a}_i$ define a primitive unit

cell, containing a single lattice point, but other unit cells can be chosen. In three dimensions 14 Bravais lattices exist, belonging to seven crystal systems (triclinic, monoclinic, orthorhombic, tetragonal, rhombohedral, hexagonal, and cubic) with up to four centering types (primitive or simple, base-centered, body-centered, and face-centered) [260, pp. 14–20]. A complete classification of crystal lattices is achieved via the 230 space groups, which result from a combination of the 32 crystallographic point groups with the Bravais lattices. The underlying symmetry elements (rotation axes, mirror planes, screw axes and glide planes) can be read off from the international (Hermann-Mauguin) notation of the space groups [314].

Planes in a crystal (see e.g. Figure 2.16 a) are referred to by Miller indices $(h\,k\,l)$ [260, pp. 20 f.]. The spacing of lattice planes d_{hkl} has a reciprocal relationship with the corresponding scattering vector

$$d_{hkl} = \frac{2\pi}{q_{hkl}} \tag{2.14}$$

The vectors $\boldsymbol{G}$ of the reciprocal lattice are defined as

$$\boldsymbol{G} = h\boldsymbol{a}_1^* + k\boldsymbol{a}_2^* + l\boldsymbol{a}_3^*, \qquad \boldsymbol{a}_i \cdot \boldsymbol{a}_j^* = 2\pi\delta_{ij} = \begin{cases} 2\pi & \text{for } i = j \\ 0 & \text{for } i \neq j \end{cases} \tag{2.15}$$

with the reciprocal basis vectors $\boldsymbol{a}_i^*$. The Laue condition states that the scattering vector must be equal to a vector of the reciprocal lattice, $\boldsymbol{q} = \boldsymbol{G}$, in order to observe constructive interference [308, pp. 151 ff.]. The dispersions of nanocrystals studied in this thesis represent *powder samples* in the sense that crystallites are present in many random orientations with respect to the incident X-ray beam. In this way the Laue condition can be fulfilled without rotating the sample. The diffraction maxima of a powder sample are observed as cones of constant scattering angle around the primary beam.

The following sections summarize the basic equations of SAXS, WAXS, and TS, which are the main experimental methods of this thesis. Solution scattering data are denoted by "wide angle scattering" (WAXS) and data from actual dried powders by "powder X-ray diffraction" (PXRD).

2.4.2 Small-angle X-ray scattering

While deviations from the average density at atomic (i.e., sub-nm) length scales lead to characteristic scattering at wide angles (see, e.g., Equation 2.14 for crystalline lattice planes), longer-ranged density fluctuations such as the volume envelopes of nanocrystals in a solvent affect the small-angle scattering signal. Also mesophases of surfactants, polymers, and grains in solids are structured on the length scale of 1 to 100 nm. References [38] and [315] are introductory texts on the applications of small-angle scattering in nanoparticle research and soft matter, respectively.

At small scattering angle (e.g., $2\theta = 0.4°$ for $d = 10$ nm and Mo K_α radiation, see Equation 2.10) the relevant signal is close to the primary, unscattered beam (7 mm at 1 m distance in this example), and must be carefully be separated from it. SAXS instruments use long sample-to-detector distances (SDDs), a collimation, i.e., parallelization of the primary beam using mirrors [308, chapter 3] or moderate focusing using lenses [316], apertures with reduced small-angle background ("scatterless slits"), vacuum before and

after the sample to suppress air scattering, and a beam stop shadowing the primary beam, before the scattered light reaches the detector.

A schematic drawing of the two laboratory SAXS setups at the chair of Prof. Dr. Joachim Rädler at Ludwig-Maximilians-Universität München (LMU) is shown in Figure 2.17. The vacuum tubes are interrupted at the sample position to integrate large, custom sample environments, with the air gaps kept minimal. The beam stop is placed on the flight tube exit window and the detector is outside of the vacuum. The entire flight tube is moved to align the beam stop to the primary beam. This allows for a low air scattering background and avoids costly in-vacuum positioning or in-vacuum detector placement.

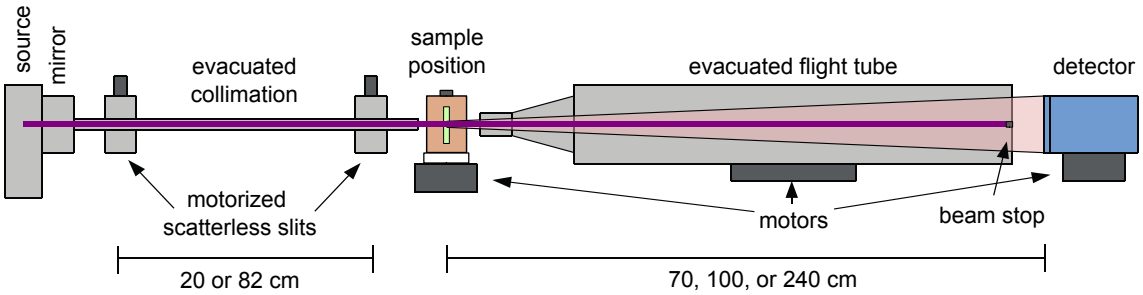

Figure 2.17: Schematic layout of the two laboratory SAXS setups at LMU. In the high-resolution SAXS setup the collimation length is 0.82 m and the SDD between 1 and 2.6 m depending on the configuration. In the multipurpose reflectometer/diffractometer/SAXS setup the collimation length is 0.23 m and the SDD is between 0.23 and 0.78 m. There, only the slit closer to the sample is scatterless.

An illustration of a SAXS experiment and the resulting signal are given in Figure 2.18. For randomly oriented structures in the sample the intensity $I(q)$ is isotropic and may contain diffraction rings (shown in **a**) and/or a smoothly decaying signal as a function of q (shown in **b**).

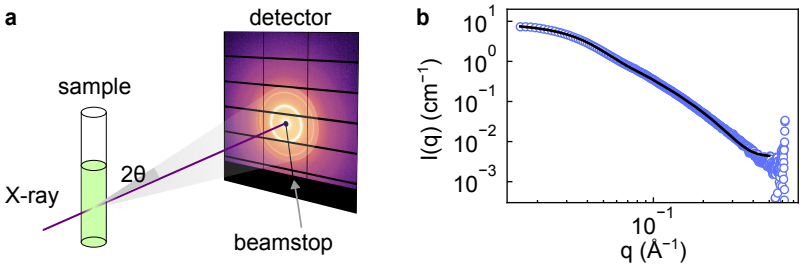

Figure 2.18: Small-angle X-ray scattering. **a**, Schematic illustration of a SAXS experiment. **b**, Exemplary background-subtracted scattering intensity $I(q)$ (dots) with a model fit (black line).

SAXS signal is often assumed to originate from a two-phase system, such as a blend of regions of different electron density (see, e.g., the inset to Figure 2.3) or particles in a homogeneous environment, the solvent or matrix. The signal then comes from the scattering length density (SLD) contrast between the two phases. For X-rays the SLD is proportional to the electron density ρ_e via

$$SLD = r_0 \rho_e \tag{2.16}$$

r_0 is the Thomson scattering length (Equation 2.9). SLD is typically expressed in units of 10^{-6}Å^{-2}. The *Porod invariant* Q [38, p. 11136], calculated from the SAXS intensity, accumulates the contrast $\Delta\rho$ from all density fluctuations in a single number

$$Q = \int_0^\infty I(q) q^2 \, dq = 2\pi^2 \, \Delta\rho^2 \tag{2.17}$$

In practice, the integral is approximated by a cut-off at a finite q value, where the intensity decays into the experimental background. In a two-phase system the exact value of Q can be calculated from the SLDs of the two components and their volume fractions:

$$Q = 2\pi^2 \, x_A(1 - x_A)(\rho_A - \rho_B)^2 \tag{2.18}$$

x_A and $(1 - x_A)$ are the volume fractions of phase A and B, which have SLDs ρ_A and ρ_B, respectively.

The SAXS intensity of a system of freely dispersed particles, e.g., dilute colloids in a solvent or pores in a solid matrix, which are uncorrelated in position, can be approximated by a *Guinier law* [317, pp. 25 f.], [263]

$$I(q) = I_0 \, \mathrm{e}^{-\frac{1}{3}(qR_g)^2} \tag{2.19}$$

It relates the decay of intensity at low angle ($qR_g < 1.3$) to the radius of gyration R_g. R_g can be calculated for any particle shape like a moment of inertia in mechanics, with SLD contrast as the equivalent of mass density. For a sphere with diameter d, $R_g = \sqrt{\frac{3}{5}}\frac{d}{2}$ and for an ellipsoid with diameters a, b, c, $R_g = \frac{1}{2\sqrt{5}}\sqrt{a^2 + b^2 + c^2}$. This simple analysis is insensitive to particle anisotropy.

SAXS intensity can be accurately *modeled* by carrying out an analytical Fourier transform of an object's shape function. The scattering from an object of SLD contrast $\Delta\rho(\boldsymbol{r})$ with volume V is

$$P(q) = |F(q)|^2 = \left| \int_V \Delta\rho(\boldsymbol{r}) \, \mathrm{e}^{\mathrm{i}\boldsymbol{q}\cdot\boldsymbol{r}} \, d\boldsymbol{r} \right|^2 \tag{2.20}$$

$P(q)$ is called the form factor. For a homogeneous sphere with radius R one obtains

$$F(q)_{\text{sphere}} = \Delta\rho \, \frac{4\pi}{3} R^3 \, \frac{3\left[\sin(qR) - qR\cos(qR)\right]}{(qR)^3} \tag{2.21}$$

More form factors relevant to this work are listed in Section 3.3.1.

The effect of a particle shell of decaying density on $P(q)$ is illustrated in Figure 2.19 a. The minima, characteristic of the particle size, are shifted to smaller q for thicker shells and the decay at large q becomes steeper. The effect of particle anisotropy, i.e., oblate or prolate particles of equal volume, is shown in Figure 2.19 b. Anisotropy affects the shape of the form factor decay as well as the depth and position of the minima.

The result can be approximated if no analytic expression of the form factor is available, e.g., by decomposing the shape into spherical basis functions [318] or into beads of a simple shape [319]. The intensity of a mixture of different, non-interacting particles is the sum of their individual intensities. Size polydispersity is modeled by summation of intensities over Gaussian or Schulz-Zimm size distributions [38, 54]. Due to the square dependence of $P(q)$ on the particle volume, large particles in the distribution dominate the intensity.

SAXS intensity can be measured on an absolute scale as a differential scattering cross section, as detailed in Appendix A.2. If the model is calculated on the same intensity scale, the scale prefactor of $P(q)$ can be interpreted as a volume fraction η, which allows to determine the concentration [320]. A mean number density n of particles can be calculated by dividing by the mean volume $\langle V \rangle$ of a particle:

$$n = \frac{\eta}{\langle V \rangle} \tag{2.22}$$

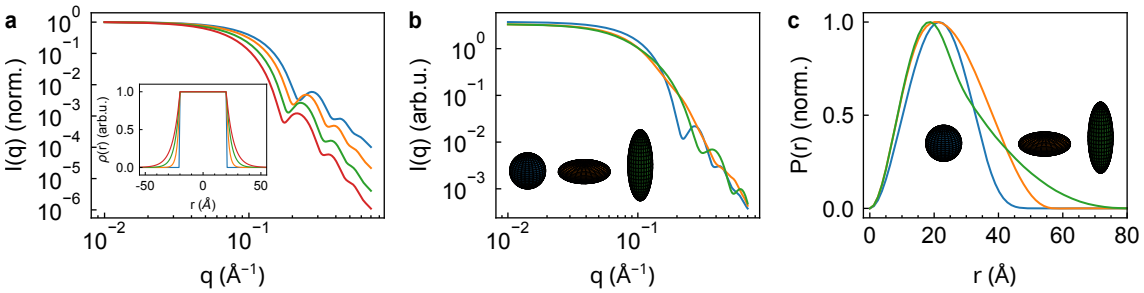

Figure 2.19: Effect of particle shell and anisotropy on the form factor. **a**, Simulated SAXS intensity $I(q) = P(q)$ of 4 nm diameter solid spheres with shells of decaying density with different width. **b**, Simulated SAXS intensity of ellipsoidal particles of identical volume and different aspect ratios ($d_{polar}/d_{equatorial} = 3$, "rod"; 1, "sphere", 1/3, "disk", see insets). **c**, Pair-distance distribution functions $P(r)$ obtained from the simulations shown in **b**.

To simplify analysis, the SAXS intensity $I(q)$ of a dilute system can be transformed to the *pair distance distribution function* $P(r)$, abbreviated here as PDDF when referring to the SAXS regime [317, pp. 126 ff.].

$$I(q) = 4\pi \int_0^\infty P(r) \frac{\sin(qr)}{qr} dr \tag{2.23}$$

This is a special case of the Debye scattering equation (DSE), introduced in detail in Section 2.4.4. $P(r)$ can be considered a histogram of two-point distances within the sample, weighted with the scattering contrast at the two points. Being a function of distance, its interpretation may be more intuitive compared to an analysis of $I(q)$. This can help the detection of particle anisotropy, as shown in Figure 2.19 c. Experimental noise and finite data range ($q_{\max}$ and $d_{\max}$) can complicate the transformation and introduce artifacts.

At high particle concentration interparticle interactions become important. The SAXS intensity is then described as

$$I(q) = P(q)S(q) \tag{2.24}$$

in the local monodisperse approximation [321]. $S(q)$ is called the *structure factor*. The product contains information about the particle in $P(q)$ and about the spatial arrangement in $S(q)$. $S(q)$ of spheres interacting with a hard core potential ("hard spheres") is calculated via the Percus-Yevick closure relation of the Ornstein-Zernike equation [321, 322].

$$S(q) = \frac{1}{1 + \frac{24\,\eta\,G(q)}{q\,d_{\text{effective}}}} \tag{2.25}$$

$d_{\text{effective}}$ is the diameter of hard core potential, which can be different from the particle diameter. η is the volume fraction of particles. The full expression for $G(q)$ is given in Equation 3.4. This structure factor is often a good approximation for short-range order (SRO) of particles, such as in a liquid or glass. Figure 2.20 a shows the effect of different η on the SAXS intensity. The observed peak position depends on $d_{\text{effective}}$ and η in a correlated manner, as illustrated in Figure 2.20 b. Additional information or complementary experiments are necessary to determine the two parameters individually. The reciprocal peak position $2\pi/q_{\text{peak}}$ can be used as a proxy for the typical interparticle distance. Alternatively, the mean interparticle distance of nearest neighbors d_{nn} (center

to center) can be calculated as the side length of a cube in which a particle with diameter $d_{\text{effective}}$ occupies the volume fraction η.

$$d_{nn} = \sqrt[3]{\frac{\pi d_{\text{effective}}^3}{6\eta}} \tag{2.26}$$

The reciprocal peak position typically underestimates the mean interparticle distance (Figure 2.20 c).

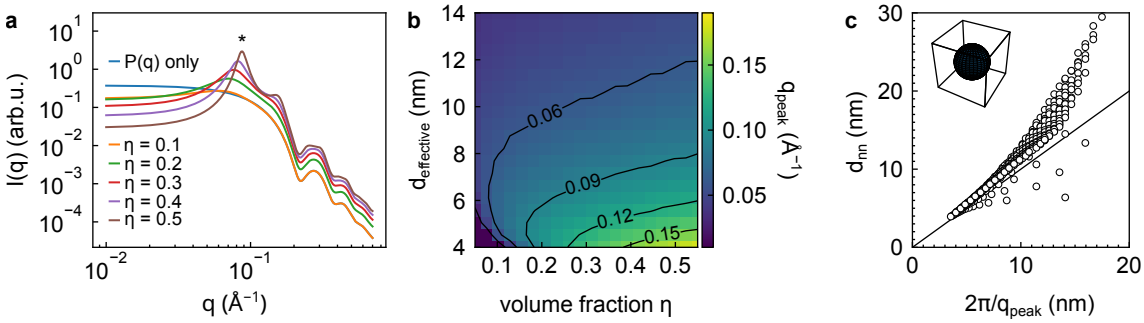

Figure 2.20: Effect of short-range order on the structure factor. **a**, Simulated SAXS intensity $I(q)$ of 4 nm diameter sphere with a hard sphere structure factor $S(q)$ with effective diameter 8 nm at different volume fractions η (see legend). Simulations with $\eta = 1{\cdot}10^{-3}$ and $\eta = 1{\cdot}10^{-2}$ are visually indistinguishable from the $P(q)$ curve. **b**, Peak position q_{peak}, indicated by an asterisk (*) in **a**, as a function of η and effective diameter. Contour lines indicate parameter pairs with equal peak position. **c**, Correlation of the reciprocal peak position and the mean interparticle distance calculated via Equation 2.26.

A porous structure can be either described as particles of negative SLD contrast in a matrix, as described above, or by a continuous density function $\rho(\boldsymbol{r})$ [263, 323, 324].

Fractal materials have a self-similar structure, which is invariant after a change of scale [325, 326]. In these systems, $I(q)$ follows a power law decay:

$$I(q) \propto q^{-\alpha} \propto \begin{cases} R^{d_f} q^{-d_f} & \text{for mass fractals} \\ R^{d_s} q^{-(2d-d_s)} & \text{for surface fractals} \end{cases} \tag{2.27}$$

For mass fractals, the density ρ decreases with size R as $\rho \propto R^{d-d_f}$. d_f is called the mass fractal dimension and d is the dimension of space (here, $d = 3$). $d = d_f$ describes a solid body with a mass proportional to its volume. For surface fractals, the $(d-1)$-dimensional surface area A decreases with $A \propto R^{d_s}$. d_s is the surface fractal dimension. $d_s = d - 1$ corresponds to a perfectly smooth, $d_s = d$ to an extremely wrinkled surface. For a smooth surface $\alpha = 4$ is obtained [317, pp. 29 ff.]. Any wrinkles reduce the exponent. Linear polymer chains in a good solvent can be described by $\alpha = 1.7$ [327].

On *large* enough scales such as the finite size of a fractal aggregate, a material may appear compact and produce a flat intensity (Guinier law). It may also appear smooth on sufficiently *small* scales [326], leading to a crossover from a shallow small-angle ($\alpha < 4$) to a steeper wide-angle exponent ($\alpha \approx 4$). If the bulk and the surface are structured at different length scales, there can be another crossover of the exponent approximately at the inverse spatial correlation length [326].

SAXS analysis is applicable to (liquid) *crystalline structures* on the nanoscale, such as mesophases of amphiphiles [328], polymers [315, chapter 5], or assemblies of nanocrystals [38, pp. 11159 ff.]. Here, the structure factor arising from the regular arrangement of the

molecules or nanocrystals shows strong crystalline reflections and is the dominant component [329, 330]. $I(q)$ of spherical particles in a fcc arrangement is shown in Figure 2.21. Analogous to diffraction from crystalline lattices on the atomic scale (see Equation 2.36) the supercrystalline structure can often be derived from the positions of the Bragg peaks.

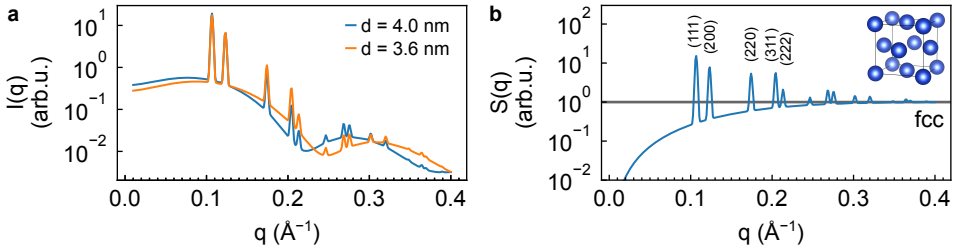

Figure 2.21: Structure factor and SAXS intensity of a fcc supercrystal a, Simulated SAXS intensity $I(q)$ of fcc supercrystals with a lattice constant of 10.2 nm and different particle diameters. A fraction of 10% non-assembled particles is added to the signal. **b**, Corresponding fcc structure factor $S(q)$, identical for both simulations. Inset: fcc lattice of spherical particles. $S(q)$ shows a sloped baseline with a large-q limit of 1 and the allowed fcc reflections. Note that despite the large contribution of the Bragg peaks of $S(q)$ to $I(q)$, the oscillation of the underlying form factor remains distinguishable for the different particle diameters, also by the different suppression of the Bragg peaks.

The structure factors of supercrystals used in this work are based on references [329] and [330]: Using the local decoupling approximation [321], $S(q)$ is composed of a sum of peaks

$$S(q) = 1 - \beta(q)\,(Z_0(q) - 1)\,G(q) \tag{2.28}$$

$$Z_0(q) = \frac{1}{q^2}\sum_{hkl} B(q, q_{hkl}, h, \mathrm{FWHM}, \eta) \tag{2.29}$$

$$\beta(q) = \mathrm{e}^{-\sigma_R^2 R^2 q^2}, \qquad G(q) = \mathrm{e}^{-\sigma_d^2 a^2 q^2} \tag{2.30}$$

$\beta(q)$ and $G(q)$ describe particle size polydispersity σ_R and positional disorder σ_d, and add a diffuse background. R is the particle core radius and a is the lattice parameter. Bragg peaks from different sets of lattice planes are added to $Z_0(q)$. Pseudo-Voigt peaks (B) are a linear combination of Lorentzian (L) and Gaussian (G) shape:

$$B(q, q_{hkl}, h, \mathrm{FWHM}, \eta) = \eta\, L(q, q_{hkl}, h, \mathrm{FWHM}) + (1-\eta)\, G(q, q_{hkl}, h, \mathrm{FWHM}) \tag{2.31}$$

$$L(q, q_{hkl}, h, \mathrm{FWHM}) = \frac{h\,\mathrm{FWHM}^2}{4\left((q-q_{hkl})^2 + \mathrm{FWHM}^2/4\right)} \tag{2.32}$$

$$G(q, q_{hkl}, h, \mathrm{FWHM}) = h\,\mathrm{e}^{-\frac{(x-x_0)^2}{2\sigma^2}}, \qquad \sigma = \frac{\mathrm{FWHM}}{2\sqrt{2\ln 2}} \tag{2.33}$$

A mixing parameter $\eta = 0$ leads to pure Gaussian, $\eta = 1$ to pure Lorentzian peaks. Peak heights h take into account multiplicities of the reflections.

There is a vast choice of software for model fitting of experimental SAXS data [331–336]. Different models from a library can be tested, and their characteristic parameters are varied to optimize the agreement with the data. Population-based algorithms such as Differential Evolution Adaptive Metropolis (DREAM, [337, 338]) provide the necessary robustness for this optimization problem, which often suffers from multiple minima and poor convergence with gradient- or simplex-based algorithms.

The typical measure of the agreement of the model with the data in SAXS analysis is the (reduced) χ^2, defined as

$$\chi^2 = \frac{1}{N_{\text{pts}} - N_{\text{par}}} \sum_i \left(\frac{I_{\text{data,i}} - I_{\text{model,i}}}{\sigma_i} \right)^2 \tag{2.34}$$

N_{pts} is the number of data points in the fit, N_{par} is the number of free parameters in the model. $I_{\text{data,i}}$ are the measured intensity values and σ_i their respective standard error. $I_{\text{model,i}}$ is the model function evaluated at the data point. The term in brackets, called the weighted residual, can reveal discrepancies at particular q values.

2.4.3 Wide-angle X-ray scattering

Figure 2.22 a illustrates the geometry of a powder X-ray diffraction or wide angle X-ray scattering experiment with an area detector. Cones of constant scattering angle intersect the detector in a circular pattern. The isotropy of the pattern indicates the powder nature of the sample, e.g., randomly oriented particles in solution or a dried and ground crystalline material. Figure 2.22 b shows a powder pattern of dried $CsPbBr_3$ nanocrystals.

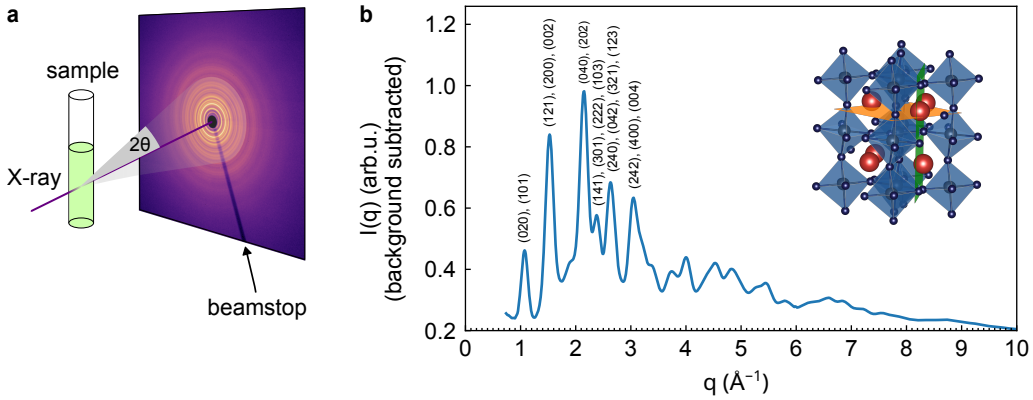

Figure 2.22: Wide-angle X-ray scattering. **a** Schematic illustration of a PXRD or WAXS experiment. **b**, Exemplary background subtracted scattering intensity $I(q)$ of 7 nm diameter spheroidal $CsPbBr_3$ nanocrystals obtained at 0.38 m sample-to-detector distance. The sample was kindly provided by Dr. Quinten Akkerman. Some of the strong peaks are indexed to orthorhombic (Pnma) $CsPbBr_3$ (COD 4510745). Inset: Illustration of (040) and (202) lattice planes in orange and green, respectively.

Taking Bragg peak positions, intensities and widths into account, a powder pattern can be calculated from a set of parameters describing the material as well as the instrument. Structural parameters can be refined against experimental data in reciprocal space via Rietveld refinement [78, vol. C, chapter 8.6, pp. 710–712], Pawley or LeBail fitting [78, vol. H, chapter 3.5, pp. 282–287], or via the DSE [78, and vol. H, chapter 5.7, pp. 649–672]. This latter approach is explained in more detail in Section 2.4.4.

Lattice parameters are calculated from the *positions* of the reflections via Equation 2.14. While the values of common crystalline materials are well known and tabulated [339, 340], superlattice parameters of nanocrystals or complex mesophases can be of interest. Lamellar assemblies with a characteristic repeat distance show a set of reflections at integer multiple

q values (see Equation 2.14). The peak positions of a two-dimensional hexagonal lattice with lattice parameter a are

$$q_{hk} = 2\pi\sqrt{\frac{4}{3}}\frac{\sqrt{h^2+hk+k^2}}{a} \tag{2.35}$$

which leads to a characteristic $1{:}\sqrt{3}{:}2{:}\sqrt{7}$ spacing. Here, $d = \frac{4\pi}{\sqrt{3}q_{10}}$ is the distance of nearest neighbor sites.

Several factors influence the *intensities* of the reflections: The unit cell structure factor is obtained by adding the scattering amplitudes of all atoms in a unit cell with their respective phase factors [308, pp. 159 f.]. Positions are given in fractional coordinates, i.e., with the lattice vectors $\boldsymbol{a}_i$ as the basis. For the face-centered cubic (fcc) lattice with a single atom basis one obtains:

$$\begin{aligned} F^{fcc}_{hkl}(\boldsymbol{G}) = f(\boldsymbol{G})\sum_i \mathrm{e}^{\mathrm{i}\boldsymbol{G}\cdot\boldsymbol{r}_i} &= f(\boldsymbol{G})\left(1+\mathrm{e}^{\mathrm{i}\pi(h+k)}+\mathrm{e}^{\mathrm{i}\pi(k+l)}+\mathrm{e}^{\mathrm{i}\pi(l+h)}\right) \\ &= f(\boldsymbol{G})\cdot\begin{cases}4 & \text{if } h,k,l \text{ all even or all odd}\\ 0 & \text{otherwise}\end{cases} \end{aligned} \tag{2.36}$$

Several reflections such as (1 0 0) are forbidden, but, e.g., (1 1 1) and (2 0 0) are observed. Based on the visibility of reflections an educated guess of the Bravais lattice to identify (super)lattice symmetry is possible. For high-symmetry lattices some information about the structure can be inferred from indexing the visible diffraction peaks with their corresponding Miller indices, as shown in Figure 2.22 b.

Intensities depend on the multiplicity, i.e., the number of equivalent sets of lattice planes of the reflection [311, p. 47]. More factors arise from the X-ray polarization [308, pp. 9, 188], the irradiated volume of the crystal, absorption, incomplete occupancy of selected atomic sites, defects , and a dampening due to thermal vibrations of the atoms [341]. The latter is described by the Debye-Waller factor

$$f_{atom}(q) = f(q)\mathrm{e}^{-\frac{1}{2}q^2\left\langle u_q^2\right\rangle} \tag{2.37}$$

which can vary for different atoms in the lattice. $\left\langle u_q^2\right\rangle$ is the mean square amplitude of thermal vibration [308, pp. 172 ff.].

The *widths* (and shapes) of Bragg reflections are affected by the size of the crystalline lattice, strain, and instrumental effects [341]. For a finite sized cuboid crystal with $N = N_x \times N_y \times N_z$ unit cells the peak intensity is proportional to $\prod_j \frac{\sin^2(0.5\,N_j\,\boldsymbol{q}\cdot\boldsymbol{a}_j)}{\sin^2(0.5\,\boldsymbol{q}\cdot\boldsymbol{a}_j)}$ [311, pp. 27 ff.].

The term for each direction $j = x, y, z$ can be approximated as a Gaussian function. For a cubic unit cell ($a_j = a$) this leads to

$$\prod_j N_j^2\,\mathrm{e}^{-\frac{1}{\pi}(0.5\,N_j\,q\,a_j)^2} = N^2\,\mathrm{e}^{-\frac{1}{\pi}\left(\frac{qa}{2}\right)^2\left[N_x^2+N_y^2+N_z^2\right]} \tag{2.38}$$

i.e., a Gaussian with FWHM $= \frac{4\sqrt{\pi\ln 2}}{\sqrt{N_x^2+N_y^2+N_z^2}\,a}$. For an anisotropic crystal such as a rod or platelet the term in the denominator is dominated by the largest N_j. The largest dimension

thus determines the peak width if reflections from differently sized directions coincide at the same q value [342].

For an isotropic crystal with size L the expression can be approximated by

$$\Delta q = \frac{2\pi}{L} \tag{2.39}$$

The relation of peak width and crystallite size was first analyzed by Paul Scherrer by the equation $D_{hkl} = \frac{K\lambda}{B_{hkl}\cos(\theta)}$. Here, D_{hkl} is the crystallite dimension in the $[h\,k\,l]$ direction, $K \approx 0.9$ is a numerical shape factor, λ the X-ray wavelength, B_{hkl} the FWHM of the reflection in radians and 2θ the scattering angle [343].

Furthermore, the reflections can be broadened as a result of crystalline strain ϵ. Microstrain in a crystal leads to small variations of the lattice spacings. The peak width varies as $B_{hkl} = C\epsilon\tan(\theta)$, where $C \approx 4$ is a numerical constant. Strain and size-related broadening can be separated due to their different angle dependencies by analyzing the width of several reflections [344].

Reflection width is also affected by instrumental imperfections such as the spread of the X-ray wavelength (e.g., $K_{\alpha 1}$ and $K_{\alpha 2}$ lines of a laboratory source), the beam diameter and divergence and the pixel size of the detector (see, e.g. Appendix A.2). This broadening is best determined by measuring a standard material such as LaB_6 powder [345]. The observed widths B are corrected by the widths B_1 of the standard. For two Gaussian peaks, this results in

$$B_{hkl} \approx \sqrt{B^2 - B_1^2} \tag{2.40}$$

2.4.4 Total scattering and the pair distribution function

In reciprocal space the diffraction experiment is described by the intensity $I(q)$. This signal can be transformed to a real space quantity as a function of distance r. The intensity used for this transformation is called the total scattering (TS). TS includes the Bragg peaks (the global structure), as well as elastic and inelastic diffuse scattering (the static and dynamic local structure) [346, p. 10]. Diffuse scattering comes from vibrations of atoms (thermal diffuse scattering) and from extended structural defects such as strain fields around vacancies or dislocations. It decays approximately as q^{-2} away from the Bragg peak position [346, pp. 37 f.]. Total scattering analysis can be carried out in reciprocal space and/or in real space. Both approaches are often applied to nanoscale materials [17, 39, 40, 194, 347–349].

The underlying Debye scattering equation (DSE), a general description of scattering from an arrangement of atoms, was formulated by Peter Debye in 1915 [350]:

$$I(q) \propto \left\langle \left| \sum_{i=1}^{N} f_i \, \mathrm{e}^{\mathrm{i}\boldsymbol{q}\cdot\boldsymbol{r}_i} \right|^2 \right\rangle_o = \sum_{i=1}^{N} |f_i|^2 + 2\sum_{i\neq j} f_i^* f_j \frac{\sin(qr_{ij})}{qr_{ij}} \tag{2.41}$$

Here, the orientational average of the phase factor between any pair of N atoms is added up. r_{ij} is the distance between two atoms with atomic form factors f_i and f_j. The "self-scattering" has been separated as the initial term, and the remaining signal consists of oscillating terms related to the atomic pair distances. Sometimes a Debye-Waller term (Equation 2.37) is included [351].

The DSE describes the orientationally averaged ("powder") diffraction intensity from crystalline as well as from partially ordered or disordered systems. For small N, as in nanocrystals, the DSE can be used to calculate $I(q)$. For large N the calculation of the r_{ij} and the double sum become computationally expensive, despite simplifying approximations [352].

Instead of comparing a calculated $I(q)$ to experimental data, the data can be transformed to an atomic pair distribution function (PDF) in real space. A detailed derivation of the formalism can be found in [346, chapter 3]. The scattering amplitude is $F(\boldsymbol{q}) = \sum_j f_j(\boldsymbol{q})\, \mathrm{e}^{\mathrm{i}\boldsymbol{q}\cdot\boldsymbol{r}_j}$. Here, $f_j(\boldsymbol{q})$ and $\boldsymbol{r}_j$ are the atomic form factor and position of the j-th atom, respectively [308, p. 11]. In an experiment the intensity

$$I(\boldsymbol{q}) = F^*(\boldsymbol{q})F(\boldsymbol{q}) = \sum_{i,j} f_i^* f_j\, \mathrm{e}^{\mathrm{i}\boldsymbol{q}\cdot\boldsymbol{r}_{ij}} \tag{2.42}$$

is measured. * denotes the complex conjugate, the $\boldsymbol{q}$-dependence of the atomic form factor has been omitted for clarity, and $\boldsymbol{r}_{ij} = \boldsymbol{r}_i - \boldsymbol{r}_j$. From the intensity the self-scattering term $\sum_i f_i^* f_i = N\left\langle f^2\right\rangle$ is separated. This defines a "mean square form factor" $\left\langle f^2\right\rangle$.

Dividing Equation 2.42 by $N\left\langle f^2\right\rangle$ yields the structure factor

$$S(\boldsymbol{q}) = 1 + \frac{1}{N\left\langle f^2\right\rangle} \sum_{i\neq j} f_i^* f_j\, \mathrm{e}^{\mathrm{i}\boldsymbol{q}\cdot\boldsymbol{r}_{ij}} \tag{2.43}$$

For an isotropic sample an orientational average $\langle ... \rangle_o$ is taken, in which every mutual orientation of $\boldsymbol{q}$ and $\boldsymbol{r}_{ij}$ has equal probability. This leads to

$$\left\langle \mathrm{e}^{\mathrm{i}\boldsymbol{q}\cdot\boldsymbol{r}_{ij}} \right\rangle_o = \frac{\sin(qr_{ij})}{qr_{ij}} \tag{2.44}$$

where $q = |\boldsymbol{q}|$ and $r_{ij} = |\boldsymbol{r}_{ij}|$. $S(q) - 1$ and $F(q) = q\,[S(q) - 1]$ are called the structure function and the reduced structure function, respectively. Since $F(q)$ is a sum of sine functions, an inverse sine Fourier transform leads to

$$f(r) = \frac{2}{\pi} \int_0^\infty F(q) \sin(qr)\, dq = \frac{1}{N\left\langle f^2\right\rangle} \frac{1}{r} \sum_{i\neq j} f_i^* f_j\, \delta(r - r_{ij}) \tag{2.45}$$

δ is the Dirac delta distribution. $f(r)$ is related to the radial distribution function (RDF) $R(r)$ and the atom pair density function $\rho(r)$ via

$$f(r) = \frac{R(r)}{r} = 4\pi\, r\, \rho(r) \tag{2.46}$$

$R(r)dr$ is the number of atoms in a shell of thickness dr away from an atom at the origin.

$$G(r) = 4\pi r\, [\rho(r) - \rho_0] \tag{2.47}$$

is called the reduced pair distribution function (abbreviated as PDF in the following). In practice, the integral in Equation 2.45 is separated into a part from the experimental minimal q_{min} to a $q_{\mathrm{SAXS/WAXS}}$ and from $q_{\mathrm{SAXS/WAXS}}$ to q_{max}. The lower q integral, $L(r) = 4\pi\rho_0\gamma_0(r)$, is treated as small-angle scattering (see Section 2.4.2) and the latter as wide-angle scattering or TS. In this case one analyzes

$$G'(r) = 4\pi r\, [\rho_{\mathrm{object}}(r) - \rho_0\gamma_0(r)] \tag{2.48}$$

$\gamma_0(r)$ is the autocorrelation of the shape function, describing the "envelope" of a particle. The atom pair density function $\rho_{\text{object}}(r)$ and $\gamma_0(r)$ go to zero at the diameter of the particle. For nanocrystals often the attenuated crystal approximation for spherical particles is used:

$$\gamma_0(r) = \left[1 - \frac{3}{2}\left(\frac{r}{d}\right) + \frac{1}{2}\left(\frac{r}{d}\right)^3\right] H(d-r) \tag{2.49}$$

d is the particle diameter and H is the Heaviside step function [39, pp. 1221 f.].

In practice, when calculating the PDF, first an assumption is made about the composition of the sample in terms of atomic form factors $f = f(q)$. The measured intensity, from which known background signals such as air, sample container, and solvent scattering have been subtracted, is corrected by these factors to arrive at $S(q)$ [39, 351].

$$S(q) = \frac{I(q)}{N\langle f\rangle^2} + \frac{\langle f\rangle^2 - \langle f^2\rangle}{\langle f\rangle^2} \tag{2.50}$$

The second term is only significant if the coherent and incoherent scattering cross sections differ [351]. Examples of $S(q)$, $F(q)$, and $G(r)$ for $CsPbBr_3$ nanocrystals are shown in Figure 2.23 a. The oscillations at large q indicate the presence of nanocrystalline signal. Weak features are amplified in $F(q)$ and aid with background subtraction. The data range for the Fourier transform to real space is chosen by inspection of $F(q)$.

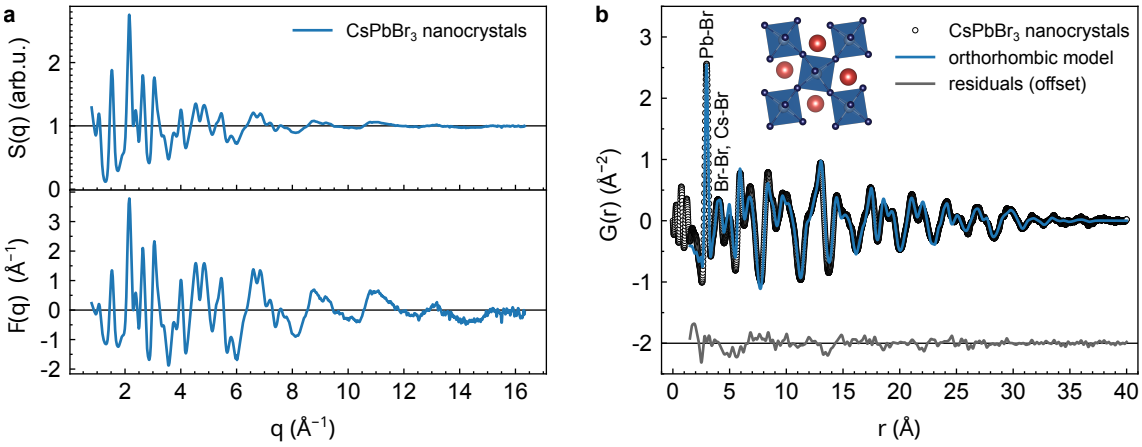

Figure 2.23: (Reduced) structure functions and pair distribution function. a, Top: Structure function $S(q)$ of spheroidal $CsPbBr_3$ nanocrystals obtained from the data shown in Figure 2.22 b. Bottom: Corresponding reduced structure function $F(q)$. The cutoff at $q = 16.5\,\text{Å}^{-1}$ is chosen based on the quality of $G(r)$. **b**, Dots: Reduced pair distribution function $G(r)$ of data in **a**. Blue line: Fit with a model of orthorhombic (Pnma) $CsPbBr_3$ (COD 4510745) up to $r = 40\,\text{Å}$. Some interatomic distances are labeled. gray line: residuals of data and fit. Inset: Projection of the refined unit cell in [0 1 0] direction.

A background correction is carried out by fitting a polynomial to $F(q)$, which removes slowly oscillating components [353]. The order of the background polynomial, $n \approx 8$, is set via $n = \frac{q_{\text{max,inst}} r_{\text{poly}}}{\pi}$, where $q_{\text{max,inst}}$ and r_{poly} are chosen based on visual inspection. r_{poly} is the length below which the PDF is altered by the correction, and should be chosen smaller than the shortest atomic bond length in the material [353]. The corrected $F(q)$ is then Fourier-transformed to the PDF via Equations 2.45 to 2.47. The resulting $G(r)$ has units Å^{-2}.

In an experiment, the accessible q range (q_{min} to q_{max}) is limited. Especially the truncation at q_{max} leads to artifacts ("ripples") in $G(r)$ and a reduced real space resolution. A large

q_{max} is required for a high quality PDF. Therefore, TS/PDF experiments are usually carried out at high X-ray energy (50 to 100 keV, [354]) and with large area detectors (tens of centimeters wide) placed at a close distance, e.g., 150 to 300 mm. Sample environments must accommodate large scattering angles, e.g., $2\theta \geq 30°$ for 100 keV and even larger values for lower energies [39, p. 1246].

$G(r)$, like $I(q)$, can be fitted using structural models. An exemplary fit is shown in Figure 2.23 b, and parameters are given in Table A1. Models for $G(r)$ consist of a sum of peaks, whose positions, amplitudes, and shapes are given by a set of structural and instrumental parameters [39, pp. 1242 ff.]. The peak positions r_{ij} depend on the positions of the atoms, which in turn are defined by the choice of a space group and the fractional coordinates inside the unit cell. $G(r)$ is calculated via the radial distribution function $R(r)$ [39, pp. 1211 and 1242–1244]. It can be understood as a histogram, to which every pair of atoms adds a "count" at the respective distance:

$$R(r) = \frac{1}{N \langle f \rangle^2} \sum_{i \neq j} \frac{f_i^* f_j}{\sqrt{2\pi}\delta_{ij}} \mathrm{e}^{-\frac{(r-r_{ij})^2}{2\delta_{ij}^2}} \tag{2.51}$$

The peak width is described by [355]:

$$\delta_{ij} = \delta'_{ij} \sqrt{1 - \frac{\delta_1}{r_{ij}} - \frac{\delta_2}{r_{ij}^2} + q_{broad}^2 r_{ij}^2} \tag{2.52}$$

Peak width and shape are affected by individual thermal motion of the associated atoms (δ'_{ij}, atomic displacement parameter), as well as by correlated motion, described by the parameters δ_1 and δ_2. Broadening due to instrumental effects enters via q_{broad}. The model function as a whole is convolved with a kernel accounting for the finite q_{min} and q_{max} of the measurement. As a result, the truncation ripples are also present in the model. Finally, $G(r)$ is multiplied by a Gaussian envelope $\mathrm{e}^{-\frac{q_{damp}^2 r^2}{2}}$ to describe the loss of long-range correlations due to limited q resolution.

The PDF of small clusters can be analyzed by computing $G(r)$ for several structural motifs with a finite number of atoms by the cluster-mining approach [356]. The effect of typical structural and microstructural features such as size, shape, or stacking faults on real- and reciprocal space patterns is visualized in reference [357]. When a structural model is refined against $G(r)$ data, the weighted residual R_w is minimized:

$$R_w = \sqrt{\frac{\sum_i \left[G(r_i)_{\mathrm{data}} - G(r_i)_{\mathrm{model}}\right]^2}{\sum_i G(r_i)_{\mathrm{data}}^2}} \tag{2.53}$$

2.4.5 Experimental considerations

The following section summarizes the important experimental aspects for X-ray scattering during nanocrystal synthesis, namely the choice of X-ray energy, the background scattering, and the resolution function.

Choice of X-ray energy

For diffraction and scattering usually hard X-rays (above approx. 6 to 10 keV) or high-energy X-rays (above approx. 30 to 50 keV) are used [317, pp. 54 ff.], [309, 341]. X-rays can be generated in the laboratory by X-ray tubes or at large storage ring facilities (synchrotrons) with bending magnets or insertion devices [315, chapter 1.2].

In an X-ray tube, electrons are focused and accelerated towards a metal anode (typically Cu or Mo, sometimes Ag) which results in the emission of a line spectrum characteristic of the anode material and a broad underlying spectrum of Bremsstrahlung radiation. For the use in powder diffraction the X-ray radiation is monochromatized. This is achieved by filtering with metal foils (Ni for a Cu anode, Zr for a Mo anode), letting pass only the $K_{\alpha 1}$ and $K_{\alpha 2}$ emission lines of the characteristic spectrum, by reflection from a multilayer optic, or by Bragg reflection from a single crystal [308, chapters 3 and 6]. In this way sufficiently monochromatic and relatively intense radiation is obtained, e.g. 10^7 photons/s for a Mo microfocus laboratory source [358].

Synchrotrons provide dedicated experimental end stations at beamlines [310, 316, 359, 360]. Electrons are kept on an orbit in a storage ring and are thus constantly accelerated, leading to the emission of radiation ranging into the X-ray spectrum. Insertion devices, i.e., wigglers or undulators, provide more intense and narrow-banded emission. The high flux (10^{11} to 10^{13} photons/s used for this work) and brilliance, achieved by a small source spot with low emittance, qualify synchrotrons as dedicated light sources [361]. Specialized beamlines provide high energy X-rays up to 100 or even 200 keV [310, 360].

Photoelectric absorption, elastic Thomson scattering, and inelastic Compton scattering vary in strength throughout the X-ray spectrum, as illustrated in Figure 2.24 a and b for $CsPbBr_3$ and n-hexane as a model sample and solvent. A graph for CuPd is given in Figure 3.2 c. Unless anomalous, i.e., energy-dependent effects are desired, the X-ray energy should be chosen away from absorption edges of the investigated materials. For a given material the diffraction angle 2θ follows an inverse relation to the X-ray energy (Equation 2.10), so that the diffraction pattern recorded at high X-ray energy appears compressed. Larger values of $q_{\max}$ can be reached at higher X-ray energy, which is crucial for a high quality PDF (see Section 2.4.4). At the same time, higher energy X-rays have a lower absorption cross-section, which allows them to traverse larger sample lengths.

Background signals

The scattering signal does not only come from the nanocrystal sample itself, but also from window materials, the air traversed by the X-ray beam, and the solvent. Minimizing the background intensity is essential if weakly scattering (i.e., small or low-Z) nanomaterials are studied. Nanocrystals typically only occupy 0.1% of the solvent volume in synthesis conditions (experimental values are given in Table A19), so that the solvent brings a majority of the background. Adapting the sample cell length along the beam changes the sample and solvent scattering alike. The length should be adapted to be equal or below the absorption length of the sample/solvent mixture, which follows an exponential law, to minimize losses [317, p. 55]. For longer cells the background from the sample container and the X-ray flight path are less important, but resolution deteriorates, as shown below. Larger reaction volumes may be more representative of laboratory conditions (see Section 2.2.3) but require higher X-ray energies to reduce the effect of absorption.

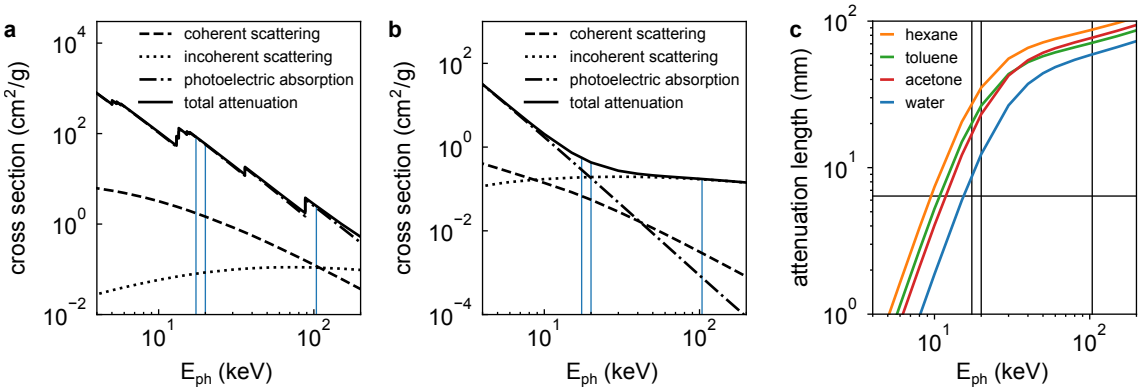

Figure 2.24: X-ray energy-dependent interaction cross sections and attenuation lengths a, Interaction cross sections for $CsPbBr_3$, as indicated in the legend. **b**, Interaction cross sections for n-hexane as a model organic solvent. Vertical lines indicate the X-ray energies used in this work (17.4 keV, 20 keV and 103.2 keV). **c**, Attenuation lengths for typical solvents (see legend). Horizontal and vertical lines indicate the conditions (sample length 6.4 mm and the three different X-ray energies) used in this work. Tabulated data from [362].

Figure 2.24 c illustrates the attenuation $(1/e)$ lengths for typical solvents. The lengths of typical sample cells used in this work are always below the attenuation length. While at low energies photoelectric absorption dominates, at above approx. 20 keV incoherent scattering is the major interaction for solvents like n-hexane (see Figure 2.24 b). There is thus an optimal energy window between approx. 10 and 40 keV for detection of coherent vs. incoherent scattering. Vertical lines indicate the three X-ray energies used here, the lower two being optimal in this regard.

The choice of detector type affects the detection efficiency at different X-ray energies. The common photon-counting complementary metal-oxide-semiconductor (CMOS) detectors, such as the Dectris Pilatus and Eiger detectors used in this work, use silicon sensors. Even at the largest available sensor thickness of 1 mm they exhibit a steep drop in detection efficiency above 20 keV [363]. CdTe as a high-Z semiconductor is the preferred sensor material at high X-ray energies [364]. Charge-coupled device (CCD) detectors with a scintillator screen, as used in medical imaging, are an economical alternative, especially considering their large area [365]. However, they suffer from lower dynamic range ($6 \cdot 10^4$ compared to approx. $2 \cdot 10^6$ counts/pixel for a Pilatus 3 detector) and even lower linear dynamic range (approx. 1 to $4 \cdot 10^4$ counts/pixel). They also show higher electronic noise and afterglow following exposure to intense signals [360].

Photon-counting detectors have such a low background noise that radiation from the environment and from space become detectable ("cosmic background"), which is significant for laboratory experiments with low X-ray flux [366, 367]. Figure 2.25 a shows a detector image recorded with the X-ray source switched off. Gamma rays or cosmic muons are visible as streaks on the detector image, whereas alpha decay from, e.g., radon gas accumulating in basements generates dot- or donut-shaped signals ("zingers"). Streaks have approx. 10 to 100 pixels in length, 1 to 2 pixels in width, and 1 count/pixel. Zingers have 7 to 10 pixels in diameter and up to 1800 counts. The resulting total count rate is $(1.7 \pm 0.2) \cdot 10^{-4}$ counts/pixel/s, which is approximately 60% of the SAXS intensity of a typical laboratory measurement of water (see Appendix A.2).

Cosmic background is the limiting background contribution for the laboratory experiments shown in this work. Figure 2.25 b shows that it is comparable to the SAXS intensity from an in situ nanocrystal synthesis. The fact that it appears as rare, but extremely short

and intense events makes it an issue for time-resolved experiments with low signals. The cosmic background removal strategies used for this work are outlined in Section 3.3.1.

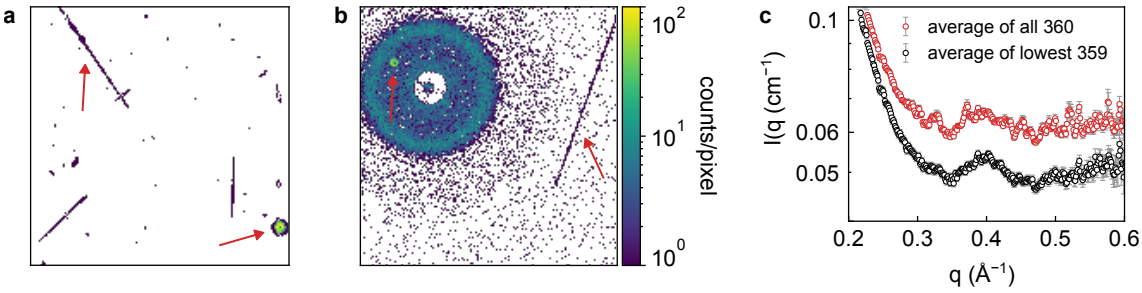

Figure 2.25: Cosmic background in laboratory SAXS experiments. **a**, 150 × 150 pixel crop of a Pilatus 3 detector image, taken for 1 min with the X-ray source switched off. Red arrows indicate streaks and zingers. **b**, Identical crop during an in situ Cu nanocrystal synthesis, taken for 10 s. The circular pattern around the semitransparent beam stop (white ring) is the SAXS signal of the sample, also shown in Figure 4.30 a as a 1d curve. Color bar as in **a**. **c**, Ex situ SAXS signal of $CsPbBr_3$ nanocrystals in hexane without solvent background subtraction, taken for 360 × 10 s (red dots). Leaving out the highest intensity per pixel reduces the background by approx. 10^{-2} cm^{-1} (black dots) and suppresses small peaks from zingers.

Reciprocal space resolution

X-ray wavelength spread, beam size and divergence, sample length, SDD, and detector pixel size contribute to the resolution Δq, i.e., the minimal observed width of diffraction peaks [366]. A shorter sample length and longer SDD improve the resolution, as described by equations A2 and A3. For PDF analysis a closer detector placement with larger q_{max} at the expense of resolution is preferred. Higher X-ray energy at equal detector placement decreases the resolution, since more q range is covered by one pixel.

High coherent to incoherent scattering ratio and high reciprocal space resolution on the one hand and large q_{max} for PDF analysis and low absorption by long sample environments on the other hand have conflicting requirements for the X-ray energy. This thesis addresses the question how to unify laboratory and synchrotron experiments in terms of analysis, regarding their different X-ray energy (Q6).

2.5 Other characterization techniques

2.5.1 Optical spectroscopy

Optical spectroscopy is commonly used to characterize materials, such as dye molecules in solution or solids [368], [205, pp. 125 ff.]. Both the absorption and emission of a material in the ultraviolet and visible range (UV/vis spectroscopy) contain information about its electronic structure. In absorption spectroscopy (Figure 2.26 a) white light with intensity I_0 is guided through the sample, e.g., a dilute suspension of nanocrystals, and the transmitted light is recorded with a spectrometer. A grating separates the light as a function of wavelength λ onto a linear CCD detector [369]. The reduction of transmitted light intensity $I(\lambda)$ depends on the molar absorption coefficient $\epsilon(\lambda)$, the molar concentration c and the sample thickness d by the Beer-Lambert law: $T(\lambda) = \frac{I}{I_0} = \mathrm{e}^{-\epsilon(\lambda)\,c\,d}$. $\epsilon(\lambda)$ is a material- and wavelength dependent quantity and contains information about the allowed optical

transitions in the sample. The absorbance or optical density is defined as $-\log_{10}\left(\frac{I}{I_0}\right)$ [205, p. 4]. The bandgap can be determined from the absorption onset. Excitonic transitions are visible as peaks in the absorbance [205, p. 99 and pp. 170 f.].

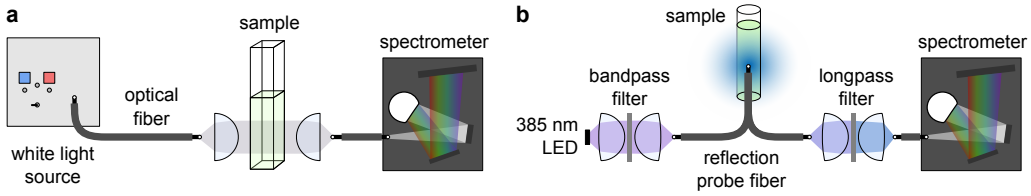

Figure 2.26: Absorption and PL spectroscopy. **a**, Schematic illustration of an optical absorption measurement with a white light source using optical fibers. **b**, Schematic illustration of a PL measurement in reflection geometry using a LED excitation, a reflection probe fiber and a grating-based spectrometer.

For semiconductor nanocrystals photoluminescence (PL) spectroscopy, i.e., the detection of emitted light following optical excitation, offers an alternative readout. Here, a monochromatic light source, such as a LED with a narrow bandpass filter, a xenon lamp with a grating monochromator, or a tunable laser, is used as the excitation [368, chapter 2.2]. The PL emission is redshifted compared to the excitation by the Stokes shift. If the emitting nanocrystals or fluorophores are randomly aligned, emission occurs equally in all directions. Upon traversing the material the emitted light can be reabsorbed or scattered, which complicates the detection in transmission geometry. Therefore, PL is often detected in reflection geometry [368, pp. 56 f.]. The excitation light must be blocked by an appropriate long-pass filter and/or a second (emission) monochromator [368, pp. 38 ff.]. Different from absorption spectroscopy, no dilution or shortening of the path length is necessary to get signal from highly concentrated samples if the correct geometry is chosen. The photoluminescence quantum yield (PLQY) is a combined measure of the efficiency to absorb a photon and to radiatively emit a photon [368, pp. 8 ff.]. It is determined by using an integrating sphere with a highly reflective internal coating and comparing emission and scatter of the sample to a reference blank.

2.5.2 Electron microscopy

Transmission electron microscopy

Transmission electron microscopy (TEM) is a method for imaging nanocrystals and their assemblies using the principle of a light microscope with an electron beam and electromagnetic lenses, as shown in Figure 2.27 a [370]. Electrons are emitted from a heated filament, accelerated by an electrical field to several 100 keV, and passed through a condenser lens and an aperture onto the sample. The sample is produced by drying a solution of nanocrystals on a carbon-coated copper grid, and placed in high vacuum. In the imaging process, electrons are partly absorbed, scattered, or diffracted depending on the material composition and thickness, leading to a combination of amplitude and phase contrast [370, p. 371]. Below the sample a system of objective and projector lens and apertures create a magnified image on a scintillator screen or a CCD camera. The resolution of a TEM routinely reaches the sub-nanometer range. High-resolution instruments allow the visualization of single atoms [370, p. 108].

Scanning electron microscopy

Scanning electron microscopy (SEM), illustrated in Figure 2.27 b, is used to image topography and compositional microstructure of a sample by scanning it with a finely focused electron beam [371, pp. VII ff.]. The incident electron energy is typically between 0.1 and 30 keV, much lower than for a TEM. The sample of washed and dried nanocrystals is placed under high vacuum and grounded to provide an electrical discharge path. Backscattered electrons, deflected by the electric fields of the atoms in the sample, and secondary electrons, escaping the sample surface following electron irradiation, are recorded using separate detectors to form the image. Due to the size of the focal spot and the interaction volume with the sample the resolution is typically larger than 1 nm [371, pp. IX ff.].

Annular dark field scanning transmission electron microscopy

Annular dark field scanning transmission electron microscopy (ADF-STEM) is a high-resolution imaging technique that combines the principles of scanning transmission electron microscopy (STEM) with an annular dark field detector, as illustrated in Figure 2.27 c. It makes use of electrons scattered from their path of propagation by the sample (dark field imaging) and records them using an annular (ring-shaped) detector in a plane conjugate to the back-focal plane [370, pp. 158–161]. By scanning the beam across the sample an image is formed without an objective lens, which reduces optical aberrations. In high angle annular dark field (HAADF)-STEM the central aperture of the detector is large (> 50 mrad off-axis). Here, Rutherford scattering of electrons by the nuclei leads to Z-contrast based on the atomic number of the imaged elements [370, pp. 379 f.].

Energy-dispersive X-ray spectroscopy

Energy-dispersive X-ray spectroscopy (EDX) makes electron microscopy sensitive to the elemental composition of a sample (see Figure 2.27 b). After ejection of a bound inner shell electron of the sample material upon electron irradiation, an outer shell valence electron fills its place. The difference in energy is emitted as X-ray radiation, which is characteristic of the atom of origin. Spectral analysis allows to distinguish different elements. By scanning the beam across the sample the spatial distribution of elements is recorded [371, pp. 210 ff.].

2.5.3 X-ray absorption spectroscopy

X-ray absorption near edge structure

X-ray absorption near edge structure (XANES) is a spectroscopic method for studying the unoccupied electronic states of a material, and thereby, e.g., the oxidation state [37, 372]. An incident X-ray beam is fine-tuned in energy around an absorption edge of the material under study (see, e.g., Figure 2.24 a for exemplary absorption edges) and traverses the sample. The linear absorption coefficient is calculated from the transmitted intensity via the Beer-Lambert law. As soon as the photon energy exceeds the absorption edge, the absorption cross section abruptly increases. In the near-edge region up to approx. 30 eV above the edge an electron is excited into a higher energy unoccupied state allowed by the selection rules. The measured linear absorption coefficient thus represents the unoccupied density of states as a function of energy. The position of the absorption edge depends on

the oxidation state, as the binding energy of core-level electrons slightly increases in higher oxidation states. Further away from the edge, oscillations in the measured absorption arise from scattering of the excited electron in the environment of the absorbing atom (extended X-ray absorption fine structure, EXAFS).

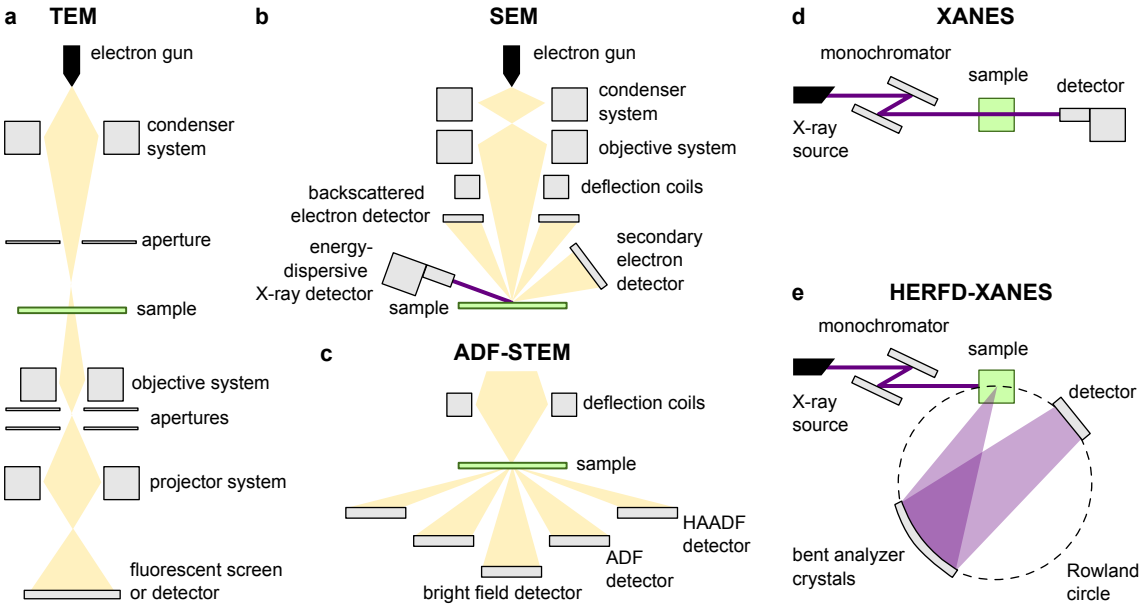

Figure 2.27: Electron microscopy and X-ray spectroscopy techniques. **a**, Transmission electron microscope (TEM). **b**, Scanning electron microscope (SEM) with energy dispersive X-ray (EDX) detector. **c**, Annular dark field scanning transmission electron microscope (ADF-STEM). **d**, X-ray absorption spectroscopy setup for X-ray absorption near edge structure (XANES). **e**, Setup for high energy resolution fluorescence-detected XANES (HERFD-XANES).

High-resolution fluorescence detection and multivariate curve resolution

High-resolution fluorescence-detected XANES circumvents the resolution limitations of conventional X-ray absorption spectroscopy by detecting fluorescent X-ray emission. The emitted intensity is detected with analyzers (monochromators) with a high energy resolution at a specific emission line, while varying the incident energy [37, 373].

Multivariate curve resolution is a family of methods to obtain a bilinear model of pure contributions $\boldsymbol{D} = \sum_i \boldsymbol{s}_i^T \boldsymbol{c}_i + \boldsymbol{E}$ from a mixture measurement, such as time-resolved XANES [374]. The spectra of the components $\boldsymbol{s}_i^T$ and the time-dependent amplitude profiles $\boldsymbol{c}_i$ represent the measured data $\boldsymbol{D}$ up to an error $\boldsymbol{E}$.

In multivariate curve resolution by alternating least squares (MCR-ALS) the $\boldsymbol{s}_i$ and $\boldsymbol{c}_i$ are obtained using an iterative procedure. Physical constraints enforce meaningful component spectra, which leads to more interpretable results compared to, e.g., singular value decomposition or principal component analysis. Typical constraints are non-negativity, unimodality, or mass conservation of amplitudes [374].

2.5.4 Fourier-transform infrared spectroscopy

Fourier-transform infrared (FTIR) spectroscopy is a method used to obtain the infrared absorption spectrum of a material. The spectrum contains bands corresponding to the

vibrational modes of molecules, each occurring at a specific resonant frequency [375]. A vibrational mode is infrared-active if it involves a change in the molecular dipole moment. Functional groups within a molecule produce absorption bands at characteristic frequencies, which can be used to identify compounds by comparison to reference databases or known spectra. The attenuated total reflection (ATR) mode requires less sample volume compared to a transmission experiment. Here, the infrared light undergoes total reflection at the interface between a crystal chosen for its high refractive index (e.g., germanium or diamond) and the sample [375, pp. 129 ff.]. At the absorption bands of the sample the reflected light is attenuated.

3 Materials and methods

3.1 Synthesis procedures

3.1.1 Lead halide perovskite nanocrystals

The synthesis of anisotropic LHP nanocrystals was developed by Nina A. Henke and Carola Lampe from the group of Prof. Dr. Alexander S. Urban at LMU based on the procedures in references [200, 234]. Chemicals are listed in Table 3.1. Simplified precursor structures are shown in Figure A25. Cs-oleate precursor was prepared by dissolving Cs_2CO_3 (0.1 mmol, 32.6 mg) in oleic acid (10 mL). The mixture was stirred at 85 °C until a clear solution was obtained. $PbBr_2$ precursor was prepared by dissolving $PbBr_2$ (0.1 mmol, 36.7 mg) in a mixture of toluene (10 mL), OlAc and OlAm (100 µL each) under stirring at 85 °C for up to three hours until a clear solution was obtained. Precursors were stored under ambient conditions. The given precursor concentrations are denoted as c_0.

Table 3.1: Chemicals for the synthesis of LHP nanocrystals. List of chemicals, purity, and supplier. All chemicals were used without purification.

chemical	chemical formula	purity	supplier
acetone	C_3H_6O	$\geq$ 99.9%	VWR
acetonitrile	CH_3CN	$\geq$ 99.5%	VWR
acetophenone	C_8H_8O	for synthesis	Merck
butanone	C_4H_8O	$\geq$ 99%	VWR
cyclopentanone	C_5H_8O	for synthesis	Merck
diethyl ether	$CH_5OC_2H_5$	$\geq$ 97.5%	Sigma Aldrich
dimethylformamide	$HCONC_2H_6$	for synthesis	Merck
dimethylsulfoxide	CH_3SOCH_3	$\geq$ 99.9%	Sigma Aldrich
n-butanol	C_4H_9OH	99%	Sigma Aldrich
cesium carbonate	Cs_2CO_3	97.5%	Sigma Aldrich
ethanol	C_2H_5OH	$\geq$ 99.5%	Sigma Aldrich
ethyl acetate	$C_4H_8O_2$	for synthesis	Merck
n-hexane	C_6H_{14}	$\geq$ 97%	VWR
lead (II) bromide	$PbBr_2$	$\geq$ 98%	Sigma Aldrich
lanthanum hexaboride	LaB_6	powder, 10 µm, 99%	Sigma Aldrich
methanol	CH_3OH	$\geq$ 99.8%	Sigma Aldrich
methyl acetate	$C_3H_6O_2$	for synthesis	Merck
oleic acid (OlAc)	$C_{18}H_{34}O_2$	technical grade, 90%	Sigma Aldrich
oleylamine (OlAm)	$C_{18}H_{37}N$	technical grade, 70%	Sigma Aldrich
isopropanol	C_3H_7OH	for analysis	Merck
n-propanol	C_3H_7OH	$\geq$ 99%	VWR
silver behenate	$AgC_{22}H_{43}O_2$	$\geq$ 95%	ThermoFisher
toluene	$C_6H_5CH_3$	> 99.9%	VWR

LHP nanocrystals were synthesized via a ligand-assisted spontaneous crystallization at room temperature in ambient air (25 °C, 20 to 40% relative humidity). The syntheses of 3ML nanorods and 2ML nanoplatelets differ in the amounts of precursors and antisolvent, as given in Table 3.2. For the in situ SAXS/WAXS/PL experiments reaction volumes were

scaled down compared to normal laboratory conditions so that the total volume does not exceed 1 mL.

Table 3.2: Synthesis parameters used for the LHP in situ SAXS/WAXS/PL experiments.

	3ML nanorods	2ML nanoplatelets
load $PbBr_2$ precursor	300 µL	400 µL
start SAXS, (WAXS), and PL measurement		
inject Cs-oleate	30 µL	20 µL
wait and stir	10 s	10 s
inject acetone antisolvent	400 µL	267 µL
wait and stir	until $\leq$ 480 s total duration	
stop SAXS, (WAXS), and PL measurement		

First, the $PbBr_2$ precursor was added to the glass capillary of the in situ reaction cell (see Section 3.2), and vigorously stirred. The Cs-oleate precursor was injected using a motorized syringe pump, which sets the time $t = 0$ s of the reaction. After 10 s the antisolvent was injected through a second motorized syringe pump. The reaction mixture was stirred for up to 4 min for combined in situ experiments and for up to 20 min for particular PL measurements. Centrifugation and redispersion served as the final purification. The mixture was centrifuged for 3 min at $1075 \times g$ with an Eppendorf MiniSpin Plus. The supernatant was discarded and the precipitate, containing the LHP nanocrystals, was redispersed in n-hexane for further characterization.

For post-synthetic modification by halide salts, $PbBr_2$ or PbI_2 (0.1 mmol, 36.7 mg or 46.1 mg, respectively) were dissolved in a mixture of n-hexane (1 mL), OlAc and OlAm (100 µL each) to produce the salt solutions. 300 µL of purified 3ML $CsPbBr_3$ nanorods in n-hexane were added to the capillary of the in situ reaction cell and vigorously stirred. The respective salt solution was injected in six steps of 50 µL every 5 min to the nanorod solution using a motorized syringe pump. The PbX_2 and ligand concentrations were ten-fold higher compared to the values reported in reference [200] to increase the signal-to-noise ratio of the WAXS/TS data and to reduce the effect of dilution by the additional solvent. After 30 min the reaction was stopped and the product was taken from the capillary for storage without additional purification.

3.1.2 Cu nanospheres

The synthesis of 8 nm diameter Cu nanospheres was developed by Valeria Mantella from the group of Prof. Dr. Raffaella Buonsanti from EPFL, based on reference [376]. Chemicals are listed in Table 3.3. Water and dissolved O_2 were removed from TOA (10 mL) by heating it to 130 °C for 30 min under N_2 flow. After cooling to room temperature, TOA was added to the in situ glass reaction cell shown in Figure 3.1 and vigorously stirred. Cu(OAc) (1 mmol, 123 mg, shown in Figure A25) and TDPA (0.5 mmol, 139 mg) were added through a top opening, while maintaining the N_2 flow. The mixture was heated to 180 °C at 4 °C/min, followed by a temperature plateau at 180 °C for 30 min. Time $t = 0$ min was chosen as the start of the heating ramp. Subsequent heating to 270 °C at 5 °C/min followed by a 30 min plateau produced a dark red/purple colloidal solution. After cooling to room temperature by removing the heating cord the product was divided into 2×50 mL centrifuge tubes and 20 mL of an ethanol/n-hexane mixture (1:1 v/v) was added to each

of them. The precipitate was collected after centrifugation at 5000 rpm for 15 min. After another resuspension/precipitation cycle, the nanospheres were suspended in anhydrous n-hexane and stored in a glovebox. For in situ control experiments, TDPA was omitted from the reaction, or TOA was replaced with ODE.

Table 3.3: Chemicals for the synthesis of Cu nanospheres. List of chemicals, purity, supplier and amount used in one synthesis. All chemicals were used without purification.

chemical	chemical formula	purity	supplier	amount
trioctylamine (TOA)	$C_{24}H_{51}N$	98%	Sigma Aldrich	10 mL
copper (I) acetate	$CuCO_2CH_3$	98%	Sigma Aldrich	1 mmol
tetradecylphosphonic acid (TDPA)	$C_{14}H_{31}O_3P$	97%	Sigma Aldrich	0.5 mmol
1-octadecene (ODE)	$C_{18}H_{36}$	technical grade, 90%	Sigma Aldrich	10 mL
ethanol	C_2H_6O	anhydrous, 95%	Acros	(for purification)
n-hexane	C_6H_{14}	anhydrous, 95%	TCI	(solvent for ex situ SAXS)

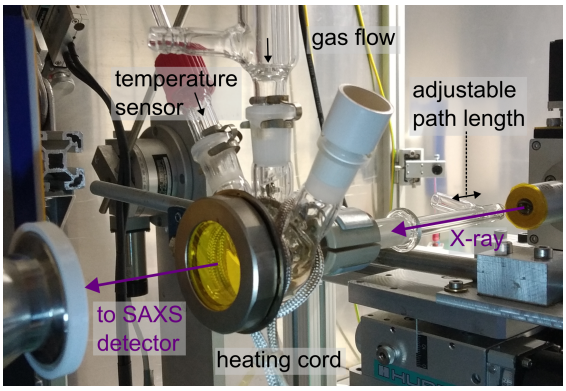

Figure 3.1: Photograph of the glass in situ reaction cell for Cu nanosphere synthesis.

3.1.3 CuPd nanocrystals and supercrystals

The CuPd nanocrystal synthesis was developed by Davide Derelli and Federica Mancini from the group of Prof. Dr. Dorota Koziej at the UHH. Chemicals are listed in Table 3.4. Simplified precursor structures are shown in Figure A25. A precursor mixture of $Cu(acac)_2$ (0.467 mmol, 123.1 mg) and $Pd(acac)_2$ (0.253 mmol, 77.6 mg) in OlAm (3 mL), OlAc (1 mL), and dioctyl ether (0.8 mL) was prepared in an argon-filled glovebox. A small volume of the precursor mixture (80 µL or 300 µL, depending on the capillary used) was loaded into either of the in situ reaction cells, described in Section 3.2 and Figure 3.2. Sample loading was performed either directly in the argon-filled glovebox via a sealed liner, or under argon flow. The mixture was heated to 220 °C at 10 °C/min. Time $t = 0$ min was chosen as the time at which 220 °C were reached. After 30 min at 220 °C the mixture was cooled down to 100 °C to induce the directed self-assembly of the nanocrystals into supercrystals. After synthesis, the nanocrystals were purified by adding ethanol (3:1 v/v) followed by centrifugation and redispersion in toluene. Three centrifugation/redispersion steps were used in total. For dispersion of the assembled supercrystals in different solvents 42 mg of unpurified reaction product were used per mL of solvent.

Table 3.4: Chemicals for CuPd synthesis. List of chemicals, purity, supplier and amount used in one synthesis. All chemicals were used without purification.

chemical	chemical formula	purity	supplier	amount
copper acetylacetonate ($Cu(acac)_2$)	$C_{10}H_{14}CuO_4$	>99.9%	Sigma Aldrich	123.1 mg (0.467 mmol)
palladium acetylacetonate ($Pd(acac)_2$)	$C_{10}H_{14}PdO_4$	99%	Sigma Aldrich	77.6 mg (0.253 mmol)
oleylamine	$C_{18}H_{37}N$	99%	Sigma Aldrich	3 mL
oleic acid	$C_{18}H_{34}O_2$	>99.0%	Sigma Aldrich	1 mL
dioctyl ether	$C_{16}H_{34}O$	99%	Sigma Aldrich	0.8 mL
n-hexane	C_6H_{14}	>99%	Sigma Aldrich	for dilution
ethanol	C_2H_5OH	AnalR Normapur	VWR	for dilution

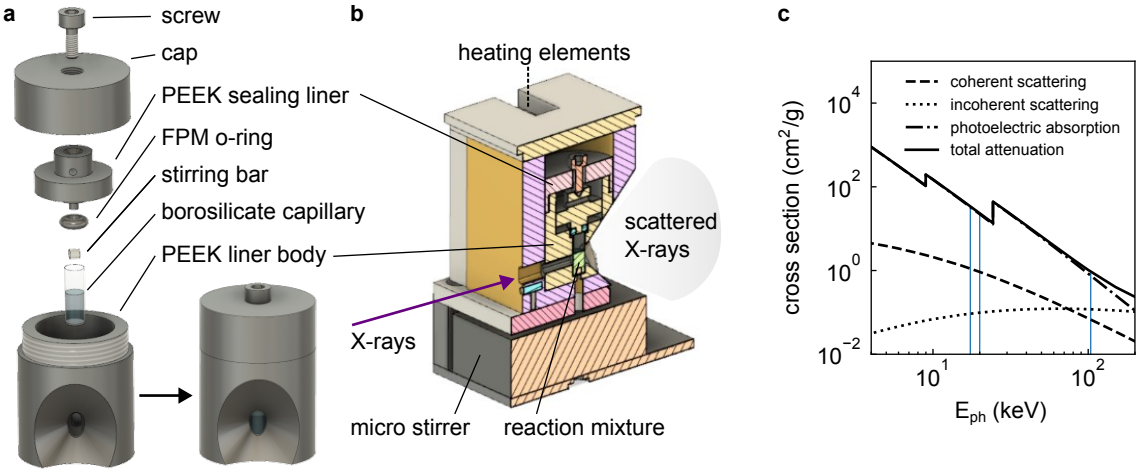

Figure 3.2: In situ cell used for CuPd supercrystal synthesis and X-ray energy-dependent interaction cross section. a, Schematic illustration of the PEEK liner holding and sealing the capillary. **b**, Cross-section view of the reaction cell containing the liner. **c**, X-ray energy-dependent interaction cross section for CuPd. Vertical lines indicate the X-ray energies used for this work (17.4 keV, 20 keV and 103.2 keV).

3.1.4 CoO nanoassemblies

The CoO nanocrystal synthesis was developed by Lukas Grote from the group of Prof. Dr. Dorota Koziej at the UHH. Chemicals are listed in Table 3.5. $Co(acac)_3$ (0.5 mmol, 178 mg, shown in Figure A25) was added to BnOH (5 mL) and stirred for 5 min at room temperature. 0.8 mL of the mixture were loaded into an in situ reaction cell, without stirring. The cell has been specifically designed for heating of a precursor mixture and simultaneous X-ray spectroscopy or diffraction, prior to this work [281]. It has been further optimized by Lukas Grote (UHH) as described in reference [377, Supplementary Information].

After a 6 min temperature plateau at 60 °C for dissolution of the precursor the mixture was heated to 160 °C at 60 °C/min. The start of the heating ramp was chosen as time $t = 0$ min. The aliquots for SAXS analysis were obtained by stopping the reaction by cooling the in situ cell to room temperature with a cold metal block. The aliquots were measured without further treatment. For TEM/SEM imaging the reaction product was washed three times with ethanol and dried at 60 °C.

Table 3.5: Chemicals for CoO synthesis. List of chemicals, purity, supplier and amount used in one synthesis. All chemicals were used without purification.

chemical	chemical formula	purity	supplier	amount
benzyl alcohol (BnOH)	C_7H_8O	$> 99\%$	Sigma Aldrich	5 mL
$Co(acac)_3$	$C_{15}H_{21}CoO_6$	99.99%	Sigma Aldrich	0.5 mmol

3.2 In situ reaction cell

A dedicated in situ reaction cell, shown in Figure 3.3 a, was constructed for the experiments of this thesis and used for LHP and CuPd nanocrystal synthesis. An X-ray transparent borosilicate capillary (6.4 mm inner diameter, 0.05 mm wall thickness, Hilgenberg) was chosen as the reaction vessel. The resulting sample length is compatible with molybdenum anode laboratory X-ray setups [378] and the beamlines P62 and P07 of PETRA III (Hamburg, Germany) [310, 316] (see Section 2.4.5 for the choice of X-ray energy). The capillary is enclosed in a sealable metal liner with several openings, shown in Figure 3.3 . The X-ray beam enters the capillary from one side and the scattered intensity exits on the opposite side, up to $2\theta = 45°$. TS experiments with large q_{max} (see Section 2.4.4) are therefore possible with high energy X-ray radiation. The combination of X-ray scattering, optical spectroscopy, heating, stirring, and reagent injection makes the cell usable for a wide range of colloidal nanocrystal syntheses.

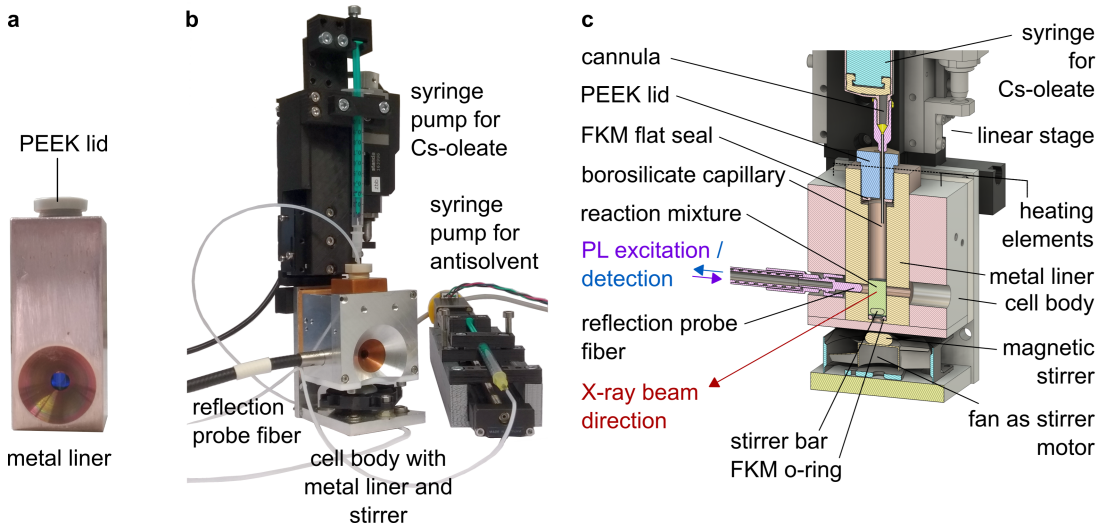

Figure 3.3: In situ setup for SAXS, WAXS, and PL spectroscopy. **a**, Photograph of the metal liner with a PEEK lid. **b**, Assembled reaction cell. A capillary is placed inside the metal liner and then inside the cell body with several openings. A syringe pump injects the viscous Cs-oleate precursor directly into the capillary from the top. A second syringe pump injects the antisolvent through a tube. An optical reflection probe fiber points at the capillary from the side. **c**, Cross-section view of the reaction cell through the middle of the capillary, cut perpendicular to the X-ray beam direction. **b** and **c** adapted from [379, Supplementary Information] with permission. CC-BY license 2024, Springer Nature.

Perpendicular to the X-ray beam there are two openings for optical probes. PL emission is excited and detected in a reflection geometry, shown in Figure 3.3 c and Figure 4.4 b. A high-power LED (Roschwege RSW-P01-385-2) with 385 nm peak emission wavelength is used as the excitation. The LED is operated at a current of 30 to 200 mA, which is set by a custom-built step-down constant current power supply (Recom Lightline RCD-24-1.20

0-1200 mA). The light is collimated using a 16 mm focal length aspheric lens (Thorlabs ACL25416U-A) and further monochromatized using a bandpass filter (Thorlabs FBH380-10, center wavelength 380 nm, FWHM 10 nm) before being focused into the core fiber of an optical reflection probe fiber bundle (Thorlabs RP20, diameter 200 µm) with a 20.1 mm lens (Thorlabs LA4647). The optical fiber is approached as close as possible to the capillary with the reaction mixture. In this way the emitted PL is efficiently collected back into the six outer fibers of the reflection probe bundle. The emission is then collimated with a lens (Thorlabs LA4647) at the exit of the fiber and traverses a high quality longpass filter (Thorlabs FELH0400, cut-on wavelength 400 nm) for separation from the excitation light. The filtered emission is refocused into a 600 µm diameter multimode fiber patch cable (Thorlabs M114L01) and coupled into a small CCD-based UV/visible spectrometer (Ocean optics Flame-S/Ocean Insight QE-Pro) [369].

During the in situ experiments the reaction cell was placed in the experimental hutch of the beamline or inside the laboratory X-ray setup and the experiment was controlled remotely from the control hutch. Therefore, heating, stirring, and the addition of ingredients must be remote-controlled as well. The temperature of the cell is set via two cartridge heating elements (Otom group, 8 × 40 mm, 100 W, 24 V) placed on the sides of the metal liner shown in Figure 3.3 c. A 3 mm Pt100 temperature sensor or a K-type thermocouple can be placed inside the cell body at equal distance of the heating elements and the liner for temperature control. A Lake Shore temperature controller (Model 325 or 335) with an external power supply (Elektro-Automatik EA-PS series) was connected to the heating elements and the temperature sensor. The majority of the experiments was carried out at room temperature (25 °C).

The reaction medium is stirred with a small magnetic stirring bar (length ≤ 6 mm) and a magnetic stirrer placed underneath. A pulse-width modulated DC fan (Sunon MF40060V1-1000U-S99, 40 × 40 × 6 mm) is used to rotate a pair of magnets (AlNiCo, 4 × 9 mm). The magnets are fixed to the rotor with high-temperature epoxy glue (UHU Plus Endfest 300). The use of a fan as the stirrer motor has the advantage that the mounting plate at the bottom of the reaction cell is constantly cooled. The custom stirring device allows remote-control of speed via an Arduino Uno microcontroller, and battery-powered operation, e.g., if stirring needs to be continued during transport of the sample.

Liquid reagents can be injected into the capillary via motorized syringe pumps. The cell lid has three 1.5 mm diameter holes for syringe pump access, into which either tubes or cannulas can be placed. For the injection of the antisolvent in this work a 1 mL disposable syringe (Braun Injekt-F) was connected to a Teflon tube (VWR 16-PTFE-30-10M, 0.762 mm internal diameter) via a 0.9 × 40 mm cannula (Braun Sterican) and placed on a custom-built stepper-motor driven syringe pump. The pump consists of a ball screw linear drive (Misumi LX1502-B1-T1528-200-XA2, 150 mm travel range) with a stepper motor (Oriental Motor PKP225D15B2). Stepper motor drivers are commonly available at beamlines and are already integrated into the control software. Commercial stand-alone syringe pumps are compatible with the setup as well.

During optimization of the injection of the Cs-oleate precursor it was found that the viscous liquid cannot be well injected through long tubes. Air bubbles accumulate in the tubing and can only be eliminated at a considerable loss of material. The dispensing process depends on the profile of the cut end of the tube, which negatively affects reproducibility. Therefore, Cs-oleate was injected directly into the capillary from a 1 mL disposable syringe placed on top of the reaction cell through a 0.4 × 25 mm cannula (Braun Sterican, Figure 3.3 a). This

syringe is driven by a small micrometer-screw driven linear stage (Standa 8MT184-13, 13 mm travel range) due to space constraints.

3.3 X-ray scattering

3.3.1 SAXS

In situ SAXS data of *LHP nanocrystals* were recorded at beamline P62 of PETRA III (DESY, Hamburg) [316]. The setup parameters are given in Table 3.6. The in situ reaction cell presented in Section 3.2 was used as the sample environment and placed as shown in Figure 3.4. The SAXS detector was placed inside the vacuum of a permanently installed flight tube.

Table 3.6: Parameters of the X-ray setups.

	P62 [316]	**P07** [310]	**laboratory SAXS setup** [378]
E (keV)	20	103.2 to 104	17.4
λ (Å)	0.62	0.12	0.71
SDD (m)	1.87 (SAXS)	4.66 (SAXS) 0.77 (WAXS/TS)	1.0 to 2.6
detector	Dectris Eiger2 X 9M (SAXS) and Dectris Eiger2 X 4M-DESY (WAXS)	Varex XRD4343CT (SAXS, WAXS) [365] or Dexela 1512 (SAXS) [380]	Dectris Pilatus 3R 300K (SAXS) [363] and Dectris Pilatus 100K (WAXS)
pixel size (mm^2)	0.075×0.075	0.15×0.15 or 0.075×0.075	0.172×0.172
	laboratory multipurpose setup	**P03** [359]	**P21.1** [360]
E(keV)	17.4	12.9	102.9
λ(Å)	0.71	0.961	0.121
SDD (m)	0.78 (SAXS) 0.23 (PXRD)	2.0 or 5.2	0.411
detector	Dectris Pilatus 100K	Dectris Pilatus 1M	Perkin Elmer XRD1621
pixel size (mm^2)	0.172×0.172	0.172×0.172	0.2×0.2

SAXS and WAXS data were recorded simultaneously with 50 ms per frame (20 Hz). Only SAXS data were used further, resulting in approx. 39 MiB per frame and up to 360 GiB of detector images per synthesis (uncompressed). Due to the large number of zero-valued pixels from the photon counting detector, a 50 to 100-fold compression via the hierarchical data format (.hdf) was possible.

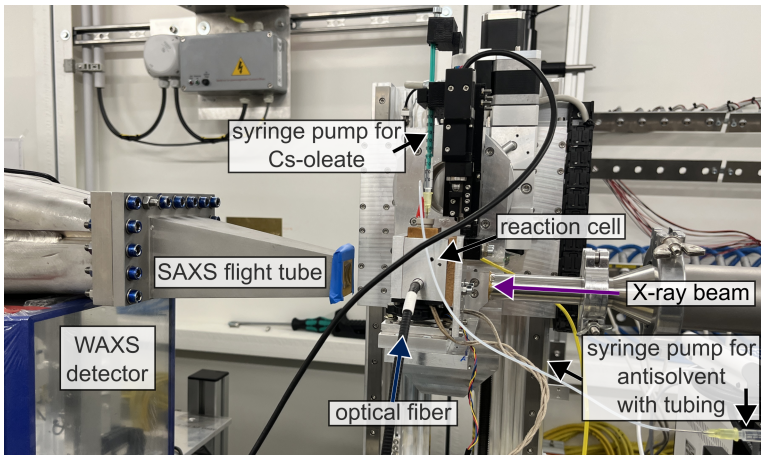

Figure 3.4: Setup at beamline P62 for simultaneous SAXS and PL spectroscopy.

For post-synthetic modification SAXS, WAXS/TS and PL data were recorded simultaneously at beamline P07 of PETRA III (DESY, Hamburg) [310] with parameters given in Table 3.6. Two detectors (Varex Imaging XRD4343CT) were used for SAXS and WAXS/TS. Images were recorded with 0.5 s per frame (2 Hz), resulting in an uncompressed data rate of approx. 39 MiB per frame. Due to the electronic noise of the CCD detectors compression for storage was found to be inefficient, and raw 32 bit .tif images were stored.

Ex situ SAXS data of LHP nanocrystals were recorded at the laboratory SAXS setup [378] and the laboratory multipurpose setup at LMU. Parameters are given in Table 3.6. A high resolution configuration with a sample-to-detector distance (SDD) of 1 m and a high flux configuration with a SDD of 0.78 m were used. Measurement times ranged from 5 min to 1 h per sample.

The cosmic background was removed with the "all but one" approach: During averaging of detector images or azimuthal integration rare and intense events were excluded by taking the mean of all but the highest intensities per bin ("all but one"). Many short exposures ($N = 10^2$ to 10^4) were taken, and $N-1$ values were averaged, as illustrated in Figure 2.25 c. This procedure was found to lower the cosmic background while preserving the signal from the sample.

All detector positions were calibrated with silver behenate (see Table 3.1) using pyFAI [381]. Data were transformed to intensity as a function of scattering vector with pyFAI, using Equation 2.11. The signal of toluene and the antisolvent were subtracted as a background, scaled by the respective ratios. SAXS data were fitted using SasView version 5.0.5 and 5.0.6 [331]. A two-component SAXS model describes the $PbBr_2$ precursor as core-shell spherical micelles with a hard sphere structure factor (Equation 3.4) and the growing intermediate nanoclusters as ellipsoids (Equation 3.1). Details on model selection, including alternative models such as cylinders and cuboids, are given in Section 4.1.2.2. The fitting sequence for time-resolved data is given below. The program code is published along with the raw data in the repository [382]. Ellipsoid diameter and length, scale factors for precursor and nanoclusters, and a constant background term were allowed to vary. For post-synthetic modification the same two-component SAXS model of spherical micelles with a hard sphere structure factor and ellipsoidal nanocrystals was used. Here, the size parameters were determined on the pure salt and nanocrystal solutions and only the scale factors were refined for the in situ mixing experiment. GNOM from the ATSAS package was used to calculate the PDDF of purified LHP nanocrystals [336].

SAXS form and structure factors

$\Delta\rho$ is the scattering length density (SLD) contrast. V is the particle volume. $\langle ... \rangle_o$ represents an orientational average, carried out by numerical integration.

Ellipsoid with polar radius R_p and equatorial radius R_e ($V = \frac{4\pi}{3} R_p R_e^2$):

$$\begin{aligned} R(u) &= R_e \sqrt{1 + u^2 \left(\frac{R_p^2}{R_e^2} - 1 \right)}, \qquad F(q,u) = \frac{3\left[\sin\left(qR(u)\right) - qR\cos\left(qR(u)\right)\right]}{\left(qR(u)\right)^3} \\ \left\langle F^2(q) \right\rangle_o &= (\Delta\rho V)^2 \int_0^1 F^2(q,u)\, du \end{aligned} \tag{3.1}$$

Cylinder with radius R and length L ($V = \pi R^2 L$):

$$F(q,\alpha) = \frac{\sin\left(0.5qL\cos\alpha\right)}{0.5qL\cos\alpha} \frac{J_1(qR\sin\alpha)}{qR\sin\alpha}, \qquad \left\langle F^2(q) \right\rangle_o = (2\Delta\rho V)^2 \int_0^{\pi/2} F^2(q,\alpha) \sin\alpha\, d\alpha \tag{3.2}$$

J_1 is the first order Bessel function of first kind.

Cuboid with side lengths A, B, C ($V = ABC$):

$$\begin{aligned} F(q,\theta,\phi) &= \frac{\sin\left(0.5qA\sin\theta\sin\phi\right)}{0.5qA\sin\theta\sin\phi} \frac{\sin\left(0.5qB\sin\theta\cos\phi\right)}{0.5qB\sin\theta\cos\phi} \frac{\sin\left(0.5qC\cos\theta\right)}{0.5qC\cos\theta} \\ \left\langle F^2(q) \right\rangle_o &= 2(\Delta\rho V)^2 \int_0^{\pi/2} \int_0^{\pi/2} F^2(q,\theta,\phi) \sin\theta\, d\theta d\phi \end{aligned} \tag{3.3}$$

Percus-Yevick structure factor of hard spheres:

$$\begin{aligned} S(q) &= \frac{1}{1 + \frac{24\,\eta\,G(q)}{q\,d_{\text{effective}}}}, \qquad A(q) = q\,d_{\text{effective}} \\ \alpha &= \frac{(1+2\eta)^2}{(1-\eta)^4}, \qquad \beta = -6\eta \frac{\left(1+\frac{\eta}{2}\right)^2}{(1-\eta)^4}, \qquad \gamma = 0.5\eta \frac{(1+2\eta)^2}{(1-\eta)^4} \\ G(q) &= \frac{\alpha}{A^2}\left(\sin A - A\cos A\right) + \frac{\beta}{A^3}\left(2A\sin A + (2-A^2)\cos A - 2\right) \\ &\quad + \frac{\gamma}{A^5}\left(-A^4\cos A + 4\left((3A^2-6)\cos A + (A^3-6A)\sin A + 6\right)\right) \end{aligned} \tag{3.4}$$

$d_{\text{effective}}$ is the effective diameter of the hard sphere potential. η is the volume fraction occupied by the hard spheres.

Fitting sequence for precursor micelles and intermediate nanoclusters

1. Fit the initial frame using the product of a core-shell sphere form factor and a hard sphere structure factor for the $PbBr_2$ precursor micelles.
2. Initialize a weighted sum model using the parameters of the initial frame for the first component (precursor micelles) and a separate form factor for the second component (growing nanoclusters).
3. If the second component is an anisotropic model (ellipsoid, cylinder or cuboid), initialize it as isotropic, so that any potential anisotropy (oblate or prolate) is explored during the refinement.

4. Fit the final frame before antisolvent injection using the two-component model and verify that the parameters are physically plausible.
5. Fit all frames in between, going forward in time and starting from the same initial parameters ("batch fit") to avoid correlations between successive time points.
6. Verify that the temporal evolutions of the parameters are physically plausible.

In situ SAXS data of *Cu nanosphere synthesis* were recorded with the laboratory SAXS setup at LMU. Typical setup parameters are given in Table 3.6. The photon flux at the sample position was $2.57 \cdot 10^6$ photons/s. The beam size on the sample was approx. $0.9 \times 0.6\,\mathrm{mm}^2$ (h×v, FWHM). The in situ reaction cell shown in Figure 3.1 served as the sample environment. The cell is a three-neck flask with a large polyimide exit window, sealed by a FKM o-ring (Angst&Pfister, Switzerland). The cell is wrapped with a heating cord (Omega Engineering), insulated with aluminium foil, and a magnetic stirring plate (IKA lab disc) is placed underneath. A K-type thermocouple is inserted into the reaction mixture through a septum from the top and connected to a temperature controller (J-KEM). A small entrance window is sealed onto a hollow glass insert, which can be moved back and forth to adjust the X-ray path length in the sample. A probed sample length of approx. 20 mm was used. This corresponds to the absorption length of 17.4 keV X-ray radiation in the mixture to maximize the signal above the instrumental background (see Figure 2.24).

The detector distance of 0.952 m was calibrated with silver behenate using pyFAI [381]. The resulting q range was 0.016 to $0.69\,\mathrm{Å}^{-1}$. SAXS and WAXS data were recorded simultaneously with 10 s per frame. Only SAXS data were analyzed further. The cosmic background was removed with the "remove outliers" approach: Single pixels, regions on the detector, or data points in the integrated curve were masked if they had a too high count rate compared to a temporal or spatial mean value. Values exceeding three standard deviations around the temporal mean were masked.

The Porod invariant (Equation 2.17) was calculated by trapezoidal integration below $q = 0.14\,\mathrm{Å}^{-1}$, i.e., omitting the peak of the lamellar phase. SAXS data were fitted with a model of spherical nanocrystals with a Gaussian size distribution and a hard sphere structure factor (Equation 3.4). All polydispersity distributions in this work were calculated as particle number distributions, with values sampled at 31 points placed within three standard deviations around the mean, following the implementation in [331]. Peaks representing the reflections from the lamellar phase and a power law term were added to the model for the early and intermediate reaction phases.

For ex situ SAXS, a sample in anhydrous n-hexane was filled in a polyimide tube with inner diameter 2.55 mm (Rotima, Switzerland) in a N_2-filled glovebox and sealed at both ends to avoid oxidation. SAXS was measured along a 20 mm tube segment. Calibration and integration were done with pyFAI [381]. A model of spherical nanocrystals with a Gaussian size distribution and a fuzzy interface (SasView's "fuzzy sphere" model) was fitted to the data using SasView version 4.2.2 [331]. In this model the sphere form factor amplitude (Equation 2.21) is multiplied with $\mathrm{e}^{-\frac{1}{2}(q\sigma)^2}$, where σ represents the fuzziness of the interface.

In situ SAXS data of *CuPd supercrystal synthesis* were recorded simultaneously with WAXS/TS data in the second experimental hutch EH2 of beamline P07 (PETRA III,

DESY, Hamburg). The beamline setup is shown in Figure 3.5 and parameters are given in Table 3.6.

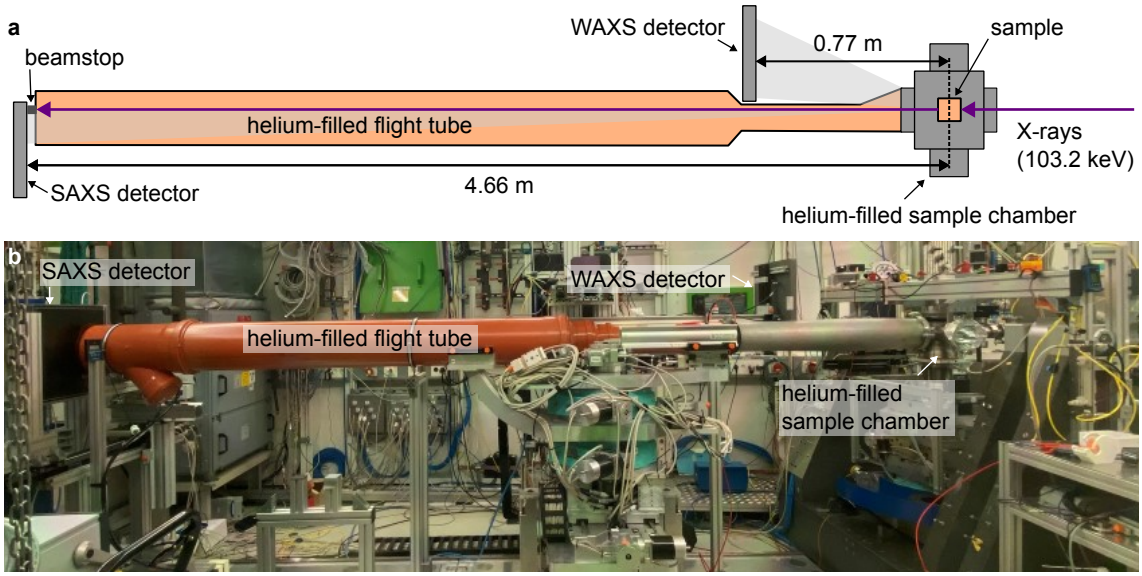

Figure 3.5: Setup at beamline P07 for in situ SAXS and TS of CuPd supercrystals. **a**, Schematic illustration of the main components of the setup. **b**, Photograph of the setup.

X-ray images were recorded with two large-area detectors (XRD 4343CT and Dexela 1512, Varex Imaging). The in situ reaction cell shown in Figure 3.2 was used as the sample environment. The path from the reaction cell to the SAXS detector was filled with helium to reduce the air scattering background. Data were recorded at 1 Hz and subsequent images were binned for analysis. The SDD was calibrated with silver behenate in a 1 mm polyimide capillary (Detakta) at the sample position using pyFAI [381]. The time- and temperature-dependent background signal was determined from a reaction mixture without metal precursors and an empty borosilicate capillary measurement.

Complementary laboratory in situ SAXS data were recorded with the SAXS setup at LMU (Table 3.6) at a SDD of 0.98 m for assembly experiments and 2.59 m for pure Cu and Pd syntheses. Data were recorded with 10 s per frame and the cosmic background was removed with the "all but one" approach as described in Section 2.4.5. Ex situ SAXS data of dilutions with different solvents were recorded for 1 h at a SDD of 1 m. The signal of an empty reaction capillary was used as a background.

Calibration and integration were done with pyFAI [381]. SAXS data were fitted using SasView version 5.0.5 [331] and custom fit routines using the lmfit, numpy, scipy, and jupyter notebook packages [383–386]. The signal of freely dispersed nanocrystals was fitted with a polydisperse sphere form factor (Equation 3.5) or a form factor with a core of homogeneous density and an exponentially decaying shell (SasView's "onion" model, Equation 3.6). For the SRO phase, a hard sphere structure factor (Equation 3.4) was multiplied with the form factor. The form factors and the fitting sequence for supercrystal assembly are given below. Porod invariants (Equation 2.17) were calculated by trapezoidal integration of the model intensities of the components within the fit range (0.018 to 0.42 $Å^{-1}$).

Polydisperse spheres on a power law background

$$\begin{aligned} I(q) = & \frac{\text{scale}_{\text{sphere}}}{\sum_i w_i V_i} \sum_i w_i \left[3\,\Delta\rho\, V_i \frac{\sin(qR_i) - qR_i\cos(qR_i)}{(qR_i)^3} \right]^2 \\ & + \text{background} \\ & + \text{scale}_{\text{power law}}\, q^{-\alpha} \end{aligned} \tag{3.5}$$

Polydispersity was described by a Gaussian distribution of particle radii R_i with weights w_i. The distribution was sampled at 31 points within six standard deviations σ_R around the mean. $V_i = \frac{4\pi}{3} R_i^3$ is the particle volume. For an in situ synthesis of CuPd nanocrystals a Gaussian distribution lead to slightly lower χ^2 compared to a Schulz-Zimm distribution [54]. The intensity was divided by the averaged particle volume $\sum_i w_i V_i$ to match the definition of $\text{scale}_{\text{sphere}}$ as a volume fraction as used in SasView [331]. $\Delta\rho$ is the scattering contrast between particle and solvent and was set to 1, as the data are not on absolute scale. The power law exponent α was allowed to vary between 1 and 4.

Polydisperse spheres with a radially decaying shell

The radial SLD profile of the shell is given by

$$\rho_{\text{shell}}(r) = B\mathrm{e}^{\frac{A(r-r_{\text{core}})}{\Delta t_{\text{shell}}}} + C \tag{3.6}$$

The scattering intensity was calculated using SasView's built-in "onion" model. The value of the decay constant A was fixed to -5 and the shell thickness Δt_{shell} was set to 1 nm. $B = 1$ and $C = 0$ were used as the core and solvent SLDs, respectively.

The corresponding scattering amplitude of the shell is

$$\begin{aligned} f_{\text{shell}} &= 4\pi \int_{r_{\text{shell}-1}}^{r_{\text{shell}}} \left[B\exp\left(\frac{A(r - r_{\text{shell}-1})}{\Delta t_{\text{shell}}} \right) + C \right] \frac{\sin(qr)}{qr}\, r^2\, dr \\ &= 3B\, V(r_{\text{shell}})\, \mathrm{e}^A\, h(\alpha_{\text{out}}, \beta_{\text{out}}) - 3B\, V(r_{\text{shell}-1})\, h(\alpha_{\text{in}}, \beta_{\text{in}}) \\ &+ 3C\, V(r_{\text{shell}}) \frac{j_1(\beta_{\text{out}})}{\beta_{\text{out}}} - 3C\, V(r_{\text{shell}-1}) \frac{j_1(\beta_{\text{in}})}{\beta_{\text{in}}} \end{aligned} \tag{3.7}$$

where

$$\begin{aligned} B &= \frac{\rho_{\text{out}} - \rho_{\text{in}}}{\mathrm{e}^A - 1}, \qquad C = \frac{\rho_{\text{in}}\mathrm{e}^A - \rho_{\text{out}}}{\mathrm{e}^A - 1}, \qquad \alpha_{\text{in}} = A\frac{r_{\text{shell}-1}}{\Delta t_{\text{shell}}} \\ \alpha_{\text{out}} &= A\frac{r_{\text{shell}}}{\Delta t_{\text{shell}}}, \qquad \beta_{\text{in}} = qr_{\text{shell}-1}, \qquad \beta_{\text{out}} = qr_{\text{shell}} \end{aligned} \tag{3.8}$$

and

$$h(x,y) = \frac{x\sin(y) - y\cos(y)}{(x^2+y^2)y} - \frac{(x^2-y^2)\sin(y) - 2xy\cos(y)}{(x^2+y^2)^2 y}$$

j_1 is the first spherical Bessel function of first kind.

Icosahedral particles

The SAXS intensity of icosahedral particles was calculated using the DSE [308, p. 117]. Atomic coordinates of an icosahedron with $N_{shells} = 7$ were calculated with the ase python package [387] assuming the lattice constant of 3.893 Å of Pd. Then a list of pairwise distances d_{ij} was generated. The SAXS intensity was calculated as

$$I(q) = \frac{1}{\sum_i V_i} \left(\sum_i f_i^2 + 2 \sum_{i \neq j} f_i f_j \frac{\sin(q d_{ij})}{q d_{ij}} \right) \tag{3.9}$$

The atomic form factors f_i were approximated by spherical form factors (Equation 2.21). $V_i = \frac{4\pi}{3} r_i^3$ are the volumes of the scattering atoms. r_i was set to half the distance between neighboring atoms. The normalization by the sum of the atomic volumes is arbitrary and was included to match the definition in Equation 3.5.

Multicomponent model for supercrystal assembly

The intensity was modeled as the sum of these terms:

$$I(q) = I_{\text{fcc}} + I_{\text{SRO}} + I_{\text{free}} + I_{\text{solvent}} + I_{\text{bkg}} \tag{3.10}$$

The intensity of supercrystals is

$$I_{\text{fcc}}(q) = \text{scale}_{\text{fcc}}\, P(q) S_{\text{fcc}}(q) \tag{3.11}$$

with $S_{\text{fcc}}(q)$ as defined in Equation 2.28 and pure Gaussian peaks ($\eta = 0$).

The intensity of the short-range ordered phase is

$$I_{\text{SRO}}(q) = \text{scale}_{\text{SRO}}\, P(q) S_{\text{SRO}}(q) \tag{3.12}$$

with $S_{\text{SRO}}(q)$ as defined in Equation 3.4.

The intensity of free particles is the form factor of polydisperse spheres with a Gaussian distribution of radii as defined in Equation 3.5.

$$I_{\text{free}}(q) = \text{scale}_{\text{free}}\, P(q) \tag{3.13}$$

I_{fcc}, I_{SRO} and I_{free} use the same form factor to avoid overfitting.

The intensity of the solvent lamellae was modeled by two Gaussian peaks (Equation 2.31, $\eta = 0$) with coupled peak positions ($q_2 = 2\, q_1$) and independent heights and widths

$$I_{\text{solvent}}(q) = B(q, q_1, h, \text{FWHM}, \eta) + B(q, q_2, h, \text{FWHM}, \eta) \tag{3.14}$$

The background intensity was modeled by a constant term, a power law, and a Guinier law (Equation 2.19) with a radius of gyration R_g

$$I_{\text{bkg}}(q) = \text{background} + \text{scale}_{\text{power law}}\, q^{-\alpha} + \text{scale}_{\text{Guinier}}\, \mathrm{e}^{-\frac{1}{3}(qR_g)^2} \tag{3.15}$$

Fitting sequence for supercrystal assembly

The model was refined in a six-step procedure for each frame, going backwards in time from an almost fully assembled state, to avoid local minima or unphysical parameter results:

1. Refinement of the background terms and scales of the components.
2. Refinement of the form factor terms (mean diameter and standard deviation) and the scales of the components.
3. Refinement of the fcc lattice parameter and peak width, and the scales of the components.
4. Refinement of the SRO phase (effective diameter and volume fraction) and the scales of the components.
5. Refinement of the form factor terms and the scales of the components.
6. Refinement of the peaks of the solvent lamellae and the scales of the components.

The refined parameters were used as the starting parameters for the next frame ("chain fit").

For estimation of the organic ligand shell contrast with respect to the metal core and the solvent mixture, SLDs were calculated based on the material composition, as given in Table 3.7. SLDs for 17.4 keV were calculated using SasView 5.0.5 [331]. SLDs for 103.2 keV were calculated based on the atomic form factors from the NIST FFAST database [313]. The real and imaginary part of the form factor $f_1 = f'(E)$ and $f_2 = f''(E)$ are given in units of electrons per atom. δ and β are the real and imaginary refractive index decrements ($n = 1 - \delta + \mathrm{i}\beta$) [308, pp. 75 ff.]. For an elemental composition described by n_j they are calculated as

$$\delta, \beta = \frac{\rho N_A r_0 \lambda^2 \sum_j (n_j f_j(\lambda))}{2\pi \sum_j (n_j M_j)} \tag{3.16}$$

with $f_j = f_{j,1}$ and $f_{j,2}$, respectively. ρ is the mass density, r_0 is the classical electron radius (Equation 2.9), M_j is the atomic weight and λ is the X-ray wavelength. The real and imaginary part of the SLD are $\frac{2\pi\delta}{\lambda^2}$ and $\frac{2\pi\beta}{\lambda^2}$. The real part is given in the table. Both X-ray energies used are sufficiently far away from absorption edges so that the energy-dependent SLD variation is small (below 3%). Variations in the metal composition also affect the SLD by less than 10%.

Table 3.7: Scattering length densities (SLDs) used in the CuPd SAXS analysis.

material	**density** (g/cm^3)	**effective elemental composition** n_j	**SLD** (10^{-6}Å^{-2}) at 17.4 keV	**SLD** (10^{-6}Å^{-2}) at 103.2 keV
Cu	8.96	Cu	70.2	69.5
Pd	12.023	Pd	86.3	88.6
Cu:Pd 70:30	9.879	Cu_7Pd_3	74.7	75.1
Cu:Pd 60:40	10.185	Cu_6Pd_4	76.3	77.0
Cu:Pd 20:80	11.410	Cu_2Pd_8	82.9	84.7
OlAc	0.895	$C_{18}H_{34}O_2$	8.5	8.5
OlAm	0.813	$C_{18}H_{37}N$	7.84	7.85
dioctyl ether	0.806	$C_{16}H_{34}O$	7.86	7.79
solvent mixture	0.8289	$C_{85}H_{172}N_3O_3$	7.97	7.97

SAXS data of *CoO nanoassemblies* were recorded at beamline P03 [359] at PETRA III, DESY, Hamburg, and with the laboratory SAXS setup. Setup parameters are given in Table 3.6. At P03, samples were loaded in 2 mm diameter glass capillaries (Hilgenberg). Data from 5×0.1 s at 5.2 m SDD and 0.5 s at 2.0 m SDD were transformed to intensity as a function of scattering vector using the Nika package [388] for IGOR Pro (Wavemetrics), and combined. A solution of $Co(acac)_3$ in BnOH was recorded and subtracted as a background. At the laboratory setup, samples were loaded in custom-made 10 mm long aluminium chambers with polyimide windows and measured for 5×20 min and 7×20 min for samples taken at 20 and 90 min reaction time, respectively. The cosmic background was removed by taking the median of successive images. Data were fitted with a spherical form factor and a Schulz-Zimm polydispersity distribution [54], using SasView version 4.2.2 [331].

3.3.2 WAXS and TS

WAXS and TS data of LHP nanocrystals were recorded at beamline P07 of PETRA III (DESY, Hamburg) [310]. The TS data of spheroidal LHP nanocrystals shown in Section 2.4.4 were recorded at beamline P21.1. The setup parameters are given in Table 3.6. Images were recorded at 0.5 s per frame (2 Hz). Calibration and integration were done with pyFAI [381]. The solvent background was subtracted as described for the SAXS data analysis. WAXS data were fitted using a Pseudo-Voigt peak on a linear background between 1.92 and 2.18 $Å^{-1}$. The peak position, height, FWHM, Lorentz/Gauss ratio and two background parameters were allowed to vary. An instrumental resolution of $(3.342 \pm 0.008) \cdot 10^{-2}$ $Å^{-1}$ was estimated by fitting a reflection of LaB_6 at 2.11 $Å^{-1}$ and subtracted from the fitted FWHM, using Equation 2.40. The fit is shown in Figure A1. The crystallite size was calculated as $\frac{2\pi}{\Delta q}$. Δq is the resolution-corrected FWHM.

The reduced PDF $G(r)$ was obtained from the TS data using PDFgetX3 [353] with parameters given in Table 3.8. Instrumental parameters were obtained from a refinement of a LaB_6 powder standard. PDF refinement was carried out using DiffPy-CMI [389]. For precursor clusters, the cluster motifs were generated as .xyz files containing octahedral units, using python. The models were then refined against $G(r)$ by varying a scale factor, the δ_2 parameter, the isotropic displacement parameters of lead and halide, and between one and three expansion factors. These factors, xscale, yscale and zscale, stretch the cluster motif along the cartesian axes. Here, z corresponds to the axial direction and x and y to the equatorial directions of an octahedron.

Table 3.8: Parameters of the PDF transformation and refinement for LHP nanocrystals.

	q_{min} ($Å^{-1}$)	q_{max} ($Å^{-1}$)	$q_{max,inst}$ ($Å^{-1}$)	r_{poly} (Å)	q_{damp} ($Å^{-1}$)	q_{broad} ($Å^{-1}$)
spheroidal nanocrystals	0.1	16.5	17.9	1.13	0.042	0.039
precursor micelles	1.8	14.3	18.2	1.23	0.010	0.010
post-synthetic modification	1.5	10	15.9	1.09	0.013	0.012

In situ WAXS data of *Cu nanosphere synthesis* were recorded at the Swiss-Norwegian beamline BM31 [390] at the European Synchrotron Radiation Facility (ESRF), Grenoble, and analyzed by the group of Prof. Dr. Raffaella Buonsanti, EPFL, prior to this work [144]. An X-ray energy of 25 keV ($\lambda = 0.5107$ Å) and a sample length of 10 mm were used.

Images were taken every 60 s. The data were integrated using the FIT2D software [391] and transformed to a 2θ scale for Cu K_α radiation for comparison with literature.

In situ TS data of *CuPd nanocrystal synthesis* were taken simultaneously with the in situ SAXS data at beamline P07. Setup parameters are given in Table 3.6. Calibration of the WAXS/TS detector with a LaB_6 standard and integration were performed with pyFAI [381]. Background subtraction and transformation to the reduced PDF $G(r)$ were done using PDFgetX3 [353] with parameters given in Table 3.9. Instrumental parameters were determined using a silicon powder standard loaded into the reaction capillary. PDF data were analyzed by Davide Derelli from the group of Prof. Dr. Dorota Koziej, UHH, using DiffPy-CMI [389]. Atomistic models were created with the ase python package [387]. Details on the Monte Carlo optimization of atomic positions in the icosahedral clusters are given in reference [392, Supplementary Information].

Table 3.9: Parameters of the PDF transformation for CuPd nanocrystals.

q_{min} (Å^{-1})	q_{max} (Å^{-1})	$q_{\mathrm{max,inst}}$ (Å^{-1})	r_{poly} (Å)
2.35	14.6	18.3	0.9

In situ TS data of *CoO nanoassemblies* were taken at beamline P21.1, PETRA III, DESY, Hamburg [360], and analyzed by the group of Prof. Dr. Dorota Koziej, UHH, prior to this work. The in situ cell described in reference [377, Supplementary Information] was used as the sample environment. Setup parameters are given in Table 3.6. Data were recorded with 10 s per frame. A capillary filled with BnOH was measured as the background signal. The SDD was calibrated with a CeO_2 powder standard placed in the capillary of the in situ cell. Integration was performed with pyFAI [381] and the intensity was background-subtracted and transformed to $G(r)$ using xPDFsuite and PDFgetX3 [353]. The parameters of the PDF transform and refinement, determined from the CeO_2 standard, are given in Table 3.10.

Table 3.10: Parameters of the PDF transformation and refinement for CoO nanoassemblies.

q_{min}(Å^{-1})	q_{max}(Å^{-1})	q_{damp}(Å^{-1})	q_{broad}(Å^{-1})
0.59	16.5	0.0463	0.0574

3.3.3 PXRD

PXRD data of LHP nanocrystals were recorded with the laboratory multipurpose setup at LMU (see Table 3.6). Purified samples of colloidal nanocrystals were drop casted on adhesive tape (3M Scotch Magic 810) and dried under ambient conditions. The Pilatus 100K detector was placed at 0.23 m distance from the sample and raster-scanned perpendicularly to the X-ray beam. The total measurement time was 1 h 40 min per sample. Cosmic background was removed using the "all but one" approach as described above. The background signal of the adhesive tape was subtracted. Calibration of the detector position with a LaB_6 standard on adhesive tape and azimuthal integration of the powder patterns were done using pyFAI [381]. Powder diffraction patterns were simulated with Mercury [393]. Nanocrystal structures were drawn using VESTA [394].

3.4 Spectroscopy, microscopy and DLVO calculation

3.4.1 Optical spectroscopy

In situ PL spectra of LHP nanocrystal synthesis were recorded with the reaction cell described in Section 3.2, typically simultaneously with SAXS and WAXS data. Either a spectrum of a non-emissive precursor mixture or a constant intensity was subtracted as a background. For analysis, the emission peak position, height and FWHM were tracked and the results from subsequent frames were binned for further analysis. To distinguish emission from 2ML and 3ML nanocrystals the signal at wavelengths below and above 450 nm was separated. The intensities were summed in bins ranging from 415 to 450 nm and from 450 to 470 nm, respectively.

Ex situ absorption spectra, PL spectra, and PLQY values were recorded by Nina A. Henke from the group of Prof. Dr. Alexander S. Urban at LMU. A Horiba FluoroMax-4Plus spectrometer with a xenon arc lamp, a F-3031 transmission accessory with quartz cuvettes (Hellma Analytics), and a Horiba Quanta-ϕ F-3029 integrating sphere were used for absorption and PLQY measurements, respectively. The excitation wavelength for PL spectra was set to 380 nm.

3.4.2 Electron microscopy

TEM images of LHP nanocrystals were recorded by Nina A. Henke with a JEOL JEM-1011 at the chair of Prof. Dr. Joachim Rädler, LMU, at an acceleration voltage of 80 kV.

TEM images of Cu nanospheres were recorded by Valeria Mantella using an Analytical JEOL-2100F FETEM at EPFL, equipped with a Gatan camera, at an acceleration voltage of 120 kV. Samples were prepared by placing one drop of the nanocrystal solution in n-hexane on the surface of copper grids (Ted Pella, Inc.).

HRTEM images of CuPd nanocrystals were recorded with a JEOL JEM-2200FS, operating at 200 kV, at the electron microscopy facility of the UHH by Stefan Werner and Andrea Köppen. EDX measurements of CuPd nanocrystals were done using a Si(Li) JEOL JED-2300 detector with the JEOL JEM-2200FS.

TEM images of CoO nanoassemblies were recorded with the JEOL JEM-2200FS at an acceleration voltage of 100 kV by Andreas Kornowski, Andrea Köppen and Stefan Werner.

SEM images of CoO nanoassemblies were recorded using a probe-corrected Hitachi Regulus 8220 at the chair of Prof. Dr. Dorota Koziej, UHH. Images were obtained with an acceleration voltage of 10 kV, using the secondary electron signal.

ADF-STEM images of LHP nanocrystals were recorded by Tizian Lorenzen and Dr. Benjamin März from the group of Prof. Dr. Knut Müller-Caspary at LMU. A probe-corrected FEI Titan Themis 60-300 was operated at an acceleration voltage of 300 kV with a semi-convergence angle of 16.6 mrad. The inner and outer collection angles of the annular dark field detector were 33 and 198 mrad. No further filtering was applied to the micrographs. Samples were drop casted onto TEM grids (Quantifoil R2/2, 2 nm ultrathin carbon).

3.4.3 X-ray absorption spectroscopy

In situ XANES spectra of *Cu nanosphere synthesis* were recorded and analyzed by Valeria Mantella and others from the group of Prof. Dr. Raffaella Buonsanti, EPFL, prior to this work. Data were recorded at the Swiss-Norwegian beamline BM31 at the ESRF [390], operating in transmission mode with 30 cm ionization chambers and a 5 mm diameter beam. The flight path in the glass cell was adapted between 5 and 20 mm to optimize the signal. Spectra were recorded every 7 min 40 s. A Cu foil was used as an internal standard.

In situ HERFD-XANES spectra of *CoO nanoassemblies* were recorded and analyzed by Lukas Grote and others from the group of Prof. Dr. Dorota Koziej, UHH, prior to this work. Experiments were carried out at beamline ID26 at the ESRF, Grenoble [395]. The incident energy was varied from 7.70 to 7.78 keV around the Co K edge using a Si (1 1 1) double crystal monochromator. An emission spectrometer in Rowland geometry with five Si (5 3 1) analyzer crystals was aligned to a Bragg angle of 77° for the maximum of the Co K_{α_1} fluorescence line. HERFD-XANES data were recorded every 80 s with a step width of 0.05 eV and an energy resolution of 1.22 eV, alternating the beam position on the sample.

The HERFD-XANES data were reduced and binned using PyMCA [396]. The in situ dataset was then decomposed with MCR-ALS [374] in MATLAB (The MathWorks Inc.). The number of components (three) was determined using singular value decomposition and the initial spectra and concentration profiles were estimated using the purest variables detection method. Non-negativity of spectra and concentrations, unimodality of concentrations with 20% tolerance, and a convergence criterion of 0.1 were used as constraints.

3.4.4 FTIR spectroscopy

FTIR spectra of CuPd nanocrystals were recorded by Davide Derelli from the group of Prof. Dr. Dorota Koziej, UHH. A Bruker Alpha II spectrometer was used in ATR mode.

3.4.5 Calculation of interaction potentials

The DLVO interaction potential of CuPd nanocrystals was estimated by a sum of vdW attraction and steric repulsion as described in reference [103]. The non-retarded Hamaker constant A, valid for small separations, was calculated using Lifshitz theory:

$$A = \frac{3}{4}k_BT + \frac{3h\nu_e}{16\sqrt{2}}\frac{(\sqrt{2}+c)^3 - (\sqrt{2}+2c)(n^2-1) + (n^2-1)^2/c}{\left((\sqrt{2}+c)^2+n^2-1\right)^{3/2}}, \qquad c = \frac{\nu_e}{\nu_{e,d}} \tag{3.17}$$

n is the refractive index of the medium, approximated here by the value of ODE [103]. ν_e and $\nu_{e,d}$ are the plasma frequencies of nanocrystal and medium, respectively. The first term, including k_BT as the thermal energy, is negligibly small for metal nanocrystals (<1% according to reference [103]). The dominant second term A_2 results from an integration of the frequency-dependent dielectric response $\epsilon(\nu)$. The prefactor $\frac{3h\nu_e}{16\sqrt{2}}$ is the value of the Hamaker constant in vacuum. h is the Planck constant. The following factor takes into account the nanocrystal material as well as the medium in between:

$$A_2 = \frac{3h}{4\pi}\int_0^\infty \left(\frac{\epsilon_1(\nu)-\epsilon_3(\nu)}{\epsilon_1(\nu)+\epsilon_3(\nu)}\right)^2 d\nu, \qquad \epsilon_1(\nu) = 1+\frac{\nu_e^2}{\nu^2}, \qquad \epsilon_3(\nu) = 1+\frac{n^2-1}{1+\frac{\nu^2}{\nu_{e,d}^2}} \tag{3.18}$$

The vdW attraction of the metallic cores and the steric repulsion were estimated using Equations 2.2, 2.3 and 3.17 with parameters given in Table 3.11:

Table 3.11: Parameters of the DLVO potential calculation for CuPd nanocrystals.

parameter	**symbol**	**value**
diameter	d	3 nm
plasma frequency of Cu	ν_e	$4.6 \cdot 10^{15}$ Hz [397]
plasma frequency of Pd	ν_e	$6.2 \cdot 10^{15}$ Hz [397]
weighted average for CuPd	ν_e	$5.2 \cdot 10^{15}$ Hz
refractive index of oleylamine/oleic acid	n	1.44 [103]
plasma frequency of oleylamine/oleic acid	ν_{ed}	$3 \cdot 10^{15}$ Hz [102, chapter 13]
temperature	T	100 °C
resulting Hamaker constant	A	2.1 eV
grafting density	σ	10 nm^{-2}
length	L_0	2 nm
entropic repulsion parameter	Re^2	2 nm^2 [85–87]

4 Results

4.1 Shape control of lead halide perovskite nanocrystals by an antisolvent

Part of the results shown in this chapter have been published in reference [379].

Frank, K. (*), Henke, N. A. (*), Lampe, C., Lorenzen, T., März, B., Sun, X., Haas, S., Gutowski, O., Dippel, A.-C., Mayer, V., Müller-Caspary, K., Urban, A. S., and Nickel, B. Antisolvent controls the shape and size of anisotropic lead halide perovskite nanocrystals. *Nat. Commun.* 15, 8952 (2024). doi: 10.1038/s41467-024-53221-5

(*) equal contribution

Preprint: doi: 10.26434/chemrxiv-2024-psrh2

Data repository: doi: 10.57970/nb26d-cak63

Abstract

This chapter is focused on the in situ X-ray scattering analysis of LHP nanocrystal synthesis and the origin of nanocrystal shape anisotropy. The synthesis has been developed prior to this work by the group of Prof. Dr. Alexander S. Urban (LMU). Ligand-assisted spontaneous crystallization of LHP nanocrystals at room temperature begins by mixing of a lead bromide and a cesium precursor containing OlAm and OlAc ligands in toluene. Mixing is followed by injection of a polar antisolvent such as acetone, i.e., a poor solvent for the forming ligand-coated nanocrystals. A seemingly small variation of precursor and antisolvent volumes results in a different nanocrystal anisotropy. Either prolate nanorods or oblate nanoplatelets are obtained. To reveal what is the shape-determining step of this synthesis **I developed a custom in situ reaction cell for X-ray scattering, PL spectroscopy, and injection of reagents**. **I then analyzed the in situ SAXS, WAXS, TS and PL data obtained with this cell** at the beamlines P62 and P07 of PETRA III, DESY in Hamburg and at LMU. Following the course of the reaction, firstly, SAXS and TS data show a reverse micellar cluster structure of the $PbBr_2$ precursor. Secondly, small prolate LHP nanoclusters are identified as reaction intermediates based on a combination of in situ SAXS, WAXS, and PL spectroscopy. Thirdly, the formation of a hexagonal mesophase following antisolvent injection is found to be the crucial step for obtaining nanorods. Nanoplatelets, instead, grow freely dispersed from the intermediate nanoclusters and precursor clusters at lower antisolvent volumes and only later stack in a lamellar mesophase. These distinct reaction pathways are rationalized by classifying the involved solvents in terms of different parameters. Dipole moment and Hansen hydrogen bonding parameter lead to the best classification of products. Additionally, **I investigated the post-synthetic modification of the nanocrystals by addition of lead halide salt solutions.** WAXS, TS, and PL data, complemented by SAXS, again show a reverse micellar structure of the salt solution and a successful and quantitative substitution of bromine by iodine in the nanocrystals.

4.1.1 Synthesis and characterization of anisotropic LHP nanocrystals

4.1.1.1 Synthesis procedure

Anisotropic LHP nanocrystals are synthesized via a ligand-assisted spontaneous crystallization at room temperature, as described in Section 3.1.1. Two specific reaction conditions are chosen for the in situ studies, differing only by the amounts of precursors and antisolvent. The different precursor volumes produce 3ML thick nanorods or 2ML thick nanoplatelets, respectively. Here, the characteristic small dimension is given as the number of monolayers (ML) of $PbBr_6$ octahedra. The two reaction products are easily distinguishable by PL spectroscopy for a quick inspection. All syntheses work in a Cs-deficient regime, which promotes the formation of anisotropic nanocrystals [25, 200]. Prior to this work the ratio of Cs-oleate and $PbBr_2$ precursor has been tuned to reliably obtain different LHP nanocrystals with different thickness and anisotropy. The reaction scheme is illustrated in Figure 4.1 a.

The synthesis begins with a small volume of $PbBr_2$-precursor, which is filled into the reaction cell and vigorously stirred. A Cs-oleate precursor is then injected, which defines the time $t = 0\,s$. After a delay of 10 s acetone is injected into the mixture as an antisolvent. In addition to the effect of the antisolvent on the nanocrystal morphology, which is investigated in detail below, the addition leads to formation of a turbid solution and to a precipitate, which can be separated in a centrifugation step. After 1 to 8 min the reaction is terminated by centrifugation and the precipitate is redispersed in n-hexane. The obtained anisotropic nanocrystals are quasi-1D nanorods or quasi-2D nanoplatelets of $CsPbBr_3$, as sketched in Figure 4.1 b. The nanocrystals are visualized as being terminated by complete octahedral units. When ligands are shown, they occupy some Cs^+ and some Br^- positions. This assignment is based on studies on surface termination and ligand binding of LHPs (see Section 2.3.1), and not further investigated in this work.

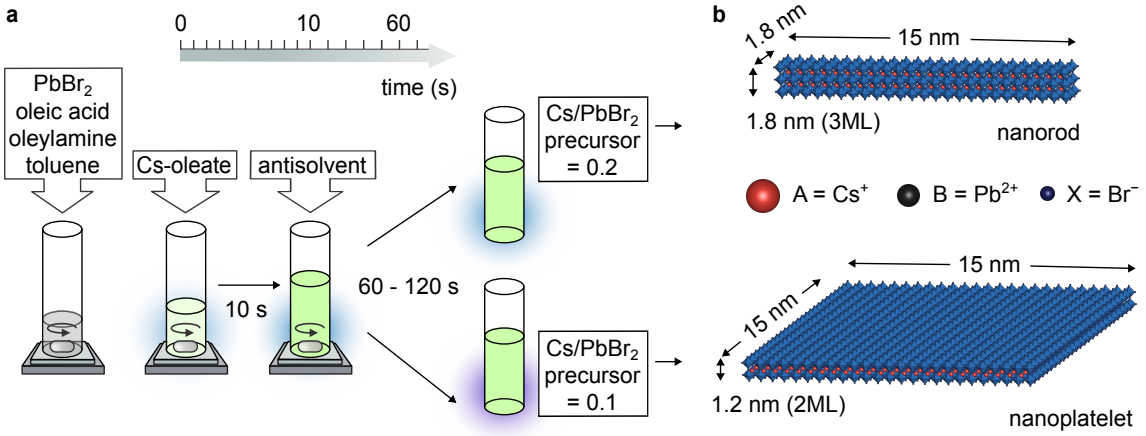

Figure 4.1: Schematic illustration of the synthesis of anisotropic LHP nanocrystals. **a**, A $PbBr_2$ precursor is loaded in the capillary of the in situ reaction cell and vigorously stirred. Cs-oleate is injected as the second precursor. After 10 s antisolvent is injected. After 60 to 120 s the reaction is terminated by centrifuging the mixture and redispersing the precipitate in n-hexane. **b**, Schematic illustration of anisotropic LHP nanocrystals obtained for different Cs-oleate to $PbBr_2$ precursor ratios: 3ML nanorods and 2ML nanoplatelets. Figure adapted from [379] with permission. CC-BY license 2024, Springer Nature.

The hypothetical stoichiometry, neglecting the contribution of the bound ligands, is then given by the following formula for the number of Cs, Pb and Br atoms:

$$N_{\mathrm{Cs}} = (N_x - 1)(N_y - 1)(N_z - 1) \tag{4.1}$$

$$N_{\mathrm{Pb}} = N_x N_y N_z \tag{4.2}$$

$$N_{\mathrm{Br}} = 6\,N_{\mathrm{Pb}} - [(N_x - 1)N_y N_z + N_x(N_y - 1)N_z + N_x N_y(N_z - 1)] \tag{4.3}$$

N_x, N_y, N_z are the nanocrystal dimensions given as the number of monolayers. For three large values the stoichiometry approaches bulk $CsPbBr_3$. 3ML nanorods with a size of $1.8 \times 1.8 \times 15$ nm^3 ($3 \times 3 \times 25$ ML) have a composition of $Cs_{0.43}PbBr_{3.71}$ and 2ML nanoplatelets ($1.2 \times 15 \times 15$ nm^3, $2 \times 25 \times 25$ ML) are composed of $Cs_{0.46}PbBr_{3.58}$. Nanorods should therefore have a slightly more pronounced Cs-deficiency compared to nanoplatelets. The Cs-deficiency imposed by the precursor ratios is even more extreme ($Cs/PbBr_2$=0.2 for nanorods and 0.1 for nanoplatelets), since a ratio closer to 1 would lead to isotropic nanocrystals, such as nanocubes [379, Supplementary Information].

4.1.1.2 Spectroscopy, electron microscopy and X-ray characterization

The usual characterization of LHP nanocrystals is carried out by PL spectroscopy of a purified dispersion. Exemplary PL spectra of 3ML nanorods and 2ML nanoplatelets are shown in Figure 4.2 a and b. The characteristic emission wavelength serves as an indication of the thickness of the nanocrystals due to quantum and dielectric confinement effects, as detailed in Section 2.3.1. The dominant contribution to the confinement comes from the smallest nanocrystal dimension. Therefore, these spectral characteristics are typically used to classify the monolayer thickness [25, 398]. They have been used as optimization targets in machine learning-based exploratory synthesis campaigns [234], but they do not allow to distinguish the dimensionality of the nanocrystals without additional information. Low emission linewidth is characteristic of a monodisperse sample. 3ML nanorods show a sharp excitonic absorption at 448 nm and a relatively narrow PL at 460 nm (FWHM 18 nm). 2ML nanoplatelets show excitonic absorption at 428 nm and even narrower PL at 434 nm (FWHM 14 nm).

Furthermore, absorption spectroscopy on diluted dispersions is routinely carried out, as also shown in Figure 4.2 a and b. The absorption spectra contain information about the ML thickness via the excitonic absorption peak. Potential side products lead to additional peaks, even if these products are non-emissive or emit only weakly. PL spectroscopy would not detect such non-emissive side products. It is, however, better compatible with a fast in situ characterization due to its relaxed concentration requirements, as no dilution is required and the sample can be maintained at synthesis conditions.

The dimensions of the resulting nanocrystals are additionally studied by TEM or high-resolution ADF-STEM. Exemplary ADF-STEM images of 3ML nanorods and 2ML nanoplatelets are shown in Figure 4.2 c. Nanoplatelets are identified in these images by the coexistence of flat-lying, rectangular nanocrystals and stacks of nanocrystals seen from the side. Nanorods may also assemble into regular arrangements on the TEM grid, but they are rarely observed standing up, i.e., with both small sides visible at once. The nanorod shape is therefore usually inferred by the absence of large flat-lying nanocrystals in the image.

The size of the small nanocrystal dimension is difficult to obtain from electron microscopy images. Usually, statistics over several measurements are shown. A fast Fourier transform

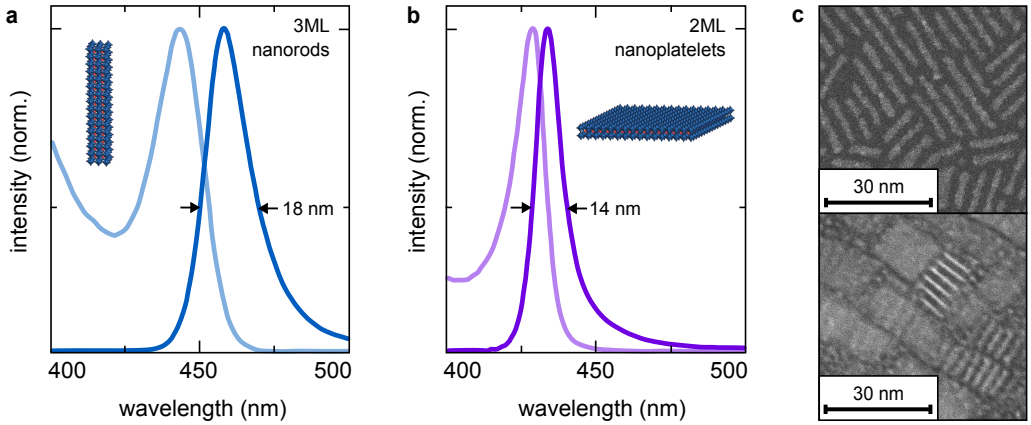

Figure 4.2: Ex situ characterization of LHP nanocrystals by spectroscopy and electron microscopy. a, b, Optical absorption and PL spectroscopy characterization of 3ML nanorods and 2ML nanoplatelets. **c**, ADF-STEM images of 3ML nanorods (top) and 2ML nanoplatelets (bottom). Optical spectra were recorded by Nina A. Henke, ADF-STEM images by Tizian Lorenzen. Figure adapted from [379] with permission. CC-BY license 2024, Springer Nature.

(FFT) of the image is often used to identify typical repeat distances, from which the size is calculated. 3ML nanorods show an average width of (1.9 ± 0.2) nm and a length of (15.0 ± 2.2) nm. Here, a square cross section is assumed, since without thickness information along the zone axis of the TEM image a slight difference in the widths of the two short axes would remain undetected. 2ML nanoplatelets show an average thickness of (1.3 ± 0.1) nm and a square shape with an edge length of (15.6 ± 2.3) nm.

The statistics over a large number of individually observed nanocrystals and a resolution down to the spacing of rows of single atoms in ADF-STEM make electron microscopy a useful method of characterization. However, the necessary drop casting on TEM grids and the transfer to the electron microscope are rather time-consuming. The search for a good image within the sample is usually the time-limiting step, ranging from tens of minutes to hours if atomic resolution in ADF-STEM is required[1]. Particle anisotropy may remain somewhat ambiguous in the electron microscopy images due to the projection of the image along one direction and preferred orientation effects [200, 399]. Furthermore, the heavy lead ions are frequently reduced to Pb^0 by the intense electron beam, contaminating and damaging the sample [400].

TEM samples must be dried on a substrate, meaning that observed assemblies such as stacks of nanoplatelets are likely not representative of the state in dispersion. Electron microscopy investigation of reaction pathways, which may involve intermediate structures, requires either elaborate miniaturized in situ reaction environments or techniques for reliably stopping the reaction and extracting and preparing non-reacting aliquots (see Section 2.2.3). For LHP syntheses this is particularly challenging due to the quickly reacting ionic species present [13]. Syntheses carried out at room temperature would essentially have to be frozen to fully arrest the reaction. This results in similar issues with the characterization of LHP nanocrystals as with CoO nanoassemblies, shown in Section 4.4.

The crystalline structure of the synthesized nanocrystals is verified by powder X-ray diffraction (PXRD) on dried aliquots. Powder diffractograms of purified and drop casted samples of 3ML nanorods and 2ML nanoplatelets are shown in Figure 4.3. Both samples show pronounced reflections, which match the expected positions for orthorhombic (Pnma)

[1] Tizian Lorenzen, personal communication, October 25, 2024.

$CsPbBr_3$ (COD 4510745, [168], green curve). Some indexed reflections are sharper for 2ML nanoplatelets than for 3ML nanorods, suggesting a larger crystalline domain size in the nanoplatelets. A simple Scherrer analysis (Equation 2.39) of the (0 4 0)/(2 0 2) reflections yields domain sizes of (9.9 ± 0.2) nm and (22.3 ± 0.8) nm for 3ML nanorods and 2ML nanoplatelets, respectively. Nanoplatelets thus likely consist of only one large domain, whereas nanorods may be polycrystalline. It should be noted, however, that a simplified Scherrer analysis is inaccurate for strongly anisotropic nanocrystals, since several reflections may overlap and experience different broadening. For the same reflection arising from smaller and larger crystal dimensions, the largest dimension often dominates (see Equation 2.38). Therefore, more detailed modeling, e.g., using the DSE over an extended q range (Equation 2.41), would be required to obtain more precise domain size values from the powder diffractograms.

A strong background, which is mainly visible as a broad peak at $1.4\,\text{Å}^{-1}$, is observed underneath the reflections. This signal likely originates from excess OlAm and OlAc ligands and is also seen for the ligand-rich $PbBr_2$ precursor solution after drying (blue curve). A similar intensity is reported in literature for amorphous OlAm [401].

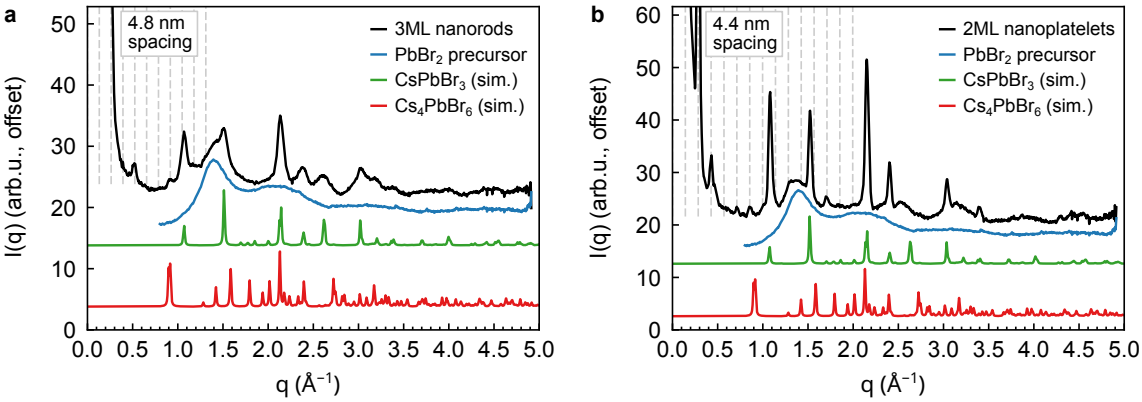

Figure 4.3: PXRD of purified LHP nanocrystals. **a**, PXRD intensity of 3ML nanorods. **b**, PXRD intensity of 2ML nanoplatelets. The intensity of dried $PbBr_2$ solution is shown for comparison. Simulated intensities of $CsPbBr_3$ and Cs_4PbBr_6 are additionally shown. Vertical dashed lines indicate a regular spacing of the nanocrystals due to drying on the substrate. Figure adapted from [379, Supplementary Information] with permission. CC-BY license 2024, Springer Nature.

The remaining reflections can be assigned to a regular series, starting at low q. This signal corresponds to a spacing of 4.8 nm for 3ML nanorods and 4.4 nm for 2ML nanoplatelets, respectively. Therefore, the nanocrystals form a regular assembly upon drying on the adhesive tape substrate. These reflections are more pronounced for 2ML nanoplatelets, which likely show a higher assembly tendency due to their larger common facets. Despite assembly formation no preferred orientation of the sample with the tape substrate, i.e., textured diffraction rings in transmission geometry, was observed. Therefore, the PXRD peak amplitudes are representative of a true powder, and can be readily compared to the simulated intensities.

In particular, the simulated intensity of trigonal Cs_4PbBr_6 ($R\bar{3}c$:H, 167, COD 1538416, a typical non-emissive byproduct or intermediate [197]) is additionally shown as a red curve. The corresponding reflections are not observed in the data. This indicates that no Cs_4PbBr_6 byproduct is present in the purified LHP nanocrystal samples. It should be noted that very small amounts of small Cs_4PbBr_6 nanocrystals with broad reflections would not be detectable in the pattern, but also TEM images show no such byproducts.

As outlined above, despite providing substantial quantitative information about the optical properties, dimensions, and crystalline structure of synthesized anisotropic LHP nanocrystals, ex situ PL and absorption spectroscopy, electron microscopy, and powder X-ray diffraction are not well suited for investigating reaction pathways. Additional in situ compatible techniques are required for studying nucleation and growth processes, as summarized in Section 2.2.3. In this work, a combination of structural and optical probes is chosen, as illustrated in Figure 4.4, since crystalline structure and emission are closely intertwined. Both SAXS and WAXS are used to relate information about morphology and assembly on the nanometer scale with crystallographic information, i.e., phase and domain size. A special, miniaturized in situ reaction cell was constructed for this purpose and is described in detail in Section 3.2 (see Q4).

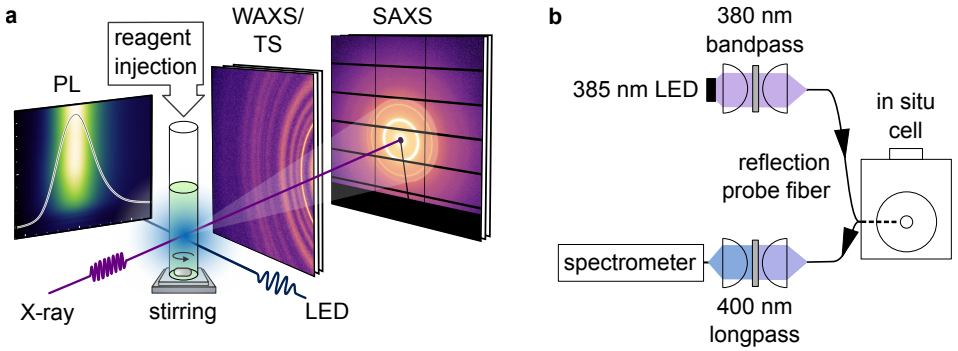

Figure 4.4: In situ setup for SAXS, WAXS, TS, and PL spectroscopy. **a**, Schematic illustration of the simultaneous detection during synthesis. **b**, Optical setup for PL excitation and detection. **a** adapted from [379] with permission. CC-BY license 2024, Springer Nature.

4.1.2 Precursor micelles and intermediate nanoclusters

4.1.2.1 Identification of nanoclusters via PL and WAXS

Using the in situ cell, the full synthesis of anisotropic LHP nanocrystals is investigated by analysis of the scattering and PL signals. The results are shown going forward in time through the different phases of the reaction.

Before Cs-oleate precursor injection, no PL emission above the instrumental background is detected from the $PbBr_2$ precursor. After injection of the Cs-oleate precursor an emission at 446 nm with a FWHM of 40 nm is observed within 2 s (Figure 4.5 a), indicating the formation of strongly quantum confined LHP. The emission wavelength approximately corresponds to a size of 3ML, i.e., 1.8 nm, in the smallest direction.

Due to the rapid formation of this initial emission, it is worthwhile discussing how precisely the experiment can be timed: The syringe is moving for (2 ± 0.5) s while injecting precursor. Time $t = 0$ s in the figure indicates the end of Cs-oleate injection. The uncertainty of the motion comes from the fact that the syringe position is only read out at the frequency of 2 Hz of the WAXS detector. Mixing of the viscous Cs-oleate with the $PbBr_2$ precursor leads to an additional (sub-second) delay until the mixture is visually homogeneous. With the present cell geometry no faster injection or mixing could be achieved. Nevertheless, the relevant structural intermediates could be detected with this mixing and timing strategy.

The particles forming at this stage are called intermediate nanoclusters due to their quantum-confined emission and nanocrystalline size. The size is analyzed in more detail

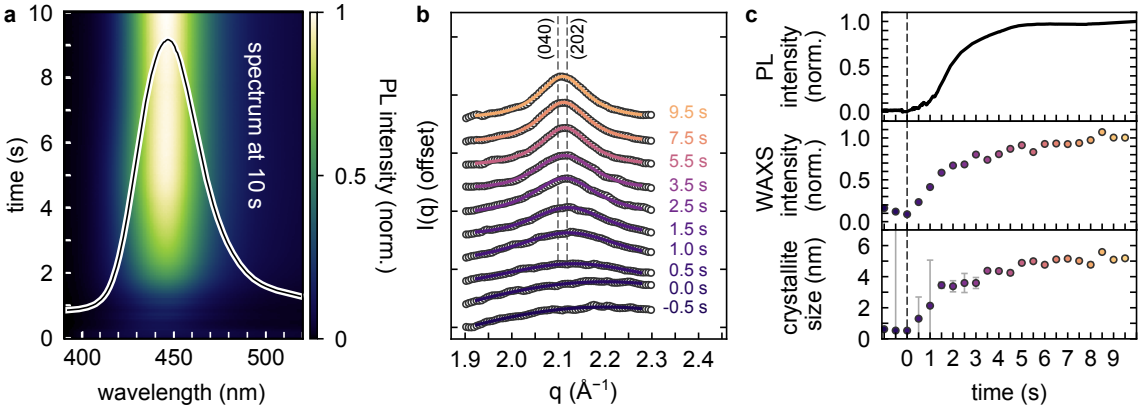

Figure 4.5: In situ PL and WAXS data after mixing of $PbBr_2$ and Cs-oleate precursors. a, In situ PL intensity shown as a function of wavelength and time, after subtraction of a constant background. Time $t = 0$ s corresponds to the end of Cs-oleate injection. A broad emission at 446 nm (FWHM 40 nm) is observed within 2 s after Cs-oleate injection. **b**, In situ WAXS intensity after background subtraction of the toluene signal and a fitted linear component. A diffraction signal appears at the position of the (0 4 0) and (2 0 2) Bragg reflections of orthorhombic $CsPbBr_3$. **c**, PL intensity, WAXS peak intensity, and crystallite size derived from **a** and **b**. Error bars correspond to the propagated standard error of the fitted WAXS peak width. Figure adapted from [379] with permission. CC-BY license 2024, Springer Nature.

below. First, the WAXS intensities, recorded simultaneously with the PL signal, are analyzed to verify the source of the emission. Data at selected times are shown in Figure 4.5 b.

$CsPbBr_3$ exhibits a tilt of the $PbBr_6$ octahedra along two axes, which leads to a non-cubic unit cell and a splitting of the (0 4 0) and (2 0 2) reflections (in orthorhombic notation, see Section 2.3.1). These reflections are located at $q \approx 2.1\,\text{Å}^{-1}$. Therefore, the signal in this region is used to detect LHP formation.

Indeed, the rise of a broad peak is observed in the WAXS intensity in this region within 2 s after Cs-oleate injection. This indicates that the formation of $CsPbBr_3$ occurs simultaneously with the appearing PL emission. Due to the small size of the forming nanoclusters the reflections are strongly broadened and overlap, so that the orthorhombic splitting cannot be explicitly observed. A Scherrer analysis (Equation 2.39) of the peak width reveals a crystallite domain size reaching (5.1 ± 0.3) nm after 5 s. Taking into account the instrumental resolution (determined in Figure A1) only leads to a minor correction of the value.

The subsequent evolution of the PL and WAXS signals over time is shown in Figure 4.5 c. The PL emission reaches a plateau in intensity after 5 s. In combination with the WAXS result this shows that the transformation of precursor into emissive nanoclusters is soon terminated. While the nanoclusters still grow slowly after 2 s, the emission wavelength and FWHM remain stationary until the later injection of the antisolvent, as shown in Figure 4.6 . This indicates that at least one dimension of the nanoclusters must stay within the quantum-confined regime. Typically, diffraction peak widths are dominated by the largest contributing domain size. The emission wavelength due to confinement, however, is mainly determined by the smallest dimension, as shown in Section 2.3.1. Therefore a comparison of the PL emission wavelength, hinting at a size of 1.8 nm, and the crystallite domain size (5.1 nm) already suggests the presence of an anisotropic structure at this stage. This finding is further supported by a detailed SAXS analysis below, since PL and WAXS analysis alone do not reveal whether the forming nanoclusters are oblate or prolate.

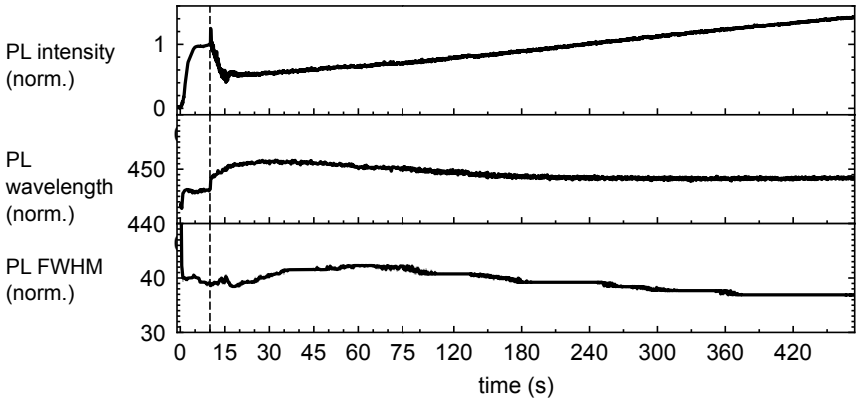

Figure 4.6: In situ PL analysis after mixing of $PbBr_2$ and Cs-oleate precursors. PL intensity, peak wavelength and FWHM are shown for the full reaction. Time $t = 0\,s$ corresponds to the end of Cs-oleate injection. A vertical dashed line at $t = 10\,s$ indicates the beginning of acetone injection. Figure adapted from [379, Supplementary Information] with permission. CC-BY license 2024, Springer Nature.

4.1.2.2 SAXS of precursor micelles and nanoclusters

The information obtained so far from in situ PL and WAXS analysis is limited to emissive and/or crystalline products of the reaction. Therefore, SAXS data are additionally analyzed to reveal potential non-emissive or amorphous structures and to distinguish any anisotropy of the intermediate nanoclusters. Figure 4.7 a shows the in situ SAXS data of a 2ML nanoplatelet synthesis starting slightly before the injection of Cs-oleate ($t = 0\,s$) until the injection of the antisolvent ($t = 10\,s$).

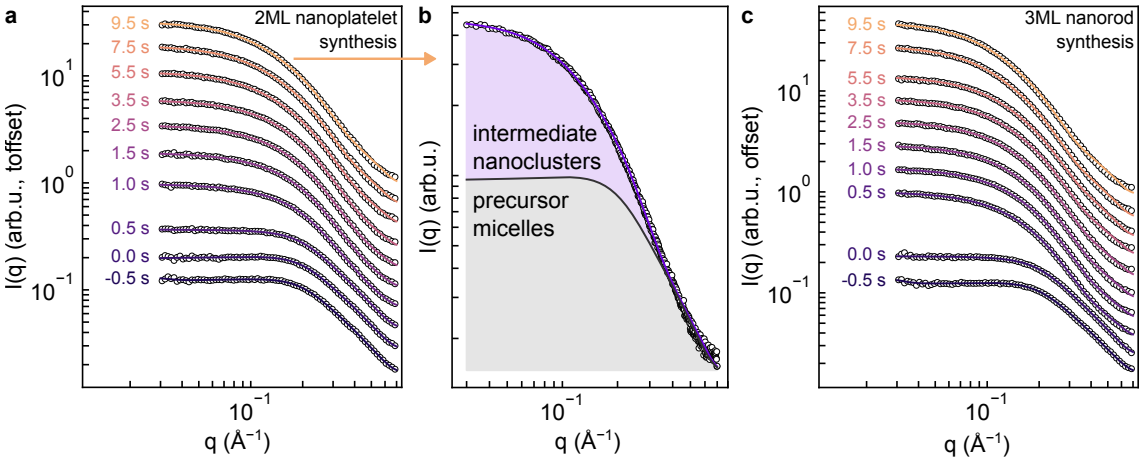

Figure 4.7: In situ SAXS data after mixing of $PbBr_2$ and Cs-oleate precursors. **a**, Dots: In situ SAXS data of a 2ML nanoplatelet synthesis shown from slightly before Cs-oleate injection ($t = 0\,s$). Solid lines are fits to the data as detailed in the text. After injection, the intensity at low q starts to increase. **b**, The signal immediately before antisolvent injection ($t = 9.5\,s$) is decomposed into the contributions of precursor micelles (gray) and intermediate nanoclusters (violet), as obtained from the fit. **c**, In situ SAXS data of a 3ML nanorod synthesis in the same time frame show identical behavior. Figure adapted from [379] with permission. CC-BY license 2024, Springer Nature.

Already before the Cs-oleate injection ($t = -0.5\,s$) a characteristic broad peak at $0.12\,Å^{-1}$ is observed in the SAXS data, representative of the $PbBr_2$-precursor. Addition of Cs-oleate leads to a rise of the intensity at low q and a smoothly decaying intensity profile at larger q. A full understanding of the evolution of this SAXS intensity requires a two-component model, accounting for the $PbBr_2$-precursor as a first component and for the

growing nanoclusters as a second component (see Q7 and Q8). With such a model, described in detail below, a very good agreement to the data is achieved. As a result, the solid lines representing the model fits coincide closely with the data points in Figure 4.7 a. Quantitative information about the temporal evolution of the amount of precursor, the density of nuclei, and the sizes of growing nanoclusters are extracted from the model fit.

In the model, the first component of the *$PbBr_2$-precursor* is described by micellar particles, i.e., core-shell spheres with a 1.2 nm diameter $PbBr_2$ cluster core and a shell of OlAm and OlAc ligands. This model component is refined against the SAXS data before Cs-oleate injection, shown as blue dots in Figure 4.8 a. Fit parameters are given in Table A3. The SAXS analysis shows that each micelle contains on average 9.6 ± 2.2 $PbBr_2$ units, as detailed in Table A6.

The dominant contribution to the precursor SAXS intensity comes from the structure factor $S(q)$, which leads to the broad peak in the intensity at $0.12\,\text{Å}^{-1}$. $S(q)$ describes the interactions of the precursor micelles as hard spheres. The details of this structure factor model are described in Section 2.4.2. Quantitatively similar SAXS patterns have been observed for gold precursors with OlAm in hexane [161]. The hard sphere model has proven to be effective for several other interacting nanoparticles as well, as shown in Sections 4.2.2 and 4.3.3.1. Here, the effective diameter of the hard sphere interaction corresponds to the diameter of the outer ligand shell (2.8 nm). This finding indicates that the ligand shell around the $PbBr_2$ cores keeps the small $PbBr_2$ clusters separated. It prevents further aggregation and coalescence, and thus the formation of larger $PbBr_2$ clusters.

The internal structure of the $PbBr_2$ core is further analyzed via the PDF $G(r)$ obtained from the TS signal (see Section 2.4.4). $G(r)$ is given in Figure 4.8 b and shows three major peaks at 3.06 Å, 4.46 Å, and 6.27 Å, corresponding to typical interatomic distances inside the $PbBr_2$ core. These positions match the distances of Pb–Br, Br–Br, and Br–Br (opposite) inside a $PbBr_6{}^{4-}$ octahedron as depicted in the inset. The interatomic distances for bulk crystalline $PbBr_2$ (COD 1530324, calculated below 7.5 Å) are shown as red lines for comparison and do not match the observed distances. This indicates that the lead ion in the $PbBr_2$ precursor is likely in a six-fold octahedral coordination. It can be surrounded by either Br or O/N, which belong to the OlAc or OlAm ligands. Such a coordination is similar to Pb_xBr_y magic sized clusters identified in LHP nanocrystal synthesis by spectroscopy [402] and extended X-ray absorption fine structure experiments [403]. It also resembles the solvent coordination of polyiodide plumbate complexes described in literature [404]. This octahedral coordination is already very close to the local environment of the lead ion in the perovskite structure, in which slightly closer distances of 2.96 Å, 4.16 to 4.22 Å, and 5.92 to 5.93 Å (COD 4510745) occur. The PDF reveals no signal above the noise for distances above 7.5 Å, which is in approximate agreement with the cluster core diameter of 1.2 nm obtained from SAXS.

The Cs-oleate precursor is measured separately and exhibits a SAXS signal with an even more pronounced structure factor peak at $0.22\,\text{Å}^{-1}$. The data (orange dots) and a fit with a core-shell sphere model with hard sphere structure factor are shown in Figure 4.8 a. Fit parameters are given in Table A3. For this precursor a micellar structure with a 1.2 nm core and a 0.6 nm ligand shell is obtained from the fit. A micellar structure of a Cs-oleate precursor has been previously reported in literature based on dynamic light scattering (DLS) experiments [405]. It is referred to as a "coordination complex or small reverse micelle" of 3.1 nm hydrodynamic radius [405, p. 64]. The size discrepancy comes

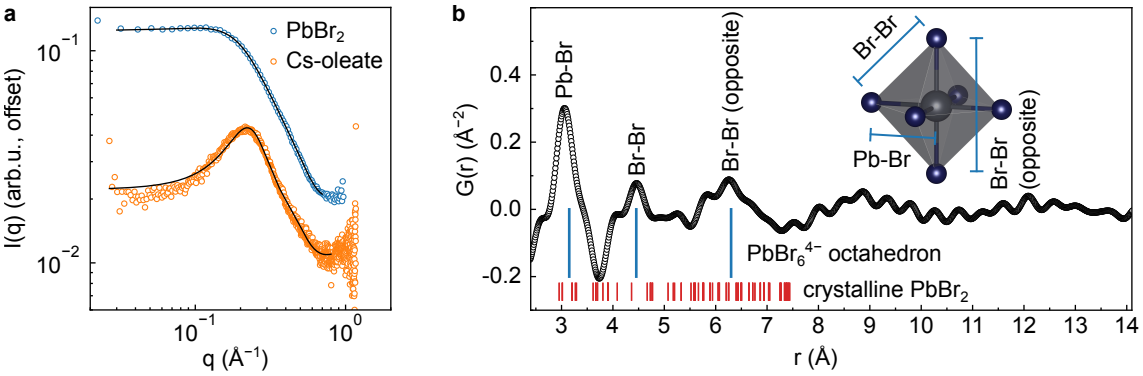

Figure 4.8: SAXS analysis of the $PbBr_2$ and Cs-oleate precursor and PDF analysis. a, SAXS analysis. Dots are background-subtracted SAXS data of the precursors. Solid lines are fits with a model of core-shell spheres with a hard sphere structure factor. The core consists of $PbBr_2$ or Cs and the shell represents organic ligands with lower scattering contrast. **b**, PDF analysis of $PbBr_2$ precursor. Dots show the reduced PDF $G(r)$ obtained from background-subtracted TS data. Interatomic distances corresponding to an octahedral coordination of Pb (blue lines, inset) are highlighted. The interatomic distances for bulk crystalline $PbBr_2$ (red lines) are shown for comparison. Figure adapted from [379, Supplementary Information] with permission. CC-BY license 2024, Springer Nature.

partly from the low detection efficiency of DLS at small sizes and from the contributions of the ligand shell and the core to the hydrodynamic radius. Indeed, the term "reverse" micelle should be preferred, since the unpolar ligand tails face outwards and the headgroups surround the Cs (or Pb_xBr_y) ions. For the analysis of the time-resolved in situ SAXS data the signal of the Cs-oleate precursor is not explicitly taken into account, since no immediate change of SAXS signal upon its injection is observed. In addition, its contribution to the intensity is lower than the one of $PbBr_2$, especially at low q (see also Figure A5), and a three-component model might lead to overfitting of the data.

The remaining second component in the model for the in situ SAXS data represents the nucleating and growing *intermediate $CsPbBr_3$ nanoclusters*. For this component, several isotropic and anisotropic models were examined (spheres, cubes, ellipsoids, cylinders and cuboids). Also polydisperse models were tested, as detailed in Figure A2 and Tables A4 and A5. Size parameters were compared with PL and WAXS results and models leading to too small or too large sizes were rejected, as such nanoclusters would not show the simultaneously observed PL emission or crystallite size. Furthermore, robustness of the fitting procedure, i.e., similar size parameters for successive and visually similar datasets, were taken as a criterion for a suitable SAXS model. The fitting procedure is detailed in Section 3.3.1.

Anisotropy is found to be a crucial model ingredient in order to obtain plausible size parameters for the growing nanoclusters. A comparison of the sphere, ellipsoid, and cuboid models is shown in Figure 4.9 a. The two anisotropic models show a better χ^2 value (Equation 2.34) and a weighted residual curve closer to 0. Unlike anisotropy, size polydispersity in the model does not significantly improve the fit result.

As a result of this extensive screening, ellipsoid and cuboid models are found to provide good agreement with the data. For these models, parameter values are physically plausible at all times between precursor mixing and antisolvent injection. An ellipsoid model is chosen for the further analysis. It likely represents the rounded shape of a ligand-coated nanocluster better than a cuboid and its computation is less time-consuming. A cuboid shape would be more representative of the LHP nanocluster core. It should be noted

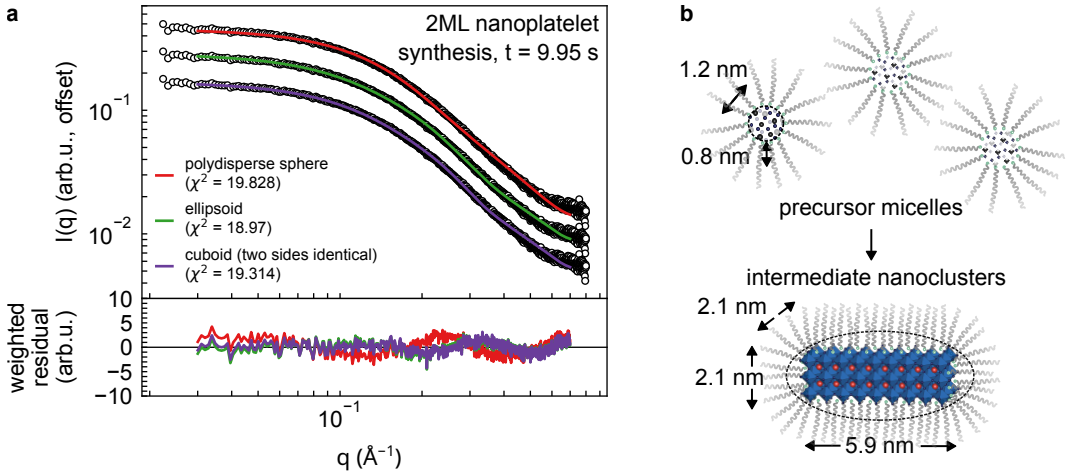

Figure 4.9: Different SAXS models of intermediate nanoclusters and illustration of nanocluster dimensions. a, Dots: SAXS data immediately before acetone injection ($t = 9.95\,\mathrm{s}$) with three representative model fits. Red curve: polydisperse sphere model (diameter $d = 0.61\,\mathrm{nm}$, $\frac{\sigma d}{d} = 2$), green: ellipsoid model ($d = 2.0\,\mathrm{nm}$, length $l = 5.6\,\mathrm{nm}$), purple: cuboid model with two identical sides ($a = b = 1.68\,\mathrm{nm}$, $c = 4.0\,\mathrm{nm}$), see Table A5. Bottom panel: weighted residuals between data and fit. **b**, Average dimensions of the $PbBr_2$ precursor micelles and the final size of intermediate nanoclusters before antisolvent injection, as obtained from SAXS analysis of both 2ML nanoplatelet and 3ML nanorod syntheses. **b** adapted from [379] with permission. CC-BY license 2024, Springer Nature.

that the ligand shell of the growing nanoclusters is not explicitly included in this (second) model component to reduce complexity. In contrast to the signal of the precursor, in which the peak in the SAXS intensity indicates an interparticle interaction, no such interaction between the growing nanoclusters is apparent from the data at later times. Most importantly, there is no structure factor peak visible. Furthermore, an effective description of the particle size without an explicit ligand shell leads to a more robust computation. Therefore, both structure factor and shell are omitted from the model of the intermediate nanoclusters.

Using the results from the two-component model, even at 9.5 s after Cs-oleate injection the $PbBr_2$-precursor micelles constitute a considerable fraction of the SAXS intensity (see Figure 4.7 b). Based on number densities of the components, shown in Figure 4.10 a, 75 to 80% of precursor micelles remain present. Based on the respective Porod invariants obtained from the fits at 9.5 s 84% of precursor remains. This indicates that only 20 to 25% of precursor micelles (by number) are transformed in this initial stage of the reaction.

The following increase of intensity at low q (Figure 4.7 a) is then mainly due to growth of the intermediate nanoclusters. This growth process is quantified in terms of the ellipsoidal nanocluster diameter d and length l, shown in Figure 4.10 b. The diameter grows only moderately from $(1.8 \pm 0.2)\,\mathrm{nm}$ to $(2.1 \pm 0.2)\,\mathrm{nm}$ at a rate of 0.03 to $0.04\,\mathrm{nm\,s^{-1}}$, while the length grows linearly from $(4.3 \pm 0.2)\,\mathrm{nm}$ to $(5.9 \pm 0.4)\,\mathrm{nm}$ at a rate of 0.16 to $0.19\,\mathrm{nm\,s^{-1}}$. A comparison of the core sizes of the $PbBr_2$ precursor micelles and the nanoclusters, given in Table A6, shows that 4 to 6 $PbBr_2$ micelles contribute to nucleation, and additional material is incorporated during growth.

The second component in the model fit is neither constrained to a prolate nor to an oblate particle shape, and d and l are free to vary. For all investigated syntheses the SAXS analysis therefore shows, without a prior assumption on the shape, that the resulting nanoclusters are moderately prolate ellipsoids, i.e., rod-shaped. This finding is in perfect agreement

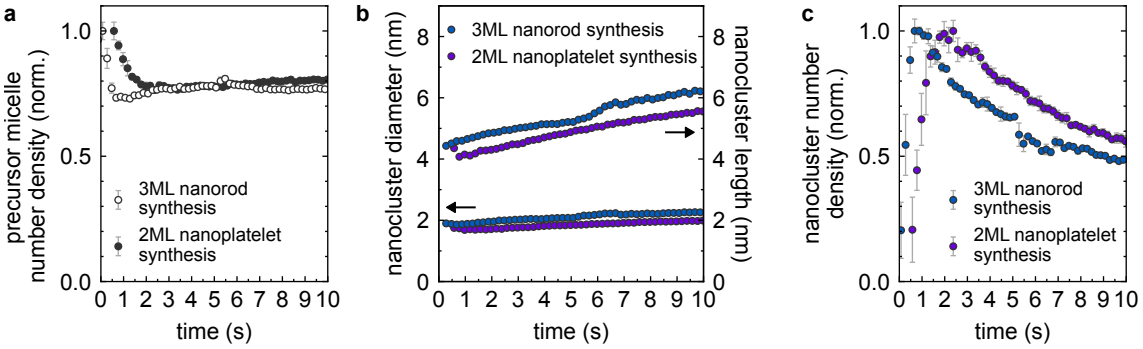

Figure 4.10: Densities and sizes obtained from in situ SAXS analysis. **a**, Precursor micelle number density as a function of time for 3ML nanorod and 2ML nanoplatelet synthesis. Values are obtained from fits to the SAXS data shown in Figure 4.7 a and c, respectively. The initial drop coincides in time with the rapid nucleation of intermediate nanoclusters, shown in **c**. The following slight increase is likely within the experimental uncertainty of the fitted scale factors and of the precursor micelle core volume. **b**, Nanocluster diameter and length from fits to the SAXS data with an ellipsoid model. **c**, Number densities of nanoclusters obtained from the fits. Error bars correspond to the standard deviation of four consecutive fit results. **b, c** adapted from [379] with permission. CC-BY license 2024, Springer Nature.

with the observations of a growing crystallite size and a stagnating emission wavelength from WAXS and PL, respectively (see Figure 4.6).

Most importantly, the size parameters of the nanoclusters derived from SAXS analysis do not substantially differ for 3ML nanorod and 2ML nanoplatelet syntheses, i.e., syntheses with different ratios of $PbBr_2$- and Cs-oleate precursor (see Figure 4.10 b). Variations in the onset of nucleation, and, as a result, variations of the final size within the studied time frame from 0 to 10 s, are likely due to a delay resulting from differences in mixing and equilibration of the viscous precursors after injection. A screening of this delay for identical reaction conditions is shown in Figure A3. Despite the different onset of nucleation an intermediate nanocluster diameter of (2.3 ± 0.2) nm and a length of (6.1 ± 0.3) nm are reproduced in all repeat experiments. Therefore, the SAXS analysis shows that the syntheses of 3ML nanorods and 2ML nanoplatelets proceed via the same, prolate nanoclusters, which are thus identified as common reaction intermediates.

Furthermore, the temporal evolution of the number density of nanoclusters can be extracted from SAXS using equation Equation 2.22. A quick rise of nanocluster number density, shown in Figure 4.10 c, indicates a fast nucleation in the beginning of the reaction. This phase is followed by a slow decay, representing a phase of coalescence or Ostwald ripening. The model does not account for polydispersity of the nanoclusters and therefore does not allow to distinguish between different ripening processes: Larger nanoclusters contribute more strongly to the intensity, proportionally to the square of the particle volume (see, e.g., Equation 2.21). Larger clusters growing at the expense of material from smaller ones by Ostwald ripening would quickly overshadow the SAXS intensity of smaller clusters, even if such clusters were still present.

JMAK and Gualtieri model fits to the scale factor of the growing nanocrystals (see Section 2.2.3, Figure A4 a, b, and Table A7) yield growth rate constants k_g ranging from 0.5 to 1.5 s^{-1} depending on the assumed exponent n. This allows an approximate timing of the initial structural transformation (see Q2). Nucleation time distributions extracted from the Gualtieri fits depend on the choice of the dimensionality parameter n. Therefore, they do not allow more precise conclusions on the duration of nucleation and growth phases than

the visual inspection of Figure 4.10 c. Considering the abundance of well-defined lead halide precursor nanoclusters at this reaction stage, LHP formation may even be "nucleationless" and fully seeded or templated by the nanoclusters. Clarification of these earliest reaction steps would require more defined precursor mixing conditions, as discussed in Chapter 5.

To confirm the structure of intermediate nanoclusters by an ex situ measurement an unpurified precursor mixture is drop casted on a TEM grid at 10 s after precursor mixing. TEM and PL spectroscopy data are shown in Figure 4.11, with a regular monolayer of nanoclusters visible in the TEM micrographs. Either two short (a) or one short and one long side of the nanoclusters (b) are facing up, indicating the presence of prolate, ellipsoidal particles. The distances of 5.01 nm, 4.85 nm and 7.41 nm obtained via the FFT are in close agreement with dimensions obtained from SAXS if an intercalated double layer of ligands (3 nm) between the nanoclusters is assumed. The optical spectra show absorption at 437 nm and photoluminescence at 450 nm (FWHM = 22 nm), in good agreement with the in situ PL data at this stage of the reaction (Figure 4.5 a). The narrower and redshifted emission of the extracted aliquot likely results from further growth and size-focusing of the nanoclusters during transfer of the reaction mixture to the spectrometer.

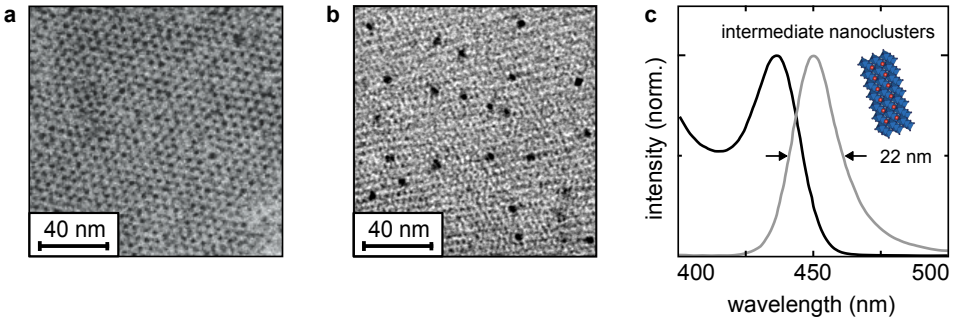

Figure 4.11: Characterization of intermediate nanoclusters by TEM and optical spectroscopy. **a, b**, TEM images of precursor mixtures drop casted onto TEM grids without addition of antisolvent or purification. Regular monolayers with a hexagonal assembly of intermediate nanoclusters are observed. Dimensions are extracted by FFT of the images of standing (**a**) and flat-lying (**b**) assemblies. **c**, Absorption and PL spectra of the precursor mixture, showing an absorbance peak at 437 nm and emission at 450 nm (FWHM = 22 nm). Data provided by Nina A. Henke. Figure adapted from [379, Supplementary Information] with permission. CC-BY license 2024, Springer Nature.

4.1.3 Antisolvent-induced mesophase assembly

4.1.3.1 Templated growth of nanorods in a hexagonal mesophase

The above results show that the syntheses of both rod- and platelet-shaped LHP nanocrystals proceed via the same intermediates. Therefore, the anisotropy-determining step must follow later in the reaction. Indeed, the injection of the antisolvent determines the shape, as shown in this section.

The moderately polar acetone (0.355 on the $E_T(30)$ scale, compared to 0.099 for toluene, see Section 2.1.4 and Table A8) is injected into the reaction mixture at $t = 10$ s while SAXS, WAXS and PL intensities are being recorded. Injection of a large volume of acetone in a 3ML nanorod synthesis leads to a pronounced change in the SAXS and PL data, shown in Figure 4.12 a-c.

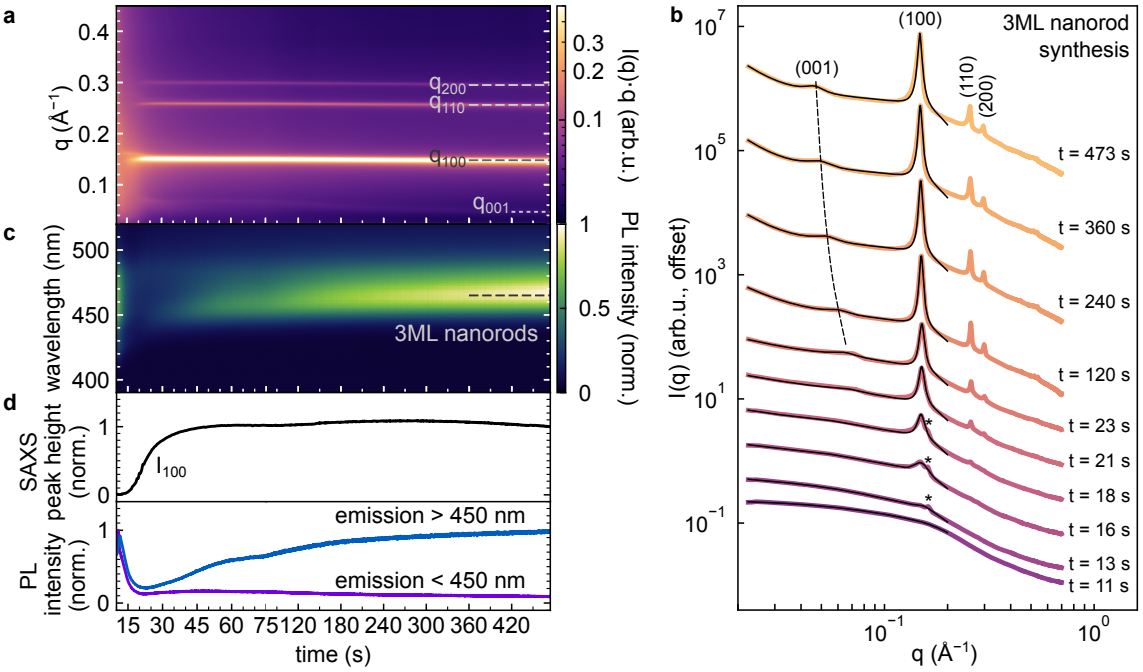

Figure 4.12: In situ SAXS and PL intensities after injection of acetone in a 3ML nanorod synthesis. **a**, In situ SAXS intensity, shown as $I(q) \cdot q$ to amplify small signals at larger scattering vector. A set of $(h\,k\,0)$ peaks, indicating a hexagonal phase, and a $(0\,0\,1)$ peak at lower q appear within 15 s after acetone injection ($t = 10$ s). **b**, Selected intensities from **a** to visualize the evolution of peak intensities and positions. A dashed line highlights the shift of the $(0\,0\,1)$ peak while the $(h\,k\,0)$ peaks remain stationary. Asterisks highlight an additional peak visible from 13 to 18 s, as detailed in the text. **c**, Corresponding in situ PL intensity. After a sharp decrease of the PL intensity of intermediate nanocrystals, an emission at 450 to 460 nm is recovered. **d**, SAXS peak height and PL intensities extracted from **a** and **c**. The dominant emission above 450 nm indicates the formation of 3ML nanorods. Figure adapted from [379] with permission. CC-BY license 2024, Springer Nature.

Within 15 s after the injection, a set of intense peaks is observed in the SAXS signal. The peaks spaced at $q_{100} = 0.150$ Å^{-1}, $q_{110} = \sqrt{3} \cdot q_{100}$, and $q_{200} = 2 \cdot q_{100}$ indicate the formation of a two-dimensional hexagonal assembly with a spacing of $d = \frac{4\pi}{\sqrt{3} q_{100}} = (4.8 \pm 0.1)$ nm (see Equation 2.35). These reflections are indexed as $(h\,k\,0)$. The spacing corresponds to the diameter of the just formed intermediate nanoclusters (1.8 to 2.1 nm) surrounded by an approximately 3 nm ligand shell. The prolate intermediates therefore rapidly order side by side with the long axis oriented in the same direction.

Approximately 10 s after the first observation of the $(h\,k\,0)$ reflections in the SAXS signal, another peak at $q = 0.07$ Å^{-1} is found, which does not belong to the $(h\,k\,0)$ series and corresponds to a distance larger than the previously observed spacing. The emergence of this peak, indexed as $(0\,0\,1)$, indicates that the nanoclusters now also assemble along their long axis and stack end-to-end. While the hexagonal $(h\,k\,0)$ peaks barely shift over time, as further discussed below, the $(0\,0\,1)$ peak shifts to lower q during the remaining 8 min of reaction time. The shift corresponds to an increase of the associated d-spacing from 9.8 nm to 13.7 nm. This suggests that neighboring nanoclusters fuse together into larger particles along their long axis, i.e., intermediate nanoclusters evolve to nanorods by fusion inside the dense assembly.

The assembly is called a mesophase, as it shows properties in between ("meso") those of a liquid or dispersion of nanoclusters and a supercrystalline solid, e.g., regarding particle density: Before antisolvent injection the average volume fraction of intermediate nanoclus-

ters in the synthesis is between $1.2 \cdot 10^{-4}$ and $2.3 \cdot 10^{-4}$ (see Table A19). After antisolvent injection the average volume fraction is between $7.5 \cdot 10^{-5}$ and $1.1 \cdot 10^{-4}$, caused by the increase of total volume. Inside the hexagonal mesophase, however, a much higher volume fraction between 17 % and 27 % is found, based on the nanocluster sizes and spacings (see Table A20). The remaining 73 to 83 % of the volume inside the mesophase is occupied by the ligands surrounding the nanoclusters and by the solvent mixture. The term "mesophase" also applies to the length scale of the observed inter-nanocluster spacings, which lie in between atomic (Ångstrom-sized) and micrometer-sized spacings. The term "phase" is appropriate, since the emergence of peaks in the SAXS intensity is accompanied by a visible increase of turbidity and by flocculation of the reaction mixture. These observations indicate a macroscopic separation into nanocluster-rich and -poor fractions of the sample.

Considering the thickness of the ligand shell around the nanocrystals, the final spacing of 13.7 nm inside the mesophase is in reasonable agreement with the length of nanorods observed in TEM (see e.g. Figure 4.2 c). The exact length of the nanorods depends on the duration of the synthesis before centrifugation and on the concentration of precursors. Higher concentrations of precursors lead to the formation of shorter rods, as shown in Figure A8 and further discussed below.

The PL intensity recorded simultaneously with the SAXS data provides additional insight into the nanorod formation. The PL signal is separated into regions above and below 450 nm to distinguish signals from potential 2ML and 3ML nanocrystals. After antisolvent injection, the PL intensity of the intermediate nanoclusters, centered at 446 nm, sharply decreases, as shown in Figure 4.12 c and d and Figure 4.6. This indicates a destabilization of the intermediate nanoclusters by the rapid change of solvent properties [47], during which the intermediate nanoclusters partly dissolve. After the mesophase has formed, indicated by the (1 0 0) SAXS peak intensity superimposed on the graph in Figure 4.12 c, the PL intensity gradually recovers. The emission at the end of the reaction is slightly redshifted compared to the intermediate nanoclusters. It is dominated by an emission at approx. 460 nm, which is characteristic of 3ML thick nanorods.

A closer inspection of SAXS peak intensities, backgrounds, and domain sizes is shown in Figure A7. Already Figure 4.12 b reveals that the broad (0 0 1) peak barely rises above the background compared to the very sharp and intense ($h\,k\,0$) peaks. The elevated background at the (0 0 1) position contains a strong contribution from the form factor of freely dispersed intermediate nanoclusters, which additionally varies with time. The large width of the (0 0 1) reflection is related to a rather small domain size (20 to 55 nm). In the hexagonally ordered plane perpendicular to the long axis of the nanoclusters the domain size is much larger (50 to 120 nm) and the associated peaks are much sharper. Several effects can contribute to the different domain sizes in the two directions:

Firstly, attractive van der Waals forces between prolate nanoclusters are stronger between the larger facets ("sides") compared to the small facets ("tips"), which leads to a parallel arrangement. A similar colloidal stability argument based on facet size has been formulated for nanoplatelets [406], where stacking of the largest facets dominates. Secondly, potential depletion interactions, which are exerted by excess ligands in the solution, likely favor a side-by-side arrangement of the nanorods due to a larger entropic effect [114]. Due to both factors "side-to-side" interactions are dominant and the structure of the mesophase may be governed by two-dimensional sheets of assembled nanoclusters (see Figure 4.13 a). Bending fluctuations of such smectic sheets or "membranes" are well known and have been

thoroughly investigated by X-ray scattering methods [315, chapter 3.3]. Alternatively, the growing nanorods could assume a nematic ordering inside the mesophase once they are assembled "end-to-end". In this structure neighboring columns of rods are offset along the rod direction but the side-to-side spacing shows only small variations. Therefore, both smectic and nematic ordering of the mesophase with their associated fluctuations would suppress the (0 0 1) compared to the ($h\,k\,0$) reflections. Finally, stochastic fusion of the crystalline lattices of neighboring nanoclusters along their long axis changes their repeat distance due to expulsion of the ligand shell at the tips (see Figure 4.13 b). In summary, both fluctuations and fusion of nanoclusters suppress long-range order mainly in the ⟨0 0 1⟩ direction of the mesophase.

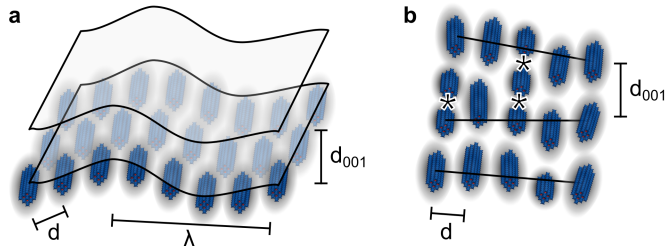

Figure 4.13: Schematic illustration of the fluctuations inside the mesophase formed by the nanorods. a, Oscillations of smectic sheets separated by a distance d_{001} with a characteristic periodicity λ. **b**, Longitudinal offset of nanorod centers in the [0 0 1] direction in a nematic mesophase with ongoing fusion (*) of neighboring rods. d denotes the lateral nearest-neighbor spacing.

Between 13 and 18 s after antisolvent injection a small additional peak on the right of the (1 0 0) reflection is visible, as highlighted by an asterisk in Figure 4.12 b. The slightly larger q position compared to the (1 0 0) reflection of the mesophase indicates a narrower spacing. The peak therefore originates from an assembly of clusters smaller than the intermediate nanoclusters. Since it vanishes for syntheses at lower precursor concentration it may be related to assembly of residual $PbBr_2$ precursor micelles in the reaction mixture. The reaction product is unaffected by this phenomenon, since remaining precursor material can later be incorporated into the growing nanorods.

To additionally determine the structural changes of the remaining precursor micelles during antisolvent addition, in situ SAXS experiments were carried out, leaving out one of the precursors and thus preventing LHP formation. The corresponding SAXS data are shown in Figure A5. Precursor micelles remain stable during the addition of antisolvent despite the polarity increase of the solvent mixture. Inter-micellar interactions are visible as the structure factor peak. This signal is weakened by the diluting effect of the antisolvent. Meanwhile the cluster core structure remains intact, as shown by the remaining form factor signal. The precursor clusters, contrary to the intermediate LHP nanoclusters, do not assemble into a mesophase upon antisolvent addition. Due to their small size (0.9 nm^3 compared to between 7 and 17 nm^3 core volume) mutual vdW attraction is likely insufficient.

4.1.3.2 Nanoplatelet growth followed by lamellar assembly

The synthesis of 2ML thick nanoplatelets begins to differ from the 3ML nanorod synthesis after antisolvent injection. In terms of reaction parameters, the nanoplatelet synthesis requires a slightly lower Cs-oleate volume and a lower antisolvent volume (see Table 3.2).

Despite these seemingly small differences, the SAXS signal after antisolvent injection shows a fundamentally distinct behavior, as shown in Figure 4.12 a. At first, the SAXS intensity remains a smoothly decaying curve for ≈ 55 s, shown in Figure 4.12 b. Only the upturn at low q is slightly amplified. This suggests that the intermediate nanoclusters present at this stage remain freely dispersed, do not yet assemble, and potentially grow by addition of precursor material from solution. This mechanism will be further corroborated by PL analysis below.

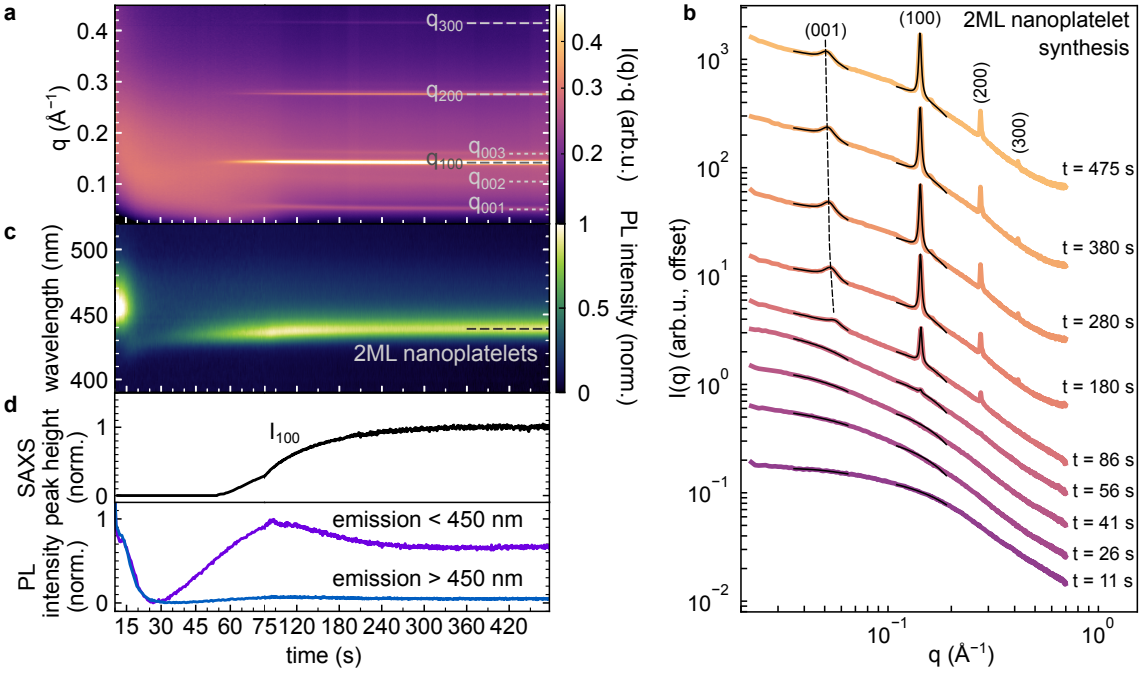

Figure 4.14: In situ SAXS and PL intensities after injection of acetone in a 2ML nanoplatelet synthesis. **a**, In situ SAXS intensity. Two sets of peaks, $(h\,0\,0)$ and $(0\,0\,l)$, appear ≈ 55 s after acetone injection. **b**, Selected intensities from **a**. A dashed line indicates the position of the $(0\,0\,1)$ peak, which only weakly shifts to lower q. The $(0\,0\,3)$ peak is visible on the right of the $(1\,0\,0)$ peak, while the $(0\,0\,2)$ peak is likely shadowed by the underlying form factor intensity. **c**, Corresponding in situ PL intensity. After the decay of the emission of intermediate nanoclusters an emission at 430 to 440 nm appears. **d**, SAXS peak height and PL intensities extracted from **a** and **c**. The rise of the emission at < 450 nm, characteristic of 2ML nanoplatelets, starts before appearance of the peaks in the SAXS signal and reaches its maximum shortly thereafter. Figure adapted from [379] with permission. CC-BY license 2024, Springer Nature.

After ≈ 60 s a set of $(h\,0\,0)$ reflections appears in the SAXS intensity at integer multiples of 0.143 Å^{-1}. This regular spacing of peaks is characteristic of a lamellar arrangement with a repeat distance of $\frac{2\pi}{q_{100}} = (4.4 \pm 0.1)$ nm. Such a spacing agrees very well with a lamellar stacking of 1.4 nm thick nanoplatelets, considering an intercalated double layer of ligands. A second set of peaks is observed at lower q (0.05 Å^{-1}), simultaneously with the lamellar reflections. This $(0\,0\,l)$ peak series corresponds to a final repeat distance of $\frac{2\pi}{q_{001}} = (12.1 \pm 0.4)$ nm at the end of the reaction. This distance matches the long axis of the nanoplatelets, indicating that stacks of ligand-coated, 9.1 nm wide nanoplatelets also stack side-to-side. This arrangement corresponds to a columnar/discotic or lamellar mesophase of quasi-two-dimensional 2ML nanoplatelets (see Figure 2.8) induced as a consequence of antisolvent injection. This mesophase forms only after the nanoplatelets have grown to their final size, in contrast to the instantaneous assembly in the nanorod synthesis.

In the 2ML nanoplatelet synthesis the PL intensity of intermediate nanoclusters, given in Figure 4.14 c, shows a similarly steep decrease as in the 3ML nanorod synthesis, indi-

cating the partial dissolution of nanoclusters. The PL emission at later times, however, is clearly different. After 20 s, i.e., before the formation of the lamellar phase, a sharp emission at 433 nm emerges, which is blue-shifted compared to the intermediate nanoclusters and characteristic of 2ML thick nanoplatelets [25, 200, 216]. The emission of 3ML thick nanocrystals at > 450 nm is strongly suppressed. A maximum of PL intensity is observed shortly after the appearance of the lamellar reflections, shown superimposed in Figure 4.14 d. At later times the emission intensity at < 450 nm is reduced and levels off at a lower value, which is likely due to scattering and reabsorption of light in the dense lamellar stacks of the mesophase.

In contrast to the 3ML nanorod synthesis the 2ML nanoplatelet synthesis shows very little shift of all mesophase reflections, both $(h\,0\,0)$ and $(0\,0\,l)$, over time. The temporal evolution of the interparticle separations is shown for comparison in Figure 4.15. The narrow spacing of nanorods, approximately representative of their thickness plus the ligand shell, grows at $0.012\,\mathrm{nm\,min^{-1}}$, while the narrow spacing of nanoplatelets grows at only $0.003\,\mathrm{nm\,min^{-1}}$. The wide spacing, serving as a proxy for nanorod length or nanoplatelet lateral size plus the ligand shell, shows a more pronounced difference: Nanorods grow at $0.72\,\mathrm{nm\,min^{-1}}$ initially and at $0.39\,\mathrm{nm\,min^{-1}}$ after 5 min. Nanoplatelets show an even slower growth of $0.34\,\mathrm{nm\,min^{-1}}$ initially and $0.08\,\mathrm{nm\,min^{-1}}$ after 4 min. The initial fluctuation of the wide nanorod spacing is likely related to the large uncertainty of the (0 0 1) peak amplitude, which suffers from a high background (see Figure A7 a). Also a competition of dense packing, leading to a progressively narrower spacing, and fusion of intermediate nanoclusters, leading to larger nanorods and thus a wider spacing, may contribute to the opposite trends.

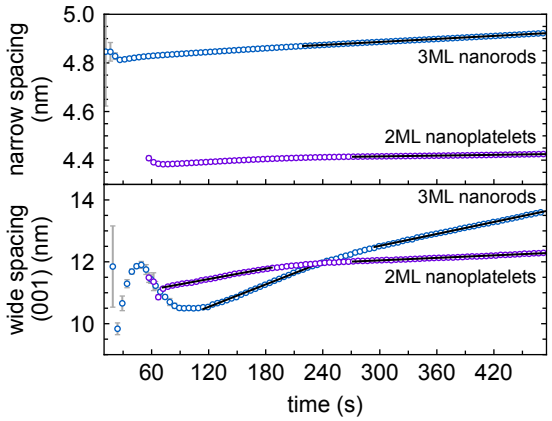

Figure 4.15: Evolution of the spacing of the hexagonal and lamellar mesophases. Top: Evolution of the narrow spacing of the hexagonal phase for 3ML nanorod synthesis and the lamellar phase for 2ML nanoplatelet synthesis. Dots represent averages of 10 consecutive fit results and error bars are the standard deviations. The initial points show larger uncertainty due to the low peak intensity. Bottom: Evolution of the wide mesophase spacing, i.e., end-to-end stacking of 3ML nanorods and side-to-side stacking of 2ML nanoplatelets. Black lines are linear fits to extract the growth rates given in the text.

The low growth rates of the 2ML nanoplatelets inside the mesophase suggest that, firstly, their distinct monolayer thickness is achieved before assembly. Once assembled in the mesophase, the large facets are well passivated against further growth. A similar passivation by stacking has been reported for $Cu_{2-x}S$ nanosheets [74] whereas modified nucleation energies on different facets are invoked as the shape-determining mechanism for CdSe nanoplatelets [140]. Secondly, the narrow sides of platelets inside the mesophase are rather inaccessible for addition of further monomers. As a consequence, almost no further

growth occurs also along the lateral platelet dimension. Therefore, a very narrow size polydispersity of the product is achieved. The size dispersity is potentially even enhanced due to a size-selective assembly of similarly large platelets.

4.1.4 Understanding and tuning antisolvent effects

4.1.4.1 The different effects of the antisolvent

By comparing the distinct behavior of the SAXS and PL intensities after the injection of different volumes of antisolvent two separate effects of the antisolvent on the reaction mixtures can be deduced. The different strength of these effects, depending on the antisolvent volume and type, eventually determines the anisotropy of the resulting nanocrystals.

Firstly, the addition of acetone as an antisolvent increases the polarity of the reaction mixture compared to the initial polarity of toluene (see Section 2.1.4 and Table A8). As a result, the *solubility of the intermediate nanoclusters*, which expose their non-polar ligand chains to the solvent, is reduced. If a sufficient amount of acetone is added, the interaction between ligands and individual solvent molecules becomes less favorable than ligand-ligand interactions. As a result, the nanocluster dispersion phase-separates into a nanocluster-rich mesophase and polar solvent-rich surroundings. To show the dependence on antisolvent volume, the effect of a step-wise addition of 0.4 mL acetone in a 3ML nanorod synthesis is illustrated in Figure 4.16. After addition of 0.2 mL acetone the conditions become favorable for mesophase assembly.

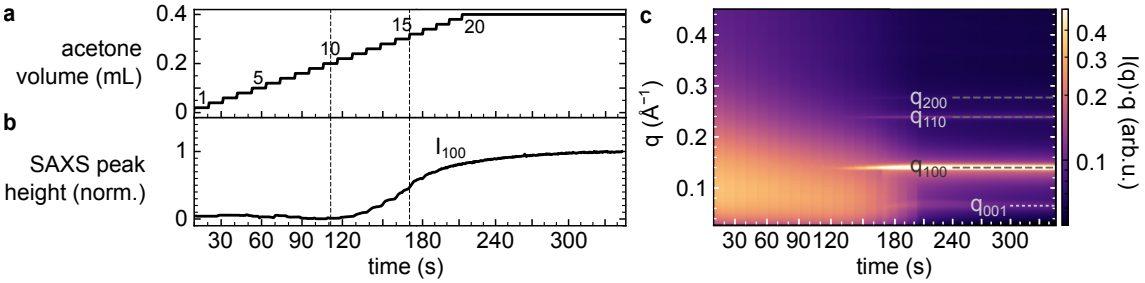

Figure 4.16: Stepwise addition of acetone to probe the threshold for mesophase formation. a, 0.4 mL acetone is injected to a 3ML nanorod precursor mixture at five-fold concentration ($5\,c_0$ compared to Section 4.1.1) in 20 steps of 0.02 mL. Vertical dashed lines indicate that the (1 0 0) and (0 0 1) reflections of the mesophase are first observed after the 10^{th} and 15^{th} injection, respectively. **b**, Peak height of the (1 0 0) reflection extracted from in situ SAXS data. **c**, In situ SAXS data. Note that the (0 0 1) peak does not shift to smaller q at later times, indicating that the high concentration of intermediate nanoclusters is unfavorable for fusion inside the mesophase. Figure adapted from [379, Supplementary Information] with permission. CC-BY license 2024, Springer Nature.

Secondly, the increased polarity of the reaction mixture improves the *solubility of LHP precursor ions*, Cs^+, Pb^{2+}, Br^-, and potentially also cluster ions such as $PbBr_6{}^{4-}$ octahedral units. Unreacted precursors from the initial mixing step are still present in the reaction mixture when the antisolvent is added, as shown in Figure 4.10 a by SAXS analysis. Additional ions can be redissolved after antisolvent addition by decomposing part of the intermediate nanoclusters. The removal of organic ligands from LHP nanocrystals by polar solvents has been previously reported [47, 407]. Antisolvent addition, even in small volumes, may therefore destabilize the intermediate nanoclusters by stripping ligands and by introducing surface defects, a scenario which is supported by the strong decrease in PL emission of intermediate nanoclusters shown in Figures 4.12 and 4.14.

A variation of the antisolvent volume affects the relative importance of these two processes: If a large volume of acetone is added to a highly concentrated reaction mixture, the instantaneous phase separation dominates. This protects the intermediate nanoclusters from dissolution by assembling them in a dense mesophase, before sufficient destabilization can take place. In the dense, regular environment nanoclusters can fuse into the kinetically favored nanorods and their shape is templated by the hexagonal symmetry of the mesophase.

This mechanism is supported by the observation that the (0 4 0)/(2 0 2) reflection of $CsPbBr_3$ in the WAXS signal of a nanorod synthesis is weakened by antisolvent injection, but not fully suppressed, as displayed in Figure 4.17. This shows that intermediate nanocrystals are destabilized, yet not fully dissolved. Even more importantly, the growing trend of the crystallite size obtained from the WAXS peak width remains undisturbed (Figure 4.17 b), further corroborating the hypothesis of a templated growth by fusion and recrystallization of intermediate nanoclusters. This suggested reaction pathway for nanorods is illustrated in Figure 4.18 (top).

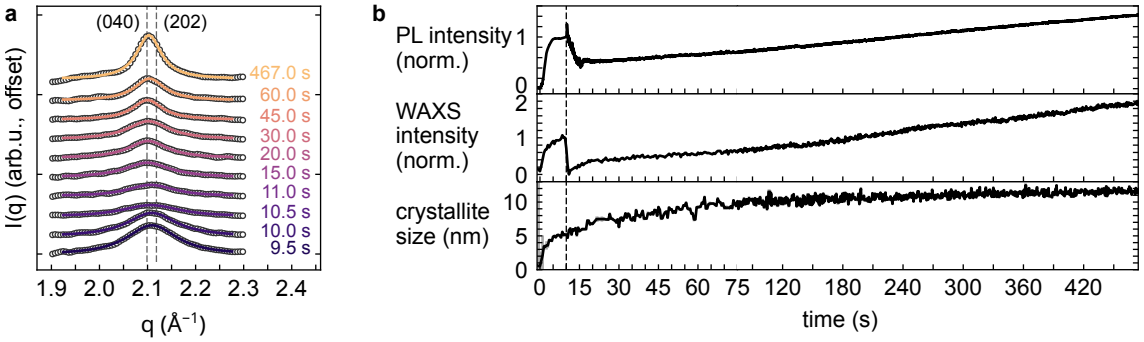

Figure 4.17: WAXS analysis beyond the antisolvent injection. **a**, Dots are WAXS data around the (0 4 0) and (2 0 2) reflections of orthorhombic $CsPbBr_3$ after subtraction of the experimental background and a fitted linear background. Lines are fits to the data. **b**, PL intensity, intensity of the WAXS peak shown in **a**, and crystallite size obtained from Scherrer analysis. The vertical dashed line indicates the acetone injection at $t = 10\,s$. Figure adapted from [379, Supplementary Information] with permission. CC-BY license 2024, Springer Nature.

At lower antisolvent volumes and lower concentrations of intermediate nanoclusters the tendency of nanoclusters to assemble in a mesophase is insufficient, and they partly dissolve. At this stage the reaction mixture has a lower ion concentration and a higher ion solubility compared to the initial mixture in toluene. Under these conditions the growth of freely dispersed 2ML nanoplatelets is favored. 2ML nanoplatelets are likely the thermodynamically stable polymorph in the Cs-deficient regime studied here, since they also form without antisolvent with longer reaction times ($> 10\,min$, see Figure A9). Several theoretical models have been proposed to explain a stable two-dimensional shape in LHPs and semiconductor nanocrystals in general, based on different surface termination and distinct nucleation barriers on wide and narrow facets [408–410]. Further slow in situ scattering studies without antisolvent would be required to clarify these specific growth mechanisms.

The suggested reaction pathway, in which nanoplatelets grow freely in solution from destabilized intermediate nanoclusters and redissolved precursor material is illustrated in Figure 4.18 (bottom). The absence of mesophase reflections until 55 s after antisolvent addition in the nanoplatelet synthesis and the emergence of a new and separate, blueshifted PL emission (Figure 4.14 c) support this mechanism. Once the nanoplatelets have reached a sufficient size, attractive vdW forces between large platelet facets [406], as well as solva-

tion forces [411] and interactions between ligands [412] favor their assembly into lamellar stacks. In this scenario, therefore, the observation of a lamellar mesophase is only a consequence of the regular shape and homogeneous size of the anisotropic nanocrystals. The lamellar mesophase hardly acts as a structure-directing template, since further growth is dramatically slowed down once it is formed, as shown in Figure 4.15.

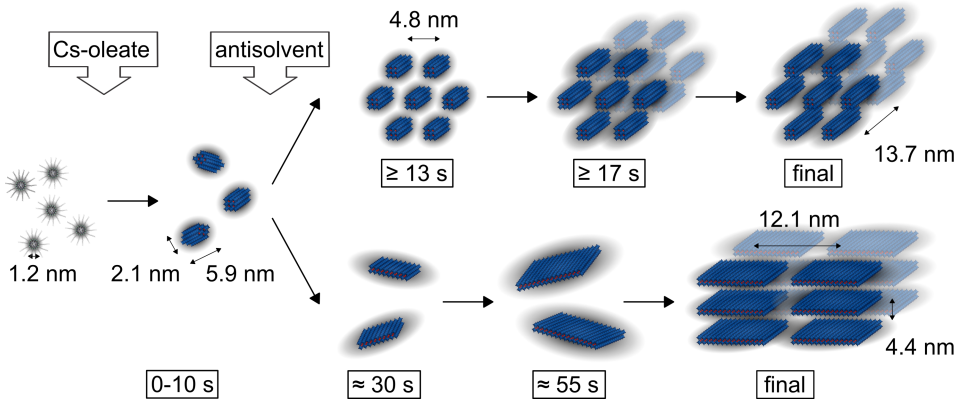

Figure 4.18: Schematic illustration of the formation mechanisms of 3ML nanorods and 2ML nanoplatelets. For both nanocrystal shapes, intermediate nanoclusters form from $PbBr_2$ precursor micelles after addition of Cs-oleate. Starting from the same nanoclusters, injection of different amounts of acetone antisolvent leads either to the growth of nanorods in a hexagonal mesophase (top) at large volumes or to growth of nanoplatelets in dispersion at low volumes (bottom). Sizes and spacings are obtained from SAXS analysis.

4.1.4.2 Shape and size control by classification of solvent properties

Having found that the anisotropy of LHP nanocrystals is determined by the antisolvent, the next step is to study what determines the underlying solvent-nanocluster interactions on a fundamental level. For this purpose 17 potential antisolvents were screened by the Urban group regarding their effect on the reaction product. Antisolvent polarity and volume were varied, using a wide range of solvents with $E_T(30)$ polarity ranging from 0.099 (toluene) to 0.762 (methanol, see Section 2.1.4 and Table A8). Miscibility with toluene and safe usage in a laboratory fume hood, i.e., a high boiling point and low toxicity were further requirements for the screening.

The nanocrystal products obtained by this screening can be classified into four categories: 2ML nanoplatelets, 3ML nanorods, 3ML nanoplatelets and no LHP product, indicating the dissolution of intermediate nanoclusters. These reaction outcomes are shown in Figure 4.19.

The classification of the reaction products shows that the addition of low polarity solvents still leads to the formation of 2ML nanoplatelets, whereas high polarity solvents typically increase the nanoplatelet thickness to 3ML. This trend is more pronounced for the higher Cs-oleate to $PbBr_2$ ratio, where 2ML nanoplatelets are only observed for antisolvents with polarity lower than acetone. Solvents with intermediate polarities show a more diverse reaction outcome, especially at the higher Cs-oleate to $PbBr_2$ ratio of 0.2. 3ML nanorods are only observed when using acetone, which is further investigated below. Several solvents at moderate polarity dissolve intermediate nanoclusters and prevent the formation of LHP nanocrystals altogether.

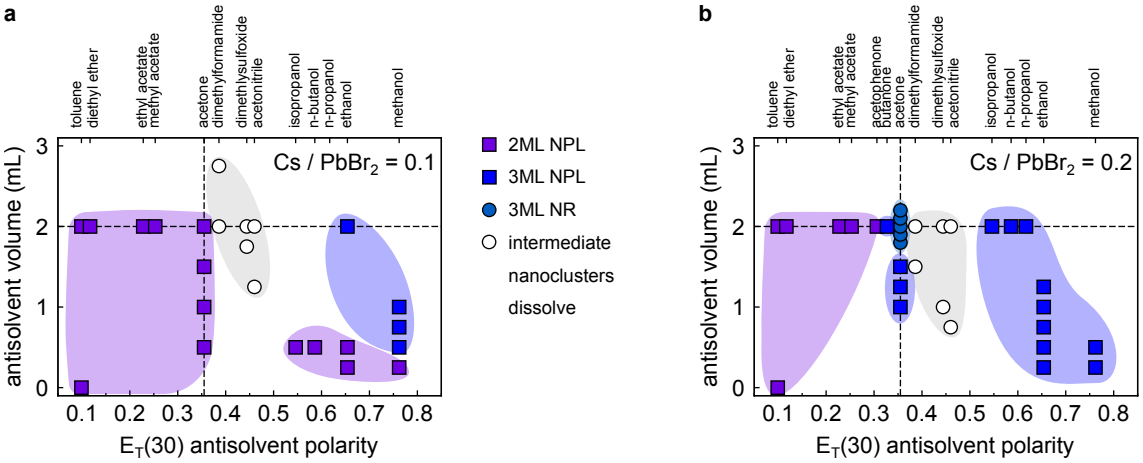

Figure 4.19: Classification of the anisotropic LHP nanocrystals depending on precursor ratio, antisolvent polarity and volume. a ($Cs/PbBr_2 = 0.1$) and **b** ($Cs/PbBr_2 = 0.2$) represent the typical precursor ratios for 2ML nanoplatelets and 3ML nanorods, respectively. Symbols are defined in the legend. Shaded areas are a guide to the eye. Dashed lines highlight the standard conditions for the synthesis of 2ML nanoplatelets and 3ML nanorods. Data provided by Nina A. Henke.

Solvents for lead halide perovskites have been classified in literature according to empirical properties for the purpose of thin film processing [45]. The four categories of inert, weak, strong, and AX-selective solvents are based on dipole moment μ, Hansen hydrogen bonding parameter δ_H and donor number DN, which are introduced in Section 2.1.4. Using this scheme, the nanocrystal products obtained in the screening are classified as a function of μ, δ_H and DN. In a μ-δ_H representation, shown in Figure 4.20 a, the reaction products appear in distinct clusters and new trends appear compared to a classification by polarity and volume alone (Figure 4.19). Most importantly, anisotropy and monolayer thickness are found to depend on distinct solvent properties. A similar clustering of products is observed in a μ-DN representation (Figure 4.20 b), but the conditions for 2ML and 3ML nanoplatelets are not separated as clearly. Strikingly, clusters of products coincide to a large extent with the solvent categories introduced in reference [45]. In the following, the mechanisms leading to the respective products are therefore rationalized individually for each category.

Inert solvents (n-hexane and toluene) are characterized by low values of μ, δ_H, and DN. These solvents do not show any interaction with ligand-passivated LHP nanocrystals or intermediate nanoclusters, leaving them both well-dispersed. They therefore do not induce a deviation from the thermodynamically favored shape of 2ML nanoplatelets.

Weak solvents (e.g. diethyl ether, methyl acetate) show a slightly higher solubility for LHP precursor ions and weakly interact with the intermediate nanoclusters. They therefore accelerate nanoplatelet formation, since ions are incorporated more rapidly into the growing nanocrystals. If added in sufficient volume, these solvents enable stacking of the as-formed nanoplatelets into a lamellar mesophase. This allows a simplified precipitation of the product. With weak antisolvents and slightly increased Cs-oleate/$PbBr_2$ precursor ratio intermediate nanoclusters can be isolated at early reaction times. Nanoplatelets with varying aspect ratio are obtained at later times [379, Supplementary Figures 32-33].

Strong solvents (acetonitrile, dimethylsulfoxide, dimethylformamide) exhibit a large dipole moment and/or a large donor number. They strongly coordinate Pb^{2+} ions and therefore lead to the dissolution of intermediate nanoclusters. No LHP product is obtained

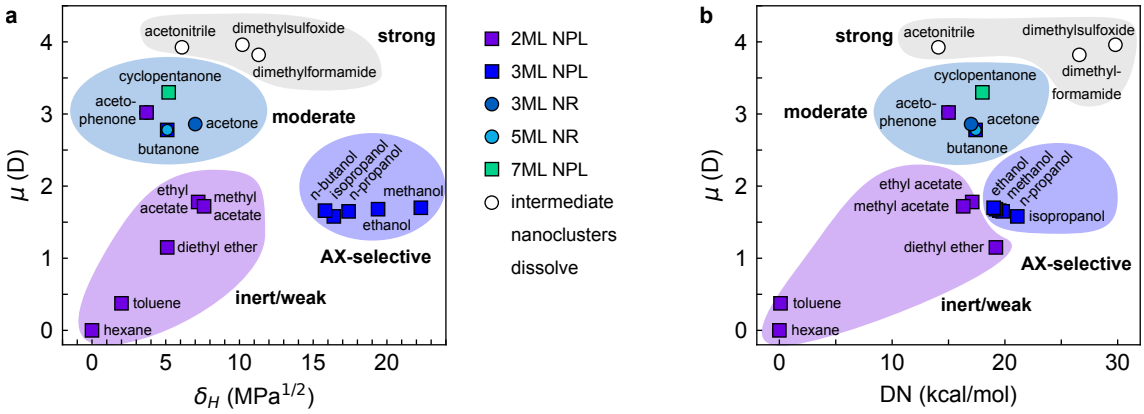

Figure 4.20: Classification of nanocrystals by antisolvent dipole moment, Hansen hydrogen bonding parameter and donor number. Symbols (legend) indicate the shape and thickness of the reaction product, combining the results of syntheses at different Cs-oleate to $PbBr_2$ precursor ratios and antisolvent volumes. Shaded areas illustrate the classification of antisolvents. Low amounts of acetone and AX-selective solvents can also yield 2ML nanoplatelets at Cs-oleate to $PbBr_2$ precursor ratio < 0.2, which is not shown in the chart for clarity. The most diverse range of products is obtained using moderate solvents. Data provided by Nina A. Henke.

The so-called *AX-selective solvents* form a separate category, originally due to their ability to coordinate organic A cations in organic-inorganic LHP film processing [45]. Primary (e.g. ethanol) and secondary alcohols (e.g. 2-propanol) fall into this category. These solvents coordinate not only cations, but also OlAm ligands via hydrogen bonding [47], as suggested by their large δ_H value. Removal of these ligands from the intermediate nanocluster surfaces by addition of AX-selective solvents enables further attachment of precursor ions. This potentially promotes a seeded growth mechanism towards 3ML nanoplatelets starting from intermediate nanoclusters as seeds. As a result, 3ML thick nanoplatelets are observed as the reaction product for all AX-selective antisolvents if a sufficient amount of antisolvent is added.

The class of *moderate solvents*, characterized by an intermediate dipole moment and donor number and a low hydrogen bonding parameter, includes mainly ketones, e.g., acetone and butanone. Reactions with these antisolvents show a variety of products, namely 2ML nanoplatelets, 3ML nanorods, 3ML nanoplatelets, 5ML nanorods, and 7ML nanoplatelets. 3ML nanorods were only observed with acetone as an antisolvent. These solvents are found to play a special role in the synthesis of anisotropic LHP nanocrystals. On the one hand, their destabilizing effect on intermediate nanoclusters is lower than for strong or AX-selective solvents due to their lower δ_H values. On the other hand, acetone is known to mediate surface-tension mismatch in dispersions of colloidal nanocrystals when transferring them from, e.g., water to a less polar environment [50]. This property is likely the essential ingredient for a mesophase of intermediate nanoclusters. The mesophase formation, in turn, is crucial for obtaining nanorods, as this shape of the product is only observed with moderate solvents in this synthesis scheme.

In the screening, 5ML thick nanorods are observed for butanone as an antisolvent if a correspondingly higher Cs-oleate to $PbBr_2$ precursor ratio of 0.5 is used. This trend is in agreement with the original synthesis strategy, in which a weaker stoichiometric Cs-deficiency should induce thicker nanocrystals. The successful synthesis of 5ML nanorods suggests that the use of moderate ketone antisolvents can lead to a wider thickness-tunability of nanorods if the size control of intermediate nanoclusters is advanced. In future experiments

new antisolvents (or mixtures) and rationally derived antisolvent-precursor ratios may be used to extend the range of shape and size control even further.

Judging from the syntheses investigated to date, the intermediate nanocluster size and their slightly prolate shape is largely conserved across parameter space. It is independent of precursor ratio within the investigated range of Cs-oleate/$PbBr_2$ ratio from 0.1 to 0.2 with variation mainly due to reaction timing and precursor mixing (see Figure A3). Larger sizes of nanoclusters may be possible via larger ratios up to 0.5 at room temperature. Alternatively, a faster growth of prolate intermediate nanoclusters to a larger size ($3.2 \times 3.2 \times 10.1\,nm^3$, i.e., 5ML nanorods) can be achieved by injecting Cs-oleate into $PbBr_2$ stirred at 50 °C, as shown in Figure A10 a. This synthesis shows an intricate coexistence of two mesophases (Figure A10 b). The lattice spacings, analyzed in Figure A11 a and b, suggest the immediate formation of a hexagonal phase of 5ML nanorods, and a delayed appearance of a lamellar phase of 3ML nanoplatelets. Both nanocrystals are identified in the PL emission of the purified product, recorded ex situ (Figure A11 c). These preliminary results suggest that size-tunability of nanorods and nanoplatelets can be extended to larger thicknesses by including reaction temperature as an additional parameter.

Nanorod thickness engineering via intermediate nanoclusters will also require an investigation of alternative ligands. Such ligands should either lead to different precursor clusters and therefore a modified precursor conversion rate, stabilize differently sized intermediate nanoclusters, directly favor a rod-shaped particle via the binding preference or steric attachment geometry, or induce a tube-shaped mesophase by the intrinsic ligand curvature. The effects of polymorphism and intrinsic curvature on the mesophases of amphiphiles have been widely investigated in the context of, e.g., phospholipids [328] and might inspire the development of new ligands for LHP nanocrystal synthesis [34, 413]. More complex mesophase geometries could induce different crystal shapes such as nanocuboids with three different sides, relevant for fundamental studies of the optoelectronic properties under strong quantum confinement [34], or hollow structures [414].

Regarding thickness-tunability of *nanoplatelets*, the results presented here rather suggest that careful destabilization of the growing nanocrystal facets should be pursued as a future strategy, since all nanoplatelets are found to grow to their final thickness while freely dispersed. Contrarily, in dense, lamellar assemblies of nanoplatelets the large facets are protected from further growth. To exploit this protective effect, assembly may be delayed or induced on purpose by separate additives such as inert depletants (see Section 2.2) in addition to the antisolvent.

To find subtle structural changes resulting from antisolvent addition, the crystalline structure of intermediate LHP nanoclusters could be investigated by two-phase PDF refinement, taking into account the unreacted precursor. The octahedral tilt in the final nanocrystals (see Section 2.3.1) may differ from the intermediates due to a larger surface-to-volume ratio and strain exerted by the ligands. PDF refinement could reveal a potential registry of the orthorhombic unit cell axes with the nanorod shape, as hypothesized in literature [415]. Nanorods, resulting from fusion of intermediates inside a mesophase, may show twinning or stacking faults as remnants of the fusion sites. Such nanotwins have already been observed in $CsPbX_3$ nanocrystals [189]. Defects at the domain boundaries could explain the relatively broad PL linewidth of nanorods compared to nanoplatelets of similar dimensions (see, e.g., Figure 4.2).

A further in situ diffraction and PL spectroscopy study could target the transformation of rod-shaped intermediates to nanoplatelets of different thickness (e.g., 2ML and 3ML),

following the antisolvent injection. This could reveal whether nanoplatelets form mainly by attachment of rod-like monomers or via seeded growth of one or few rods and many precursor monomers. Preliminary experiments on $CsPbI_3$ nanoplatelet synthesis suggest the formation of rod-like intermediates, followed by nanoplatelets, and a later degradation to the δ-phase, but remain rather ambiguous regarding the rod-to-platelet transition. Studying $CsPbI_3$ and other compositions could establish universal reaction pathways for LHPs and new compatible antisolvents.

4.1.4.3 Shape determination of fully grown LHP nanocrystals

In Section 4.1.2.2 an ellipsoidal model was identified as a good description of the intermediate LHP nanoclusters based on SAXS data. This model also describes purified anisotropic nanocrystals after the reaction, which can help shape determination of unknown products from new syntheses. Exemplary ex situ SAXS data with model fits are shown in Figure 4.21 a and fit parameters, including size polydispersities, are given in Table A9. Based on these fits the prolate shape of nanorods (3ML and 5ML) and the oblate shape of nanoplatelets (2ML, 3ML, 7ML) can be distinguished. The size parameters are in reasonable agreement with values obtained from electron microscopy. SAXS yields sizes of $2.0 \times 2.0 \times 17.1\,\mathrm{nm}^3$ and $2.2 \times 2.2 \times 10.4\,\mathrm{nm}^3$ for the 3ML nanorod samples, and $2.2 \times 2.2 \times 14.1\,\mathrm{nm}^3$ for 5ML nanorods. For 2ML nanoplatelets $1.7 \times 14.6 \times 14.6\,\mathrm{nm}^3$ or $1.7 \times 12.9 \times 12.9\,\mathrm{nm}^3$ are obtained. $2.2 \times 10.4 \times 10.4\,\mathrm{nm}^3$ are obtained for 3ML nanoplatelets, and $5.6 \times 11.9 \times 11.9\,\mathrm{nm}^3$ for 7ML nanoplatelets. The pair distance distribution function (PDDF, see Section 2.4.2), shown in Figure 4.21 b can be used to quickly assess the particle anisotropy if several datasets are available for comparison. PDDFs are shown separately for data from a high resolution (top) and a high-flux, lower resolution (bottom) laboratory SAXS setup (see Table 3.6), leading to a different maximal resolved distance. While nanoplatelet samples (2ML, 3ML, 7ML) show a rather symmetric curve as a function of distance r, nanorods (3ML and 5ML) exhibit a peak at low r followed by an asymmetric, elevated tail towards larger r. This asymmetry can be taken as a quick indication of the prolate morphology, as confirmed by the simulations shown in Figure 2.19 b and c.

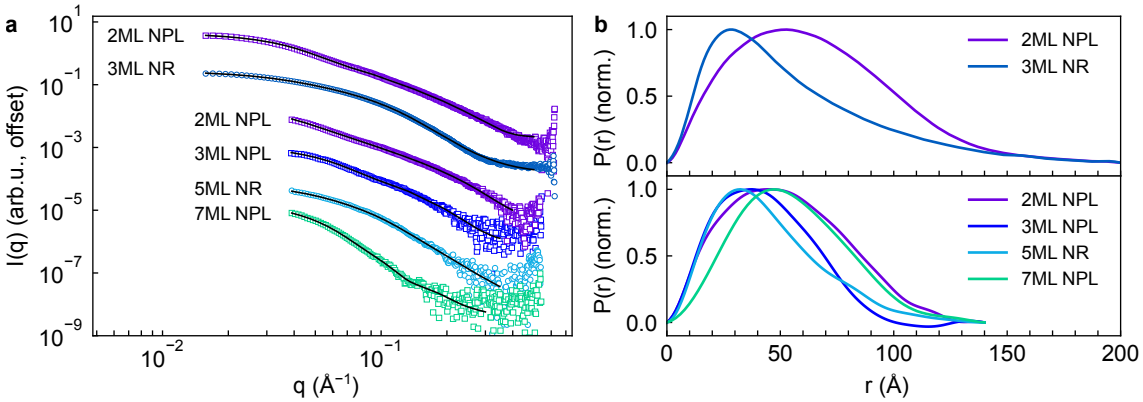

Figure 4.21: Shape analysis of purified anisotropic nanocrystals by laboratory SAXS. a, Dots: SAXS intensities of 2ML nanoplatelets, 3ML nanorods, 5ML nanorods, and 7ML nanoplatelets, recorded on two different laboratory SAXS setups, once in a low flux, high resolution (top) and once in a high flux, low resolution configuration (bottom, note the smaller q range). Solid lines are fits to the data. **b**, Top: Pair distribution functions (PDDFs) obtained from high resolution data in **a**. Bottom: PDDFs obtained from low resolution data in **a**. PDDFs were calculated using a value of $d_{\mathrm{max}} = 200$ Å and 140 Å, respectively.

Additionally, the mesophase symmetry, hexagonal or lamellar, gives a strong indication of the nanocrystal shape in the final phase of the synthesis. If nanocrystals assemble in this way, a rapid shape classification based on low resolution (laboratory) SAXS data becomes feasible without model fitting. Figure 4.22 shows in situ SAXS data of a 3ML nanorod synthesis and a 2ML nanoplatelet synthesis recorded with the high-flux laboratory setup. The onset of mesophase formation can be detected with 10 s and 1 min time resolution, for 3ML and 2ML, respectively. The observed mesophase symmetry, namely the presence or absence of the (1 1 0) reflection of a two-dimensional hexagonal lattice, indicates the particle shape.

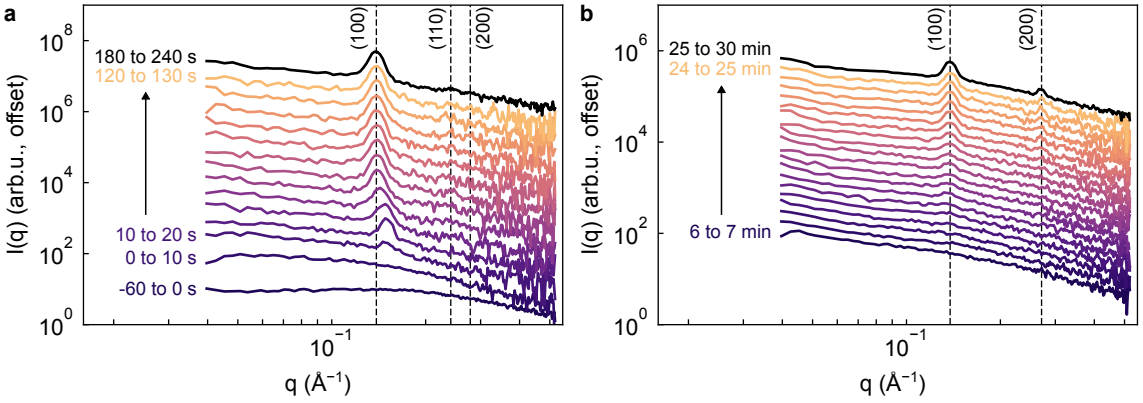

Figure 4.22: In situ identification of mesophases on a laboratory SAXS setup. a, In situ SAXS data of a 3ML nanorod synthesis shown with 10 s time resolution. Cs-oleate injection is at $t = 0$ s. The first and last curve shown are binned from six consecutive curves to show the signal of precursor micelles and the hexagonal mesophase with improved statistics. Vertical dashed lines indicate the reflections of a hexagonal mesophase with 4.9 to 5.2 nm spacing. **b**, In situ SAXS data of a 2ML nanoplatelet synthesis shown with 1 min time resolution. Cs-oleate injection is at $t = 0$ s. The last curve is binned from five consecutive curves and shows the reflections of a lamellar mesophase with a spacing of (4.59 ± 0.04) nm.

4.1.5 Post-synthetic modification by lead halide salts

4.1.5.1 Intensity enhancement and redshift of emission

Having clarified the mechanisms responsible for the anisotropic shape of LHP nanorods and nanoplatelets, this section focuses on their post-synthetic modification by addition of lead halide salt solutions.

Addition of $PbBr_2$ to purified LHP nanocrystals in solution is used to enhance the PLQY [200]. Bromide vacancies and undercoordinated lead atoms left at the nanocrystal surface after synthesis are responsible for a PL intensity loss due to non-radiative recombination of excitons [200, 213, 235] (see also Section 2.3.1). Added $PbBr_2$ acts as a source for Pb^{2+} and Br^- ions which passivate these surface defects. This boosts the PLQY from (9.0 ± 4.0)% to (38.9 ± 11.9)% for 3ML nanorods and from (8.4 ± 4.0) % to (16.4 ± 3.8)% for 2ML nanoplatelets, when treated with 10% (by volume) of $PbBr_2$ solution in hexane [379, Supplementary Information].

Addition of PbI_2 leads to partial anion exchange of Br^- by I^-. As a result, a redshift of the emission of 5ML thick nanocrystals from an initial 487 nm to up to 612 nm has been observed [235, pp. 67 ff.]. Partial anion substitution to $CsPbBr_{3(1-x)}I_{3x}$ by adding different amounts of salt allows for a precise tuning of the emission color from blue to red and a drastic improvement of PLQY [235, pp. 67 f.]. With pure and non-quantum-

confined $CsPbI_3$ an emission wavelength of up to 710 nm can be reached [2]. For moderately quantum-confined $CsPbI_3$ nanocrystals emission between 673 and 682 nm is reported in literature [416], 4ML $CsPbI_3$ nanoplatelets show emission at 620 nm [417] and 3ML $CsPbI_3$ nanoplatelets with 25 nm square dimensions emit at 596 to 600 nm [418]. Direct synthesis of pure $CsPbI_3$ nanocrystals remains an experimental challenge due to stability issues. $CsPbI_3$ nanocrystals often quickly decay from the emissive cubic phase to a non-emissive, yellow orthorhombic (δ) phase [2, 416]. The two modification strategies, starting from stable $CsPbBr_3$ nanocrystals and using Br^- and I^- anions, therefore enhance both the efficiency and the accessible emission wavelength range at low synthetic complexity.

By *addition of $PbCl_2$* to $CsPbBr_3$ nanocrystals a blueshift of emission down to 427 nm can be achieved for 5ML thick nanocrystals [235], but due to the relatively low PLQY of $CsPbBr_{3(1-x)}Cl_{3x}$ no in situ experiments were attempted on this mixture. Here, changes of emission wavelength and intensity are correlated with structural changes. For this purpose simultaneous in situ SAXS/WAXS/TS and PL spectroscopy are carried out during the addition of salt.

Figure 4.23 a shows the reaction scheme, as detailed in Section 3.1.1. A 300 µL solution of purified 3ML $CsPbBr_3$ nanorods in n-hexane is stirred in the in situ reaction cell (see Section 3.2). Salt solution consisting of PbX_2 in n-hexane with OlAm and OlAc is added in six steps of 50 µL every 5 min to the nanorod solution, using the motorized syringe pump shown in Figure 3.3.

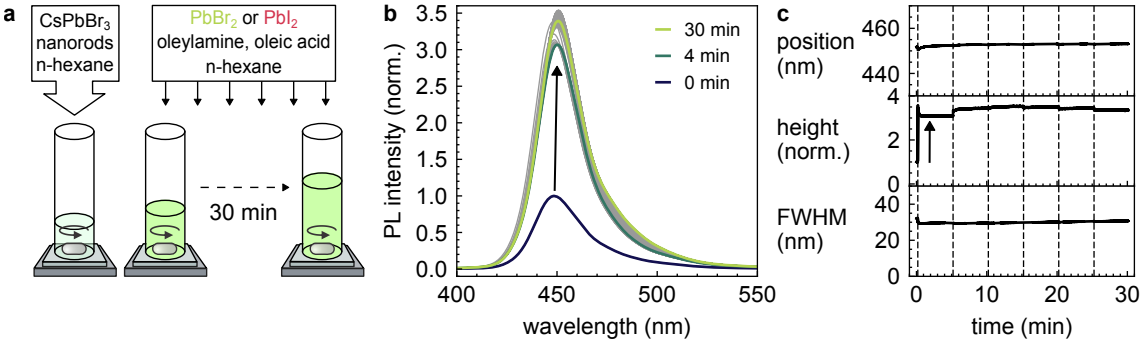

Figure 4.23: Reaction scheme and evolution of PL during $PbBr_2$ addition. **a**, Reaction scheme for in situ studies of post-synthetic modification. **b**, Selected in situ PL intensities of a $CsPbBr_3$ 3ML nanorod sample before and after one addition of $PbBr_2$ (4 min) and after six additions (30 min). gray curves represent PL intensities in between, shown for every 5 s. **c**, PL peak position, height, and FWHM extracted by a Gaussian fit to the data in **b**. A vertical arrow highlights the three-fold intensity increase after the first of six $PbBr_2$ additions (vertical dashed lines).

The PL intensity during $PbBr_2$ addition is shown in Figure 4.23 b. It shows a three-fold intensity increase following the first injection, and only minor intensity fluctuations after the following injections.

PbI_2 addition, shown in Figure 4.24, leads to an eight-fold suppression of the emission at approx. 450 nm and a redshift to 508 nm. The following injections initiate a recovery and a two-fold amplification of emission compared to the initial intensity. The peak wavelength becomes more strongly redshifted to up to 572 nm after six additions. This shift is due to the partial replacement of Br^- with I^- in the nanorods. A weak additional feature at 668 nm, marked with an asterisk (*) is also observed. This indicates the presence of a small contamination of the initial sample with nanocrystals with a larger monolayer thickness, whose emission is likewise redshifted.

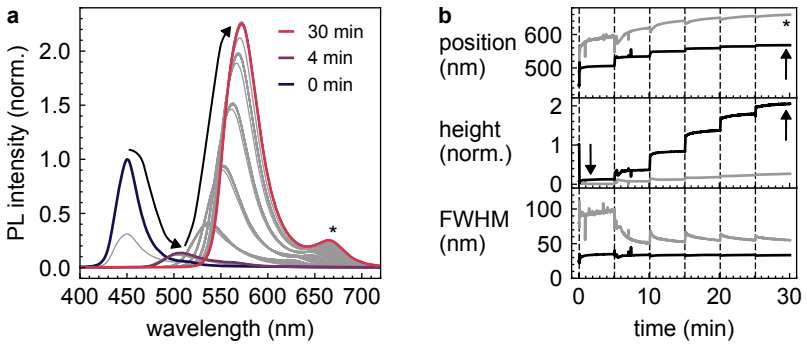

Figure 4.24: Evolution of PL during PbI_2 addition. **a**, Selected in situ PL intensities of a $CsPbBr_3$ 3ML nanorod sample before and after one addition of PbI_2 (4 min) and after six additions (30 min). gray curves represent PL intensities in between, shown for every 5 s. **b**, PL peak position, height, and FWHM extracted by a fit with two Gaussian peaks to the data in **a**, accounting for a contamination emitting at longer wavelengths (gray curves in **b**, *). Vertical arrows highlight the redshift of emission, the initial drop and the final recovery of PL intensity.

4.1.5.2 Nanocrystal structure by WAXS and TS

Figure 4.25 shows selected in situ WAXS intensities, recorded simultaneously with the PL spectroscopy measurements shown above. Intensities before (0 min) and after addition of $PbBr_2$ salt solution (4 min and 30 min) are displayed on the same scale, showing a strong rise of the diffuse signal after repeated additions. The WAXS signal of the $PbBr_2$ solution, recorded separately, is additionally shown.

A vertical line in Figure 4.25 a shows the position of the $CsPbBr_3$ (0 4 0)/(2 0 2) Bragg reflection at approx. 2.119 $Å^{-1}$, which is fitted with a Pseudo-Voigt function (Equation 2.31) on a linear background. The peak area, shown in Figure 4.25 b as a function of time, represents the intensity from nanocrystalline $CsPbBr_3$. The area under the linear background curve serves as a measure for the diffuse intensity.

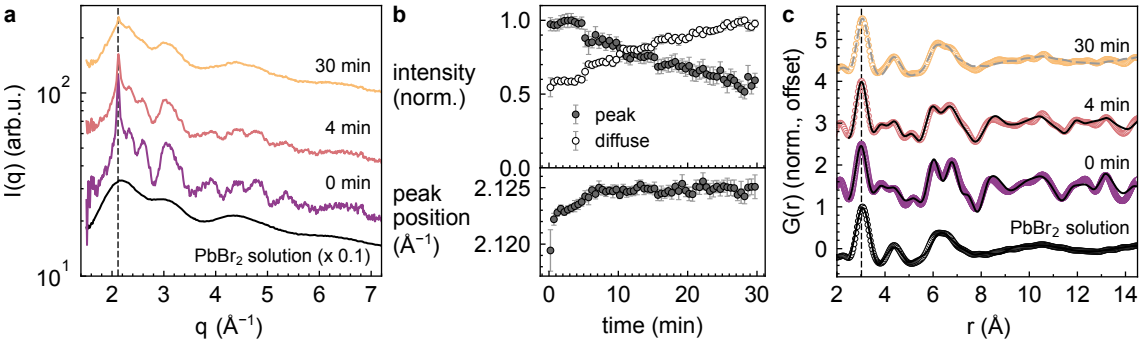

Figure 4.25: Evolution of WAXS intensity and PDF during $PbBr_2$ addition. **a**, In situ WAXS intensity of a $CsPbBr_3$ 3ML nanorod sample before (0 min) and after one addition of $PbBr_2$ (4 min) and after six additions (30 min). The signal of the $PbBr_2$ solution is additionally shown and scaled by 0.1 for clarity. A vertical dashed line indicates the initial (0 4 0)/(2 0 2) peak position. **b** Evolution of the peak area and diffuse signal intensity and the peak position extracted from **a**. **c**, PDF of the WAXS/TS data shown in **a**. Solid black curves are fits to the data as detailed in the text. The signal at 30 min closely resembles the signal of the $PbBr_2$ solution (dashed gray curve). A vertical dashed line indicates the shortest Pb–Br distance.

Based on the strong enhancement of PLQY upon salt addition it might be expected that the healing of defects also leads to an enhanced diffraction signal of the nanocrystals. Contrastingly, the intensities given in Figure 4.25 b (top panel) show that the Bragg peak

intensity is reduced by 50% throughout the reaction. This reduction corresponds quantitatively to the effect of dilution. The addition of ions does therefore not amplify the Bragg diffraction signal, which is dominated by the bulk of the nanocrystals. It most likely only affects lead and bromide defect sites present at the nanocrystal surface, which contribute negligibly to the diffraction signal.

The diffuse intensity contribution, mainly originating from the added salt solution, is simultaneously doubled, showing that at most a small fraction of the supplied additional ions is incorporated into the nanocrystals. The final intensity is well described as a mixture, i.e., a linear superposition of the nanocrystal and $PbBr_2$ intensities. This suggests that the unused $PbBr_2$ remains in solution in the form of micelles, as further substantiated below.

Importantly, an abrupt shift of the analyzed reflection to a larger q value of $2.122\,Å^{-1}$ is observed after the first injection of $PbBr_2$ solution (Figure 4.25 b, bottom panel). The shift continues at a much slower pace after the second injection and then reaches a plateau at $2.125\,Å^{-1}$. This shift of the reflection corresponds to a compression of the crystalline lattice by 0.3%, which potentially results from a release of strain accompanying the passivation of surface defects. Here, the first injection already supplies enough material to significantly affect the lattice.

To analyze the large diffuse signal in the WAXS intensity a real space representation of the data via the PDF (Figure 4.25 c) obtained from TS data is beneficial (see Section 2.4.4). As shown before in Section 4.1.2.2, the analysis of $G(r)$ is particularly well suited for the study of materials without long-range crystalline order. In the non-polar n-hexane solvent (0.009 on the $E_T(30)$ scale) the $PbBr_2$ salt is expected to be encapsulated as small reverse micellar clusters. These clusters are stabilized by the OlAm and OlAc ligands with their tails exposed to the solvent, similar to what was found for the $PbBr_2$ precursor in toluene in Figure 4.8 b.

Indeed, the reduced PDF of the $PbBr_2$ solution (black dots in Figure 4.25 c) shows pronounced peaks at 3.06 Å, 4.38 Å and 6.22 to 6.52 Å. These values match the distances of Pb–Br, Br–Br, and Br–Br (opposite) in an octahedral coordination of Pb. The lead ion is thus likely surrounded by an octahedron of Br or O/N belonging to the OlAc/OlAm ligands, analogous to the analysis shown in Figure 4.8 b.

To further clarify the $PbBr_2$ micellar structure a fit with different cluster models of octahedral $PbBr_6^{4-}$ units is carried out. Several models, containing a different number of octahedra in linear or planar arrangements, lead to a similar agreement with the experimental $G(r)$, as shown in Figure A13. This is likely due to the limited real space resolution of $G(r)$ as a consequence of the small q_{max} value of $10\,Å^{-1}$, resulting from a high solvent background. The fit curve in Figure 4.25 c corresponds to a model of two PbX_6 octahedra sharing one edge, with Br in the equatorial and N in the polar positions, which agrees best with the data ($R_w = 0.161$, see Table A10).

$G(r)$ of the $CsPbBr_3$ nanorods before salt addition (0 min, purple curve in Figure 4.25 c) can be fitted using the structure of orthorhombic (Pnma) $CsPbBr_3$ (COD 4510745) with an acceptable R_w of 0.357. The fit approximately matches the characteristic interatomic distances between 2.5 and 14 Å, which are particularly sensitive to the octahedral tilt. Fit parameters are given in Table A11. The fit serves as a good indication of the perovskite structure of the sample. The agreement between model and data is significantly improved after one salt addition (4 min, red curve, $R_w = 0.252$). The refined Pb–Br bond angles are closer to the reported values for orthorhombic $CsPbBr_3$, given in Section 2.3.1, after

one salt addition, especially for equatorial Br atoms. Potentially a structural relaxation, suggested by the lattice compression found in WAXS analysis, leads to a less strained crystalline perovskite structure. A PDF refinement of as-synthesized anisotropic $CsPbBr_3$ clusters found in literature has found a highly distorted, orthorhombic structure [188]. Here, a similar distortion may be present, before being reduced by the added bromide.

After repeated addition of $PbBr_2$ solution (yellow curve, 30 min) $G(r)$ resembles the signal of the $PbBr_2$ solution (superimposed dashed line) and is therefore dominated by the added micelles. The smallest Pb–Br distance in the PDF, shown in Figure A12 a also reflects this behavior, as it evolves from 3.02 Å to 3.06 Å, the value of the $PbBr_2$ solution, after repeated addition. This serves as a further indication that the first addition of $PbBr_2$ solution already supplies sufficient material for passivation of surface defects, which was already evident in the PL spectra in Figure 4.23. The fact that mainly bromide vacancies are filled by the added salt suggests that lead-rich micelles remain in solution after the first addition.

The same analysis is carried out for the ion exchange reaction using PbI_2. Selected in situ WAXS data are shown on the same scale in Figure 4.26 a. As seen for $PbBr_2$, the addition of PbI_2 solution to the 3ML $CsPbBr_3$ nanorods mainly leads to a rise of the diffuse scattering signal, with broad oscillations extending to large q. Here, however, an additional shift of the (0 4 0)/(2 0 2) reflection from 2.09 $Å^{-1}$ to lower q values is observed (Figure 4.26 b, vertical dashed line). All six PbI_2 injections lead to such a shift, and a peak position of 2.01 $Å^{-1}$ is reached after six injections. This indicates an expansion of the crystalline lattice by 4%, and therefore a successful incorporation of the larger iodide ions into the nanocrystals.

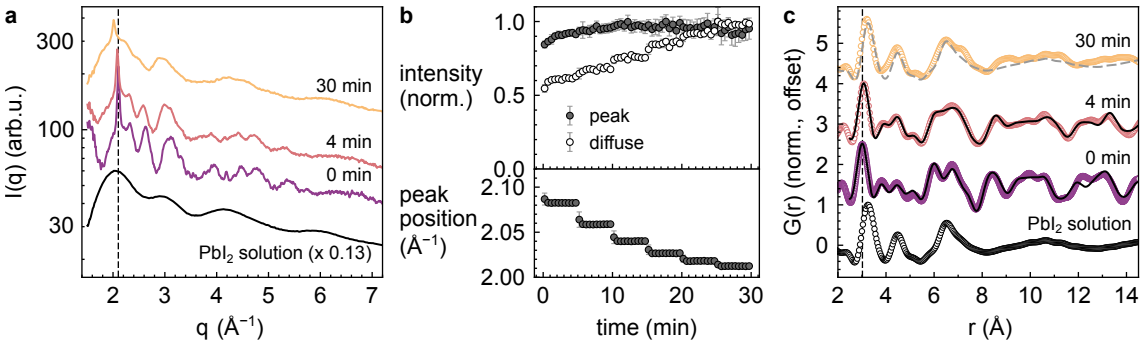

Figure 4.26: Evolution of WAXS intensity and PDF during PbI_2 addition. **a**, In situ WAXS intensity of a $CsPbBr_3$ nanorod sample before (0 min) and after one addition of PbI_2 (4 min) and after six additions (30 min). The signal of the PbI_2 solution is scaled by 0.13 for clarity. A vertical dashed line shows the initial position of the (0 4 0)/(2 0 2) Bragg reflection analyzed in **b**. **b** Evolution of the peak area and diffuse signal intensity and the peak position. **c**, PDF of the WAXS/TS data shown in **a**. Solid black lines are fits to the data as detailed in the text. The signal at 30 min closely resembles the signal of the PbI_2 solution (dashed gray line). A vertical dashed line indicates the shortest Pb–X distance of the sample at 0 min.

The diffuse intensity rises and the peak intensity stays approximately constant, despite the effect of dilution due to the addition of PbI_2 solution. Dilution is thus at least partly counteracted by a beneficial effect of the added salt on the nanocrystalline lattice. This finding is in agreement with the drastically improved PLQY upon PbI_2 addition, seen in Figure 4.24 and also previously reported [235, pp. 67 f.]. The effect of later injections becomes gradually smaller and thereby resembles the response of the emission wavelength, which shows a less pronounced redshift following the later injections.

In Figure 4.26 c the reduced PDF is analyzed. The PbI_2 solution (black dots) shows three pronounced peaks at 3.26 Å, 4.49 Å, and 6.53 Å. These interatomic distances correspond to the Pb–I, I–I, and I–I (opposite) distances in a PbI_6^{4-} octahedron, analogous to the $PbBr_2$ case. Here, all distances are wider (2.5 to 6.5%), which is in approximate agreement with the difference in crystal ionic radii (see Section 2.3.1).

In the mixture of $CsPbBr_3$ nanorods and PbI_2 solution the smallest Pb–X distance should evolve between 2.96 Å in $CsPbBr_3$ (COD 4510745) and 3.21 Å in $CsPbI_3$ (mp-1069538). This assumes that a complete, but gradual replacement of the ions occurs and no phase transition takes place. Indeed, a shift of the Pb–X distance occurs in $G(r)$ from 3.01 Å to 3.16 Å in Figure A12 b, corresponding to a partial replacement of Br^- by I^-. Notably, the Pb–X distance levels off at 3.08 Å and 3.11 Å after one and two injections, respectively. All further injections lead to an approximately linear increase of the distance with time. This is likely a consequence of the simultaneous presence of Pb–Br and Pb–I distances in the LHP nanocrystals, Pb–I distances in the micelles, and potentially also Pb–Br distances resulting from expelled Br^- ions. TS experiments with higher resolution and a two-phase refinement of $I(q)$ or $G(r)$ using a model for the nanocrystals and the micelles would have to be carried out to disentangle these contributions.

As described above, a model of orthorhombic $CsPbBr_3$ provides an acceptable fit to $G(r)$ before and after one PbI_2 addition ($R_w = 0.295$ and 0.227, respectively, see Table A11). The Pb–Br bond angles change only moderately and are rather close to the literature values for orthorhombic $CsPbBr_3$. After six additions the signal is dominated by the excess PbI_2 (gray dashed line in Figure 4.26 c).

Based on these observations the fraction of I/Br ions in the nanocrystals are derived for different amounts of added salt. This leads to a quantitative approach to color tuning via post-synthetic modification. Vegard's law (Equation 2.6) is used to estimate the fraction of Br^- replaced by I^- in the process based on the in situ WAXS data. Figure 4.27 a shows the lattice parameters for $CsPbBr_3$ and $CsPbI_3$ from literature and the experimentally determined values from Figure 4.25 and Figure 4.26, summarized in Table A12. The reported values for orthorhombic and tetragonal $CsPbBr_3$ are transformed to an effective cubic lattice parameter for easier comparison. A linear relationship of the I/Br ratio x in $CsPbBr_{3(1-x)}I_{3x}$ and the lattice parameter can be constructed between the limiting values for $CsPbBr_3$ and $CsPbI_3$. Using this linear relationship, x is derived from the observed lattice parameters during PbI_2 addition in Figure 4.27 a. The shaded area indicates the uncertainty due to the spread of the reference lattice parameters. After one injection of PbI_2 solution into the $CsPbBr_3$ nanocrystal dispersion, i.e., 17% volume added, (25 ± 20)% of Br^- is replaced by I^-. After six additions, i.e., 100% volume added, (76 ± 17)% of Br^- is replaced.

This procedure has limited accuracy because of the uncertainty of the lattice parameters of pure $CsPbBr_3$ and $CsPbI_3$. Firstly, reported lattice parameters for $CsPbBr_3$ and $CsPbI_3$ were obtained from bulk material. They may therefore slightly differ for the actual nanocrystals due to the precise stoichiometry, the finite crystal size, the surface ligands [194], or differences in crystalline phase resulting from the particular synthesis [195]. The experimental values for $CsPbBr_3$ determined in this work (open dots in Figure 4.27 a) show a slightly lower spread than the literature values (blue diamonds), indicating that nanorods synthesized as described here show reproducible lattice parameters. More precise values for the exact crystal structure at hand could be obtained through high-resolution WAXS,

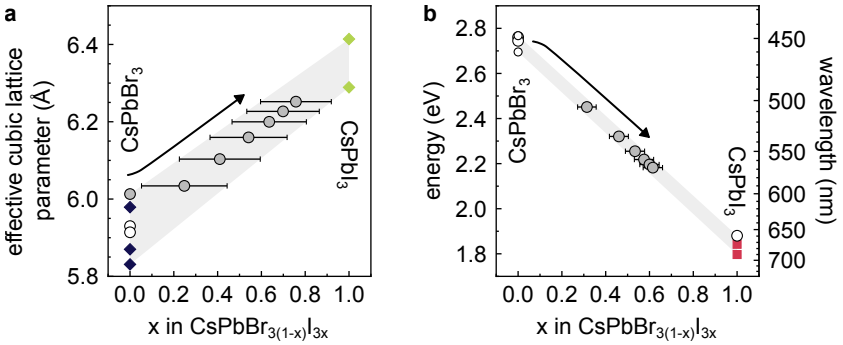

Figure 4.27: Derivation of halide ratio by Vegard's law for WAXS and PL. a, Effective cubic lattice parameter $a_{\text{effective}}$ as a function of I/Br ratio x in $CsPbBr_{3(1-x)}I_{3x}$. Diamond symbols: literature values of pure $CsPbBr_3$ and $CsPbI_3$ given in Table A12. The lattice parameters are obtained from WAXS analysis in Figure 4.25 (open dots) and Figure 4.26 (gray dots). The values of x are calculated assuming a linear relationship between x and $a_{\text{effective}}$. The arrow indicates the temporal evolution to a final value of $x = (76 \pm 17)\%$ via six additions of PbI_2. Uncertainties arise mainly from the variation in the lattice parameter of the pure substances. **b**, PL emission energy E and wavelength λ as a function of I/Br ratio x. Red squares: literature values for $CsPbI_3$ nanocrystals. Open dots: measured values for 3ML $CsPbBr_3$ nanorods and $CsPbI_3$ nanocrystals as detailed in the text. gray dots: Evolution of the PL emission energy via six additions of PbI_2. The values of x are obtained assuming a linear relationship between x and E.

TS, or PXRD of the unmodified $CsPbBr_3$ nanocrystals and directly synthesized $CsPbI_3$ nanocrystals. This would allow a more precise determination of the I/Br ratio.

An approximately linear dependence of the PL emission energy on the Br/I ratio has been reported in literature [419]. Vegard's law is therefore also applied to the spectroscopy data. Here, the I/Br ratio x is inferred from the PL emission energy, as shown in Figure 4.27 b. The emission energy (or wavelength) of 3ML nanorods observed in this work for standard synthesis concentrations (c_0 to $5\,c_0$) shows only a small spread, which is mainly related to variations in nanorod length (see Figure A8). Also the reported and measured emission energies of $CsPbI_3$ nanocrystals deviate by less than 4%. As a consequence, the values of x for the mixed $CsPbBr_{3(1-x)}I_{3x}$ nanocrystals obtained from this linear relationship show very low uncertainty. After one injection of PbI_2 solution $(31.4 \pm 4.2)\%$ of Br^- is replaced by I^-. After six additions, i.e., 100% volume added, $(60.0 \pm 4.4)\%$ of Br^- is replaced.

These values differ considerably from the results obtained from WAXS data. The applicability of the relationship between I/Br ratio and PL emission energy is therefore limited. Firstly, emission energies for small nanocrystals such as the 3ML nanorods studied here crucially depend on the degree of quantum confinement, which is mainly governed by the smallest dimension. Care must therefore be taken that the calibration spectra of pure $CsPbBr_3$ and $CsPbI_3$ are measured from particles of identical size and anisotropy. Only then can one separate the effects of confinement and ion substitution. Secondly, the dependence of emission energy on I/Br ratio may be intrinsically nonlinear: In reference [419] Vegard's law overestimates the PL peak energy for several given Br/I ratios. For mixed semiconductor materials the optical bandgap can follow a nonlinear dependence on composition, a phenomenon known as band bowing. Computational studies, however, suggest a small effect of bowing in mixed halide LHPs [420]. Diffraction and spectroscopy experiments on methylammonium-based mixed halide perovskite show the existence of a miscibility gap at intermediate I/Br ratios and a nonlinear evolution of the emission wavelength in this range [421]. Cs-based mixed halide LHP nanocrystals may be kinetically trapped in metastable structures, as suggested by a series of PDF refinements at different I/Br ratios [186]. Mixed halide nanocrystals could show a spatially heterogeneous anion distribution,

either transiently or permanently, due to incomplete interdiffusion [202]. In such a structure, emission would be dominated by the iodide-rich lower bandgap domains, leading to a redshift. This phenomenon is well known as a consequence of halide segregation during photon absorption or current injection in mixed halide perovskites [212]. Considering these complex relationships between ion ratio, local composition, optical bandgap, and emission wavelength, the laws governing the structure and optoelectronics of mixed halide LHP nanocrystals certainly warrant further investigation.

4.1.5.3 SAXS of the post-synthetic modification

To conclude the present study of post-synthetic modification of LHP nanocrystals, in situ SAXS data were analyzed to reveal potential changes of the nanocrystal morphology. Particle growth, aggregation or coalescence may occur in response to salt addition, due to exchange of material or a change of the electrostatic colloidal interactions (see Section 2.2). The SAXS data of both $PbBr_2$ enhancement and PbI_2 ion exchange reactions are shown in Figure 4.28.

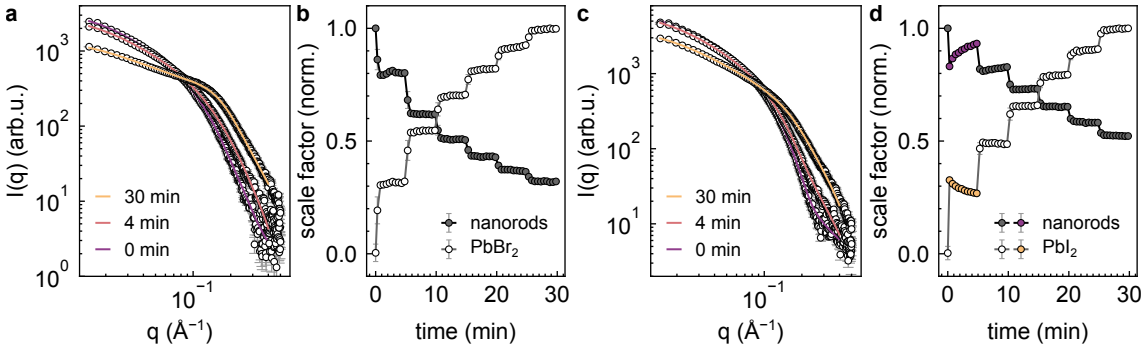

Figure 4.28: Evolution of SAXS intensity during post-synthetic modification. **a**, Selected in situ SAXS intensities of the 3ML nanorod sample before addition of $PbBr_2$ (0 min), after one (4 min) and six additions (30 min). **b**, Evolution of the scale factors of nanorods and $PbBr_2$ micelles in the SAXS model. **c**, Selected in situ SAXS intensities for addition of PbI_2. **d**, Evolution of the scale factors of nanorods and PbI_2 micelles.

For both $PbBr_2$ and PbI_2 addition (Figure 4.28 a and Figure 4.28 c) a change of the intensity from the characteristic, decaying form factor of freely suspended, rod-like nanocrystals (purple lines) to a more peaked signal (yellow lines) is observed. The rise of the peaked signal indicates a strong contribution of the respective salt solutions to the SAXS intensity, as found above for WAXS. Indeed, the signals of the salt solutions are dominated by a peak at 0.132 and 0.138 Å^{-1}, respectively (see Figure A12 c). This resembles $PbBr_2$ precursor micelles in toluene, analyzed in Figure 4.8. The intensities are well described by a model of spherical micelles interacting with a hard sphere structure factor. Both $PbBr_2$ micelles and PbI_2 micelles in n-hexane have a core and shell diameter of 1.4 nm and 3.6 nm, respectively. The nanocrystals are modeled as freely dispersed, polydisperse ellipsoids with average dimensions of $1.2 \times 1.2 \times 8.2$ nm^3 and $3.0 \times 3.0 \times 8.2$ nm^3 for the two syntheses. All fit parameters are given in Table A13.

This two-component SAXS model is used to analyze the temporal evolution of the scale factors and potential size changes of the nanocrystals due to ion incorporation. The scale factors, corresponding to volume fractions of the components on a common but arbitrary scale, are shown in Figure 4.28 b and Figure 4.28 d. Overall, $PbBr_2$ and PbI_2 addition show

a similar behavior. The volume fraction of nanorods decays stepwise while the volume fraction of PbX_2 salt micelles increases.

A notable difference between $PbBr_2$ and PbI_2 occurs after the first injection. For PbI_2 addition the PbI_2 volume fraction decays again after an initial overshoot (orange dots in Figure 4.28 d). This indicates that part of the PbI_2 micelles added at this stage (21% by volume) are dissolved in the process. Such a decay is not observed for $PbBr_2$. Simultaneously, the mixed halide nanocrystals occupy 16% more volume by taking up the released ions, and the scale factor increases accordingly (purple dots in Figure 4.28 d). The process follows a first order exponential law with a time constant of (1.8 ± 0.2) min. A similar effect, although much less pronounced, is observed after the second injection of PbI_2. No such response is detectable for the addition of $PbBr_2$ micelles, indicating that the passivation of surface defects has no significant influence on the nanocrystal volume.

No improvement of the fits could be achieved for either of the reactions when allowing an explicit size increase of the nanocrystals. This shows that the structural changes during post-synthetic modification occur mainly at the atomic scale and leave the nanocrystal morphology unaltered, with the exception of a small volume increase in response to the first PbI_2 additions (see Q3). A potential change of the structure factor of the LHP nanocrystals (from freely dispersed to more closely interacting) by the salt addition was not further investigated. Taking into account the absence of peaked signals at $q < 0.1\,\text{Å}^{-1}$ in the initial and final SAXS data, it is considered unlikely.

More detailed titration studies, as recently carried out for LHP quantum dots with $BiBr_3$ [422] or InP quantum dots with $ZnCl_2$ [423], would be required to fully elucidate the role of the reverse micellar structure of the salt solutions on the delivery of ions to the nanocrystals. In particular the effect of diffusion of ions through a ligand (double) layer, compared to a homogeneous solvent, could be investigated. Optimized ligand/solvent combinations for improvement of PLQY and better controlled ion exchange may be derived from such experiments. The dominant effect of bromide surface vacancies suggests that lead-free salt solutions, such as oleylammonium bromide solution, may be more efficient additives for post-synthetic modification [424]. Furthermore, the initial suppression and later recovery of PL intensity upon ion exchange requires further investigation. The improvement of the R_w values for a PDF model of orthorhombic $CsPbBr_3$ after one addition of salt solution suggests that a significant structural change occurs on short length scales (3 to 20 Å). More advanced in situ PDF analysis with data at higher resolution could reveal the relevant changes in the local environment of the lead atoms, such as a change of tilt or a release of strain following ion incorporation. Structural results could serve as an input for DFT calculations. In this way, the origin of the (opto)electronic properties of these very small nanocrystals with a heterogeneous composition could be better understood.

In summary, this chapter provides a detailed study of LHP nanocrystal synthesis ranging from the initial precursor structures in solution via nanoclusters and mesophases as reaction intermediates towards post-synthetic modification by salt solutions. Several experimental methods (SAXS, WAXS, TS and PL spectroscopy) were used in combination to establish the temporal and causal relationships between nanocrystal anisotropy, (meso)crystalline structure, and light emission.

4.2 Lamellar intermediates in the synthesis of Cu nanospheres

This chapter is partly based on the findings presented in reference [144].

Mantella, V. (*), Strach, M. (*), **Frank, K.**, Pankhurst, J. R., Stoian, D., Gadiyar, C., Nickel, B. and Buonsanti, R. Polymer Lamellae as Reaction Intermediates in the Formation of Copper Nanospheres as Evidenced by In Situ X-ray Studies. *Angew. Chem. Int. Ed.* 59, 11627–11633 (2020). doi: 10.1002/ange.202004081

(*) equal contribution

Abstract

This chapter is focused on the role of intermediates with lamellar structure in a copper nanocrystal synthesis. The synthesis of monodisperse copper nanospheres involves a heteropolymer consisting of alternating metal precursor and phosphonate ligand molecules. Building on results from in situ WAXS and XANES experiments carried out prior to this work by the group of Prof. Dr. Raffaella Buonsanti (EPFL Lausanne), **I conducted laboratory in situ SAXS experiments and analyzed the temporal evolution of form and structure factors**. After publication of the associated paper [144] **I reanalyzed the SAXS data for presentation in this thesis** with improved data processing and fitting routines. A less invasive cosmic background removal strategy increased the time resolution six-fold, i.e., to 10 s. Time- and temperature resolved SAXS analysis reveal the conditions for the formation of lamellar intermediates and spherical nanocrystals. A quantitative analysis of the structure factor shows a dense packing during nanocrystal growth. The lamellae most likely serve as reaction hotspots for the heating-induced reduction of precursor and are fully transformed in the growth process.

4.2.1 Synthesis and characterization of Cu nanospheres

The copper nanosphere synthesis studied here requires heating, stirring, the use of organic solvents, and a protective N_2 atmosphere. Typically, a reaction volume between 10 and 20 mL is used for in situ experiments. A shape-adapted glass reaction cell has been developed by the group of Prof. Dr. Raffaella Buonsanti (EPFL Lausanne) prior to this work. Details are given in Figure 3.1 and in references [144, 145] in the respective Supplementary Information. A second copy of the cell was developed and built by the glass workshop of LMU after the in situ experiments shown in this thesis were completed.

The synthesis is described in detail in Section 3.1.2. In short, spherical Cu nanocrystals are synthesized by adding copper (I) acetate (Cu(OAc)) to trioctylamine (TOA), followed by addition of tetradecylphosphonic acid (TDPA) powder while under vigorous stirring and gentle N_2 flow (see Table 3.1). The reaction is initiated by starting a heating ramp to 180 °C at 4 °C/min, shown in Figure 4.29 a, followed by a temperature plateau at 180 °C for 30 min. The second temperature ramp to 270 °C at 5 °C/min leads to the formation of Cu nanocrystals. After cooling down, the product is extracted by centrifugation in an ethanol/n-hexane mixture and resuspended in anhydrous n-hexane.

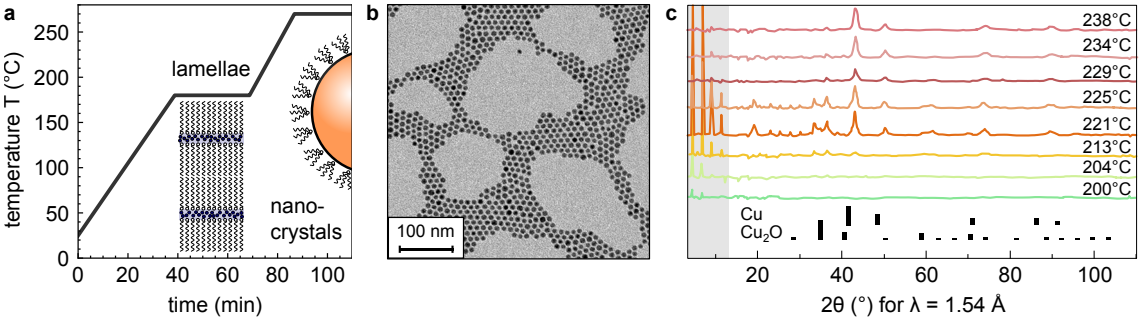

Figure 4.29: Synthesis scheme and characterization of Cu nanospheres. **a**, Temperature ramp. The insets illustrate the lamellar intermediate of TDPA and Cu ions during the 180 °C temperature plateau and the formation of nanocrystals upon further heating. One spherical Cu nanocrystal with a final diameter of 8 nm and TOA ligands are drawn to scale. **b**, TEM of Cu nanospheres with low polydispersity obtained as the reaction product. **c**, In situ WAXS patterns at selected times during the transformation from lamellar intermediates (reflections in the shaded area at low angle) to Cu via Cu_2O. Crystalline reflections appear slightly shifted compared to the reference positions due to an offset of the sample center along the X-ray beam. Figure adapted from [144] with permission. Copyright 2020, John Wiley and Sons.

TEM images (Figure 4.29 b) show highly monodisperse, spherical nanocrystals with (8.08 ± 0.34) nm diameter as the product. In situ XANES and WAXS measurements were carried out prior to the SAXS experiment[2]. Both techniques (WAXS shown in Figure 4.29 c) reveal a transformation of Cu^I to Cu^0 during the second temperature ramp and the formation of crystalline Cu via Cu_2O as an intermediate. In the WAXS data a lamellar intermediate phase is identified by the presence of sharp Bragg reflections. These are spaced at regular intervals, which correspond to a *d*-spacing of 3.85 nm. The lamellar intermediate is found to be consisting of Cu ions surrounded by TDPA ligands in a coordination polymer [144]. Due to the large minimal scattering angle of the WAXS experiment, however, the first diffraction order of this lamellar phase was not observed, and no small-angle signal indicative of nanocrystal formation could be detected. Nanocrystal formation was, at this stage, only inferred by inspection of the Cu Bragg reflections in the wide-angle scattering data. These

[2]The term *WAXS* is used here for a measurement in solution for consistency. Reference [144] refers to the data as in situ *XRD*.

peaks appear strongly broadened compared to the resolution-limited reflections of the lamellar intermediate phase, which indicates a nanocrystalline material (see Equation 2.39).

4.2.2 In situ SAXS of the transition from lamellae to nanocrystals

To detect the nanocrystal formation and to further clarify the structure of the lamellae, the in situ synthesis was repeated with the identical reaction cell placed in the laboratory SAXS setup (see Figures 2.17 and 3.1 and Table 3.6). Selected SAXS data as a function of time are shown in Figure 4.30 a. A time resolution of 10 s is achieved by selective masking of cosmic background events in the data, as detailed in Section 2.4.5.

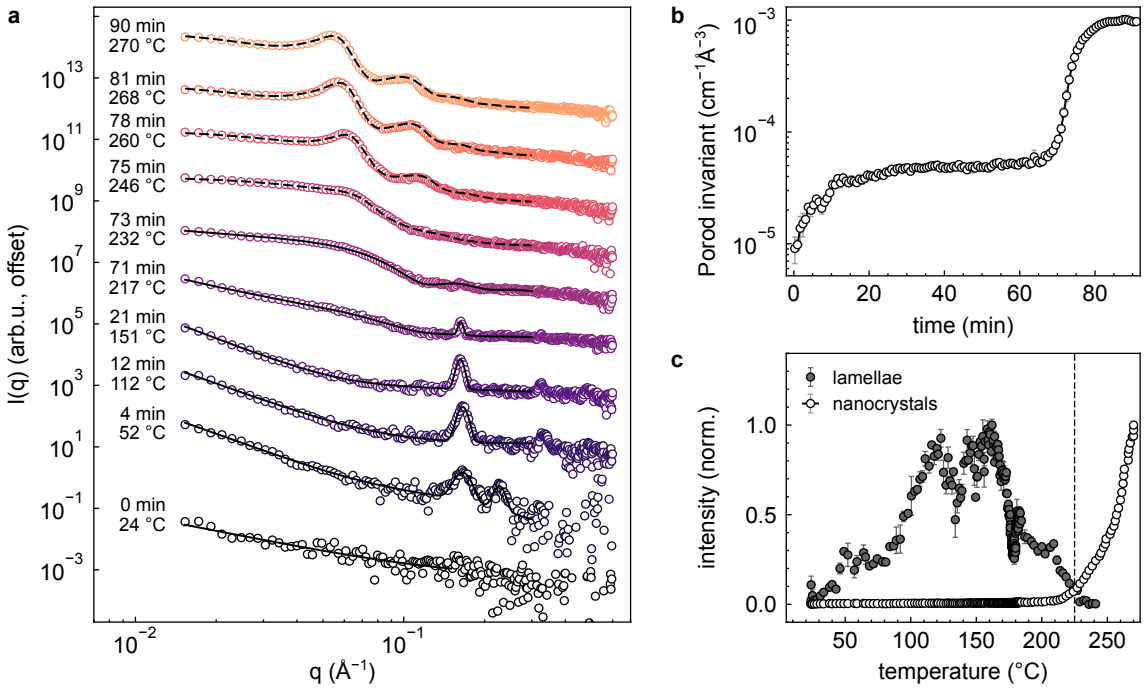

Figure 4.30: SAXS data and phenomenological analysis of the transition from lamellae to nanocrystals. **a**, Dots: Selected in situ SAXS data. Curves and associated temperatures represent 1 min averages. Dashed lines: Fits with a model of spherical nanocrystals with a hard sphere structure factor. Solid lines: Fits with a sum of a power law and Gaussian peaks for the signal of the lamellae. **b**, Porod invariant extracted from the data shown in **a** as a function of time, indicating a two-step behavior of the scattering contrast. **c**, Signal of the lamellae and the growing nanocrystals from **a** as a function of temperature. A vertical dashed line at 225 °C indicates the crossover of intensities.

At the beginning of the reaction before heating (time $t = 0\,\text{min}$) only a weak SAXS intensity is observed, resembling a power law decay $q^{-\alpha}$, $\alpha = 1.7 \pm 0.4$. The relatively large uncertainty of the exponent α complicates the interpretation. By comparison to Equation 2.27 a surface fractal can be excluded: A surface fractal dimension $d_s > d = 3$ would be unphysical. Instead, the intensity could originate from a mass fractal with approximately $d_f \leq 2$. Mass fractals of linear swollen polymers in a good solvent in particular show an exponent $\alpha = 1.7$ [327], close to the observed value. This suggests that initially the aliphatic chains of TDPA and TOA are well intermixed and dominate the intensity.

During the first heating ramp and at slightly elevated temperatures (30 to 67 °C, Figure 4.30 a and Figure A14) two reflections at 0.165 and 0.227 Å^{-1} emerge. The first one corresponds

to a d-spacing of 3.83 nm, and thus comes from the lamellar intermediate. The fact that this intermediate is observed at lower temperature than in the in situ WAXS experiment might be due to differences in sample homogenization by stirring, as the lamellae are only poorly soluble [144, 145]. The smaller, incommensurate d-spacing of 2.77 nm of the second reflection suggests that a lamellar phase of only TDPA without metal ions shortly coexists, before homogenizing with the metal-containing lamellar phase at 60 °C. The observed spacing shows excellent agreement with a lamellar phase of TDPA powder, as well as of TDPA in TOA at 80 °C [144, Supplementary Information].

At later times and at temperatures between 50 and 160 °C, the SAXS intensity belonging to the metal-containing lamellae is amplified and the second and third diffraction orders become visible at 0.328 $Å^{-1}$ and 0.492 $Å^{-1}$, respectively. These positions correspond to integer multiples of the first observed peak position. This confirms a lamellar stacking, in which metal ions are separated by ligand bilayers. Simultaneously, there is a more pronounced increase of SAXS intensity at low q. Here the intensity does not yet show a plateau, but instead a power law decay. This signal likely results from the microphase separation of the reaction mixture into a lamellar, Cu-rich minority phase and a liquid, Cu-poor and TOA-rich majority phase by spinodal decomposition. This type of phase separation proceeds without a significant nucleation barrier and therefore results in interpenetrating phase regions with a self-similar structure across several length scales, as introduced in Sections 2.1 and 2.4.2. Such a fractal structure is again characterized by a power law in the SAXS intensity. The exponent $\alpha = (3.0 \pm 0.2)$ determined from the model matches both a mass fractal with $d_f = 3$ or a surface fractal of $d_s = 3$. Both are accurate descriptions of the interpenetrating structures characteristic of spinodal decomposition [263].

During the second temperature ramp from 180 to 270 °C the intensity of the lamellar peaks is weakened and the low-angle intensity forms a plateau-like signal. This feature is most pronounced at 73 min and 232 °C. The decrease of peak intensity indicates that the lamellar intermediate is now decomposed. The emerging intensity plateau shows that compact regions of high electron density contrast dominate the signal. Fits with a superposition of a power law, a spherical particle form factor, and the lamellar peak provides a good description of these data. These fits are shown for $t \leq 73$ min as solid black lines in Figure 4.30 a. The extracted scale factors are given in Figure 4.30 c. A more detailed decomposition of the signal at early times including the precursor signal is given in Figure A14.

The compact regions of high electron density leading to the dominant scattering contrast can be interpreted as inverse micelles containing Cu ions, surrounded by TDPA or TOA as ligands, or alternatively already as the nucleating Cu nanocrystals. A temporal correlation of SAXS with WAXS (or TS) signal with sub-10 s time resolution would be required to determine whether the material is already crystalline at this stage. Using the difference in scattering contrast of either Cu (I) acetate precursor or metallic copper with the majority phase in a SAXS analysis on absolute scale would not be enough to distinguish the species at this stage. The volume fraction and the scattering contrast enter the modeled spherical particle form factor as a product, as shown in Equation 2.21, and both are unknown.

For CdSe nanospheres a transformation of a lamellar intermediate species into inverse micelles has been suggested as the nucleation mechanism in literature [72]. The data shown here also suggest that a local segregation of Cu ions within "reaction hotspots" inside the lamellae takes place. More precisely, some lamellar signal remains visible while the intensity at low q begins to show a plateau representing compact particles. A "secondary" nucleation of particles outside of the lamellar minority phase cannot be excluded based on the SAXS

data alone, but is considered unlikely given the low size polydispersity of the product, as discussed below. The nature of the short-lived micellar intermediate as well as the precise duration of the nucleation and growth phases could be further investigated.

In the final stage of the reaction, i.e., at $t \geq 75$ min, the SAXS intensity is fully dominated by the signal of the growing Cu nanospheres and the lamellar reflection is absent. Between 75 and 90 min the plateau-like form factor signal of the nanospheres becomes modulated with structure factor oscillations, imprinted on the intensity as broad peaks. This signal is well described by a model of spherical nanocrystals with a hard sphere structure factor (black dashed lines), as introduced in Section 2.4.2. To reduce the number of free parameters the diameter of the hard sphere repulsion is set identical to the nanocrystal diameter. A second, larger sphere form factor is added as a background term. This improves the agreement of the fit at low q values and likely corresponds to the finite size of nanocrystal agglomerates. The volume fraction of nanocrystals obtained from the fit is between 0.21 ± 0.01 at 73 min and 0.42 ± 0.01 at 79 to 90 min. Exemplary fit parameters for 90 min are given in Table A14.

After nucleating from within the lamellar intermediate phase the nanocrystals grow in a locally dense environment, which probably acts in favor of a narrow size distribution due to the well-regulated supply of precursor. Also the balance of repulsion and vdW attraction of the as-formed nanocrystals (see Section 2.2) may act as a shape-determining and size-controlling force at this stage.

4.2.3 Quantifying the growth of lamellae and nanocrystals

To further quantify the course of the reaction, i.e., the sequence of lamellae formation and nanocrystal growth, the SAXS data were analyzed first by low-complexity techniques and then by more detailed structural models. Figure 4.30 b shows the Porod invariant Q, introduced in Equation 2.17 as a measure of scattering contrast. Q is obtained from the in situ SAXS data in Figure 4.30 a by numerical integration up to $q = 0.14\,\text{Å}^{-1}$, i.e., omitting the peak of the lamellar phase.

The temporal evolution of the Porod invariant clearly reflects the two-step behavior of the reaction as two plateaus. The first plateau corresponds to the separation of the lamellar minority phase from the TOA-rich majority ("solvent") phase. The second plateau represents the accumulation of high electron density contrast in the growing nanocrystals. Figure 4.30 c shows the normalized amplitude of the peak of the lamellar phase, extracted from the fits shown in Figure 4.30 a. Additionally, the intensity at $q_{min} = 0.015\,\text{Å}^{-1}$ is shown as a measure for the signal coming from the growing nanocrystals. A vertical dashed line at 225 °C indicates the temperature at which the nanocrystals begin to dominate the intensity. This temperature coincides with good accuracy with the temperature of 230 °C, at which reduction of the copper species has been observed by X-ray spectroscopy [144]. Therefore, precursor reduction and nanocrystal nucleation are found to occur simultaneously within the experimental accuracy.

A series of ex situ control experiments was carried out by the Buonsanti group to identify the roles of TDPA and TOA, as well as of the lamellar intermediate, by leaving out individual reagents. It was found that reactions with TOA alone lead to Cu nanocrystals as large as 500 nm with poor size control, and to the absence of the lamellar intermediate. Replacing TOA with 1-octadecene (ODE) stabilized the lamellar phase and did not lead to Cu nanocrystal formation. This observation was also corroborated by in situ SAXS

experiments, shown in Figure A15 a and b. In the presence of ODE instead of TOA only a minor increase of the Porod invariant during the second heating ramp is found. The intensity of the peak from the lamellar phase persists until the end of the reaction and no strong low-q intensity, characteristic of nanocrystals, is observed.

TOA is therefore found to be responsible for the reduction of the intermediate to metallic copper. It is essential for nanocrystal formation. Simultaneously, TOA acts as the main ligand on the surface of the final nanocrystals, which has been confirmed by by FTIR spectroscopy [144]. TDPA is mainly involved in the initial stage of the reaction as an integral part of the lamellar intermediate. Without it, monodispersity of the product is compromised. A well-defined lamellar intermediate is beneficial for a narrow size distribution of the final nanocrystals. This has been established by experiments varying the Cu(OAc):TDPA molar ratio, reaching an optimum at a 2:1 ratio.

The data in Figure 4.31 a show the temporal evolution of the lamellar phase during the reaction. Keeping the mixture at 180 °C for annealing leads to a significant increase of the lamellar peak height and to a moderate peak narrowing. This indicates an increase of the concentration of the lamellar phase and/or a growing domain size. Longer annealing times result in a more abundant lamellar phase and a higher yield of nanospheres [144]. This supports the claim that nanospheres indeed evolve only from within the lamellae.

In a follow-up study by the Buonsanti group, the length of the phosphonic acid molecule was varied from 4 to 14 carbon atoms [145]. Short-chain ligands lead to triangular plates similar to $Cu_{2-x}S$ nanosheets [74] whereas long-chain ligands produced spheres. Lamellae formed with short-chain ligands were found to be stable up to the reduction temperature, which lead to a templating effect.

Complementing the study of the intermediate, the SAXS intensity at low q after nucleation of the nanocrystals was analyzed here in further detail. This analysis is based on the fit of the in situ SAXS intensity, i.e., a model of form and structure factor of interacting spherical particles. Model curves are shown as dashed lines in Figure 4.30 a. The typical interparticle distance (center to center) is derived from the fit parameters using Equation 2.26 and its temporal evolution is shown in Figure 4.31 b.

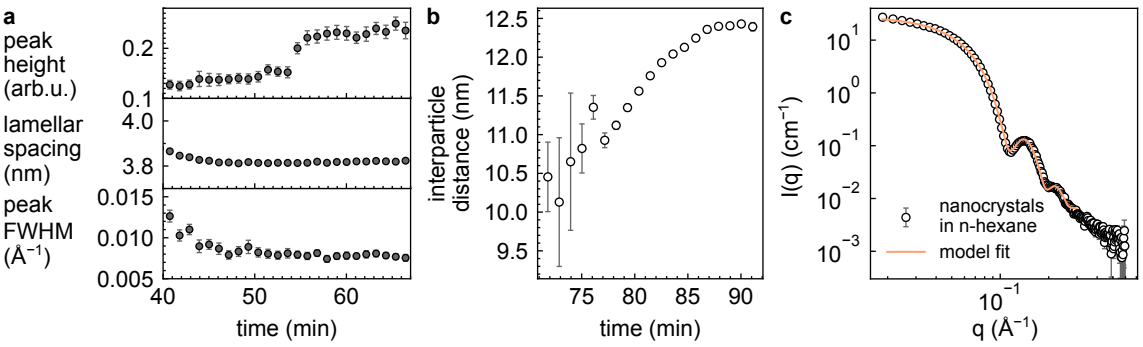

Figure 4.31: SAXS analysis of lamellae, growing nanocrystals, and purified nanocrystals. **a**, Peak height, lamellar spacing, and peak FWHM obtained from a fit of the SAXS signal of the lamellar phase. **b**, Typical interparticle distance of the growing nanocrystals in the final stage of the reaction, obtained from fits to the in situ SAXS data. **c**, Ex situ SAXS data of Cu nanocrystals purified and resuspended in n-hexane with a spherical model fit.

The typical interparticle distance follows a linear increase with slope $(0.14 \pm 0.01)\,\mathrm{nm\,min^{-1}}$ between 72 and 85 min. This increase is attributed to a significant growth of the nanocrystals while they are in close proximity. During this process, Cu precursor material,

which is locally enriched in the lamellae, is attached to the growing nanocrystals until it is depleted. As a result, the interparticle distance reaches a plateau at 12.4 nm. This value is 4.3 nm larger than the average nanocrystal diameter obtained from TEM. This discrepancy is plausible, considering that TOA molecules cover the nanocrystals as a ligand shell in the final product. The ligands are likely already bound to the nanocrystals during the final reaction stage and thus keep the metallic nanocrystal cores separated. The surface-to-surface spacing exceeds the length of two C8 chains of TOA (approx. 1.4 to 1.8 nm), and also of the longer C14 chains of TDPA (approx. 2.3 to 3.1 nm) [88]. The nanocrystals are therefore still far from a maximum packing density.

The size of the metallic nanocrystal cores was further characterized using ex situ SAXS on a purified and resuspended sample. The resulting SAXS intensity is shown in Figure 4.31 c. The strong structure factor oscillation imprinted on the form factor in the in situ data is now absent, as the nanocrystals are well dispersed. TOA ligands stabilize the metallic particles in n-hexane, which has the lowest polarity of all solvents used in this work (0.009 on the $E_T(30)$ scale, see Table A8).

A model of dilute spherical particles of $D = (8.06 \pm 0.03)$ nm diameter with a polydispersity of $\frac{\sigma_D}{D} = 6.7\%$ provides an excellent fit to the data. The obtained size is in very close agreement with the value measured in TEM images ($D = 8.08$ nm with $\frac{\sigma_D}{D} = 4.2\%$). Parameters are given in Table A15. Compared to ideal spherical particles with a sharp interface in this model the surface is modulated by convolution with a Gaussian function with 0.38 nm standard deviation (called "fuzziness" in the model, see Section 3.3.1). This improves the agreement with the data at large q. Since TOA ligands have a scattering length density between copper and solvent, the implied smoothing of the surface by the model may result from the ligand coverage, as simulated in Figure 2.19, or by minuscule deviations from the mean spherical shape.

The sharp oscillations visible in the SAXS intensity result from the narrow size distribution of the nanocrystals. The slightly elevated polydispersity obtained from SAXS compared to the TEM result likely results from an underestimation of the broadening due to the instrumental resolution function. The contributions to the instrumental resolution included in the model are given in Section 2.4.5. The copper nanospheres obtained by this synthesis show such a high uniformity that they may be used to test the model of the instrumental resolution by varying, e.g., sample-to-detector distance, sample length and pixel binning.

In summary, the transformation of a lamellar intermediate to copper nanospheres was characterized using laboratory in situ SAXS. Complementing the results from in situ WAXS, the low-angle signal of the nanospheres was additionally analyzed and revealed a dense local environment during nanocrystal growth. Furthermore, the size and homogeneity of the purified nanospheres were confirmed via ex situ SAXS.

4.3 One-pot self-assembly of CuPd nanocrystals into supercrystals

Part of the results shown in this chapter have been published in reference [392].

Derelli, D. (*), **Frank, K.** (*), Grote, L., Mancini, F., Dippel, A.-C., Gutowski, O., Nickel, B., and Koziej, D. Direct Synthesis of CuPd Icosahedra Supercrystals Studied by In Situ X-Ray Scattering. *Small*, 2311714 (2024). doi: 10.1002/smll.202311714

(*) equal contribution

Preprint: doi: 10.26434/chemrxiv-2023-shx8j

Data repository: doi: 10.5281/zenodo.10138086

Abstract

This chapter shows the use of simultaneous in situ SAXS and TS to study the synthesis and assembly of CuPd nanocrystals. The synthesis was developed in the group of Prof. Dr. Dorota Koziej (UHH). The results were obtained using a custom-built in situ reaction cell based on a thin-walled borosilicate capillary and a dedicated beamline setup. **I contributed to the optimization of the cell and the setup. Furthermore, I analyzed the in situ SAXS data of the structural evolution of the nanocrystal metal core and of the ligand shell.** In this synthesis a defined heating and cooling ramp induces nucleation, growth, and supercrystalline assembly of the nanocrystals. **I investigated the assembly mechanism using detailed modeling of the in situ SAXS intensities.** The analysis shows that a lamellar ordering of ligand molecules triggers a two-step assembly pathway: Nanocrystals segregate into a dense, short-range ordered subphase, from which they assemble into fcc supercrystals. The OlAm and OlAc ligand molecules play a three-fold role: Firstly, they act as a viscous solvent for the metal precursors and the growing nanocrystals. Secondly, they stabilize the nanocrystals by forming a surrounding shell. Thirdly, they induce supercrystal formation upon cooling by expelling nanocrystals from their lamellar assembly. The results presented in this chapter highlight the effect of ligand molecules on structural intermediates during synthesis. Supercrystal assembly by segregation of nanocrystals from an ordering solvent is identified as a potential strategy for the one-pot fabrication of hierarchically assembled materials.

4.3.1 Synthesis of CuPd nanocrystals

For CuPd nanocrystal synthesis a precursor mixture of copper acetylacetonate ($Cu(acac)_2$) and palladium acetylacetonate ($Pd(acac)_2$) in OlAm, OlAc, and dioctyl ether (see Table 3.4) was prepared in an argon-filled glovebox. Details are given in Section 3.1.3. The precursor mixture, a blue liquid, was loaded in one of two custom-made reaction cells: The in situ cell designed by Davide Derelli (UHH), shown in Figure 3.2 (80 µL precursor volume), or the in situ cell developed in this work, presented in Section 3.2 (300 µL precursor volume). The mixture was then heated to 220 °C at 10 °C/min as shown in Figure 4.33 a. Nucleation and growth of nanocrystals start within two minutes after reaching the high temperature plateau. Time $t = 0$ min was chosen as the time at which $T = 220$ °C is reached. After 30 min at 220 °C the mixture was cooled down to 100 °C to induce the directed self-assembly of the as-formed nanocrystals into supercrystals.

The in situ synthesis was carried out in the second experimental hutch EH2 of the high-energy beamline P07 at PETRA III, DESY, Hamburg with an X-ray energy of 103.2 keV (see Section 3.3.1) [310]. A schematic illustration of the simultaneous in situ recording of SAXS and WAXS/TS is given in Figure 4.32. The rather high X-ray energy, far above the absorption edges of the involved metals, was chosen to achieve a large q_{max} for PDF analysis. The energy-dependent interaction cross sections for CuPd are given in Figure 3.2 c. First, the analysis of the nucleation and growth phase is presented, followed by the investigation of the self-assembly process.

4.3.2 In situ SAXS and TS of nucleation and growth

4.3.2.1 Conversion of precursor to nanocrystals

The intensity from the WAXS/TS detector is analyzed for a first identification of the forming nanocrystalline structures. Selected TS data from the nucleation and growth phase of nanocrystals are shown in Figure 4.33 b after subtraction of the solvent background (OlAm, OlAc and dioctyl ether under identical conditions). At room temperature ($t = -20$ min) broad oscillations extending to large q values are visible in the data. This signal is the characteristic signature of the molecular precursors. The chemical evolution of the precursors during synthesis is subject of a separate TS-PDF and XANES study by the Koziej group, currently in preparation.

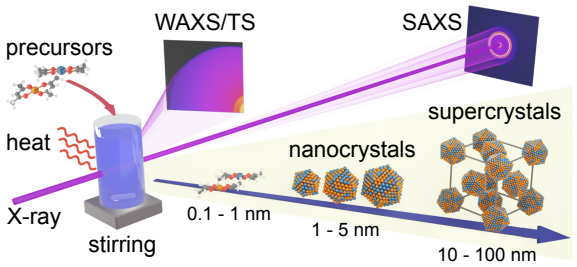

Figure 4.32: Illustration of the simultaneous SAXS and TS experiment. A precursor mixture is heated and stirred in the in situ reaction cell. The WAXS/TS and SAXS signals are recorded simultaneously. Information about the structure on the atomic scale as well as on the nanometer scale, ranging from nanocrystals to supercrystals, is obtained. Orange: Cu, Blue: Pd. Figure adapted from [392] with permission. Copyright 2024, John Wiley and Sons.

During the temperature plateau at 220 °C a series of rather broad reflections emerges in the data, indicating the formation of nanocrystals. The peak positions cannot be uniquely assigned to the expected peak positions for the Cu or Pd metals, which both have fcc structure with slightly different lattice constants ($Fm\bar{3}m$, COD 9008468 and 9008478, respectively [339]). This indicates that both metals participate in the nanocrystal formation. Also a simple assignment of the peak positions by Vegard's law (see Equation 2.6) of a Cu/Pd mixture does not fully explain the pattern. A more detailed structure determination is given in the following section. After 5 min at 220 °C the TS signal remains constant, showing that the nanocrystal formation is completed.

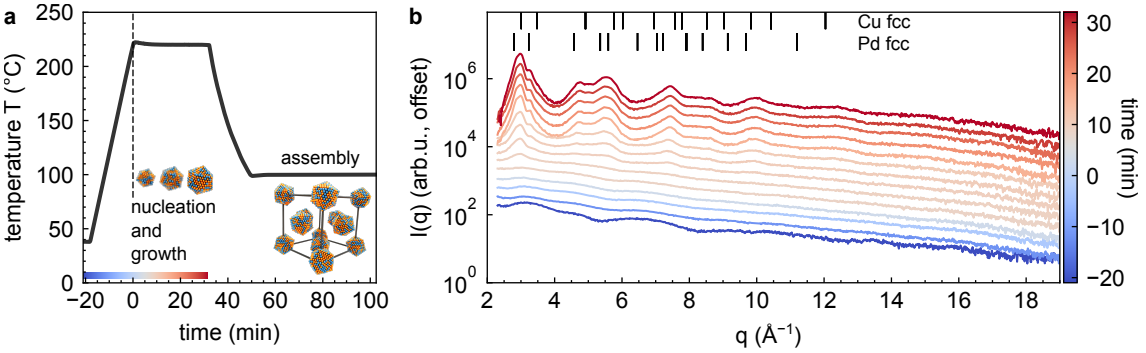

Figure 4.33: Temperature ramp and temporal evolution of the TS data during CuPd nanocrystal synthesis. **a**, Temperature ramp used for the synthesis of CuPd nanocrystals. The vertical dashed line indicates $t = 0$ min when the plateau at 220 °C is reached. The color gradient shows the initial phase of precursor dissolution and nanocrystal nucleation and growth. The 100 °C temperature plateau for supercrystal assembly is also shown. In the insets orange atoms are Cu, blue atoms are Pd. **b**, Background-subtracted in situ TS data obtained during the initial phase shown in **a**. Expected peak positions for Cu and Pd are shown as vertical dashes for a maximum Miller index of 4.

The time-resolved TS data are transformed to the reduced PDF $G(r)$, shown in Figure 4.34 a. The short-ranged structure of the precursor is visible as a decaying oscillation with a peak at 2.0 Å (dark blue curve). The signal of the forming nanocrystals shows clear oscillations beyond 15 Å, representative of their crystalline structure (dark red curve).

Figure 4.34 b shows the simultaneously recorded in situ SAXS data. A broad peak at 0.24 $Å^{-1}$, characteristic of the precursor mixture, is observed at $t < 0$ min (dark blue curve) and is soon overshadowed by a rising intensity contribution at low q (dark red curve). The rising intensity represents the form factor of the growing nanocrystals. A pronounced minimum at 0.23 $Å^{-1}$ and a second maximum at 0.3 $Å^{-1}$ in the SAXS data give a first indication of the rather narrow size distribution of the nanocrystals.

4.3.2.2 Evolution of the core structure

Before a detailed analysis of nanocrystal growth, first the structure of the nanocrystalline metal core is described. The analysis of the core structure was carried out by Davide Derelli, with details given in references [392, 425]. The core structure was investigated using PDF analysis of the in situ data at $t = 10$ min, i.e., obtained after completion of the growth phase. Furthermore, HRTEM micrographs (Figure 4.35 b and c) and EDX mapping of the purified reaction product contributed to the structural model of the core. EDX revealed an elemental composition of the final nanocrystals of Cu:Pd = 60:40, in close agreement with the molar precursor ratio of 65:35.

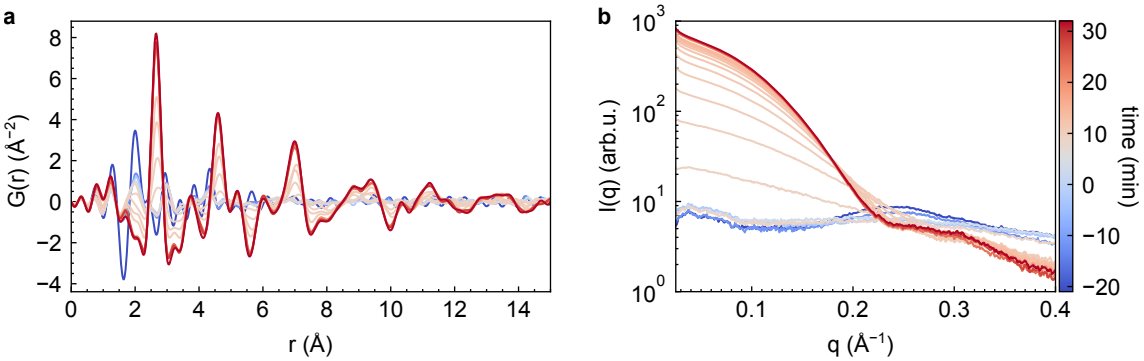

Figure 4.34: Evolution of PDF and SAXS during the high temperature plateau. **a**, PDF obtained from the TS data shown in Figure 4.33 b. A weakening of the precursor signal (blue curves) is followed by the emergence of pronounced peaks (red curves), indicating the formation of nanocrystals. **b**, Simultaneously recorded in situ SAXS data, showing the increase of the nanocrystal form factor. Reaction time is shown with a common color bar. Figure adapted from [392] with permission. Copyright 2024, John Wiley and Sons.

The analysis of the PDF was based on the cluster-mining procedure [356]. A conventional refinement with the attenuated crystal approximation, as introduced in Section 2.4.4 and used for the other syntheses in this work, was unsuccessful for the CuPd nanocrystals. In the cluster mining procedure $G(r)$ of a set of nanoclusters in the shape of spheres, octahedra, decahedra, and icosahedra was simulated based on the position of individual atoms, and compared to the data. The best-fitting structure was further refined using a Monte Carlo procedure, which adjusts individual atomic positions. The best fit was obtained with a model of icosahedral nanoclusters with seven shells, i.e., 923 atoms, and a random occupation of the atomic sites with Cu or Pd. The corresponding fit is shown in Figure 4.35 a. The icosahedral cluster structure shows a five-fold twin boundary in the cluster core, where the 20 tetrahedral domains come into contact. This structural feature was found essential for explaining the observed PDF data.

The time-resolved PDF data are shown in Figure 4.35 b. Cluster mining reveals the presence of icosahedral CuPd clusters as early as 1.7 min after reaching 220 °C. The number of shells of the best-fitting cluster N_{shells}, and thus the number of atoms in the cluster, follows a stepwise increase from five to seven shells, i.e., from 309 to 923 atoms. The final size of the metallic nanocrystal core is 3.2 nm, which corresponds to the diameter enclosing the entire icosahedron. Also in HRTEM images, shown in Figure 4.35 c and d, the characteristic arrangement of the lattice planes of a twinned icosahedral crystal can be identified. It remains unclear whether the growth actually occurs step-wise via several "magic" sizes. This is due to the limited time resolution of the present data as a consequence of the low scattering contrast of small clusters, and the size polydispersity.

A control experiment using only $Cu(acac)_2$ precursor lead to the formation of freely dispersed spherical nanocrystals with a bimodal size distribution (4.4 nm and 40 to 50 nm diameter). A synthesis with only $Pd(acac)_2$ precursor produced dense agglomerates of approximately 3.2 nm diameter Pd nanocrystals. The corresponding SAXS data of both syntheses are shown in Figure A16. These results indicate that the ratio of metal precursors of 60:40 (65:35 by precursor amount) is a local optimum regarding nanocrystal polydispersity, since the reduction rates of the two metal species are carefully balanced.

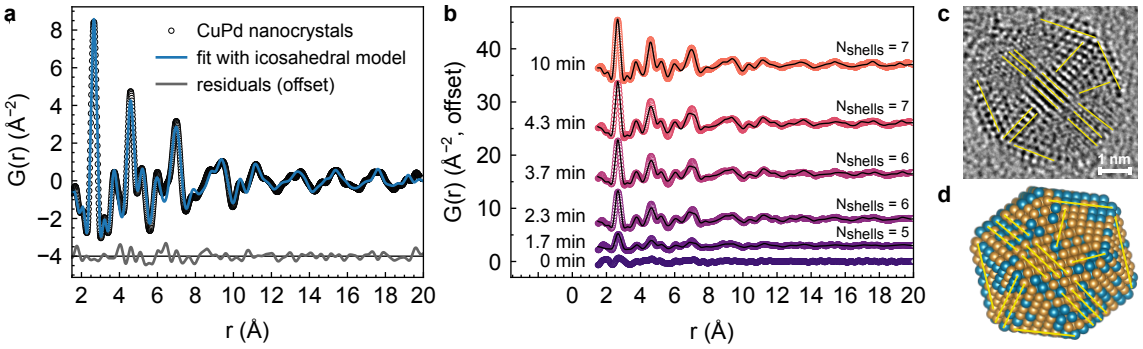

Figure 4.35: Determination of the nanocrystal core structure via PDF and HRTEM. a, PDF of the reaction mixture at $t = 10\,\text{min}$ (open dots). Fit with an icosahedral cluster model (blue line) with seven shells ($R_w = 0.151$). **b**, PDF of the reaction mixture at selected times during the beginning of the 220 °C plateau. Solid black lines indicate fits to the data using icosahedral cluster models with an increasing number of shells. **c**, HRTEM image of a CuPd nanocrystal from the purified reaction mixture. Yellow lines show the characteristic projection of lattice planes in a twinned icosahedral nanocrystal. **d**, Sketch of an atomic model of an icosahedral CuPd cluster. Orange: Cu, Blue: Pd. Yellow lines are placed as in **c** to illustrate the similarity. **b, c, d** adapted from [392] with permission. Copyright 2024, John Wiley and Sons.

4.3.2.3 Evolution of the nanocrystal size

Knowing the icosahedral structure of the metallic nanocrystal core, the simultaneously recorded SAXS and TS data can be further analyzed. The size of scattering objects affects the observed patterns at small and wide angles in different ways: At large scattering angles, a smaller crystallite size leads to wider Bragg reflections (see Section 2.4.3). Small, disordered, or twinned structures produce broad intensity oscillations. Meanwhile at smaller angles a smaller size shifts the decaying form factor curve and its minima to larger q (see Section 2.4.2). Consequently, a quantitative change of the SAXS pattern is expected to accompany the growth trend of the nanocrystal cores extracted from the TS signal.

Selected SAXS data of the growth phase of the synthesis are shown in Figure 4.36 a for the same times as the PDF data in Figure 4.35 b. A model of polydisperse spherical particles, shown as black solid lines, is in very good agreement with the data at $t > 1\,\text{min}$. The signal from the precursor ($t = 0\,\text{min}$) is only weakly dependent on q. It is therefore omitted in the model to avoid overfitting, and instead a constant background component and a power law term are included. The full model equation is given in Section 3.3.1.

The parameters resulting from the fit with the polydisperse sphere model are shown in Figure 4.36 b and c as red dots. A continuous increase of particle diameter D is observed, and simultaneously the relative polydispersity $\frac{\sigma_D}{D}$ decreases. The scale factor from PDF analysis is additionally shown in Figure 4.36 c to illustrate the increase of the signal attributed to the nanocrystals. After 5 min the relative polydispersity reaches a plateau at 13.5%. The final particle diameter of 3.9 nm is reached at 10 min.

This value exceeds the core diameter obtained by PDF, shown as blue dots, by approximately 0.7 nm. This deviation results from the different sensitivity of the PDF- and the SAXS analysis. Since the PDF analysis focuses on modeling the metallic core, it takes into account the intensity oscillations originating from interatomic distances between metal atoms. These oscillations extend to large q values and are visible as peaks in $G(r)$. Contributions of more weakly scattering or more disordered components to $G(r)$, such as the inorganic ligand shell around the nanocrystals, are not as sharply peaked, and thus

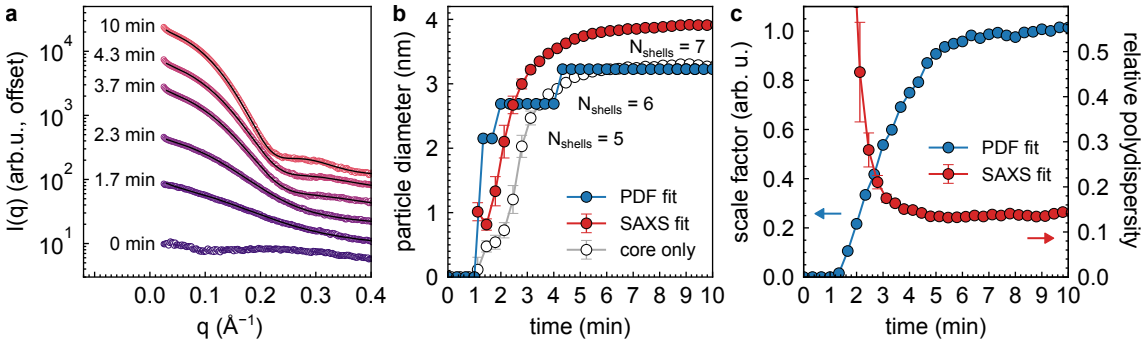

Figure 4.36: Evolution of the nanocrystal size via SAXS and PDF. a, Selected in situ SAXS data of the nucleation and growth phase, times as in Figure 4.35 d. Solid lines are fits to the data with a polydisperse sphere model. **b**, Particle diameters as a function of time obtained from PDF and SAXS analysis. The icosahedral cluster model of the PDF (blue dots) assumes discrete sizes with an increasing number of shells, whereas the spherical SAXS model (red dots) shows a continuous growth and yields a larger radius due to a contribution from the ligand shell. The core diameter of a SAXS model with a separate core and shell (open dots) leads to a better agreement with the PDF result at later times. **c**, PDF scale factor as a measure of the amount of nanocrystals, and relative particle polydispersity obtained from the SAXS fit. Figure adapted from [392] with permission. Copyright 2024, John Wiley and Sons.

overshadowed, especially at large q values. In the present analysis organic components were therefore not explicitly included in the PDF model.

Contrastingly, the SAXS intensity arises from any variation in SLD on the length scale between approximately 1 and 40 nm for the present q range. SLD is proportional to electron density (see Equation 2.16). Values for the different components in the sample are given in Table 3.7. Although the electron-dense nanocrystal core provides the dominant contrast with respect to the surrounding organic solvent molecules, the densely packed ligands forming a shell around the metallic core likely act as a layer of intermediate contrast. The ligand shell therefore affects the seen in the SAXS analysis.

The model for the SAXS intensity can incorporate an electron-dense core and a shell of radially decaying scattering contrast. The resulting SLD profile is shown in Figure A17 a and the model equations are given in Section 3.3.1. The core diameter obtained from this model, shown as open symbols in Figure 4.36 b, closely matches the PDF result at times ≥ 3 min, when the ligand shell is likely already fully formed. At earlier times the PDF result is underestimated by the SAXS model, since the shell may not yet be fully intact.

The exact SAXS intensity of an icosahedral cluster based on the atomic coordinates from PDF analysis is shown for comparison in Figure A17. The resulting curve closely resembles the signal from a sphere of equal volume as the icosahedron. It does not provide good agreement with the SAXS data, as it essentially underestimates the size and polydispersity.

JMAK and Gualtieri rate models can be used to extract nucleation and growth rates from the SAXS and PDF scale factors (see, e.g., Equation 2.4). The corresponding fits are given in Figure A18 and Table A16. Both models show especially good agreement with the scale factors extracted from PDF analysis and slightly poorer agreement with the SAXS scale factors. This is mainly due to the fact that the SAXS analysis is rather ambiguous during the earliest nucleation stages, when metal core and ligand shell provide a comparable contrast. Gualtieri analysis of the PDF scale factor yields consistent growth rates $k_g = 0.54\,\mathrm{min}^{-1}$ and a standard deviation of nucleation time b between 0.7 and 1 min, independent of the growth exponent n. Both nucleation and growth of this synthesis

therefore occur on the timescale of minutes (see Q2), which makes further studies with laboratory X-ray sources feasible.

Summarizing the results of TS and SAXS analysis for the nucleation and growth phase similar growth trends are found for both techniques. The size parameters slightly deviate due to the different bias (or focus) of the underlying models. The discrepancies can be reconciled by adding a soft shell of organic ligands to the inorganic nanocrystal cores as a layer of radially decaying contrast in the SAXS model. The existence of a shell or a clear value for its thickness cannot be directly inferred from the SAXS analysis at this stage of the reaction. The presence of a shell is, however, further corroborated by FTIR spectroscopy measurements, shown in Figure A19. Detection of a ligand shell via SAXS will be further discussed below in the context of the interparticle spacing in an assembly.

4.3.3 In situ SAXS of supercrystal assembly and melting

4.3.3.1 Decomposition of the SAXS intensity

Once the growth phase of CuPd nanocrystals is completed, their self-assembly into supercrystals is initiated by lowering the reaction temperature to 100 °C. The corresponding SAXS intensity is shown as a 2D plot in Figure 4.37 a. Representative SAXS patterns are highlighted with dashed horizontal lines and are individually shown in Figure 4.37 b.

The SAXS intensity is decomposed into four separate components: Between 220 °C and 130 °C the form factor of the *freely dispersed nanocrystals* dominates the signal. As the mixture is cooled further, different peaked signals emerge in the intensity, highlighted by asterisks (*), an upward triangle (△), and two arrows, in the order of their appearance. Most importantly, the intense diffraction peaks visible after 20 min of the temperature plateau (arrows) indicate the formation of a *supercrystal*. Here, nanocrystals assemble in a close-packed fcc arrangement with a lattice constant of 10.24 nm. The detector image given as an inset to Figure 4.37 b shows approximately isotropic rings, indicating the presence of many individual supercrystals in random orientations.

Already before the supercrystal assembly two peaks at 0.16 and 0.32 $Å^{-1}$ are observed, suggesting that a *lamellar phase* with a d-spacing of 3.9 nm forms. This spacing matches the expected repeat distance of bilayers consisting of the OlAc and OlAm solvent molecules [84, 86] (see also Section 2.1.3). Few minutes before the supercrystal assembly a faint peaked signal becomes apparent in the SAXS patterns. In Figure 4.37 b it is highlighted with an upward triangle (△). It does not match any of the expected Bragg peak positions of the supercrystal, but can be well described by a model of the approximately spherical nanocrystals interacting with a hard sphere structure factor (see Section 2.4.2). This intensity component describes *short-range order (SRO) of nanocrystals*. A similar short-ranged ordering is discussed in Section 4.2.3. Using Equation 2.26 the SRO phase yields a typical interparticle distance between 8 and 9 nm. This is wider than the nanocrystal core diameter (3.2 nm) plus a shell of fully extended OlAm/OlAc ligands (approximately 4 nm). Here, the presence of a shell acting as a spacer can be inferred from the SAXS data.

To be able to quantify the structural parameters of all four phases, freely dispersed nanocrystals, solvent lamellae, SRO phase of nanocrystals, and fcc supercrystals, a multi-step fitting procedure for the SAXS data was developed. The analysis sequence of the time-resolved data is summarized in Section 3.3.1. The resulting model, shown in Figure 4.38 a, provides excellent agreement with the data at all times and disentangles the four individual

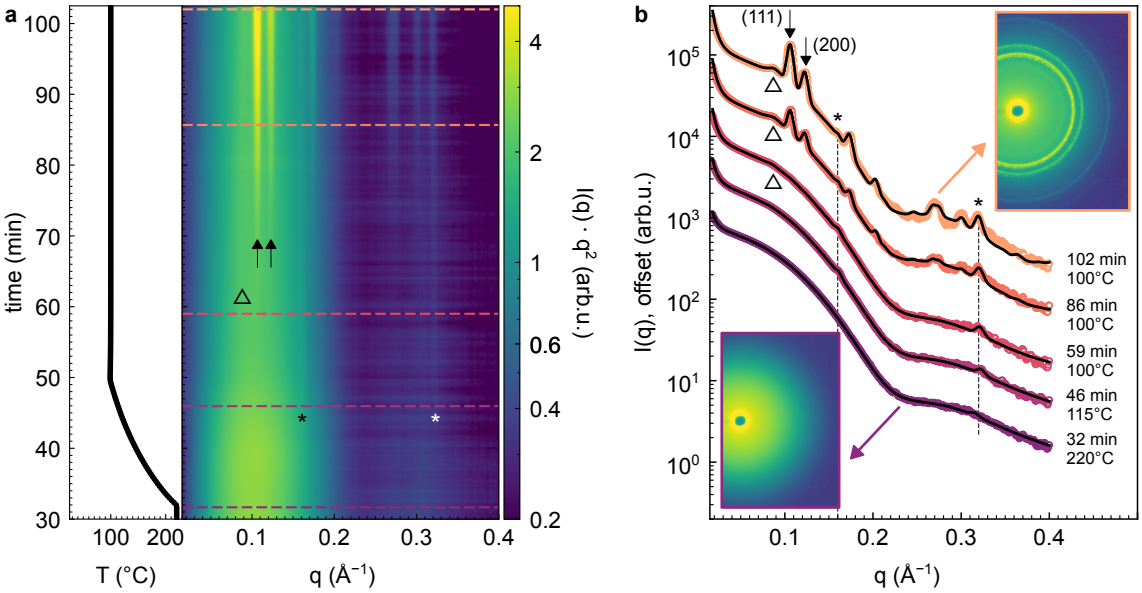

Figure 4.37: In situ SAXS data of the process of supercrystal assembly. **a**, Cooling ramp and plateau at 100 °C to induce assembly. SAXS data are shown as $I(q) \cdot q^2$ and as a function of scattering vector q and time. Asterisks (*) indicate peaks due to solvent ordering. A △ symbol shows the position of a peak from SRO of nanocrystals. Upward arrows show the (1 1 1) and (2 0 0) reflections of fcc supercrystals. **b**, Selected in situ SAXS data (20 s averages), indicated by dashed horizontal lines in **a**. Solid lines are fits to the data. Dashed vertical lines indicate the positions of peaks due to solvent ordering. Insets: SAXS detector images corresponding to the first and last curve shown. **b** adapted from [392] with permission. Copyright 2024, John Wiley and Sons.

intensity contributions as well as a background term. All terms are plausible intensities when analyzed individually, indicating a successful decomposition of the signal.

The contribution of each component to the total SAXS intensity is estimated by calculating the respective Porod invariant Q (Equation 2.17). The evolution of the Porod invariants is shown in Figure 4.38 b. The multi-step assembly pathway begins at approximately 130 °C with the formation of the solvent lamellae, which is accompanied by a drop in the intensity of free particles and immediately followed by the emergence of the SRO phase. The contribution of this phase grows continuously, whereas the signal from the solvent lamellae does not increase further. A short rise of Q of the fcc supercrystals between 46 and 57 min is at first suppressed (blue triangles). Starting from 62 min, Q of the fcc supercrystals quickly grows and supercrystals become the dominant contribution to the intensity.

The model additionally allows to visualize the evolution of the individual contributions by subtracting all other terms from the measured intensity. As an example, the growth of the first lamellar peak of the ordered solvent is shown in Figure 4.39 a. The excellent fit of the small associated intensity shows that even minuscule changes of the structure of the sample are detectable. Furthermore, the structure factor contribution of the SRO phase, obtained by dividing the respective intensity by the nanocrystal form factor, is visualized in Figure 4.39 b. Despite being a small contribution to the model, the evolution of the SRO structure factor is reliably captured.

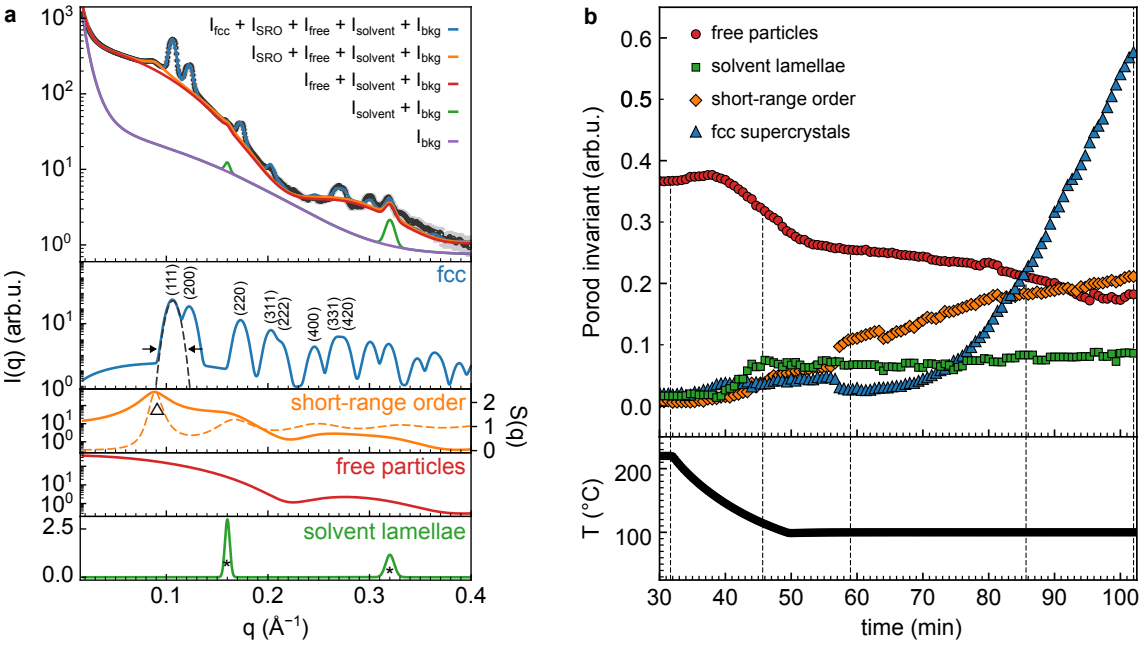

Figure 4.38: Decomposition of the SAXS intensity after supercrystal assembly. **a**, SAXS intensity at 102 min (20 s average) showing contributions of the fcc supercrystals, the SRO phase of nanocrystals, free nanocrystals, ordered solvent and a background term (bkg), as identified by a model fit. Bottom panels show the individual intensities of the components. The structure factor $S(q)$ of the SRO phase is additionally shown as a dashed orange line. **b**, Porod invariants of the components obtained from model fits as illustrated in **a** during the 100 °C plateau (bottom panel). Vertical dashed lines show the time points highlighted in Figure 4.37. **b** adapted from [392] with permission. Copyright 2024, John Wiley and Sons.

4.3.3.2 Supercrystal assembly mechanism

The underlying assembly mechanism of nanocrystals to supercrystals can be derived based on the sequence of structures observed in the one-pot synthesis. A first estimation serves to clarify which interactions dominate the process. More precisely, a calculation of the DLVO potential (see Section 2.2) shows whether pairwise interactions between colloidal nanocrystals alone would result in an interaction potential which is compatible with the observed interparticle spacings in the supercrystals.

For a similar system Wu et al. claim long-ranged vdW attraction as the driving force for self-assembly [103]. In their study of temperature-induced self-assembly of Pd nanocrystals they estimate the depth of the potential minimum by considering the core-core attractions of two particles in the surrounding solvent medium and the steric repulsion of their ligand layers. The corresponding model is summarized in Equations 2.2 and 2.3. The authors observe a 1.95 nm surface-to-surface separation for 6 nm Pd nanocrystals capped with OlAc in a supercrystal assembly experiment and predict a separation of 3 nm for 3 nm diameter nanocrystals.

In the experiments presented here a larger surface-to-surface separation of $d_{ss} = 4\,\text{nm}$ is found between the 3.2 nm CuPd nanocrystals in the supercrystals. This value is calculated from the center-to-center distance of nearest neighbors in a fcc assembly d_{nn}, using

$$d_{ss} = d_{nn} - 2R = \frac{a}{\sqrt{2}} - 2R \tag{4.4}$$

$a = 10.24\,\text{nm}$ is the measured lattice parameter of the fcc unit cell. $2R = 3.2\,\text{nm}$ is the particle diameter of the metal nanocrystal core, obtained from PDF refinement. The

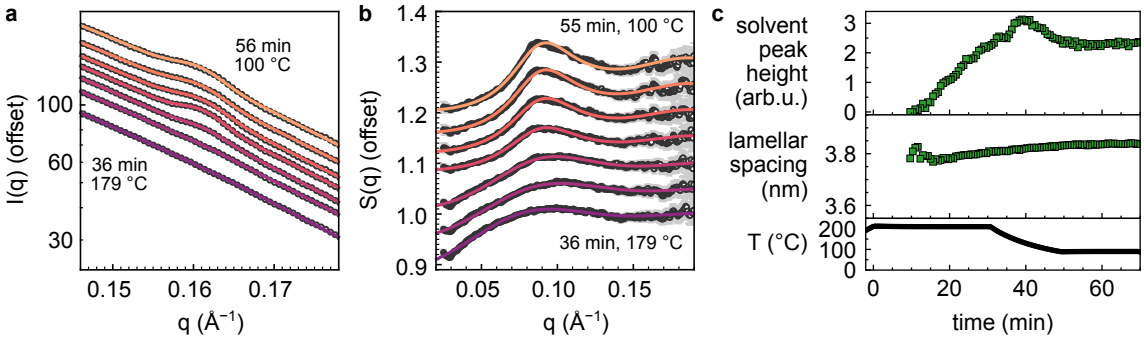

Figure 4.39: Detailed view of the solvent and SRO SAXS intensities. **a**, Zoom in to selected in situ SAXS intensities (dots, 20 s averages) during the emergence of lamellar order of the solvent. Solid lines are fits to the data. **b**, Dots: Selected structure factors of the SRO phase obtained by subtraction of the other model components, as shown in Figure 4.38 a, and division by the nanocrystal form factor. Lines: Model of the hard sphere structure factor as used in the fit of the SAXS intensity. **c**, Peak heights and lamellar spacings for a solvent mixture without metal precursors, showing the appearance of solvent lamellae already during the high temperature plateau.

separation of 4 nm indicates that two particles are separated by two fully extended OlAm or OlAc molecules and that the organic shells do not interpenetrate. Therefore, ligand-ligand interactions, which have been suggested to induce, e.g., the assembly of nanoplatelets [412], are rather unlikely to act as an attractive interaction in this case.

Repeating the calculation from reference [103] for the CuPd nanocrystals at hand leads to a very shallow minimum with a depth of $-0.02\,k_BT$ at a surface-to-surface separation of 3.9 nm, as shown in Figure A20. The position of this minimum approximately matches the experimental separation. The shallow depth of the minimum, however, is much smaller than the kinetic energy of the nanocrystals due to thermal motion. This would only lead to a weakly bound assembly and a potentially very slow assembly formation, since pairwise bound nanocrystals would frequently unbind. This suggests that in the present example an additional driving force likely facilitates the assembly of CuPd nanocrystals, and exceeds the long-ranged vdW attraction in strength.

The sequence of structures observed in the SAXS intensity prior to fcc assembly helps to identify this force and derive the following assembly mechanism (Figure 4.40): Assembly starts from freely dispersed nanocrystals in an isotropic solvent of OlAc and OlAm molecules at elevated temperature. Cooling of the mixture first introduces lamellar order of the solvent molecules. This leads to a reduced solubility of the ligand-coated, approximately spherical nanocrystals in this environment due to geometric frustration, as shown in Figure 2.7. At the interface of a spherical nanocrystal and a flat lamellar layer the ligands would need to bend and voids would have to be filled with ligand (or solvent) molecules. This is an unfavorable configuration compared to separate packing of the nanocrystals and the lamellae and restricts the volume inside which nanocrystals can diffuse. As a consequence, the nanocrystals segregate from the lamellar solvent phase and accumulate into particle-rich subphases. Their mutual interactions become visible in the SAXS intensity as short-range order. The formation of solvent lamellae acts as an initiator of assembly. As the order of the lamellar solvent increases, more and more nanocrystals segregate. A decrease in the SAXS signal from freely dispersed nanocrystals is detected (see Figure 4.38 b). The typical interparticle distance in the short-range ordered subphase is simultaneously reduced from 9.2 to 8.1 nm (Figure 4.41 a). These values correspond to surface-to-surface separations d_{ss} between 4.9 and 6 nm (see Equation 2.26). These average values exceed the minimum position of the predicted interparticle potential. Nevertheless,

particles come close enough so that single pairs in the ensemble can occasionally occupy the potential minimum.

Next, the free energy of the system is further reduced, and the packing of nanocrystals optimized, by formation of an fcc assembly. The nucleation of fcc supercrystals further increases the local particle density. For the fcc assembly an even smaller interparticle distance of 7.2 nm is observed (Figure 4.41 a). Density fluctuations inside the SRO phase or at the phase boundary to the surrounding solvent phase may act as initial nucleation sites for supercrystals.

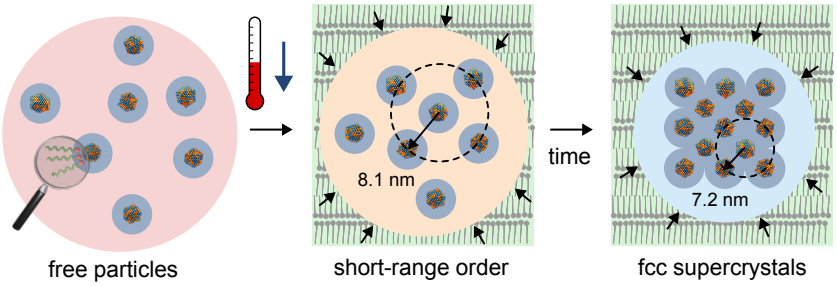

Figure 4.40: Schematic illustration of the supercrystal assembly mechanism. At elevated temperature ligand-passivated icosahedral nanocrystals are freely dispersed in a solvent (red). When cooling the mixture, the ligands, which are identical to the solvent molecules, arrange in a lamellar phase (green, shown magnified), which leads to segregation of a nanocrystal-rich, short-range ordered subphase (orange). Over time, the interparticle distance is further minimized by ordering of the nanocrystals into fcc supercrystals (blue). Figure adapted from [392] with permission. Copyright 2024, John Wiley and Sons.

The assembly formation is therefore a two-step process. Alternatively, a one-step assembly formation can be induced by varying the cooling ramp used to initiate assembly. This leads to a direct addition of the free nanocrystals to fcc supercrystals without solvent ordering or short-range order. It is observed for a stepwise cooling (130 °C to 100 °C, −5 °C every 3 h), as shown in Figure A21. Here, 4 nm diameter CuPd nanocrystals form fcc assemblies with 9.8 nm lattice parameter, i.e., $d_{ss} \approx 2.9$ nm in the course of 6 h. The cooling rate dependence of the assembly mechanism was not further investigated here beyond a qualitative comparison. The observed surface-to-surface separation suggests a more significant ligand overlap or compression inside the assemblies.

4.3.3.3 Conditions for assembly and assembly rates

The dependence of the assembly pathway on nanocrystal size and polydispersity is a crucial aspect regarding further optimization of the supercrystal product. Additionally, improved assembly strategies may be derived, once supercrystal nucleation and growth can be separately controlled. Detailed studies of the internal structure of supercrystals from PbS or gold nanoparticles have shown intricate dynamics of coarsening or annealing of defects [57, 113]. In particular, a kinetic assembly strategy, which increases the driving force over time, can lead to more highly ordered assemblies [113]. These examples show that further control of both the nanocrystal growth and the assembly stage may improve supercrystal quality.

As a basis for such an optimization, firstly, a series of repeated SAXS experiments shows that successful assembly only occurs in CuPd reaction mixtures with sufficiently large and monodisperse nanocrystals. The corresponding temporal parameter evolutions are shown in Figure A22. For too small nanocrystals the vdW attraction is likely insufficient to

induce a sizable interparticle potential minimum. Large polydispersity leads to an irregular packing, which also prevents long-range fcc order.

Secondly, regarding the separation of supercrystal nucleation and growth, analysis of the Porod invariant and the supercrystal domain size over time can provide further insights. The relative contribution of the fcc assemblies to the SAXS intensity grows monotonically once the interparticle distance has stabilized. This is visualized in Figure 4.41 with the distances shown in **a** and the Porod invariant of supercrystals shown as blue dots in **b**. A priori, an increase of the Porod invariant could be due to the nucleation of more fcc assemblies or the growth of already formed assemblies, either by incorporation of nanocrystal monomers, by coalescence (fusion of several assemblies) or Ostwald ripening (transfer of monomers from smaller to larger assemblies). To disentangle these effects the domain size of the assemblies is extracted from the peak width of the (1 1 1) reflection, as depicted in Figure 4.38 a. The result is shown in Figure 4.41 b as red dots.

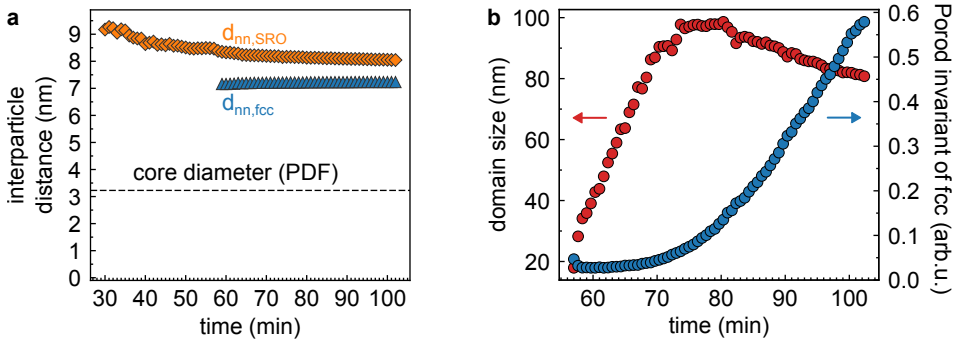

Figure 4.41: Evolution of the interparticle distance and supercrystal domain size. **a**, Interparticle distance in the SRO phase (orange) and the fcc supercrystals (blue) as a function of time. The diameter of the metal nanocrystal core, obtained from PDF analysis, is shown as a dashed line. **b**, Supercrystal domain size as a function of time, obtained from Scherrer analysis of the (1 1 1) reflection (red), and growth of the Porod invariant of fcc supercrystals (blue).

Between 57 and 75 min a steep increase of the domain size from 20 to 100 nm is observed, followed by a plateau until 82 min and a gradual decline, which coincides with a linear growth phase of the associated Porod invariant. This indicates that at first, assemblies grow to a large size, comparable to the upper resolution limit of the experiment. This limit is at approximately 90 nm, estimated via Scherrer analysis of a LaB_6 powder standard using the SAXS detector (Figure A1). Considering the fcc lattice constant of 10.24 nm the initial lateral growth of the domain size by $(4.85 \pm 0.08)\,\mathrm{nm\,min^{-1}}$ corresponds to an accelerating volumetric growth with an addition of 30 to 200 nanocrystals per minute per supercrystal. At later times the largest assemblies likely begin to sediment out of the beam. This leads to a decrease of the average domain size despite ongoing rapid assembly growth, as shown by the increasing Porod invariant. Both the addition of nanocrystal monomers to existing assemblies and the coalescence or ripening of assemblies would explain this observation.

To further clarify the underlying mechanism a more detailed analysis of the data shown in Figure 4.38 b shows that the Porod invariant of the SRO phase keeps increasing after 75 min, albeit at a smaller growth rate than the supercrystal signal. Meanwhile the contribution of free nanocrystals declines at a comparably slow rate and only reaches a plateau at 95 min. Taken together, these observations suggest that free particles segregate into the SRO phase at an approximately constant rate, which is independent of the growth rate of the supercrystalline phase. Supercrystals grow simultaneously, and noticeably faster than the SRO phase. This rate difference hints at a coalescence- or ripening-dominated

mechanism. For such a mechanism no supply of individual nanocrystal monomers directly to the supercrystals is required, and thus the growth rate of the SRO phase and the conversion rate of free nanocrystals are indeed approximately balanced.

A more detailed study of the domain size evolution could be carried out by analyzing the granularity of the diffraction rings as a function of time. This might give a rough estimate of the evolution of domain size *distribution* instead of one averaged value, and could potentially clarify the exact assembly growth mechanism. Additionally, the temperature-dependent viscosity of non-assembled and assembled mixtures could be measured. Knowing the mobility in solution of either free nanocrystal monomers or fcc-assembled monomers could help to estimate their respective addition rate to the supercrystals.

So far, freely dispersed nanocrystals and the SRO phase have been considered as separate contributions to the scattering intensity. Both could potentially be treated as a single phase with a partly attractive interaction potential. This may represent the actual interactions between the soft ligand shells better than the fully repulsive hard sphere approximation. A recent publication has characterized such interactions via the second virial coefficient B_2 [426]: B_2 appears in the power series expansion of osmotic pressure Π in units of the thermal energy k_BT with particle number density n: $\frac{\Pi}{k_BT} = n + B_2n^2 + B_3n^3 + ...$ Its value is obtained from an extrapolation of the experimental $S(q)$ to $q = 0$ at different number densities. A similar analysis could be carried out for CuPd and other syntheses with significant interparticle interactions to quantify the effect of different ligands and solvents on the interaction potentials.

4.3.3.4 Supercrystal melting and reassembly

The finding that cooling induces supercrystal assembly suggests that disassembly can be induced by heating. Heating-induced melting of the supercrystal is therefore investigated in this section, and reassembly is initiated by cooling the mixture again. For this purpose a reaction mixture containing supercrystals is first heated from 110 to 200 °C. The process is followed using the same decomposition of the in situ SAXS intensity as introduced in Figure 4.38 a. The temporal evolution of the Porod invariants is shown in Figure 4.42 a. Here, the contribution of the solvent lamellae is not shown due to its high uncertainty, as discussed below.

Starting from 116 °C the Porod invariant of the supercrystals steeply decreases. Simultaneously, the Porod invariant of the SRO phase increases until 137 °C. This indicates that particles leave the fcc assemblies, but still remain in a densely packed environment. Above 140 °C also the contribution of the SRO phase is reduced. At 164 °C free nanocrystals become the dominant component of the SAXS intensity.

When inducing reassembly of the molten sample by cooling, the same temperature dependence of the Porod invariants is observed (Figure 4.42 a) as during the initial assembly (Figure 4.38 b). At 110 °C short-range order quickly becomes the dominant intensity contribution. During a prolonged temperature plateau at 110 °C the Porod invariant of fcc supercrystals grows monotonically. The interparticle distances within the SRO phase and the fcc supercrystals are additionally shown. After an increase of the distance in the SRO phase during heating, the distances return to their initial values after cooling, 7.7 nm for the SRO phase and 7.2 nm for the fcc supercrystals. This shows that the assembly formation is fully reversible. Representative SAXS intensities before melting, in the molten state, and after reassembly are shown in Figure 4.42 b. In the molten state the signal cor-

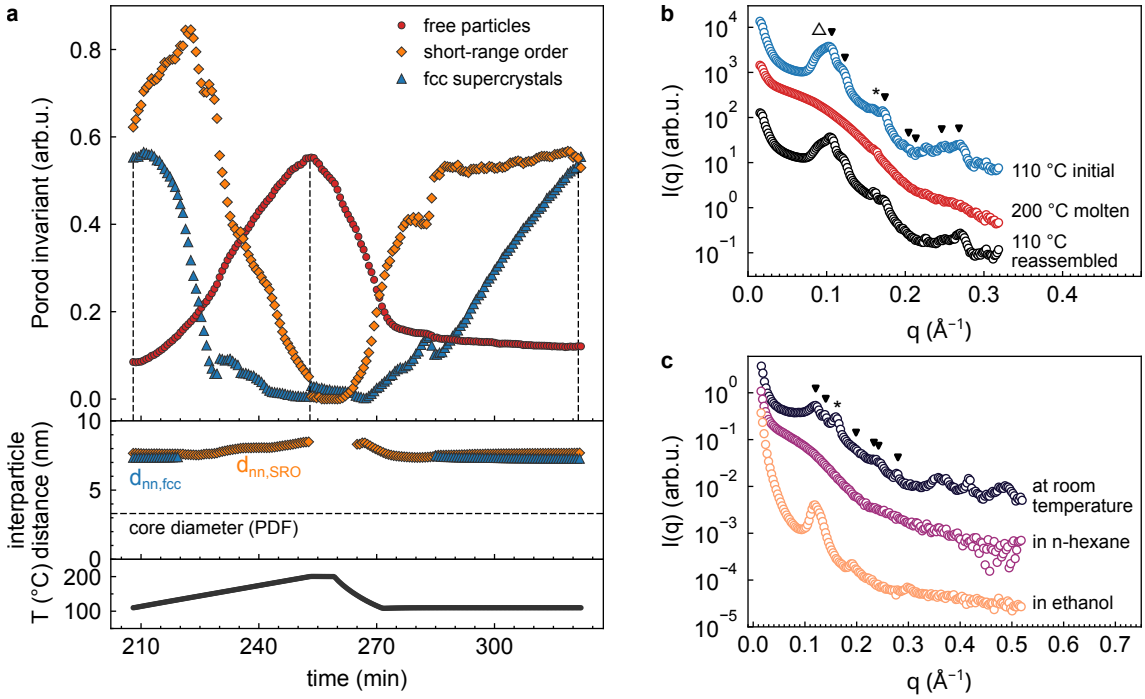

Figure 4.42: Evolution of the SAXS intensity during melting, reassembly, and dilution. **a**, Top: Porod invariants of the different contributions to the SAXS intensity. Vertical dashed lines indicate the initial, molten, and reassembled state analyzed in **b**. Middle: nearest-neighbor interparticle distances obtained from SAXS analysis and nanocrystal core diameter from PDF analysis. Bottom: Temperature ramp. **b**, In situ SAXS intensities at selected times before and after melting and reassembly. △: SRO phase, ▼: fcc reflections, *: solvent lamellae. **c**, SAXS intensities of supercrystals dispersed in different solvents.

responds almost fully to freely dispersed nanocrystals. After reassembly the signals of the SRO and fcc phases are again observed, indicated by symbols as described in the caption. Here, the SAXS intensity closely resembles the initial curve.

It should be noted that in this experiment the signature of solvent lamellae is not fully absent in the molten state. The presence of ordered solvent at high temperature might originate from slightly inhomogeneous heating inside the reaction mixture. Furthermore, a deposit on the capillary wall may have formed due to the prolonged exposure of the sample to the X-ray beam. All other components of the intensity show the expected reversible behavior upon heating and cooling, which is representative of the bulk of the sample.

The PDF obtained after the initial synthesis and after melting and reassembly (Figure A23) also shows no significant difference. This shows that the nanocrystalline metal cores are unaffected by disassembly and reassembly of the supercrystals.

In addition to the effect of temperature, dilution of the mixture with polar or non-polar solvents affects the stability of the supercrystals. During initial assembly, ligand-coated nanocrystals were found to be segregated into locally dense subphases and separated from the lamellae of OlAm and OlAc molecules. A dilution with a good solvent for any of the components of the synthesis should therefore disturb the assembly conditions and lead to a disruption of the supercrystals. In fact, no regular assemblies are observed in electron microscopy images of the reaction product, although sharp SAXS signals of supercrystals are seen for the same specimen. The necessary resuspension in solvents for electron microscopy preparation likely immediately disrupts the fragile assembly conditions, i.e., the lamellar

order of the solvent mixture. Furthermore, non-polar solvents would solubilize individual nanocrystals rather than entire assemblies, since pairwise interparticle forces are weak (see Section 4.3.3.2).

SAXS data of dilutions with n-hexane and ethanol are shown in Figure 4.42 c. Indeed, the supercrystals are disrupted by addition of n-hexane (0.009 on the $E_T(30)$ scale, see Section 2.1.4), and the signal of freely dispersed nanocrystals is observed. After addition of the rather polar ethanol (0.654 on the $E_T(30)$ scale) only few broad peaks remain present, indicating weakly ordered agglomerates. Further experiments would be required to engineer a stronger interparticle attraction and to find appropriate solvents to solubilize the intact assemblies.

In summary, this chapter shows the benefits of simultaneous in situ SAXS and TS for the characterization of a one-pot synthesis, going from molecular precursors to supercrystals. The combination of both techniques provides insight into the structure of the nanocrystal core and hints at the formation of a ligand shell during the initial nucleation and growth phase. Throughout all synthesis phases SAXS data show the various roles of OlAm and OlAc: Firstly, during the initial heating ramp they solubilize the precursors and act themselves as a viscous liquid solvent. Secondly, when bound as surface ligands they aid in stabilizing the colloidal nanocrystals. Thirdly, they participate in the assembly of nanocrystals into supercrystals due to their ability to assemble in a lamellar phase, which expels the nanocrystals into dense subphases. SAXS reveals the temporal sequence of these intermediate phases, leading to a detailed understanding of the two-step assembly mechanism. Pairwise interparticle interactions are rather weak in this case, but the overall phase behavior of the complex mixture provides favorable assembly conditions.

4.4 Formation of porous CoO nanoassemblies

The results presented in this chapter have been published in reference [377].

Grote, L. (*), Zito, C. A. (*), **Frank, K.** (*), Dippel, A.-C., Reisbeck, P., Pitala, K., Kvashnina, K. O., Bauters, S., Detlefs, B., Ivashko, O., Pandit, P., Rebber, M., Harouna-Mayer, S. Y., Nickel, B., and Koziej, D. X-ray studies bridge the molecular and macro length scales during the emergence of CoO assemblies. *Nat. Commun.*, 12, 4429 (2021). doi: 10.1038/s41467-021-24557-z

(*) equal contribution

Data repository: doi: 10.5281/zenodo.4746349

Abstract

Porous CoO nanoassemblies can be synthesized via simple heating of a precursor solution. TEM has shown that the resulting assemblies have a cavernous morphology arising from small polyhedral units. This suggests a nontrivial formation mechanism, which qualifies the synthesis for an investigation using in situ methods. In situ TS-PDF and HERFD-XANES experiments have been carried out prior to this work by the group of Prof. Dr. Dorota Koziej (UHH). These experiments have revealed a reaction mechanism in which the Co precursor is rapidly converted to an intermediate, which is then slowly transformed to the rock salt CoO product. **I complemented these characterizations by SAXS experiments** to clarify the evolution of the porous assemblies on the nanoscale. SAXS analysis of aliquots shows that the synthesis proceeds via unoriented assembly of nanometer-sized crystallites. Here, no exact multiscale model for the porous assemblies is found, so that a phenomenological crossover of power laws is used to describe the data. The small CoO crystallites grow and simultaneously attach to each other. The number of crystallites per assembly as a function of reaction time is obtained by combining SAXS and TS-PDF results.

4.4.1 Synthesis of CoO nanoassemblies

CoO nanoassemblies are synthesized by heating up 0.8 mL of a cobalt acetylacetonate ($Co(acac)_3$) precursor in benzyl alcohol (BnOH) without stirring (see Section 3.1.4). After a 6 min temperature plateau at 60 °C for dissolution of the precursor the mixture is heated to 160 °C, as shown in Figure 4.43 a. The start of the heating ramp is chosen as time $t = 0$ min. After 90 min reaction time nanoassemblies are observed in electron micrographs (Figure 4.43 b). The particles show an approximately spherical envelope and are composed of polyhedral crystallites. The hierarchical structure, containing small building blocks without common crystallographic orientation of neighboring units, is analyzed in detail in reference [377].

An initial in situ X-ray spectroscopic study of the reaction pathway has been carried out prior to this work and is summarized in Figure 4.43 c. The decomposition of HERFD-XANES data by MCR-ALS (see also Section 2.5) reveals the quick and complete transformation of the $Co(acac)_3$ precursor into $Co(acac)_2$, followed by a slower transformation into the CoO product [377]. $Co(acac)_2$ is thus established as a reaction intermediate, giving a further hint at a non-classical mechanism at play. No parallel reaction leading directly to CoO is observed.

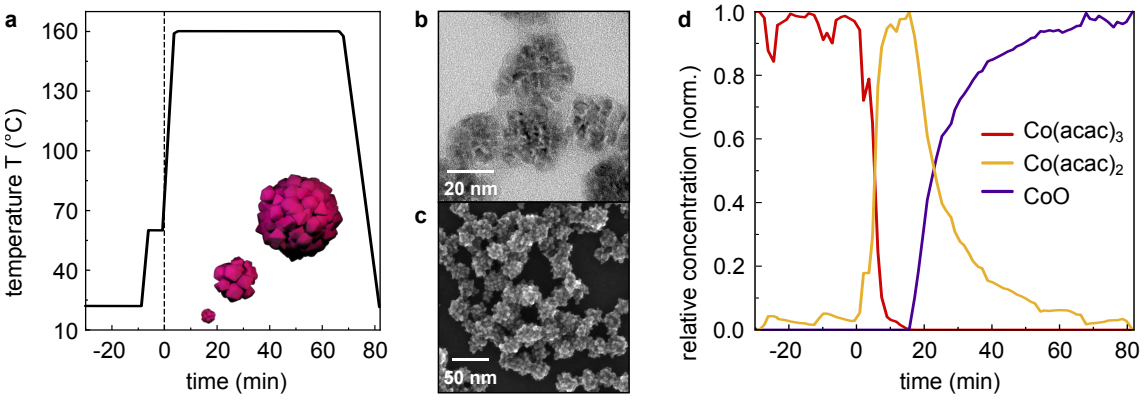

Figure 4.43: Synthesis scheme and characterization of CoO nanoassemblies. **a**, Temperature ramp for the synthesis of CoO nanoassemblies (schematic view as an inset). A vertical dashed line indicates the start of the heating to 160 °C (time $t = 0$ min). **b**, TEM image of final assemblies after 90 min reaction time. **c**, SEM image of the final assemblies. Both electron microscopy images highlight the irregular and porous structure. **d**, Relative concentrations of $Co(acac)_3$ precursor, $Co(acac)_2$ intermediate, and CoO product obtained by decomposition of in situ HERFD-XANES data via MCR-ALS. TEM, SEM and HERFD-XANES analyses were carried out by Lukas Grote (UHH). Figure adapted from [377] with permission. CC-BY license 2021, Springer Nature.

4.4.2 TS of the precursor transformation to crystallites

While the chemical state of the cobalt species during the course of the reaction was revealed in detail by X-ray spectroscopy, no structural information on the length scale of the crystallites or assemblies was obtained. Therefore, an in situ TS-PDF study (see Section 2.4.4) was carried out at beamline P21.1, DESY, Hamburg (see Table 3.6) [360]. The main findings are summarized in Figure 4.44. The reciprocal space representation of the obtained data as WAXS intensities as a function of time is shown in Figure 4.44 a. At early times and at room temperature a broad peak at $q \approx 1\,\text{Å}^{-1}$ dominates the intensity. Some intensity fluctuations are observed during heating, likely due to the slow mixing in absence of stirring of the reaction mixture. Between 15 and 20 min the peak at $q \approx 1\,\text{Å}^{-1}$

appears to be split, indicating the coexistence of precursor and intermediate. After 20 min the characteristic crystalline reflections of rock salt ($Fm\bar{3}m$) CoO appear.

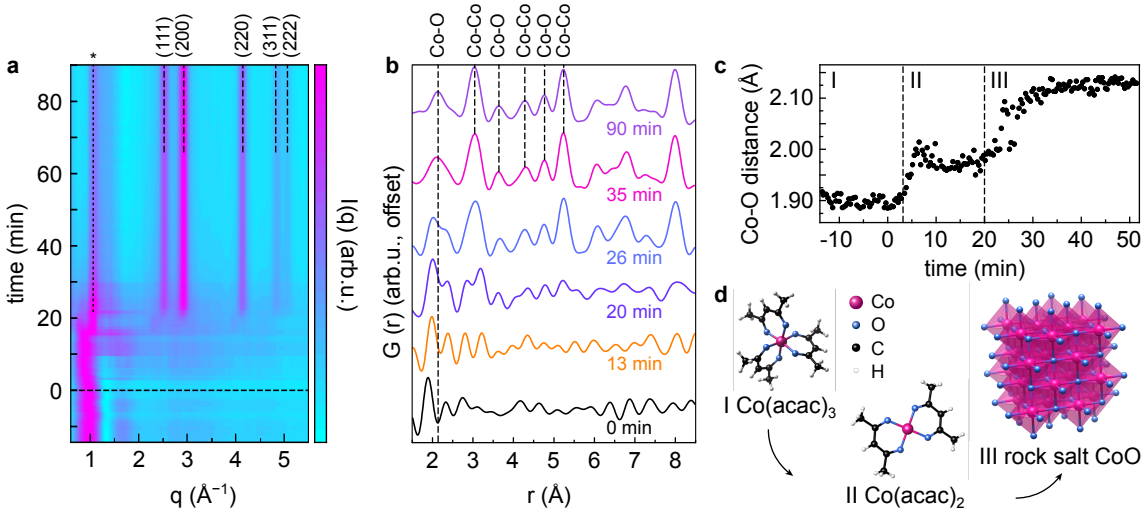

Figure 4.44: WAXS and PDF analysis of the precursor transformation. **a**, In situ WAXS data recorded during the synthesis. Horizontal dashed line: start of the heating ramp. Vertical dashed lines: Bragg reflections of rock salt CoO. The asterisk (*) highlights a peak that remains present in the data starting at approx. 20 min. **b**, PDF obtained from the data in **a**, shown for selected times. Vertical dashed lines indicate the evolution of the shortest Co–O distance and other distances observed at later times. **c**, Shortest Co–O distance as a function of time. Three distinct phases are highlighted and identified in **d**. **d**, Sketch of the transformation of the $Co(acac)_3$ precursor via $Co(acac)_2$ to CoO. PDF analysis was carried out by Cecilia A. Zito (UHH) and Ann-Christin Dippel (DESY). Figure adapted from [377] with permission. CC-BY license 2021, Springer Nature.

Due to the presence of an intermediate with a distinct chemical composition, which was revealed by in situ X-ray spectroscopy, the structural transformations between 10 and 30 min are investigated in more detail. The initial absence of sharp features in the WAXS intensity suggests that the PDF may reveal potential short-range ordered precursors or intermediates. Characteristic changes of interatomic distances preceding the formation of crystalline order can be revealed by this method. The reduced PDF obtained from the data is shown in Figure 4.44 b. The evolution of the atomic structure is best summarized by the change of the first peak in the data. Its final position is indicated by a vertical dashed line in Figure 4.44 b. It represents the smallest distance from a cobalt atom to the next oxygen atom, either in the acetylacetonate precursor or in the crystalline CoO structure. At 0 min the peak is observed at $r \approx 1.90$ Å in the data (Figure 4.44 c). Tracking the peak position an approximate three-step behavior of the Co–O distance is observed. The initial distance agrees well with the published value for $Co(acac)_3$ [427] and with experimental data shown in reference [377, Supplementary Information]. The intermediate distance of ca 1.98 Å matches data of $Co(acac)_2$ [377, Supplementary Information] and is within the range of reported DFT results [428].

Finally, the distance evolves to a value of approximately 2.12 Å, approaching the value of the first coordination shell of Co in rock salt CoO [429], drawn in Figure 4.44 d. The temporal evolution of the first Co–O distance coincides with the formation of first $Co(acac)_2$ and then CoO observed in X-ray spectroscopy. The absence of significant longer range atomic distances above the experimental background in the PDF between 0 min and 20 min indicates that the intermediate is likely present as a short-range ordered, molecular species. The presence of further Co–Co and Co–O distances after 26 min confirms the formation

of a crystalline product. Indeed, a fit of $G(r)$ with a model of rock salt CoO at 90 min reaction time provides very good agreement with the data (Figure A24 a). By using the attenuated crystal approximation a crystallite size $d = 6.4$ nm is derived from the decaying envelope of $G(r)$. The in situ data obtained at earlier times were analyzed by the same method and are discussed below in the context of nanoassembly formation.

4.4.3 SAXS of the formation of nanoassemblies

X-ray spectroscopy and TS provide a comprehensive view on the chemical and atomic-scale changes leading to the formation of CoO crystallites. Yet, information about the nanometer scale, such as the time of formation of the nanoassemblies and their shape evolution is lacking. The PDF of the final product (Figure A24 a) is fully described by the attenuated crystal model of 6.4 nm-sized crystallites. Upon close investigation it reveals no characteristic additional signal at large distances. This indicates that no structural coherence between the lattices of different adjacent crystallites exists. Therefore, X-ray spectroscopy and TS data alone cannot reveal the time of nanoassembly formation due to lack of information on these longer length scales. In fact, without complementary SAXS experiments in solution, one might believe that the several nanometer-sized nanoassemblies observed in electron microscopy only form as a result of sample preparation, i.e., during resuspension, washing, or drying. Therefore, further characterization is necessary to prove the formation of assemblies in the reaction mixture.

SAXS measurements were carried out on five aliquots, which were obtained at different times by stopping the reaction via cooling down the entire cell with a cold metal block. The SAXS intensity provides the low-q data missing in the in situ TS experiment and thus contains information about length scales up to $\frac{2\pi}{q_{min}} = 2\pi/0.003\,\text{Å}^{-1} \approx 200$ nm. To reach this low q_{min}, experiments were performed with a relatively low X-ray energy of 12.9 keV at the P03 beamline at PETRA III, DESY, Hamburg (see Table 3.6 for the experimental parameters) [359]. Data are shown in Figure 4.45 a.

At 10 min reaction time the intensity is dominated by a q^{-4} power law decay and a slight kink at low q, indicating the presence of scattering objects rather close to the resolution limit of the instrument. A Guinier analysis (see Section 2.4.2) reveals a typical diameter of the scatterers above 40 nm. At this time the $Co(acac)_2$ intermediate is the dominant component (see Figure 4.43 c). As it is only poorly soluble in BnOH it likely phase-separates or even partly precipitates from the mixture, leading to a low-q scattering signal.

At 20 min reaction time the SAXS signal starts to show a typical dominant Guinier plateau at low q followed by a q^{-4} decay, indicating the presence of compact, well-defined scattering objects [317, pp. 11 and 29 ff.]. In this range until $q \approx 0.03 - 0.04\,\text{Å}^{-1}$ a model of homogeneous spherical assemblies (black solid line) with a diameter D of 21 nm and a relative polydispersity of $\frac{\sigma_D}{D} = 25\%$ provides a good fit to the data. This suggests that assembly formation has already occurred at this time. TEM images of aliquots further support this finding [377, Supplementary Information]. Assembly is thus found to occur approximately simultaneously with the conversion of the intermediate $Co(acac)_2$ to crystalline CoO.

At later times (40 to 90 min) the plateau region shifts to smaller q, indicating the growth of the assemblies, as confirmed by the fit with the spherical model. At 90 min, a diameter D of 58 nm and a relative polydispersity of $\frac{\sigma_D}{D} = 19\%$ are obtained. All fit results are given in Table 4.1.

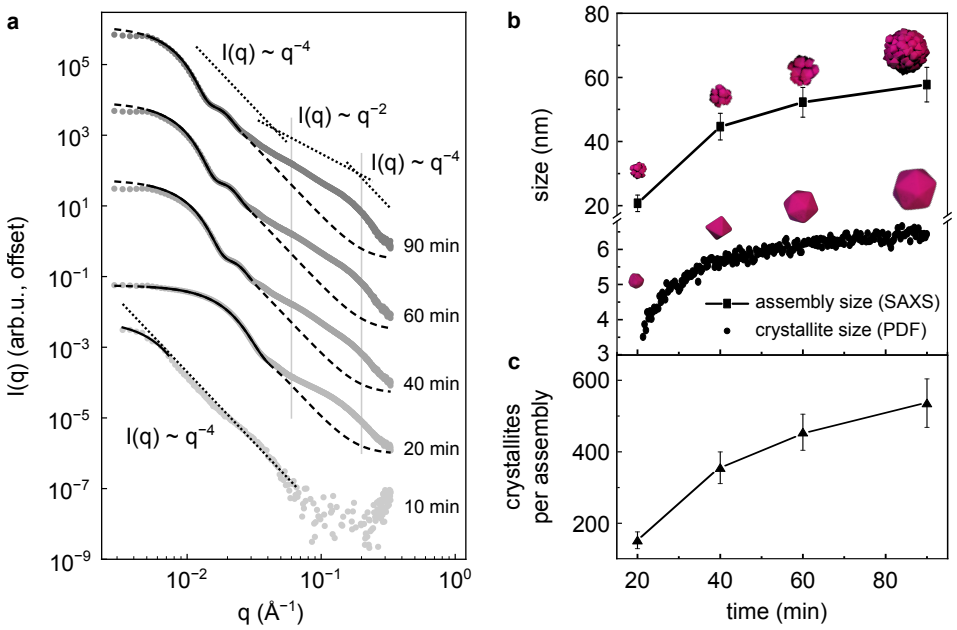

Figure 4.45: SAXS analysis of assembly formation and growth. **a**, Dots: SAXS intensities of aliquots taken at different reaction times. Solid lines: Fits with a model of solid, polydisperse spheres for the assemblies. Dashed lines: Extension of the fit to the q range where porosity and surface effects dominate. Dotted lines: Power laws indicating the crossover between the contributions of compact particle shape (q^{-4}) and rough surface and porous interior (q^{-2}) at the different length scales, separated by vertical lines. **b**, Size of the assemblies obtained by SAXS data analysis as shown in **a** and size of the small crystallites from PDF analysis. Error bars indicate the polydispersity of the assembly size. **c**, Number of crystallites per assembly obtained from the results in **b**. Figure adapted from [377] with permission. CC-BY license 2021, Springer Nature.

Table 4.1: Particle diameters D and polydispersities $\frac{\sigma_D}{D}$ obtained from a model fit.

reaction time	20 min	40 min	60 min	90 min
D (nm)	21	45	52	58
$\frac{\sigma_D}{D}$ (unitless)	0.25	0.19	0.18	0.19

The homogeneous spherical model, however, only agrees well with the data up to $q = 0.04\,\text{Å}^{-1}$. At larger q the measured intensity shows a crossover from the q^{-4} to a q^{-2} power law, and returns to a q^{-4} law at $0.2\,\text{Å}^{-1}$. The spherical model (dashed lines) continues as a q^{-4} law and therefore vastly underestimates the intensity. This deviation arises from the particular internal structure of the nanoassemblies.

Fractal and porous materials exhibit a power law decay of SAXS intensity characteristic of the fractal dimension of the interior or of the surface [326] (see also Section 2.4.2). A change of exponent occurs at the q value corresponding to the length scale of the porous structure, or the length scale at which self-similarity of the fractal becomes dominant. In the data presented here, the modified power law exponent is typically observed between 0.06 and $0.2\,\text{Å}^{-1}$, i.e., for length scales between 10 and 3 nm. This represents the internal structure of the nanoassemblies, as they are composed of approx. 3 nm-sized crystallites. At smaller length scales ($q > 0.2\,\text{Å}^{-1}$) the crystallites appear as compact objects again. Notably, the crossover of the power law is observed at all times from 20 to 90 min. This suggests that the nanoassemblies are rough and porous from the beginning. This observation is further confirmed by repeating the SAXS measurements on a laboratory setup (Figure A24 b and

Table A17). These data are on an absolute intensity scale, absolute volume fractions are obtained, and the same crossover of the power law is observed.

The diameter D of the nanoassemblies obtained from SAXS and the crystallite size d obtained from a sequential PDF refinement are combined to estimate the number of crystallites per assembly (Figure 4.45 b and c). For this purpose it is assumed that the crystallites are spherical and densely packed in the interior of the assemblies. The volume fraction is estimated as 74%, such as for fcc or hcp assemblies. The number of crystallites per assembly N is therefore $N = 0.74\,\frac{D^3}{d^3}$.

Polyhedral crystallites with a favorable shape complementarity, or particles with a size distribution which allows packing smaller crystallites in the voids between larger ones, could be packed more densely [430, 431]. Analysis of TEM images in reference [377] shows that crystallites have identical size at the center and at the surface and are polyhedral rather than spherical. It does not, however, provide a more precise estimate of the packing density due to the projected view of the nanoassemblies. Furthermore, the packing may not be homogeneous in density going from the center towards the exterior. Therefore, the number of crystallites estimated from SAXS and PDF shows a considerable uncertainty. Overall, the crystallite size, like the assembly size, follows an increasing trend from 3.5 nm at 20 min to 6.4 nm at 90 min reaction time. This suggests that in this final stage of the reaction precursor material is continuously added to the crystallites, while an increasing number of crystallites (150 to 530 on average) is added to the assemblies. Both processes, assembly and crystallite growth, contribute to the size increase of the assemblies to a similar extent. The porous morphology likely allows addition of material from precursor both at the surface and in the interior. This hypothesis is supported by the observation of homogeneous crystallite size on the inside and outside in TEM images.

In summary, SAXS analysis on aliquots of the synthesis of CoO nanoassemblies provides valuable insights into the nucleation, growth, and unoriented assembly mechanism. The nonclassical pathway from precursor droplets to unoriented polycrystals can be complex and requires a combination of spectroscopic and scattering techniques to obtain a full picture. Although SAXS is not recorded simultaneously with the HERFD-XANES or TS experiment, the origin of an essential property of the forming nanoassemblies, namely their rough and porous appearance, is revealed. A phenomenological power law model, describing the surface and interior of the nanoassemblies as fractals, is found to be an appropriate description of the intensity at larger q, while the overall morphology is well described by a spherical assembly at low q. Attempting to match the whole SAXS intensity curve by a single model, which encompasses both crystallite and assembly *shape*, would likely be overfitting. It would hide the fact that both crystallite and assembly size are rather broadly distributed (see, e.g., Figure 4.45 b). Nevertheless, a determination of the actual *porosity* as a function of reaction time (and potentially other reaction parameters) could be attempted. HERFD-XANES results indicate a full precursor conversion into CoO. Therefore, a comparison of the calculated CoO amount with the final SAXS model could potentially provide a quantitative measurement of nanoassembly porosity. This would require a fit to in situ SAXS data with low q_{min} on absolute scale and a careful calibration of porosity values with complementary electron micrographs or gas adsorption experiments.

5 Discussion

This chapter provides an overarching discussion of the common aspects among the syntheses, also regarding potential future experiments. It covers the concepts of nanoclusters, intermediate nanocrystals, assemblies and mesophases, and structured solvents. The common intermediate structures at different length and time scales and the in situ techniques to study them are summarized in Figure 5.1. Discussions of the individual results are found in Sections 4.1 to 4.4.

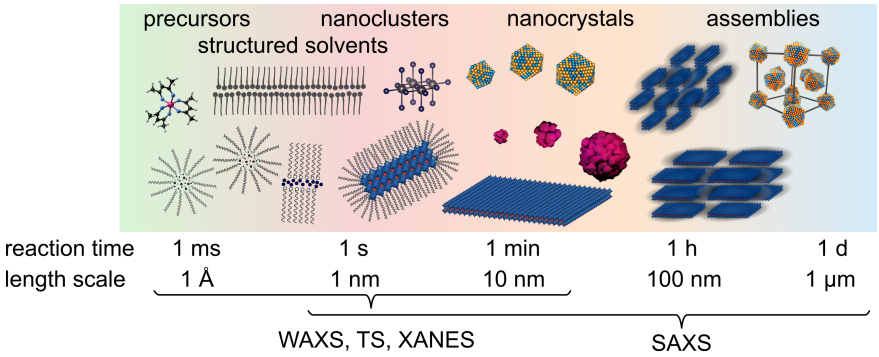

Figure 5.1: Structures in nanocrystal synthesis and complementary in situ techniques. WAXS, TS, and XANES are sensitive to transformations at short length scales in the initial phase of the synthesis. SAXS reveals the solvent structure, nanocrystal size, and assembly formation at larger length scales.

Remaining challenges of in situ characterization can concern the experiment, data analysis, and data interpretation. This chapter presents potential solutions and summarizes technological and scientific developments which may benefit future studies. In particular, the complementarity of X-ray spectroscopy and scattering, new X-ray sources and detectors, in situ and ex situ approaches, microfluidics, autonomous experiments, and the step from in situ to operando studies are discussed.

5.1 Reaction intermediates in nonclassical crystallization

Nanoclusters

In several syntheses *clusters* of few atoms are important intermediates on the trajectory from precursors to nanocrystals (see Q1 and Q7):

For CuPd, icosahedral nanoclusters as small as five shells (309 atoms) were identified by PDF analysis (see Section 4.3.2). The twinned structure of these clusters, instead of an fcc packing, may be the result of the initial confinement of metal atoms by ligands in a spherical shell, as observed for supercrystal nucleation [79]. Interestingly, also at later times the icosahedral model describes the data best, showing that no transition to the bulk metal structure occurs. Perfect icosahedra with completely filled shells may correspond to magic sizes and local energy minima for this system. Lowering the reaction speed and extracting aliquots could allow to purify such magic-sized CuPd clusters for further characterization with higher resolution TS or electrochemical studies. Due to twinning and surface faceting clusters show properties different from the bulk, and even different from few-nanometer-

sized nanocrystals. The unique surface structure may result in an enhanced catalytic activity, which could be probed by operando experiments.

Cluster nucleation and growth kinetics could be studied as a function of metal precursor ratio and ligand type. A faster reduction of the Cu precursor, shown in Figure A25, compared to Pd has been reported for CuPd intermetallic nanocrystals [162]. Different oxide intermediates have been identified, coming from $Cu(acac)_2$ as a precursor [432]. There is also evidence for a transformation from an initially Pd- or Cu-rich alloy to a homogeneous alloy in a similar synthesis [433]. Core and surface structure of the clusters may therefore differ due to Pd and Cu atoms being added at different rates. An ongoing X-ray spectroscopy study by the Koziej group aims to clarify the respective precursor transformations.

The synthesis of copper nanospheres (see Section 4.2) likely proceeds via small clusters in between the lamellar and the nanocrystalline state. The in situ SAXS and XRD data recorded so far are compatible with the existence of short-lived reverse micelles encapsulating such clusters, but do not allow to identify the micelle core structure. Cu or Cu_2O clusters could exist in the core, as suggested by the in situ XRD data. TS experiments with reaction mixtures at constant or slowly varying temperature, with and without added TDPA and/or TOA, can help to identify these clusters. Exchange of the reductants or oxidants could suppress or enhance Cu_2O formation. Simultaneous in situ SAXS and TS could further clarify the details of the lamellae-to-nanocrystal transition.

The $PbBr_2$ and PbI_2 solutions in toluene and hexane used for LHP nanocrystals (see Sections 4.1.2.2 and 4.1.5.2) contain nanoclusters from the beginning. A similar Pb_xX_y cluster structure is observed for all solvents and precursor concentrations studied here. The octahedral coordination of lead by halide ions and/or ligands dominates the TS signal. This configuration is clearly different from the bulk structure of the salts (see Figure 4.8). The lead halide clusters are even smaller than the CuPd clusters, but can still be observed by diffraction. Structural analysis is facilitated by their long-term stability in the equilibrium of the precursor mixture. The PDF analysis shown in Figure A13 suggests that, for the ratios used here, several octahedra may form a chain- or plate-like arrangement. Optical spectroscopy has identified such lead halide precursor clusters in LHP synthesis [404, 434]. Specific Pb_xX_y configurations have been found to act as templates for growing LHP nanocrystals (here called intermediate nanoclusters) [402, 435]. Which lead halide or LHP structure results depends on the ion-to-ligand and lead-to-halide ratios. Cluster anisotropy may determine the later shape of the growing nanocrystals. To further investigate the relationship between precursor- and LHP clusters, high resolution ex situ TS experiments on precursors and LHP nanoclusters are necessary. This includes variation of concentration and salt-to-ligand ratio as well as diffraction from dried samples and solutions. Complementary optical spectroscopy and EXAFS experiments could distinguish the coordination of metals by halides (e.g., Pb_xX_y) compared to ligands (e.g., in Pb-oleate or Cs-oleate).

Intermediate nanocrystals

Going forward in reaction time, several structures can be considered as *intermediate nanocrystals* in the framework of nonclassical crystallization (see Figure 2.2). This includes LHP nanoclusters, CuPd icosahedra, and polyhedral CoO crystallites. All these particles are initially suspended in solution without a defined mutual orientation, although CoO

crystallites come into contact due to the lack of stabilizing ligands. For the purpose of this discussion, the syntheses are compared in terms of the volume fraction of intermediate nanocrystals, given in Table A19. All calculated volume fractions are so low (below $1.2 \cdot 10^{-3}$) that interparticle interactions are not expected to affect the SAXS patterns (see the simulations in Figure 2.20), yet clearly distinct patterns are observed.

For LHP nanocrystal syntheses the lowest volume fractions of intermediate nanoclusters are expected based on the precursor volumes ($1.2 \cdot 10^{-4}$ to $2.3 \cdot 10^{-4}$). The actual values may be even lower due to incomplete conversion of $PbBr_2$ precursor (see Figure 4.10). This shows that, without addition of the antisolvent and its destabilizing effect, nanocrystal growth would continue in a relatively dilute environment, as studied in Figure A9. Rather surprisingly, the control of intermediate nanocluster size by external parameters in the initial reaction phase is limited (see also Q2). A change of precursor ratio and concentration leads to no significant variation of the reaction speed or nanocluster size and shape. This suggests that more substantial changes, such as an alteration of the precursor cluster structure by different ligands or the separate supply of Pb and Br precursors, are required to affect these rather universal intermediates. Preliminary experiments at 50 °C (Figure A10) show a larger intermediate nanocluster diameter compared to room temperature, which hints at reaction temperature being a further control parameter.

Currently, the experimental delay between precursor injection and nanocluster nucleation is the main limitation for the study of intermediate LHP nanoclusters. The onset of the first PL emission, SAXS, or WAXS signal fluctuates between repeat experiments and depends on precursor mixing in the small reaction capillary. As a consequence, the nanocluster dimensions at the moment of antisolvent injection vary. Figure A3 shows the dimensions obtained from SAXS analysis for eight LHP syntheses. All repeats show the same growth trends with a different temporal offset. To study nucleation on the sub-second timescale, or to make more uniform intermediate nanoclusters, a more defined mixing geometry is needed. Microfluidics, discussed in more detail below, could provide more reproducible conditions for intrinsically fast reactions, whereas slowing down the reaction may lead to a different product, as shown, e.g., in references [13, 130, 225]. The Cu, CuPd, and CoO syntheses could also be complemented by defined injection or mixing experiments. Here, the previously identified intermediates such as lamellae or precursor-ligand complexes would be suitable reagents.

In the Cu nanosphere synthesis, no intermediate nanocrystals are found, meaning that purified nanocrystals have the same size as found in situ. Based on the calculated volume fraction of nanocrystals under synthesis conditions ($7.1 \cdot 10^{-4}$) no strong interparticle interaction would be expected. Yet, an intense structure factor is observed in the in situ SAXS data at the end of the experiment (Figure 4.30). Mean interparticle distances (up to 12.5 nm) match the nanocrystal diameter (approx. 8 nm) plus a shell of ligands. This shows that nanocrystal growth, contrary to what is expected from the precursor amounts, occurs in a locally dense subphase. The ligand exchange from phosphonate in the lamellar intermediate to amine on the nanocrystals likely prevents crystallographic fusion of nanocrystals or aggregation into polycrystals.

In the CuPd synthesis the icosahedral particles can be considered to be intermediate nanocrystals. Their volume fraction is among the largest of the investigated reactions ($1.2 \cdot 10^{-3}$), yet the SAXS signal is dominated by the form factor during their nucleation and growth phase (Figure 4.34 b). In contrast to the Cu synthesis, no structure factor has to be assumed to fit the SAXS data during the growth phase (Figure 4.36 a). The homogeneous

reaction environment at elevated temperature, in which OlAm and OlAc act both as the ligand and as the solvent, most likely favors the largest possible interparticle separation. Formation of the SRO phase or fcc supercrystals requires a change of the reaction conditions, as discussed below.

The CoO synthesis has polyhedral crystallites as intermediates. Although the volume fraction ($1.2 \cdot 10^{-3}$) is the same as in the CuPd synthesis, intermediates are not observed as isolated particles here, since ligand molecules are absent. The crystallites can therefore come into contact and attach (see Figures 2.2 and 4.45). Experiments with added surfactants would be required to investigate the stability of individual crystallites. Ligands would likely change the rough morphology of the nanoassemblies towards more regular structures. A previous study has reported kinetic shape control of CoO nanocrystals from the rough quasi-spherical shape to triangles or hexagons in the presence of oleylamine [279], which corroborates this hypothesis.

Assemblies and mesophases

The syntheses studied here operate in both dilute and dense regimes as a result of different local environments. Solvent composition (Section 4.1) and temperature (Section 4.3) were used as parameters to initiate assembly. The following discussion compares the different assemblies in terms of the volume fractions occupied by the nanocrystal cores. Values are given in Table A20.

Core volume fractions in the LHP nanocrystal mesophases range from 0.17 to 0.23, which corresponds to an approx. 1000-fold increase compared to the volume fraction of intermediate nanoclusters. The densely packed mesophase constrains the growth of nanorods to the longitudinal direction (see Q2). Contrastingly, the growth of nanoplatelets is almost fully halted once they are assembled. This shows that assembly of nanocrystals can affect their growth in various ways. Also an accelerated ripening of LHP nanocrystals has been shown to occur shortly after assembly due to the decreased interparticle distance [143]. In this case the growth is stopped only later due to decreasing monomer diffusion. The authors argue that in superlattices the larger fraction of internal (and thus inaccessible) particles compared to peripheral particles prevents inhomogeneous growth. A similar effect may be responsible for the monodispersity of nanorods in this work, which first assemble laterally and later longitudinally.

Nanoplatelets almost simultaneously form lamellar stacks and assemblies of stacks, so that there is no time for templated two-dimensional growth. Once assembled, facets, edges and vertices are similarly inaccessible for monomers. A careful tuning of interparticle interactions by concentration and solvent composition would be needed to realize mutual templating of LHP nanoplatelets. In this way, platelets with larger aspect ratio, potentially up to micrometer length, could be synthesized. So far, several studies have instead reported a transformation of LHP nanoplatelets to thicker structures such as nanocubes [13, 436] or nanowires [125] upon addition of polar solvent. Solvents with increasing viscosities have been shown to induce larger stacks of LHP nanoplatelets [127]. Alternatively, additives which stabilize stacks of growing nanoplatelets could open up new synthesis routes, similar to the use of halides in the synthesis of $Cu_{2-x}S$ nanosheets [74].

In the Cu nanosphere synthesis the entire growth occurs at a volume fraction between 0.18 and 0.42, which is even denser than the SRO phase in the CuPd synthesis (0.18 to 0.27 volume fraction). This dense reaction environment in the Cu nanosphere synthesis

is remarkable, since the precursor must nevertheless reach the growing particles. This raises further questions about the reaction stages after the decomposition of the lamellar intermediate, e.g., whether small clusters, invisible to SAXS in the presence of larger nanocrystals, continue to provide metal ions. In situ HERFD-XANES and TS could be used to study the phosphonate-amine exchange occurring in between lamellae and nanocrystals in more detail, and may explain the monodisperse growth process in the dense environment.

The highest volume fraction is reached for CuPd fcc supercrystals (0.74 including the ligand shells, 0.52 for the cores only). Through the slow transformation from the SRO phase to supercrystals the system can reach the densest possible sphere packing. This two-step assembly pathway resembles the crystallization of proteins or colloids with short-range interactions, which often crystallize via a metastable liquid intermediate [60, 61, 131]. This is a result of the colloid-liquid binodal being located at lower temperature than the colloid-solid binodal in the phase diagram for short-range interactions (less than approx. 20% compared to the particle diameter) [437], [63, Fig. 1]. Temperature quenches can drive the system into the metastable region. Formation of a gel instead of a metastable liquid is also possible [438], [27, p. 11229]. Such a two-step assembly of colloidal crystals has been studied in detail with PbS nanocrystals [63, 77, 118]. Rather surprisingly, a two-step pathway can accelerate assembly and enhance supercrystalline order [63, 113], indicating a potential for further improvement of CuPd assembly quality. A comparison with the PbS studies suggests that the present work serendipitously probed two limiting cases of a complex crystallization pathway (SRO and no SRO, see Figure A21), which depend on temperature quench depth and speed.

The temperature ramps and assembly rates studied so far in a preliminary optimization are very slow (approx. 10 °C/min, less than 200 monomers added to each supercrystal per minute). This makes further SAXS studies rather time-consuming and resource-inefficient. Ligand ordering, SRO formation, and superlattice crystallization could thus be screened with calorimetry [119, 439] or viscosimetry [440]. Slightly larger nanocrystals with stronger vdW interactions could additionally speed up the assembly process.

The weak binding of CuPd supercrystals and their susceptibility to dilution limit their application potential. To improve stability, stronger interparticle interactions would need to be engineered. A permanent assembly could be achieved by modifiable ligands, which can be crosslinked with chemicals, heat, light, or electron irradiation [306, 441–443]. Electrically conducting ligands could make supercrystals conductive as a whole [27, p. 11222] and might give rise to favorable charge transport characteristics, e.g., for applications in electrocatalysis [28].

Structured solvent

The concept of a *structured solvent* is essential for explaining the X-ray scattering patterns and to rationalize the reaction mechanisms (see Q1 and Q10). The LHP, CuPd, and Cu syntheses show that precursors, even if they are well dissolved in the reaction mixture, can hardly be described as a homogeneous solution. Instead, the coordination of metal ions by ligands in a non-polar solvent provides a noticeable scattering contrast. Reverse precursor/ligand micelles imprint a characteristic shape onto the SAXS pattern (see, e.g., Sections 4.1.2.2 and 4.3.2). For strongly binding phosphonate ligands the solvent mixture phase-separates and precursor/ligand lamellae form at elevated temperature. Contrary to

the rather fragile micelles, whose stability is concentration-dependent [88], these are stable enough to be isolated or manipulated, e.g., by annealing.

During the nanocrystal growth phase, the reaction medium can remain structured by the unreacted precursor. For example, only 20 to 25% of $PbBr_2$ is transformed to LHP after precursor mixing, as shown in Figure 4.10. As a consequence, the precursor signal later needs to be included in the SAXS intensity model. Unreacted precursor can also play a significant role in the size and shape evolution in later reaction stages.

OlAm and OlAc are viscous liquids and can act both as solvents and ligands. In addition to solubilizing precursors and nanocrystals they have a tendency to assemble in lamellae and form a structured solvent (see Section 4.3). This structure is so regular that it is visible in the SAXS patterns, even in the presence of supercrystals. For small CuPd nanocrystals solvent ordering adds to the weak attractive vdW interactions, as detailed in Section 4.3.3.2, and initiates assembly. This indicates that the presence of solvent structure subtly affects the reaction pathway.

Similar to a catalyst, which appears separately from the reagents in a chemical equation, the solvent plays a peculiar role in a nanocrystal synthesis. In addition to structuring of the solvent on its own, solvent molecules can interact with nanocrystals and their ligands [47], leading to shape transitions or assembly. Vice-versa, precursors and/or nanocrystals can induce chemical transformations of ligands and solvents. The degree of unsaturation of hydrocarbon chains may change, catalyzed by the presence of metals. This can, in turn, affect the molecular ordering. A commercially relevant example is the drying of paint (e.g., ethyl linoleate) through an oxidative polymerization of the carbon-carbon double bond [444]. The effect of other (volatile) organic byproducts on nanocrystal synthesis has also been recognized in literature [445, pp. 95 f.] and characterized for CuPd [433], but has neither been studied by in situ methods nor used as a feedback mechanism for reaction control.

Solvent ordering, which changes the local environment of the suspended nanocrystals similar to freezing [166], may be applied as an assembly strategy for materials engineering. Solute-solute (i.e., inter-nanocrystal) interactions near a freezing front could be further investigated with X-ray scattering. Also the attractive effects of molecular ordering in the bulk solvent and in the ligand shells could be disentangled [446]. Early studies have reported an effect of alkyl chain freezing and melting on silver-octadecanethiol cluster superlattices, but have not studied the freezing of excess ligand molecules [439]. The relative energetic importance of the bulk and the nanocrystal surface, including depletion by unbound ligands, could be estimated using theoretical models and coarse-grained simulations. Theoretical predictions for ligand- or solvent-induced assembly could then be tested with SAXS experiments.

Even miscible solvents, which show no nanoscale structure in the absence of ligands and nanocrystals, can show non-additive behavior in a multicomponent mixture. The "Ouzo effect" is a famous example, in which a milky white oil-in-water emulsion forms from an initially clear spirit upon addition of water [447]. Nanometer-sized clusters invisible to the eye can exist in a "pre-Ouzo" composition range, and have been identified by SAXS [448].

In the presence of nanocrystals, the emulsification of a solvent mixture occurs simultaneously with reactions on the nanocrystal surface. As an example, mixing of solvent and antisolvent for LHPs leads either to a nanorod mesophase, or to ligand stripping, precursor redissolution, and formation of nanoplatelets (see Section 4.1.3). Locally, e.g., inside a

mesophase or near the ligand shell of a nanocrystal, solvent composition may differ from the bulk ratio. Different solvent molecules interact differently with the nanocrystals and the ligand chains, which can lead to local enrichment and/or bridging effects [449]. Molecular dynamics simulations of such mixtures may help to understand nonlinear trends in solubility and to establish new solvents for synthesis [450]. The coordination of lead complexes by different functional groups of solvent molecules has recently been investigated by electrostatic potential calculations, PXRD, and optical spectroscopy, giving further insight into the mode of action of antisolvents [451]. Averaging over the molecular details, the solvent behavior can also be classified using polarity or dipole moment, hydrogen bonding, and Lewis acid/base interactions (see Q10). Yet, this classification is not sufficient to explain all LHP nanocrystal syntheses. $CsPbI_3$ for example quickly degrades into the non-emissive δ-phase when using acetone as an antisolvent[3]. This shows that physicochemical solvent-ligand-nanocrystal interactions need to be understood in more detail, especially considering the solvent structure, to rationalize and generalize new synthesis strategies.

5.2 Relation of in situ studies to other techniques and developments

X-ray spectroscopy and scattering

X-ray absorption spectroscopy is a widely used in situ technique to study the evolution of chemical bonding and thus helps to characterize nanocrystal formation (see Section 2.5.3). Changes of oxidation state and metal-ligand binding, detected by (HERFD-)XANES, imply structure formation in early reaction phases (see, e.g., Sections 4.2.1 and 4.4.1). Since XANES acts as a rather local probe of the environment around high-Z atoms, it does not easily detect structure in the solvent. Solvent ordering can, however, be crucial for shape control and assembly, as discussed above. This work also shows that nanocrystal synthesis involves transient structures, compositional heterogeneity, and coexisting polymorphs. In situ SAXS, WAXS, and TS are compatible with these conditions, as they only require some recurring atomic distances or electron density fluctuations for a detectable signal. These X-ray scattering techniques are therefore ideally suited to complement the local information from X-ray spectroscopy.

X-ray sources and detectors

SAXS, WAXS, and TS benefit from the ongoing technical development of X-ray sources and detectors. The upgrades of large-scale facilities to diffraction-limited 4^{th} generation storage rings such as PETRA IV increase the available X-ray flux, especially at higher energies up to 100 keV, as well as the brilliance, maximum achievable energy, and coherence properties [361, 452]. At energies above approx. 17.4 keV (Mo K_α radiation) an X-ray beam can traverse several millimeter wide reaction cells. High energy X-rays thus allow in situ studies on large and complex reaction environments if miniaturization is not possible or to mimic advanced laboratory conditions (see Q4 and Q6, and Section 2.2.3). High flux in the high energy regime (e.g., above 50 keV) can improve the time resolution of TS/PDF experiments. The increase of coherent flux is advantageous for *imaging* nanocrystal synthesis reactions,

[3] Nina A. Henke, personal communication, January 28, 2025.

e.g., with ptychographic techniques [270]. The intense pulses of radiation from X-ray free electron lasers can help to take snapshots of nanoscale shapes via coherent diffractive imaging. Early proof-of-concept experiments with mixed nanoparticles could be adapted to in situ synthesis with microfluidic reactors [453]. Recently, TS with a free electron laser X-ray source has been demonstrated [454], paving the way towards time-resolved studies in the tens-of-femtosecond range.

In the intermediate regime between hard and high-energy X-rays (approx. 20 to 50 keV) there is an optimum in the ratio of coherent and incoherent scattering cross sections for many materials (see Section 2.4.5). This energy range, previously suffering from a lack of appropriate X-ray anode materials, beamlines, and detection capabilities, becomes more accessible with new sources and detectors. Intermediate energies are beneficial for dose-sensitive samples if radiation damage cannot be mitigated by, e.g., sample flow [134]. Such samples include biological or biomimetic materials [455], combinations of fragile organic molecules with strongly absorbing metal centers [456], and organic subphases, such as ligand molecules in nanocrystal syntheses. The impact of a reduced q_{max} at intermediate energy on PDF analysis can be mitigated by reciprocal space refinement using the DSE, as discussed below.

Simultaneously with better X-ray sources, photon-counting X-ray detectors with CdTe sensors for higher X-ray energies are becoming more common [364]. The highly absorbing sensor material with a quantum efficiency above 75% up to 80 keV [364] reduces the signal-to-noise ratio (at identical X-ray flux). This improves data quality for weak scatterers, such as small clusters. Current photon-counting detectors can be operated down to 20 Hz and 7 ms readout time [363] or 3 kHz and 3 µs readout time [457]. This may result in faster time resolution in situ if the temporal reaction control can be made equally precise. Using high frame rates and non-invasive background removal algorithms, as introduced in Section 2.4.5, faster syntheses can be studied with laboratory X-ray setups. Ultimately, the time resolution is mainly limited by the signal to background ratio. The crucial factors are the X-ray flux and the contrast of the scatterers (especially small intermediates) with respect to the solvent. Notably, adapting the sample length to the absorption length at a given X-ray energy increases the signal of the nanocrystals compared to the *instrumental* background, but likewise increases the *solvent* background (see Section 2.4.5).

Furthermore, energy dispersive detectors can be included in scattering setups for simple characterization of X-ray absorption or fluorescence, and thus the elemental composition [142, 281]. Advanced monochromatization enables the study of anomalous scattering in multi-material nanocrystals [316].

In situ, ex situ, and microfluidics

In situ studies of nanocrystal synthesis have experimental advantages compared to ex situ-only approaches: Reactions can be followed without temporal gaps or external influences. Preparation artifacts due to halting the reaction, purification, or further specimen preparation can be detected and circumvented. If several techniques are used simultaneously (such as SAXS and TS in Section 4.3.2 and WAXS and PL spectroscopy in Section 4.1.2), results represent the same sample in the same state. Short-lived intermediates may be detected (e.g., $Co(acac)_2$ in Section 4.4.1 or LHP nanoclusters in Section 4.1.2). Coexisting species can be identified (such as precursor clusters and intermediates in Section 4.1.2 or micelles and nanocrystals during ion exchange in Section 4.1.5). Real time feedback from

the experiment can be used in a closed loop to steer the reaction towards a desired product, e.g., through the dosing of additional chemicals or temperature adjustment [458].

At the same time, in situ syntheses are especially demanding: The reaction must be (made) compatible with the requirements of the experimental technique, e.g., regarding the volume and atmosphere (see Section 3.2 and Figure 3.1). The datasets are usually large and data obtained at different times and conditions may be redundant. Signals from mixtures are difficult to disentangle, especially if only a single technique is used. Intermediates observed in situ may not be isolable for further characterization or usage.

Combining in situ and ex situ techniques can be beneficial: Ex situ characterization can focus on the most promising samples and provide higher quality data by using standard protocols and reaction cells with relaxed technical constraints. Good statistics and low signal to noise are easier to achieve on long-term stable aliquots. Isolated intermediates can be used as the starting point of separate experiments, e.g., for assembly or post-synthetic modification. However, the temperature change and storage of extracted aliquots likely affect precursors and nanocrystals, which may trigger unexpected side-reactions. Phase segregation or further assembly may occur. Ex situ screening can be time-consuming without automation, especially if large datasets for machine learning are required.

As shown in this work, more advanced timing and mixing schemes are needed for the in situ study of fast (sub-second) reactions. Optical pump/X-ray probe techniques could initiate a reaction through the rapid supply of thermal energy or through a photochemical activation of reagents, and make the subsequent restructuring visible [454, 459].

Nanocrystal synthesis in flow can combine some of the advantages of in situ and ex situ studies. A flow-through setup, as shown in Section 2.2.3, combines a conventional reaction cell with probe stations for, e.g., X-ray scattering and optical spectroscopy [133]. Alternatively, both reaction and characterization can take place in a flowing liquid. Measuring at different positions means probing different reaction times. Due to the small volumes involved (typically in the microliter range) and the control over hydrodynamics by the geometry, well-defined mixing conditions for reagents can be realized. Flow-based microfluidics can use a continuous or segmented flow, and can be realized with chip- or tube/capillary-based reactors [133]. Microfluidic chips can be made from several solvent-compatible materials and combine mixing, flow-focusing and delay stages on a single device [134, pp. 2 and 4]. It should be noted that clogging or contamination of the setup can occur at high reagent concentrations [460].

X-ray scattering has been combined with both stopped and continuous flow synthesis [461]. In a continuous flow, hydrodynamic focusing in 2D or 3D sheathes the sample between streams of inert liquid. Reagents can also be enclosed in picoliter droplets moving in laminar flow. Such droplets have been used for X-ray spectroscopy of early crystallization and for scattering on supercrystalline assemblies [130, 462]. Microfluidic platforms based on tubes with mixing and heating zones have been used for LHP synthesis and optical characterization [460, 463]. Optical spectroscopy under stopped flow has elucidated the precursor chemistry leading to LHP nanosheets and nanocubes [402, 435], and could be combined with X-ray scattering at low additional complexity.

Automated experiments and self-driving labs

Besides optimizing timing and reproducibility to get better in situ data, reaction parameter space can be explored further to optimize the nanocrystals. Automation of repetitive synthesis tasks can speed up screening and help to scale up laboratory processes, making them commercially viable up to the industrial level [464]. The in situ reaction cells developed for this thesis (see, e.g., Section 3.2) can be used for automated experiments due to remote control of heating, stirring, injection, and measurement. Autonomous experiments without manual precursor loading and product extraction could be performed with only minor modifications, e.g., automated capillary unloading and rinsing, cheap and disposable inserts, or a flow-through geometry.

Robotic hardware can be combined with machine learning algorithms for synthetic optimization. In the design of experiments (DOE) approach a series of experiments is automatically suggested, incorporating prior requirements and plausible synthetic variables to explore, instead of optimizing one variable at a time [465]. Parameters can be chosen based on past experimental results, e.g., via Gaussian process optimization. This well-established technique has been applied to LHP and metal nanocrystals [234, 466, 467]. It can balance exploration of unknown parameter space and pursuit of optimal material properties through, e.g., the expected improvement acquisition function.

Despite considerable accuracy and predictive capabilities, the explainability of many state-of-the-art machine learning models for nanocrystal synthesis remains limited. This limitation becomes even more severe if reaction parameters must be found only based on the properties of the product. The results of this thesis strongly suggest that data from throughout the synthesis should be analyzed for rational optimization, as shown by the following examples: The transition from LHP nanoplatelets to nanorods with increasing acetone volume may go unnoticed when optimizing only for a narrow-banded PL emission. The role of ligands in CuPd supercrystal synthesis does not become clear from ex situ TEM and SEM images, since solvent order and the SRO phase are eliminated by purification.

Automation and machine learning are being taken a step further in so-called self-driving labs, which perform multimodal research tasks with or without human interaction [464]. With further progress in artificial intelligence (AI) and robotics the time and resources for human experimentation and decision making in such labs will likely become less significant. As a consequence, exploratory research may gravitate towards an "all that can be measured will be measured" strategy, meaning that all available techniques are used even for samples with inferior properties. Such a paradigm shift, using quantitative data from both successful and unsuccessful experiments for AI training, may involve in situ experiments as a cornerstone. Not only material properties, but general kinetic models for nanomaterials synthesis could be iteratively refined [435]. More available time-resolved data for different reaction parameters can fuel machine learning model development. Reactions could be steered based on real time feedback, even based on detailed structural or optical analysis instead of phenomenological models or trial and error. Failed reaction attempts could also be terminated early, improving time and resource efficiency.

In situ diffraction and scattering can provide the decisive insights for reaching the full potential of a nanomaterial through rational synthesis, e.g., going from 80% to 100% PLQY. These techniques are particularly useful for quantitative analysis, since any component has an interpretable signature, even precursors, ligands, and solvents. Challenges and

opportunities related to simulation and modeling of scattering data are discussed in the following section.

Reciprocal space analysis with the Debye scattering equation

Once reliable in situ scattering data have been recorded, a thorough analysis must follow. Different strategies are required for different length scales. As shown, e.g., in Section 4.1.2, reciprocal and real space analysis of SAXS and WAXS/TS data can be combined.

Distances in a real-space representation (PDF or PDDF) can be easily compared with electron microscopy images. Yet, while it might seem equivalent if the signal is analyzed in reciprocal or in real space, the transformation linking the two can introduce biases and uncertainties. The hyperparameters of the Fourier transform and the background correction (q_{max}, $q_{\mathrm{max,inst}}$, r_{poly}) must be carefully chosen and reported [351]. It should be verified that the resolution of $G(r)$ is sufficient to draw conclusions about individual distances and that ripples are not misinterpreted as features in the data. The PDDF from SAXS data depends similarly on the choice of q_{max} and d_{max}. Moreover, the PDDF of inhomogeneous samples is not easily interpretable. This complicates the real space analysis of in situ data, which is often non-ideal, as it comes from inhomogeneous samples with a high background level.

Reciprocal space analysis of SAXS and WAXS/TS data has several advantages for in situ data. In this approach, experiment and simulation meet at the level of the background-corrected intensity. Here, additive contributions from coexisting (and incoherently scattering) species are less problematic, since all intensity terms are positive and can be simulated using established approaches (see, e.g., Figures 4.7 and 4.38 for SAXS data). In situ WAXS/TS data can be similarly decomposed and analyzed. Here, the intensity computation with the DSE is essential, since it is applicable to precursor clusters, intermediate nanocrystals, assemblies and solvents, i.e., all the nonclassical structures identified here:

Precursor clusters are small enough for a fast computation of the DSE and iterative structure refinement. In combination with DFT calculations energetically plausible cluster structures could be identified using WAXS/TS data. While larger cluster motifs have already been characterized using the PDF, simulation, and machine learning [159, 356], the tools for refinement of small metal-ligand complexes based on diffraction data still need to be further developed [389]. Plausibility constraints for molecular units and atomic bond lengths and angles could be incorporated. Since nanoclusters can be surrounded by ligands and a solvent environment (the analogue of the hydration shell of biological macromolecules), the surrounding must also be correctly simulated. This has been established for SAXS of proteins [468, 469] and, recently, also for TS analysis of small molecules [470].

For high quality data clusters must be stabilized against further reaction or degradation during the experiment. Since the requirement for a large q_{max} is not as strict for DSE as for PDF analysis, as no Fourier transform of the data is involved, preliminary experiments could be carried out with laboratory setups (see Q6). Laboratory and synchrotron data could be analyzed with the same (DSE) approach, making resolution and signal-to-background directly comparable. Relatively large q_{max} can be achieved with Mo or Ag anode X-ray sources [471]. Lower X-ray flux can be compensated by longer counting times if cosmic background is removed. Imperfect monochromatization, i.e. $K_{\alpha 1}$ and $K_{\alpha 2}$ lines in the X-ray spectrum, can be included in the DSE calculation.

For *small nanocrystals* WAXS analysis via Rietveld refinement becomes inaccurate, since peak shapes and multiplicities differ from the bulk signal. SAXS and WAXS of nanocrystals can be analyzed using the DSE if an efficient computation compensates for the large number of atoms (e.g., approximately 1155 in a 3ML $CsPbBr_3$ nanorod or 6301 in a 2ML nanoplatelet, see Equation 4.1). Parallelization strategies inspired by artificial neural networks combined with distributed, GPU, and edge computing could potentially allow computations fast enough for real-time analysis. With the DSE, subtle effects such as surface termination [187], ligand structure [472], or twinning [189] can be analyzed, analogous to PDF studies [346, pp. 412 ff.]. The structural relaxation of LHP nanorods during post-synthetic modification would be a promising test case for applying the DSE to in situ WAXS/TS data.

The scattering of *assemblies and mesophases* could be simulated using a modified DSE, in which the atomic form factors are replaced by the SAXS form factors of the constituent nanocrystals. This could prove insightful for finite-sized assemblies in the early stages of supercrystal nucleation. The scattering from mesophases, in which lattice positions strongly fluctuate, could also be described by the DSE. Such a simulation might explain the difference in peak width of $(h\,k\,0)$ and $(0\,0\,l)$ reflections observed in the LHP nanorod synthesis (see Figure 4.12).

Solvent scattering can be simulated on absolute scale using the DSE, i.e., as a differential cross-section, if the molecular structure of the molecules and the bulk density are known [473]. Simulations on absolute scale, which account for nanocrystals, solvation and solvent structure, could serve as feasibility tests for in situ syntheses at low precursor concentrations or with low flux sources. Such simulations would go far beyond the phenomenological modeling of the solvent signals shown in this thesis. The accuracy could be further improved by taking into account interactions between solvent molecules, which affect the mutual molecular orientation, such as hydrogen bonding. Molecular dynamics simulations of solvent mixtures could be compared to WAXS data, going beyond simple systems [474]. In this way, short-range solvent ordering and non-additive solvation behavior, as discussed above, could be identified. A recent simulation study shows that is indeed the neglect of structural fluctuations within the liquid phase that often limits the applicability of classical nucleation theory [475]. Accurate determination of the solvent and solvation structure could therefore provide valuable input for nonclassical theories. With new software packages for fast DSE computation [476] and integration with atomistic simulations [387] reciprocal space analysis will likely become more easily usable. High quality data allows to carry out both real- and reciprocal space analysis ("dual space analysis") [477].

Detecting nanocrystal anisotropy

Compared to the complex structures of solvents and mixtures the size and shape of purified nanocrystals are relatively easy to determine. To measure anisotropy (see Q8), the SAXS signal of dispersed nanocrystals can be fitted with shape models using standard software (see Section 2.4.2). Ex situ SAXS-based sizing and shape determination yield an average signal of all particles in solution in random orientation. Bias due to sample deposition or image selection as in TEM is circumvented. While the shift of PL emission wavelength has a subtle dependence on particle anisotropy, SAXS intensity is affected by all dimensions to a similar extent, which is captured by the intensity models (see Figure 2.19). The correct model choice for shape and polydispersity is important to avoid ambiguity or erroneous

interpretation [35]. The PDDF can be used for quick inspection to reveal an oblate or prolate shape if reference data are available.

In case of a mixture (see Q8) SAXS analysis is complicated by the fact that not all intensity contributions are known a priori, and PDDF analysis is not applicable. A Guinier analysis yields a meaningless size estimate. In this case, in situ experiments help with model development since the temporal evolution of different components such as precursors can be identified, e.g., by MCR-ALS [374]. Once a robust multicomponent model is found, single components can be quantitatively characterized.

If particles form a regular assembly, the lattice symmetry often indicates the particle shape. LHP nanocluster shape has been previously identified in literature based on the symmetry of the SAXS pattern of a dried sample [188], yet at sufficient concentration also an identification in solution is possible. The data in Section 4.1.4.3 illustrate that nanorods show the (1 1 0) reflection of a two-dimensional hexagonal lattice at the "$\sqrt{3}$ position". This differentiates them from nanoplatelets, which instead form lamellar stacks with peaks only at integer multiple q positions. Particle sizes can be approximated from the lattice spacings if the thickness of the separating ligand shell is known. New automated approaches to determine particle shape and mesophase symmetry from SAXS data could steer autonomous syntheses, as discussed above [478, 479].

Simulation of more complex SAXS patterns

If nanocrystals are arranged in an unknown packing, or if they are highly polydisperse and densely packed, SAXS analysis based on analytical models may be time-consuming or unsuccessful. Models need to sample an enormous size and shape dispersity and thus result in rather "featureless" intensity curves. Interacting, slightly anisotropic particles, size- and shape-disperse mixtures during size focusing or dissolution, and random agglomerates in confinement all show complex and often enigmatic patterns. Polyhedral nanocrystals can assemble in diverse structures that range from sphere-like packing via liquid crystals to well-defined supercrystalline lattices, making accurate structure determination essential [430]. Yet, SAXS of dense powders can be so ambiguous compared to dispersions that different researchers find strongly deviating particle size distributions when analyzing the same data [480]. Therefore, more robust simulation and analysis techniques are needed for dense interacting systems such as powders, as well as for non-particulate structures. Parameter uncertainties and potential ambiguities of structural solutions, e.g., low-contrast ligand shells, will also need to be further assessed.

Recent studies have shown the potential of Gaussian random field models for simulating SAXS intensities from porous structures [481, 482]. These models involve the calculation of a 3D density field in real space, followed by a Fourier transform. Real space simulation snapshots, supported by experimental scattering data, may not be representative of the mean structure, but can help to guide the analysis. Simulation-based inference and neural posterior estimation can then provide estimates of structural ensemble parameters and uncertainties via Bayesian statistics [483–485]. Such statistical approaches, which have already been applied to in situ X-ray reflectometry, could make scattering analysis quicker and more reliable. Additionally, the concept of Shapley values, used in game theory and explainable AI to rank the importance of individual model features for the result, could be implemented [486].

Impact on materials science

The results of this thesis show that rational synthesis (or "retrosynthesis" [33, pp. 344 f.]) of size- and shape-controlled nanocrystals remains a challenge, even if the process is monitored in situ. Widely used reagents such as OlAm and OlAc ligands or ketones and alcohols as solvents can have highly specific shape-determining effects. Even small variations in the composition can induce different reaction pathways, such as the formation of bimodal or agglomerated versus monodisperse icosahedral nanocrystals in Cu, Pd, and CuPd syntheses in Section 4.3.2.2. Nonclassical crystallization pathways are common, and understanding them is key to reaction control and successful retrosynthesis. Precursor clusters, intermediate nanocrystals, and mesophases can all be used to tune the reaction outcome.

Research on materials with a large chemical variability, such as perovskites, will benefit from further in situ studies aiming at universal mechanisms. Especially a generalization of the principles found for the archetypal $CsPbBr_3$ to lead-free perovskites or other compositions with lower toxicity can promote commercialization in devices and industrial-scale production. Trial and error laboratory experiments can be complemented with strategic in situ screening. For new synthetic methods, such as microfluidic, biphasic, or microwave-assisted synthesis, a reliable in situ sample environment is key to obtaining clear and relevant results [133, 487]. Strategic cooperation between physicists, chemists, and materials scientists is required to identify desirable material characteristics, formulate open synthesis questions, and develop action plans for multimodal experimental campaigns and data analysis.

Operando X-ray scattering experiments

New questions arise for every material and synthesis taken into the spotlight of in situ experiments. Similarly, the use of novel materials in devices unveils practical challenges regarding their function, efficiency, and long-term stability. *Operando* X-ray scattering experiments, performed on (prototypical) devices such as electrodes under operating conditions, can reveal so far undiscovered structure-function relationships and degradation mechanisms [488]. Discharge products in lithium-sulfur batteries and the formation of less active planar surface sites in Cu_2O electrocatalysts have recently been identified by operando scattering [481, 489]. In situ and operando studies share many common aspects regarding both the experimental methods and the underlying principles, such as phase transformation, pore formation, nucleation, dissolution, and clustering [490]. As an example, the dissolution of copper ions and the formation of metallic bismuth during the operation of $CuBi_2O_4$ electrodes in an electrolyte resembles nucleation and growth in nanocrystal synthesis, only at a surface and with an electrostatic potential present [491]. While synthesis has been considerably advanced regarding size and shape homogeneity, high PLQY, and long shelf life, the harsh operating conditions in catalytic reactors, photo- and electrocatalytic cells are still a demanding chemical environment for new materials. Catalyst decomposition and poisoning are ubiquitous and limit practical performance [488]. Many degradation processes lead to the formation of crystalline products, changes in strain, or a restructuring on the nanoscale, and are therefore amenable to operando X-ray scattering studies [492, 493]. The instrumental improvements in automation, experiment control, data processing and analysis, implemented as part of this thesis, can facilitate operando studies both in the laboratory and at the beamline.

6 Summary and outlook

Nanocrystals, once synthesized, can be used as individual colloids or as assemblies for a variety of applications, e.g., in catalysis, sensing, or lighting. Their properties can be precisely tuned via size, shape, and composition through often elaborate synthetic approaches. Nonclassical reaction pathways during nanocrystal synthesis involve intermediate structures such as nanoclusters, primary nanoparticles, or mesophases. As shown in this work, such intermediates can fundamentally affect the size and shape evolution of nanocrystals. From ex situ characterization of aliquots the role of intermediates can only be inferred indirectly, as they are often redissolved, transformed, or removed during purification. Reaction control mechanisms using intermediates and pathways to optimized nanocrystal properties have thus remained underexplored for many syntheses.

In this thesis, in situ and ex situ SAXS and WAXS, the PDF calculated from TS, and PL spectroscopy were used to reveal the role of intermediates in four different nanocrystal syntheses. Short summaries can be found at the end of the respective Sections 4.1 to 4.4. An overarching discussion on the intermediates and the relation to other experimental developments in materials science is given in Chapter 5, including additional references. Here, the results are summarized and future research directions are pointed out.

Firstly, dedicated in situ reaction cells were designed for this thesis, namely heated and stirred capillaries for automated reagent injection (approx. 0.1 to 1 mL volume), and a shape-adapted glass cell (approx. 10 mL). These cells were used at the beamlines P62 and P07 at PETRA III, DESY, Hamburg, and at the laboratory X-ray setups at LMU. The experimental background level of laboratory experiments was substantially lowered by removing cosmic background from the X-ray images during data averaging. Data reduction and analysis routines for large datasets (up to 39 MiB per frame, 20 frames per second for a duration of 8 minutes) were developed.

Subsequently, LHP ($CsPbBr_3$) nanorods and nanoplatelets were studied by a combination of SAXS, WAXS, TS, and PL spectroscopy to investigate the origin of their shape anisotropy. While the thickness of the nanocrystals allows to tune their PL emission wavelength through strong quantum confinement, a defined anisotropy can be exploited for directional or polarized emission. In the synthesis, the $PbBr_2$ and Cs-oleate precursors were found to have a reverse micellar structure, stabilized by the OlAm and OlAc ligands. PDF revealed an octahedral cluster structure of the $PbBr_2$ precursor. Once the precursors were mixed, emissive LHP nanocluster intermediates were found to nucleate within seconds. Nanorods and nanoplatelets grow via the same prolate nanoclusters. The addition of acetone as an antisolvent was identified as the shape-determining step by in situ SAXS. Large volumes of acetone lead to almost instantaneous formation of a dense mesophase, in which nanoclusters fuse into nanorods. No antisolvent, or a smaller volume of acetone, leads to the formation of nanoplatelets. These grow freely dispersed in solution taking up ions from dissolving intermediates, and only later stack in lamellar assemblies. By a screening of several antisolvents, the dipole moment and the Hansen hydrogen bonding parameter were identified as suitable parameters to classify the synthesis outcome regarding anisotropy and monolayer thickness. Previously unexplored solvent-antisolvent combinations were used to synthesize anisotropic LHP nanocrystals of defined size, shape, and aspect ratio. Ketone antisolvents lead to particularly diverse products.

Lead halide salt solutions used in post-synthetic modification of LHP nanocrystals were found to contain reverse micelles, which closely resemble the initial precursor structure. Added $PbBr_2$ or PbI_2 leads to a strong amplification or redshift of the PL, respectively, and a dominant micelle signal in the scattering data. The question remains how thicker nanorods and nanoplatelets can be rationally synthesized with monolayer precision. The results shown here suggest that engineering the size and shape of precursor clusters and intermediate nanoclusters through different ligands may help to achieve this goal. The growth mechanisms in dilute solutions and inside dense mesophases should be further investigated so that intermediate nanocrystals can be used as seeds or building blocks for larger structures. Different precursors such as separate Pb and Br sources could be used to investigate the effects of precursor availability, stoichiometry, and kinetic control on the nanocrystal shape and composition.

The second system under investigation was a copper nanosphere synthesis, which was studied with laboratory in situ SAXS. The nanospheres were found to nucleate within lamellar intermediate structures, which consist of metal ions and phosphonate ligands. This dense nucleation and growth environment lead to a very narrow nanocrystal size distribution. The chemical and structural transformations of copper nanocrystals during synthesis should be further investigated with TS.

Metal nanocrystals, alloys and intermetallics are a promising class of materials due to their catalytic performance. Additional operando scattering studies could reveal potential degradation and restructuring pathways under operating conditions and may promote the use of economical and earth-abundant materials such as copper for catalytic applications. Compositions including noble metals such as palladium have superior properties and can be used for mixed or heterogeneous nanocrystals.

Therefore, in the next section the nucleation, growth, and assembly of CuPd nanocrystals into supercrystals were studied with simultaneous in situ SAXS and TS. An optimized setup for these experiments was installed at the beamline P07. PDF analysis revealed a twinned icosahedral structure of the nanocrystals. SAXS showed that the OlAm and OlAc molecules play several roles in the synthesis: Initially, they act as a stabilizing ligands and as a solvent, preventing coalescence and fusion of the growing nanocrystals. Later, they assemble into a lamellar subphase, which initiates the formation of a SRO phase of increased particle density. Supercrystals with fcc structure are observed after the SRO phase. The assembly process is reversible with temperature, owing to the weak interparticle interactions and the auxiliary effect of lamellar solvent ordering.

Polyhedral clusters can catalyze corner-, edge- and facet-selective reactions, which could be further studied in operando. A substantial lowering of the Pd content while leaving the icosahedral cluster structure intact would be a worthwhile challenge for synthesis and TS/PDF analysis. Cross-linkable and conductive ligands could make supercrystals more stable and usable for electrocatalytic applications. Solvent ordering and two-step assembly via a SRO intermediate may be promising strategies to synthesize other supercrystalline materials.

Lastly, cobalt oxide nanoassemblies were investigated with SAXS. These porous, polycrystalline assemblies form from small, polyhedral crystallites, to which precursor material is continuously added. The analysis shows that the porous morphology of the CoO assemblies is already present in solution before purification and drying, and allows an estimation of the number of crystallites per assembly. The fabrication and optimization of long-term stable porous oxide electrodes is an important technological challenge. Going beyond CoO, meth-

ods for the determination of nanocrystal porosity from SAXS could be developed, e.g., with Gaussian random field models. Scattering from porous or non-particulate nanomaterials could be analyzed using simulation-based inference and Bayesian statistics.

In summary, the results of this thesis show the strength of in situ X-ray scattering in identifying intermediate structures (nanoclusters, intermediate nanocrystals, assemblies and mesophases, and structured solvents) and their effect on the reaction product (size and shape control and supercrystal formation). Ordered solvents (lamellar or micellar) are frequently observed and differ from the homogeneously supersaturated medium assumed by classical nucleation theory.

4^{th} generation synchrotrons, more brilliant laboratory X-ray sources, and photon counting detectors for high X-ray energies (60 to 100 keV) will improve the experimental time resolution, so that even shorter-lived intermediates can be identified. The damaging effect of X-ray dose is reduced at intermediate X-ray energies (20 to 50 keV), where CdTe detectors are highly sensitive. This provides an opportunity for studies on beam-sensitive samples, such as organic ligand molecules with strongly absorbing metal ions. Laboratory in situ experiments are often sufficient for early characterization and could thus be integrated into the workflow of synthetic optimization. Washable and reusable or cheap and disposable reaction cells, microfluidic reactors with stopped or continuous flow, or a cycling between parallel, automated reactions can increase the experimental throughput. Inert gas atmosphere, high pressure, and microwave synthesis could be integrated into X-ray scattering setups to reproduce more advanced laboratory synthesis conditions and extend the materials library that can be studied in situ.

To keep pace with the improved instrumentation, also the software for SAXS, WAXS, TS/PDF and PL analysis should be developed further. A rapid calculation of the DSE combined with a modeling framework for solvents and ligand-coordinated clusters would bridge the gap between reciprocal space analysis in the laboratory and PDF analysis of synchrotron TS data. This would simplify initial exploratory research, e.g., on small intermediates. The solvent background could be simulated on absolute scale for feasibility studies on weakly scattering nanocrystals. Laboratory experiments would benefit from better algorithms for the removal of cosmic background.

Robotic synthesis and AI already have a strong impact on materials science and nanotechnology. Remote-controlled in situ-compatible reaction cells, as developed in this thesis, can be used to gather training data, explore reaction parameter space, and perform high-throughput closed-loop optimization. Yet, the ever-faster quest for new performant materials should not outcompete the curiosity- and discovery-driven approach to nanoscience. This thesis shows that many fundamental interactions at the Ångstrom and nanometer scale remain to be explored and understood in terms of physical theories.

DFT calculations based on atomic coordinates obtained from TS experiments could explain size-, shape- and composition-dependent optical properties of semiconductor nanocrystals beyond the effects of quantum confinement. In particular, the effect of ligand-induced strain on the octahedral tilt, the band structure, and the exciton fine structure in LHPs could be clarified.

Also the interaction between precursor ions, ligands, and solvent molecules and their role in the assembly of nanocrystals require further study. The coordination and encapsulation of precursors by ligands should be investigated further as a means of kinetic reaction control. Molecular dynamics simulations of ligands and solvents for LHPs could give a rational

explanation for the exceptional role of ketone antisolvents in the tuning of nanocrystal shape. Ligand engineering is a promising strategy to optimize PLQY and stability of LHP nanocrystals and can be driven by experiments and simulations. The results of this thesis show that solvents, which are often not written explicitly in the chemical equation, can play an active role in nanocrystal synthesis. Structuring of the solvent on the nanometer scale and a specific destabilization of the ligand shell are two frequently undetected modes of interaction with the growing nanocrystals. Yet, they can influence nanocrystal shape and assembly and thus help to achieve superior material properties.

The optimization of novel nanomaterials, in particular colloidal nanocrystals, for technical applications, has been an overarching motivation for this work. To keep pace with the synthetic progress, experimental methods must be continuously developed. Physicists and chemists must work closely together and combine experiments and computational approaches to answer fundamental questions about the underlying synthesis pathways. The environmental impact of syntheses and produced devices is another important aspect of optimization. Toxicity of materials and the full cycle from feedstocks to appliances must be taken into consideration to achieve a more sustainable use of earth's finite resources. The instrumental developments of this thesis for a study of reactions at low volumes, in situ and operando, enable an automated and resource-efficient materials screening to address this challenge.

Furthermore, a more efficient industrial production of chemicals and the development of devices with better performance, reduced energy consumption and longer life span need to be supported by research and engineering. Through advanced colloidal chemistry the realm of quantum mechanical phenomena, manifested in small crystallites, has become accessible to researchers of all disciplines and can be transferred to such everyday applications. Control of material composition and morphology across several length scales can help the optimization of, e.g., battery electrodes, metal catalysts, or LEDs. The in situ X-ray studies presented in this work may inspire a new materials design paradigm, taking control of self-assembly mechanisms from the nanocluster to the supercrystal scale.

Appendix

A.1 Exemplary PDF refinements

Table A1: PDF fit parameters for $CsPbBr_3$ nanocrystals. $G(r)$ was refined in a range from 1.5 to 40 Å with a step of 0.01 Å and a .cif file of orthorhombic (Pnma) $CsPbBr_3$ (COD 4510745 [339]). Fractional coordinates and atomic displacement parameters were also refined and the resulting positions are shown in Figure 2.23.

scale	δ_2(Å^2)	a (Å)	b (Å)	c (Å)	particle diameter (nm)	R_w
1.2665	6.770	8.3867	11.6854	8.1968	4.017	0.207

A.2 SAXS absolute intensity calculation and resolution function

The detected SAXS intensity $I(q)$ is related to the differential scattering cross section $\frac{d\Sigma}{d\Omega}(q)$ ("absolute intensity") via

$$I(q) = I_0\, t_s\, t_m\, T\, \epsilon\, \Omega\, \frac{d\Sigma}{d\Omega}(q) \tag{A1}$$

Explanations of the parameters and typical values are given in Table A2.

Table A2: Typical parameters for a laboratory SAXS measurement of water. The intensity I' is given as a value per pixel and measurement time t_m by Equation A1. The transmission is calculated for 1 cm of water at 17.4 keV using the CXRO transmission calculator [494]. The detector efficiency ϵ is calculated for 1 mm silicon using the same tool. The solid angle corresponds to a 0.172 mm square pixel at 1 m distance.

intensity per pixel and per measurement time	I'	$2.7 \cdot 10^{-4}$ counts/pixel/s
primary beam flux	I_0	$2 \cdot 10^6$ photons/s
sample thickness	t_s	1 cm
measurement time	t_m	3600 s
sample transmission	T	0.37
detector efficiency	ϵ	0.76
solid angle per pixel	Ω	$3 \cdot 10^{-8}$ 1/pixel
differential scattering cross section of the sample	$\frac{d\Sigma}{d\Omega}$	$1.6 \cdot 10^{-2}$ cm^{-1} [495]

The effect of sample length l_s on the resolution can be approximated as

$$\Delta q = \frac{4\pi}{\lambda}\left(\sin\left(\theta_+\right) - \sin\left(\theta_-\right)\right), \qquad 2\theta_\pm = \arctan\left(\frac{\tan\left(2\theta\right)\cdot SDD}{SDD \mp \frac{l_s}{2}}\right) \tag{A2}$$

SDD is the sample-to-detector distance. Placing the detector further away from the sample reduces the effect of the pixel size l_p on the resolution

$$\Delta q = \frac{4\pi}{\lambda}\left(\sin\left(\theta_+\right) - \sin\left(\theta_-\right)\right), \qquad 2\theta_\pm = \arctan\left(\frac{\tan\left(2\theta\right)\cdot SDD \pm \frac{l_p}{2}}{SDD}\right) \tag{A3}$$

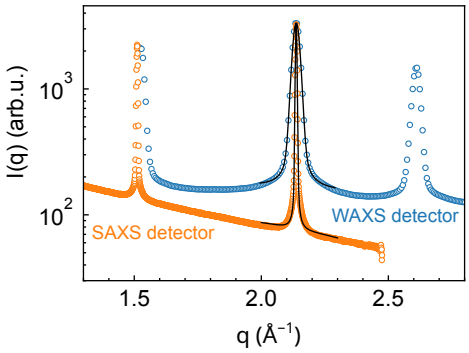

Figure A1: Resolution determination of the P07 beamline setup with LaB_6. Black lines are fits to the data with a Pseudo-Voigt peak (Equation 2.31) on a power law background. The resulting FWHM is $(3.342 \pm 0.008) \cdot 10^{-2}$Å^{-1} for the WAXS and $(6.95 \pm 0.05) \cdot 10^{-3}$Å^{-1} for the SAXS detector, respectively. WAXS intensities were scaled to match the peak height from the SAXS detector. The signal from the WAXS detector shows broadened reflections compared to the SAXS detector due to the closer detector position and the resulting larger influence of detector pixel size on the resolution. The signal from the SAXS detector shows a decaying background term, which is most likely due to scattering from residual air in the flight tube (see Figure 3.5). The FWHM values correspond to domain sizes of 19 nm (WAXS) and 90 nm (SAXS).

A.3 LHP nanocrystals – SAXS analysis and fit parameters

Table A3: SAXS fit parameters of the precursors. List of parameters obtained from the model fit to the SAXS data of the $PbBr_2$ and the Cs-oleate precursor shown in Figure 4.8. Uncertainties are provided by SasView's DREAM algorithm and correspond to 68% confidence intervals.

parameter	**$PbBr_2$**	**Cs-oleate**
scale (arb.u.)	0.239 ± 0.007	9.1 ± 0.6
background (arb.u.)	$(2.07 \pm 0.02) \cdot 10^{-2}$	$(5.5 \pm 0.7) \cdot 10^{-4}$
core diameter (nm)	1.19 ± 0.09	1.21 ± 0.02
shell thickness (nm)	0.820 ± 0.008	0.625 ± 0.009
core SLD (10^{-6}Å^{-2})	46.6 (fixed)	1 (fixed)
shell SLD (10^{-6}Å^{-2})	8.76 ± 0.03	0.017 ± 0.003
solvent SLD (10^{-6}Å^{-2})	8 (fixed)	0 (fixed)
hard sphere volume fraction (unitless)	0.0389 ± 0.0008	0.181 ± 0.003

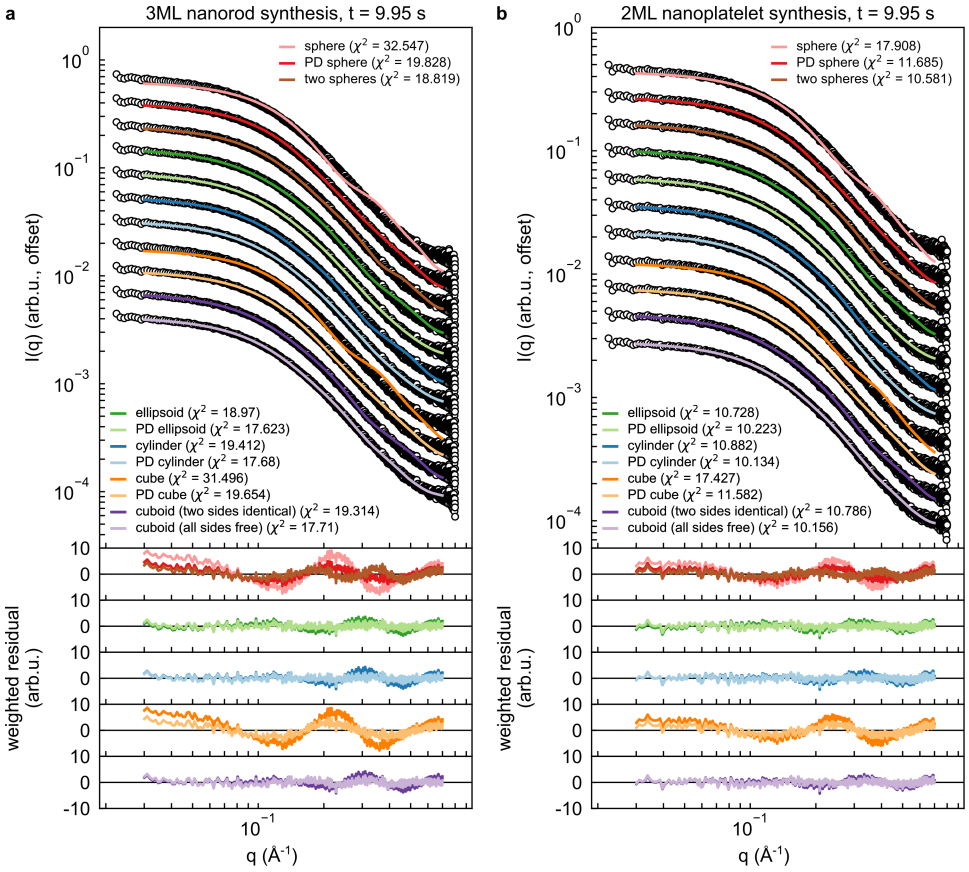

Figure A2: Comparison of different shape models for the intermediate nanoclusters. **a**, Fit of the last frame before antisolvent injection for the synthesis of 3ML nanorods. PD indicates a Gaussian size polydispersity in the model. Sphere models (red and brown curves) provide a poor fit, note the oscillating residuals. Cube models (orange curves) also show large and oscillating residuals. Anisotropic models (ellipsoid, cylinder, cuboid) provide good fits, showing on average lower values of χ^2 and flat residuals over the fitted range (green, blue, and purple curves). All anisotropic models result in prolate particles. A slight improvement of the fit can be achieved by allowing polydispersity (for ellipsoid and cylinder models) or allowing three different dimensions in the cuboid model compared to a model in which two sides are constrained equal. **b**, Fit of the last frame before antisolvent injection for the synthesis of 2ML nanoplatelets. Again, the sphere and cube models do not agree well with the data, whereas ellipsoid, cylinder and cuboid models provide satisfactory fits, indicating that nanocluster anisotropy is key to obtaining a good fit to the data.

Table A4: SAXS fit parameters for different particle shape models for 3ML nanorod synthesis. Uncertainties are provided by the DREAM algorithm of SasView and correspond to 68 % confidence intervals. Note that the "two spheres", "PD cube", and "cuboid two sides identical" models are not implemented on an absolute intensity scale and, therefore, provide different scale parameters from the other models. Relative polydispersity (rel. PD) is defined as the ratio of standard deviation and mean $\frac{\sigma_l}{l}$ or $\frac{\sigma_d}{d}$ of a Gaussian distribution of sizes.

	sphere	**PD sphere**	**two spheres**
precursor scale (arb.u.)	0.2506 ± 0.0008	0.1912 ± 0.0009	0.5468 ± 0.0005
nanocluster scale (arb.u.)	$(4.34 \pm 0.02) \cdot 10^{-4}$	$(6.72 \pm 0.03) \cdot 10^{-4}$	$(1.84 \pm 0.03) \cdot 10^{6}$
nanocluster scale 2 (arb.u.)	-	-	$(4.70 \pm 0.04) \cdot 10^{6}$
background (arb.u.)	$(1.045 \pm 0.007) \cdot 10^{-2}$	$(1.243 \pm 0.007) \cdot 10^{-2}$	$(1.327 \pm 0.008) \cdot 10^{-2}$
nanocluster diameter (nm)	3.395 ± 0.005	0.67 ± 0.02	4.13 ± 0.02
(rel. PD in brackets)		(2.00 ± 0.04)	
nanocluster diameter 2 (nm)	-	-	2.38 ± 0.02
χ^2	32.547	19.828	18.819
	ellipsoid	**PD ellipsoid**	
precursor scale (arb.u.)	0.185 ± 0.002	0.112 ± 0.003	
nanocluster scale (arb.u.)	$(6.405 \pm 0.05) \cdot 10^{-4}$	$(1.134 \pm 0.002) \cdot 10^{-2}$	
background (arb.u.)	$(1.322 \pm 0.008) \cdot 10^{-2}$	$(1.393 \pm 0.008) \cdot 10^{-2}$	
nanocluster length l (nm)	6.14 ± 0.03	5.71 ± 0.04	
(rel. PD in brackets)		(0.08 ± 0.04)	
nanocluster diameter d (nm)	2.269 ± 0.008	0.49 ± 0.01	
(rel. PD in brackets)		(1.87 ± 0.05)	
χ^2	18.97	17.623	
	cylinder	**PD cylinder**	
precursor scale (arb.u.)	0.191 ± 0.002	0.121 ± 0.002	
nanocluster scale (arb.u.)	$(6.24 \pm 0.04) \cdot 10^{-4}$	$(1.07 \pm 0.10) \cdot 10^{-4}$	
background (arb.u.)	$(1.300 \pm 0.008) \cdot 10^{-2}$	$(1.393 \pm 0.008) \cdot 10^{-2}$	
nanocluster length l (nm)	4.45 ± 0.02	4.01 ± 0.04	
(rel. PD in brackets)		(0.19 ± 0.02)	
nanocluster diameter d (nm)	2.180 ± 0.007	0.49 ± 0.02	
(rel. PD in brackets)		(1.86 ± 0.07)	
χ^2	19.412	17.68	
	cube	**PD cube**	
precursor scale (arb.u.)	0.729 ± 0.002	0.551 ± 0.003	
nanocluster scale (arb.u.)	263 ± 2	$(2.54 \pm 0.03) \cdot 10^{3}$	
background (arb.u.)	$(1.052 \pm 0.007) \cdot 10^{-2}$	$(1.24 \pm 0.008) \cdot 10^{-2}$	
nanocluster size (nm)	2.645 ± 0.004	0.548 ± 0.008	
(rel. PD in brackets)		(1.89 ± 0.03)	
χ^2	31.496	19.654	
	cuboid two sides identical	**cuboid all sides free**	
precursor scale (arb.u.)	0.565 ± 0.004	0.132 ± 0.005	
nanocluster scale (arb.u.)	414 ± 5	$(9.2 \pm 0.3) \cdot 10^{-4}$	
background (arb.u.)	$(1.295 \pm 0.008) \cdot 10^{-2}$	$(1.44 \pm 0.02) \cdot 10^{-2}$	
nanocluster length a (nm)	1.890 ± 0.006	4.23 ± 0.02	
nanocluster length b (nm)	1.890 ± 0.006	2.31 ± 0.02	
nanocluster length c (nm)	4.44 ± 0.02	1.19 ± 0.03	
χ^2	19.314	17.71	

Table A5: SAXS fit parameters for different particle shape models for 2ML nanoplatelet synthesis. Uncertainties are provided by the DREAM algorithm of SasView and correspond to 68 % confidence intervals. Note that the "two spheres", "PD cube", and "cuboid two sides identical" models are not implemented on an absolute intensity scale and, therefore, provide different scale parameters from the other models. Relative polydispersity (rel. PD) is defined as the ratio of standard deviation and mean $\frac{\sigma_l}{l}$ or $\frac{\sigma_d}{d}$ of a Gaussian distribution of sizes.

	sphere	**PD sphere**	**two spheres**
precursor scale (arb.u.)	0.2651 ± 0.0008	0.215 ± 0.002	0.581 ± 0.006
nanocluster scale (arb.u.)	$(3.33 \pm 0.02) \cdot 10^{-4}$	$(5.46 \pm 0.04) \cdot 10^{-4}$	$(4.21 \pm 0.07) \cdot 10^{6}$
nanocluster scale 2 (arb.u.)	-	-	$(1.50 \pm 0.04) \cdot 10^{6}$
background (arb.u.)	$(1.213 \pm 0.007) \cdot 10^{-2}$	$(1.3616 \pm 0.008) \cdot 10^{-2}$	$(1.4534 \pm 0.009) \cdot 10^{-2}$
nanocluster diameter (nm) (rel. PD in brackets)	3.163 ± 0.006	0.61 ± 0.02 (2.00 ± 0.06)	2.13 ± 0.02
nanocluster diameter 2 (nm)	-	-	3.78 ± 0.02
χ^2	17.908	11.685	10.581
	ellipsoid	**PD ellipsoid**	
precursor scale (arb.u.)	0.198 ± 0.002	0.117 ± 0.005	
nanocluster scale (arb.u.)	$(5.5667 \pm 0.008) \cdot 10^{-4}$	$(1.18 \pm 0.04) \cdot 10^{-3}$	
background (arb.u.)	$(1.4629 \pm 0.009) \cdot 10^{-2}$	$(0.0150 \pm 0.009) \cdot 10^{-2}$	
nanocluster length l (nm) (rel. PD in brackets)	5.56 ± 0.03	5.32 ± 0.03 (0.00 ± 0.03)	
nanocluster diameter d (nm) (rel. PD in brackets)	2.00 ± 0.02	0.60 ± 0.02 (1.15 ± 0.05)	
χ^2	10.728	10.223	
	cylinder	**PD cylinder**	
precursor scale (arb.u.)	0.205 ± 0.002	0.129 ± 0.004	
nanocluster scale (arb.u.)	$(5.40 \pm 0.06) \cdot 10^{-4}$	$(1.07 \pm 0.03) \cdot 10^{-3}$	
background (arb.u.)	$(1.439 \pm 0.009) \cdot 10^{-2}$	$(1.497 \pm 0.009) \cdot 10^{-2}$	
nanocluster length l (nm) (rel. PD in brackets)	4.04 ± 0.02	3.65 ± 0.03 (0.16 ± 0.02)	
nanocluster diameter d (nm) (rel. PD in brackets)	1.94 ± 0.01	0.56 ± 0.02 (1.27 ± 0.05)	
χ^2	10.882	10.134	
	cube	**PD cube**	
precursor scale (arb.u.)	0.761 ± 0.003	0.617 ± 0.003	
nanocluster scale (arb.u.)	250 ± 3	$(2.46 \pm 0.04) \cdot 10^{3}$	
background (arb.u.)	$(1.217 \pm 0.008) \cdot 10^{-2}$	$(1.356 \pm 0.008) \cdot 10^{-2}$	
nanocluster size (nm) (rel. PD in brackets)	2.463 ± 0.005	0.644 ± 0.008 (1.41 ± 0.02)	
χ^2	17.427	11.582	
	cuboid two sides identical	**cuboid all sides free**	
precursor scale (arb.u.)	0.595 ± 0.005	0.146 ± 0.006	
nanocluster scale (arb.u.)	501 ± 10	$(8.8 \pm 0.4) \cdot 10^{-4}$	
background (arb.u.)	$(1.436 \pm 0.009) \cdot 10^{-2}$	$(1.54 \pm 0.01) \cdot 10^{-2}$	
nanocluster length a (nm)	1.681 ± 0.009	3.82 ± 0.02	
nanocluster length b (nm)	1.681 ± 0.009	1.04 ± 0.03	
nanocluster length c (nm)	4.03 ± 0.02	1.96 ± 0.02	
χ^2	10.786	10.156	

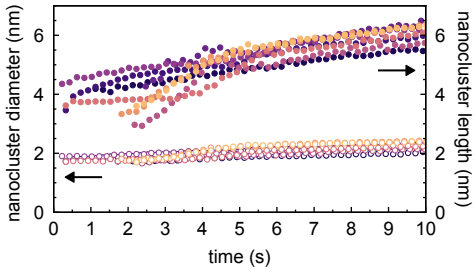

Figure A3: Reproducibility of intermediate nanocluster diameter and length. Diameter and length as a function of time were determined by SAXS analysis after Cs-oleate injection. Eight independent in situ syntheses are shown to illustrate the reproducibility of intermediate nanocluster dimensions.

Table A6: Number of precursor micelles involved in intermediate nanocluster nucleation. The micelle core diameter d was found by small-angle X-ray scattering (SAXS) analysis shown in Figure 4.8 and Table A3. The intermediate nanocluster core volume was found by SAXS analysis shown in Tables A4 and A5. The core volume was calculated using the equations in Section 3.3.1 for spheres, ellipsoids, and cuboids. The core was assumed to consist of either bulk $PbBr_2$ or bulk $CsPbBr_3$, i.e., the involved ligands were attributed fully to the shell of the micelle or nanocluster. The number of lead atoms per micelle or nanocluster was calculated as $N = \frac{V\rho}{M} N_A$, where N_A is Avogadro's number. Uncertainties were propagated based on the uncertainty of the volume.

	$PbBr_2$	**3ML nanorods initial**	**3ML nanorods final**	**2ML nanoplatelets initial**	**2ML nanoplatelets final**
core volume V (nm^3)	0.9 ± 0.2	8.4 ± 0.2	16.6 ± 0.1	7.0 ± 1.1	11.5 ± 0.2
mass density ρ (g/cm^3)	6.66	4.55	4.55	4.55	4.55
molar mass M (g/mol)	367.01	579.82	579.82	579.82	579.82
number of Pb per particle N	9.6 ± 2.2	40 ± 1	78 ± 1	33 ± 6	55 ± 2

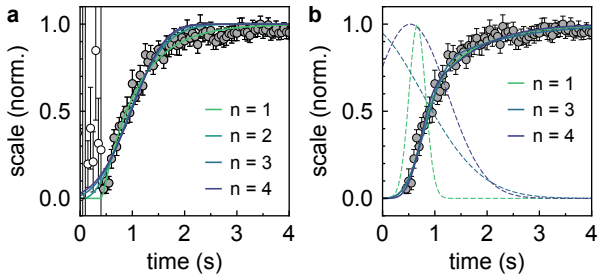

Figure A4: Modified JMAK and Gualtieri fits of PDF and SAXS data from LHP nanocrystal syntheses. Dots: Normalized nanocrystal scale factor obtained from a model fit to in situ SAXS intensities from a 2ML NPL synthesis. Error bars denote 95% confidence intervals. **a**, Lines: fits with a modified JMAK equation (Equation A4), exponents given in the legend. Open dots were excluded from the fits. **b**, Lines: fits with a modified Gualtieri equation (Equation A5), exponents given in the legend. Dashed lines: Corresponding distributions of nucleation times. All fit parameters are given in Table A7.

The modified equations allow for an arbitrary offset t_0 of time as well as fitting for $t \leq t_0$.

Modified JMAK equation

$$x(t) = \begin{cases} 1 - \mathrm{e}^{-(k_g\,(t-t_0))^n} & \text{for } t > t_0 \\ 0 & \text{otherwise} \end{cases} \tag{A4}$$

Modified Gualtieri equation

$$x(t) = \begin{cases} \frac{1}{1+\mathrm{e}^{-\frac{t-a}{b}}} \left[1 - \mathrm{e}^{-(k_g\,(t-t_0))^n}\right] & \text{for } t > t_0 \\ 0 & \text{otherwise} \end{cases} \tag{A5}$$

Table A7: Modified JMAK and Gualtieri fit results of LHP syntheses. χ^2 takes into account the uncertainty of the data points where applicable. A Gualtieri model with $n = 2$ did not provide a good fit to the NPL SAXS data.

NPLs SAXS JMAK				
n (unitless)	$\mathbf{k_g}\,(s^{-1})$	$\mathbf{t_0}\,(s)$	-	χ^2
1	1.50 ± 0.05	0.43 ± 0.02	-	0.73
2	0.93 ± 0.05	0.06 ± 0.05	-	1.30
3	0.66 ± 0.04	-0.37 ± 0.08	-	1.54
4	0.51 ± 0.03	-0.82 ± 0.11	-	1.66
NPLs SAXS Gualtieri				
n (unitless)	$\mathbf{k_g}\,(s^{-1})$	$\mathbf{a}\,(s)$	$\mathbf{b}\,(s)$	χ^2
1	1.12 ± 0.04	0.66 ± 0.02	0.18 ± 0.02	0.66
3	1.14 ± 0.04	-0.37 ± 0.35	1.12 ± 0.16	0.64
4	1.34 ± 0.04	0.53 ± 0.10	0.71 ± 0.07	0.78

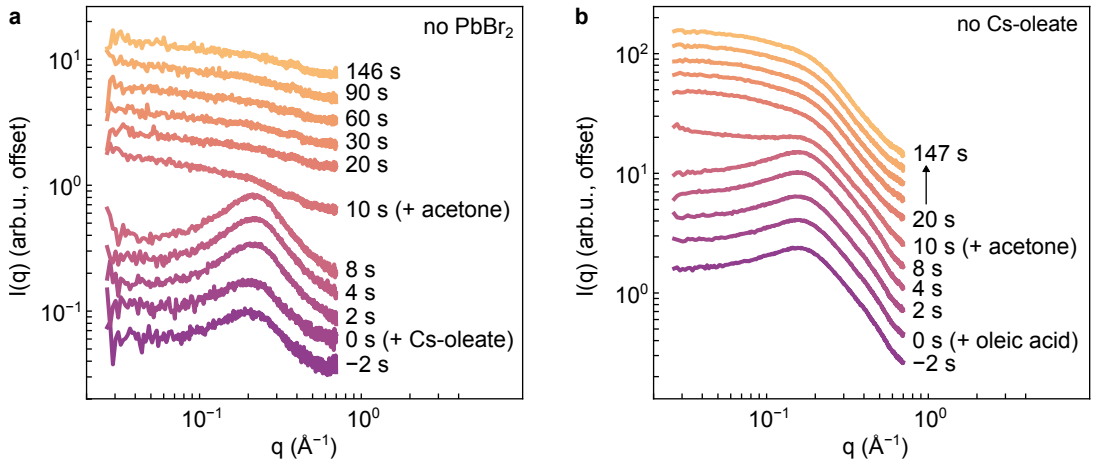

Figure A5: In situ SAXS intensities of syntheses without $PbBr_2$ or Cs-oleate. a, Synthesis, in which $PbBr_2$ was omitted from the first precursor, so that no LHP nanoclusters form. The weak signal comes from ligand micelles and the micellar Cs-oleate precursor. **b**, Synthesis, in which Cs-oleate was replaced by OlAc, so that no LHP nanoclusters form. OlAc leaves the signal from the micellar $PbBr_2$ intact. Acetone leads to a dilution and a weakening of the structure factor peak at $q = 0.17\,\text{Å}^{-1}$. No mesophase is observed for either synthesis.

A.4 LHP nanocrystals – WAXS, PL, and mesophase analysis

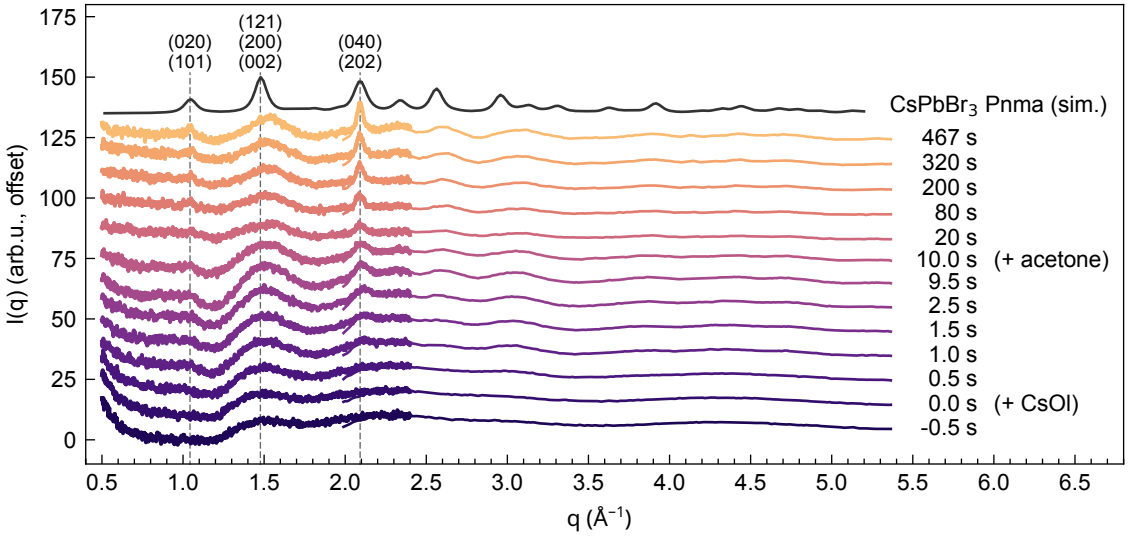

Figure A6: Selected in situ WAXS intensities of a 3ML nanorod synthesis beyond the antisolvent injection. Data are shown for selected reaction times, indicated by the labels. $t = 0\,\mathrm{s}$ corresponds to the Cs-oleate injection. At $t = 10\,\mathrm{s}$ acetone is injected as an antisolvent. This reduces the WAXS intensity, which later recovers due to growth of the nanorods. A simulated WAXS intensity of orthorhombic $CsPbBr_3$ is shown for comparison [186].

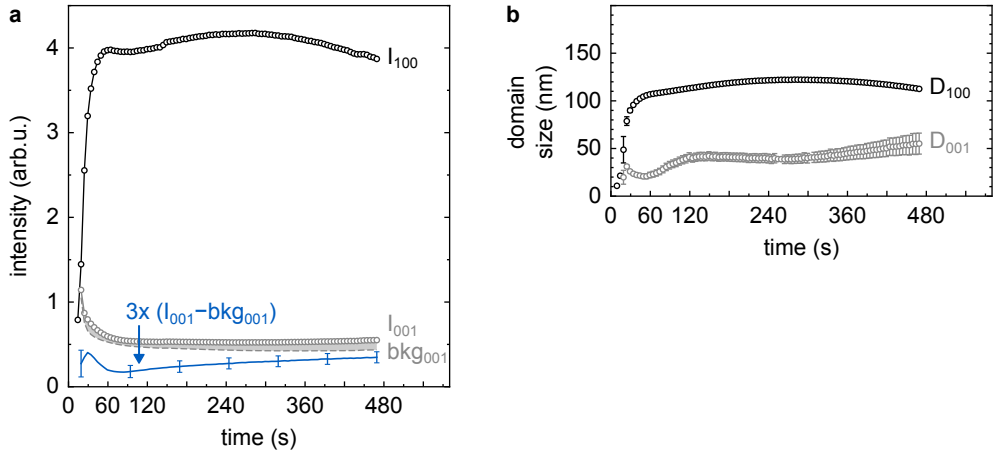

Figure A7: Background and domain size analysis of the (100) and (001) mesophase reflections. **a**, Peak intensity of the (1 0 0) and (0 0 1) mesophase reflections in the synthesis of 3ML nanorods, and background intensity at the (0 0 1) position (bkg_{001}). The small difference signal is shaded and plotted separately, scaled up 3×, in blue. **b**, Domain sizes extracted from the peak widths via Equation 2.39.

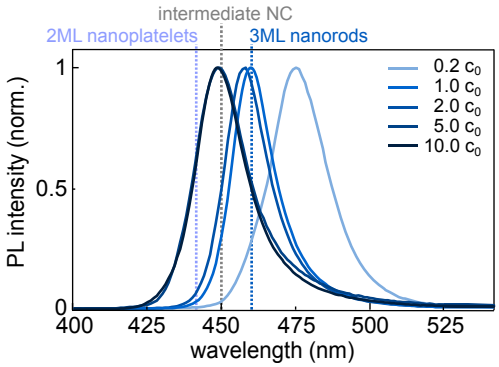

Figure A8: PL intensities of 3ML nanorod syntheses at different precursor concentration. Concentrations are given in the legend as a multiple of the default concentration c_0, given in Section 4.1.1. Low precursor concentrations (0.2 c_0) do not lead to mesophase assembly, and therefore to rather polydisperse nanocrystals and less quantum confined emission. Intermediate concentrations (1 to 5 c_0) produce 3ML nanorods (typical emission indicated by a vertical dashed line). At high concentrations nanocrystals do not grow any further inside the mesophase and therefore show the emission of intermediate nanoclusters (vertical dashed line). The emission of 2ML nanoplatelets is also shown for comparison.

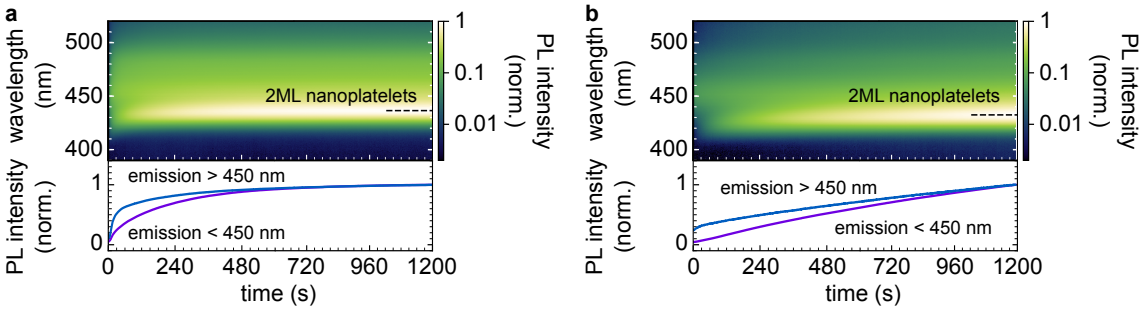

Figure A9: Evolution of PL intensity in syntheses without antisolvent. **a**, Synthesis using a reaction mixture for 3ML nanorods, leaving out the antisolvent. The PL emission indicates the formation of 2ML nanoplatelets. **b**, Synthesis using a reaction mixture for 2ML nanoplatelets, leaving out the antisolvent. Again, 2ML nanoplatelets are obtained, indicating that this is the thermodynamically stable polymorph at these precursor ratios. Bottom panels indicate the emission intensity in two bins, 415 to 450 nm and 450 to 470 nm.

Table A8: Polarity of antisolvents. Normalized $E_T(30)$ polarity value, dipole moment, Hansen hydrogen bonding parameter and donor number of the screened solvents. Solvents are sorted into categories based on their effect on the stability of intermediate nanoclusters and the shape and size of the reaction product.

solvent	$\mathbf{E_T(30)}$	μ **(D)**	δ_H $\mathbf{(MPa)^{1/2}}$	**DN (kcal/mol)**	**classification**
n-hexane	0.009	0.0	0.0	0.0	inert
toluene	0.099	0.375	2.0	0.1	inert
diethyl ether	0.117	1.150	5.1	19.2	weak
ethyl acetate	0.228	1.780	7.2	17.1	weak
methyl acetate	0.253	1.720	7.6	16.3	weak
cyclopentanone	0.269	3.300	5.2	18.0	moderate
acetophenone	0.306	3.020	3.7	15.0	moderate
butanone	0.327	2.779	5.1	17.4	moderate
acetone	0.355	2.860	7.0	17.0	moderate
dimethylformamide	0.386	3.820	11.3	26.6	strong
dimethylsulfoxide	0.444	3.960	10.2	29.8	strong
acetonitrile	0.460	3.925	6.1	14.1	strong
isopropanol	0.546	1.580	16.4	21.1	AX-selective
n-butanol	0.586	1.660	15.8	19.5	AX-selective
n-propanol	0.617	1.650	17.4	19.8	AX-selective
ethanol	0.654	1.680	19.4	19.2	AX-selective
methanol	0.762	1.700	22.3	19.0	AX-selective

Table A9: SAXS fit parameters for purified nanoplatelets and nanorods measured with a laboratory setup. Uncertainties are provided by the DREAM algorithm of SasView and correspond to 68 % confidence intervals. Nanoparticle SLD ($CsPbBr_3$): $32 \cdot 10^{-6}$Å^{-2}, solvent SLD (n-hexane): $6.5 \cdot 10^{-6}$Å^{-2}.

	2ML NPL (high resolution)	**3ML NR (high resolution)**
scale (arb.u.)	$(7.11 \pm 0.02) \cdot 10^{-4}$	$(1.774 \pm 0.002) \cdot 10^{-3}$
background (arb.u.)	$(3.67 \pm 0.07) \cdot 10^{-3}$	$(7.82 \pm 0.08) \cdot 10^{-3}$
polar diameter (nm)	1.724 ± 0.005	17.07 ± 0.07
(rel. PD in brackets)		(0.18 ± 0.02)
equatorial diameter (nm)	14.60 ± 0.02	2.05 ± 0.03
(rel. PD in brackets)		(0.69 ± 0.02)
χ^2	5.5646	5.264
	2ML NPL (low resolution)	**3ML NPL (low resolution)**
scale (arb.u.)	$(5.05 \pm 0.03) \cdot 10^{-4}$	$(1.50 \pm 0.02) \cdot 10^{-4}$
background (arb.u.)	$(1.1 \pm 0.2) \cdot 10^{-3}$	$(7.9 \pm 0.3) \cdot 10^{-4}$
polar diameter (nm)	1.67 ± 0.02	2.15 ± 0.03
(rel. PD in brackets)	(0.02)	
equatorial diameter (nm)	12.9 ± 0.2	10.38 ± 0.06
(rel. PD in brackets)	(0.22 ± 0.01)	
χ^2	2.4222	1.1786
	5ML NR (low resolution)	**7ML NPL (low resolution)**
scale (arb.u.)	$(8.17 \pm 0.07) \cdot 10^{-5}$	$(6.78 \pm 0.04) \cdot 10^{-5}$
background (arb.u.)	$(4.1 \pm 0.7) \cdot 10^{-5}$	$3 \cdot 10^{-4}$
polar diameter (nm)	14.1 ± 1.2	5.60 ± 0.04
(rel. PD in brackets)	(0.08)	(0.12 ± 0.03)
equatorial diameter (nm)	2.2 ± 0.2	11.9 ± 0.1
(rel. PD in brackets)	(0.83 ± 0.07)	(0.11 ± 0.02)
χ^2	0.88817	0.98613

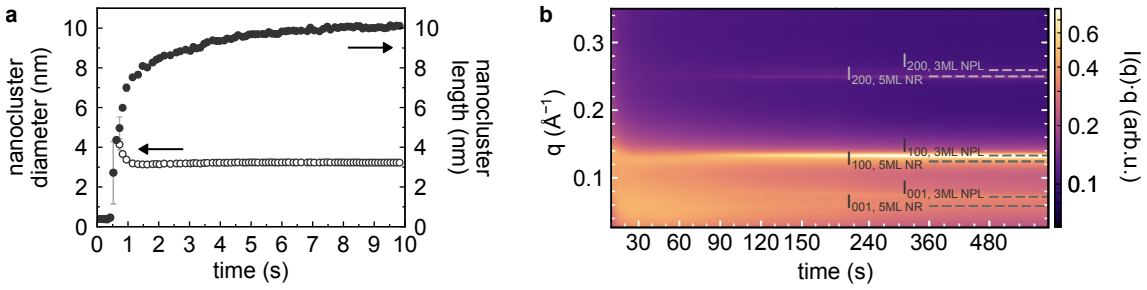

Figure A10: SAXS analysis of intermediate nanoclusters and mesophases at 50 °C. **a**, Intermediate nanocluster dimensions obtained from fits to in situ SAXS data following Cs-oleate injection at $t = 0$ s. **b**, In situ SAXS data after antisolvent injection at $t = 10$ s. Horizontal lines indicate the positions of mesophase reflections belonging to 5ML nanorods and 3ML nanoplatelets.

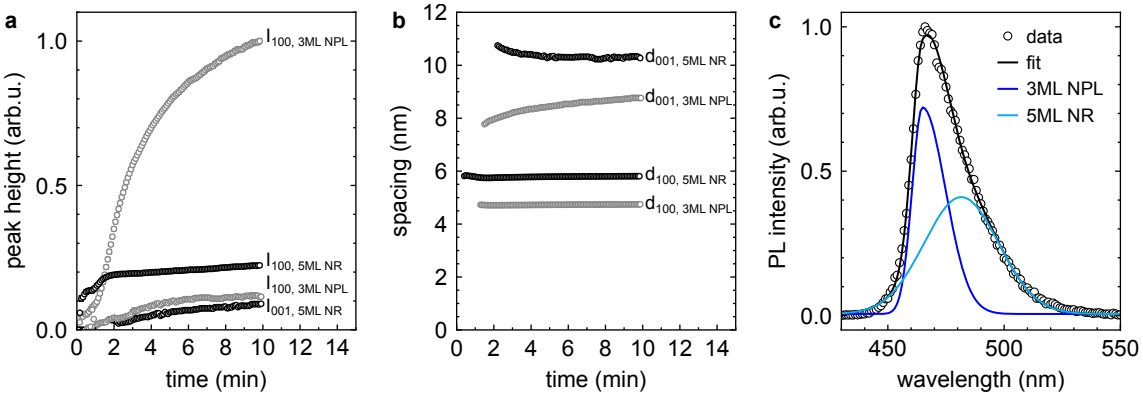

Figure A11: In situ SAXS and ex situ PL analysis of LHP nanocrystals synthesized at 50 °C. **a**, Mesophase peak height and **b**, lattice spacing of the mesophases of 5ML nanorods and 3ML nanoplatelets. Data is shown in Figure A10. **c**, Ex situ PL spectrum of a purified reaction product after synthesis at 50 °C with a two-component fit. 3ML nanoplatelets (emission at 465 nm, FWHM 17 nm) and 5ML nanorods (emission at 482 nm, FWHM 38 nm) are found in the spectrum. Ex situ PL data were recorded by Carola Lampe from the group of Prof. Dr. Alexander S. Urban, LMU.

A.5 LHP nanocrystals – post-synthetic modification

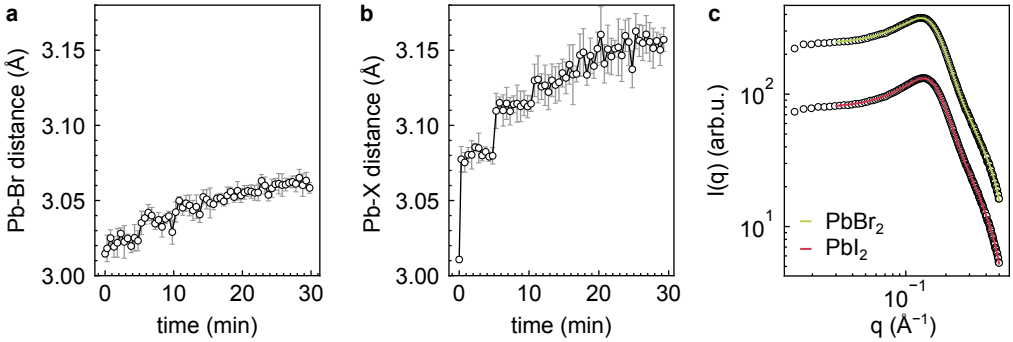

Figure A12: Evolution of the Pb–X distance for enhancement and ion exchange and SAXS of PbX_2 solutions. **a**, Pb–Br distance during addition of $PbBr_2$ to 3ML $CsPbBr_3$ nanorods. **b**, Pb–X distance during addition of PbI_2 to 3ML $CsPbBr_3$ nanorods. One injection every 5 min, distances obtained from a Pseudo-Voigt fit on a linear background to the first peak of $G(r)$ shown in Figure 4.25 c and Figure 4.26 c. **c**, SAXS intensities of PbX_2 salt solutions in n-hexane. Solid lines are fits to the data with a model of core-shell spheres interacting with a hard sphere structure factor. Fit parameters are given in Table A13.

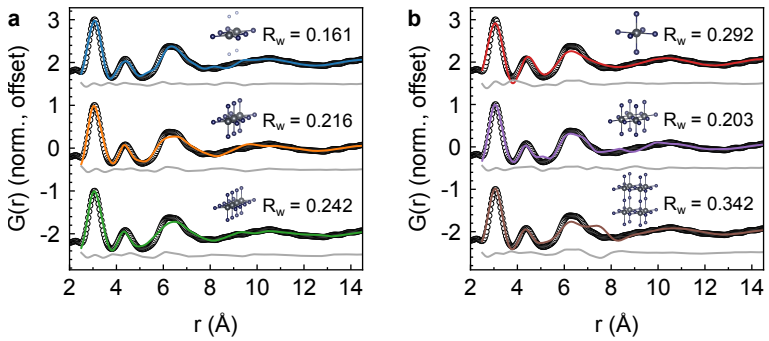

Figure A13: PDF fits of $PbBr_2$ clusters with different models. **a**, top to bottom: edge-sharing chain of two octahedra with Br in the equatorial and N in the polar positions, edge-sharing chain of three and four octahedra. **b**, single $PbBr_6^{4-}$ octahedron, 2x2 edge-sharing octahedra, 2x2x2 edge-sharing octahedra. The residual between data and fit is shown as a gray curve next to the graphs. The cluster motifs are shown as insets (Pb: black, Br: dark blue, N: light blue).

Table A10: PDF fit parameters for lead halide clusters. $G(r)$ was refined in a range from 2.5 to 20 Å with a step of 0.01 Å. The result is given for the best-fitting cluster model, an edge-sharing chain of two octahedra with Br in the equatorial and N in the polar positions, as shown in Figure A13

scale	δ_2(Å^2)	xscale	yscale	zscale	Pb_{Uiso}(Å^2)	Br_{Uiso}(Å^2)	R_w
0.585	2.577	0.964	1.097	1.077	0.112	0.029	0.161

Table A11: PDF fit parameters for LHP nanocrystals during post-synthetic modification. $G(r)$ was refined in a range from 2.5 to 20 Å with a step of 0.01 Å and a .cif file of orthorhombic (Pnma) $CsPbBr_3$ (COD 4510745) [339]. Fractional coordinates and atomic displacement parameters were also refined. Pb–Br bond angles are measured using the angle tool in VESTA [394], taking into account the lattice parameters and fractional coordinates.

	$PbBr_2$ modification 0 min	**$PbBr_2$ modification 4 min**	**PbI_2 ion exchange 0 min**	**PbI_2 ion exchange 4 min**
scale	2.797	1.019	0.889	0.507
δ_2(Å^2)	0.003	6.74	6.383	7.607
a (Å)	8.208	8.720	8.209	8.865
b (Å)	11.752	11.856	11.691	11.893
c (Å)	8.843	8.351	8.637	8.430
particle diameter (nm)	20.083	22.238	24.477	25.438
Pb–Br angle (axial, °)	173.7	157.0	164.6	169.8
Pb–Br angle (equatorial, °)	153.4	157.2	154.5	153.5
R_w	0.357	0.252	0.295	0.227

Table A12: Lattice parameters of LHPs used in the analysis. The unit cell volume V and the effective cubic lattice parameter $a_{\mathrm{effective}}$ are calculated from a, b, c. References starting with mp- are obtained from the Materials Project [340]. Lattice parameters marked with (*) were calculated from the peak position analyzed in the respective figure.

reference	**structure**	**a (Å)**	**b (Å)**	**c (Å)**	**V (Å^3)**	**$a_{\mathrm{effective}}$ (Å)**
COD 4510745	$CsPbBr_3$ orthorhombic	8.2440	11.7351	8.1982	793.128	5.831
mp-1014168	$CsPbBr_3$ tetragonal	8.4471	8.4471	11.9813	854.866	5.979
COD 1533063	$CsPbBr_3$ cubic	5.87			202.262	5.87
mp-1069538	$CsPbI_3$ cubic	6.414			263.868	6.414
[190], 634 K	$CsPbI_3$ cubic	6.2894				6.2894
this work, Figure 4.25, 0 min	$CsPbBr_3$ (*)					5.930
this work, Figure 4.25, 30 min	$CsPbBr_3$ (*)					5.914
this work, Figure 4.26, 0 min	$CsPbBr_3$ (*)					6.013
this work, Figure 4.26, 30 min	$CsPbBr_3$ (*)					6.252

Table A13: SAXS fit parameters for post-synthetic modification of LHP nanocrystals. For the $CsPbBr_3$ nanocrystals in n-hexane a core SLD of $32 \cdot 10^{-6}$Å^{-2} and a solvent SLD of $6.5 \cdot 10^{-6}$Å^{-2} were kept fixed. The different scale factors and χ^2 values arise from the fact that the data are not recorded on absolute scale. Note the large relative length polydispersity reaching the upper limit of 2 for the nanocrystals.

salt solutions		
scale (arb.u.)	137.44	194.54
background (arb.u.)	3.82	3.68
core diameter (nm)	1.39	1.40
shell thickness (nm)	2.22	2.14
core SLD (10^{-6}Å^{-2}, fixed)	46.4	42
shell SLD (10^{-6}Å^{-2})	9.77	9.4851
solvent SLD (10^{-6}Å^{-2}, fixed)	8	8
hard sphere volume fraction (unitless)	0.14	0.14
χ^2	9.27	26.8
nanocrystals		
scale (arb.u.)	0.50	0.73
background (arb.u.)	1.13	4.58
length (nm) (rel. PD in brackets)	8.16 (2)	8.21 (2)
diameter (nm) (rel. PD in brackets)	1.24 (1.05)	3.00 (0.23)
χ^2	535.7	763.4

A.6 Cu nanospheres – in situ SAXS analysis

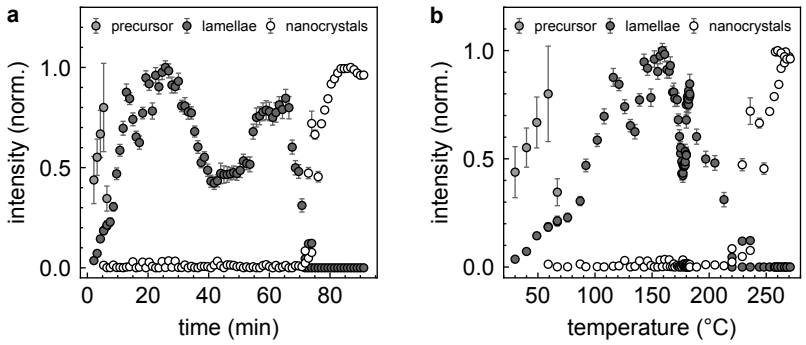

Figure A14: Decomposition of the Cu in situ SAXS data with a model fit. **a**, Normalized intensities of precursor, lamellae, and Cu nanocrystals as obtained from fits to the SAXS data, shown as a function of time. **b**, Data as in **a**, shown as a function of temperature. The precursor signal, an additional peak at $q = 0.227\,\text{Å}^{-1}$, is only visible at temperatures below 60 °C and corresponds to lamellar assemblies of TDPA molecules without intercalated metal ions.

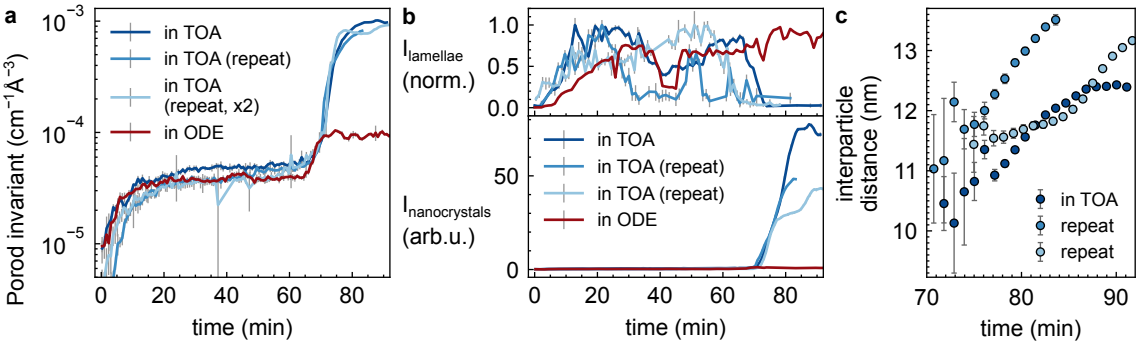

Figure A15: SAXS analysis of repeated Cu nanosphere syntheses and control experiments. a, Evolution of the Porod invariant for repeat experiments in TOA, showing a two-step behavior of lamellar intermediate formation and nanocrystal growth. The Porod invariant of a synthesis in ODE shows only a minor increase of the Porod invariant in the second heating ramp, indicating no nanocrystal formation (colors given in the legend). **b**, Intensity of the lamellar intermediate and of the growing nanocrystals, extracted from fits to the data, colors as shown in **a**. The synthesis in ODE (red lines) remains in the lamellar state and does not show the intensity of nanocrystals. **c**, Evolution of the interparticle distance in the syntheses in TOA shown in **a** and **b** showing non-saturating distance for the repeat experiments. This is presumably due to poorer quality of the lamellar intermediate because of less homogeneous heating and stirring. Also the lamellar intensity in **b** is fluctuating for the repeat experiments.

Table A14: Exemplary SAXS fit parameters and χ^2 of a Cu nanosphere synthesis at 90 min reaction time.

scale 1	**volume fraction 1** η	**diameter 1** (nm)	**relative PD** (unitless)
$(7.20 \pm 0.06) \cdot 10^{-4}$	0.418 ± 0.003	11.52 ± 0.03	0.139 ± 0.003
scale 2	**diameter 2** (nm)	**background** (cm^{-1})	χ^2
$(7.3 \pm 0.3) \cdot 10^{-6}$	20.8 ± 0.6	$(4.97 \pm 0.11) \cdot 10^{-2}$	7.76

Table A15: SAXS fit parameters and χ^2 for purified Cu nanospheres.

scale (volume fraction)	**background** (cm^{-1})	**SLD** (10^{-6} Å^{-2})	**SLD**$_{\text{solvent}}$ (10^{-6} Å^{-2})
$(2.470 \pm 0.008) \cdot 10^{-4}$	$(4.73 \pm 0.08) \cdot 10^{-3}$	69.9 (fixed)	6.49 (fixed)
diameter (nm)	**fuzziness** σ (nm)	**relative PD** (unitless)	χ^2
8.06 ± 0.03	0.385 ± 0.003	0.0665 ± 0.0006	9.69

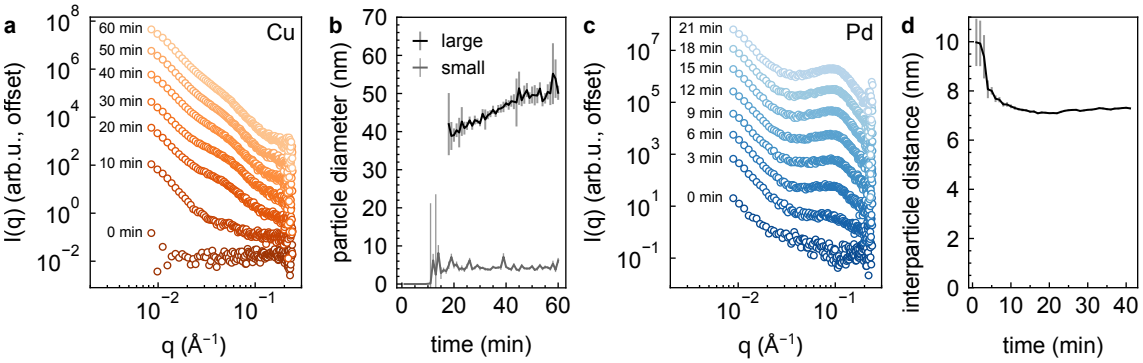

Figure A16: Characterization of Cu and Pd nanocrystal synthesis with in situ SAXS. a, Selected in situ SAXS data during the 220 °C plateau of a synthesis using only $Cu(acac)_2$ precursor. The SAXS intensity at 60 min shows two faint oscillations on top of a decaying curve and no clear plateau at low q. **b**, Analysis of the SAXS intensity from **a** by a sum of two polydisperse sphere form factors. A small diameter (approx. 4.4 nm) and a large diameter (40 to 50 nm) are found. **c**, Selected in situ SAXS data during the 190 °C plateau of a synthesis using only $Pd(acac)_2$ precursor. The intensity grows faster than for Cu and shows a power law decay with a superimposed broad peak. **d**, Interparticle distance obtained from the peak position in **c**. Assuming a 4 nm thick layer of ligands, approximately 3.2 nm diameter Pd nanocrystals form inside a dense agglomerate. Error bars in **b** and **d** indicate the propagated fit uncertainties.

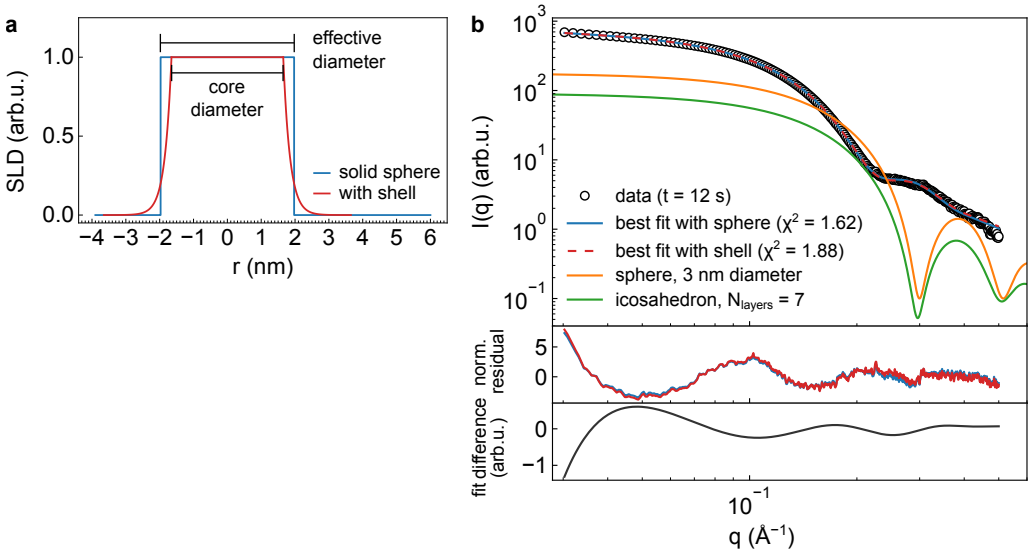

Figure A17: Fit of CuPd SAXS data with and without shell. a, Scattering length density profiles of the sphere model and the model of a sphere with a radially decaying shell. The diameter of the sphere without a shell serves as an effective particle diameter, which includes part of the contribution of the shell. **b**, Dots: SAXS data at the end of the growth phase ($t = 12$ min). Blue line: best fit using a model of solid, polydisperse spheres (mean diameter $D = 3.95$ nm, $\frac{\sigma_D}{D} = 0.138$). Red dashed line: best fit with an additional shell (mean core diameter $D_{\text{core}} = 3.30$ nm, $\frac{\sigma_D}{D_{\text{core}}} = 0.152$, $A = -5$, $\Delta t_{\text{shell}} = 1$ nm). Both models show similar residuals. This indicates that the presence of a shell cannot be directly proven from the SAXS data, but also does not contradict the observed intensity. In the lower panel the difference between the shell model and the sphere model is shown. The contribution of the shell is a low-frequency, small-amplitude oscillation and not a localized feature in the intensity curve. Orange line: exemplary model curve of spheres of 3 nm diameter, i.e., of the size obtained from PDF analysis. Green line: model curve of an icosahedral particle with seven layers, as found by PDF analysis. This model curve resembles the 3 nm spherical model but does not agree with the experimental data.

A.7 CuPd – further analysis

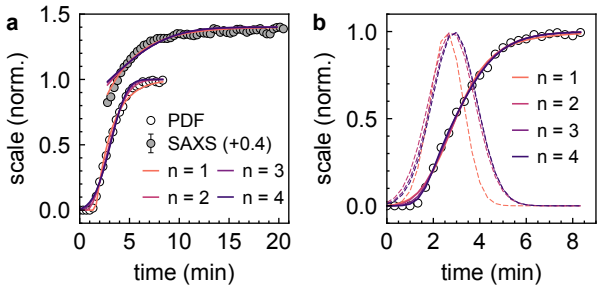

Figure A18: Modified JMAK and Gualtieri fits of PDF and SAXS data from CuPd nanocrystal syntheses. Open dots: normalized scale factor of the PDF analysis, filled dots: normalized scale factor of the SAXS analysis of a CuPd nanocrystal synthesis shown in Figure 4.36 a. **a**, Lines: fits with a modified JMAK equation, exponents given in the legend. **b**, Lines: fits with a modified Gualtieri equation, exponents given in the legend. Dashed lines: Corresponding distributions of nucleation times. All fit parameters are given in Table A16.

Table A16: Modified JMAK and Gualtieri fit results of CuPd syntheses. χ^2 takes into account the uncertainty of the data points where applicable.

CuPd PDF JMAK				
n (unitless)	$\mathbf{k_g}$ (min^{-1})	$\mathbf{t_0}$ (min)	-	χ^2
1	0.59 ± 0.02	1.59 ± 0.05	-	$9.1 \cdot 10^{-4}$
2	0.354 ± 0.008	0.63 ± 0.06	-	$3.0 \cdot 10^{-4}$
3	0.254 ± 0.010	-0.44 ± 0.14	-	$8.7 \cdot 10^{-4}$
4	0.198 ± 0.010	-1.54 ± 0.23	-	$1.3 \cdot 10^{-3}$
CuPd SAXS JMAK				
n (unitless)	$\mathbf{k_g}$ (min^{-1})	$\mathbf{t_0}$ (min)	-	χ^2
1	0.30 ± 0.02	0.57 ± 0.22	-	9.43
2	0.11 ± 0.01	-5.3 ± 0.8	-	17.9
3	0.07 ± 0.01	-11.5 ± 1.4	-	20.8
4	0.05 ± 0.01	-17.6 ± 1.9	-	22.3
CuPd PDF Gualtieri				
n (unitless)	$\mathbf{k_g}$ (min^{-1})	**a** (min)	**b** (min)	χ^2
1	0.53 ± 0.04	2.58 ± 0.07	0.71 ± 0.05	$5.5 \cdot 10^{-4}$
2	0.53 ± 0.20	2.79 ± 0.40	0.99 ± 0.18	$4.0 \cdot 10^{-4}$
3	0.54 ± 0.03	2.88 ± 0.05	0.98 ± 0.05	$1.9 \cdot 10^{-4}$
4	0.55 ± 0.02	2.92 ± 0.03	0.96 ± 0.03	$1.2 \cdot 10^{-4}$

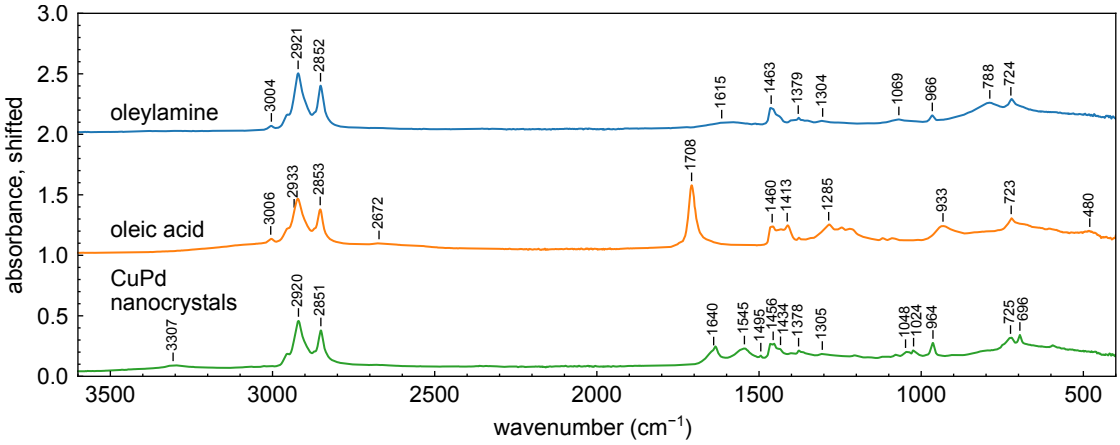

Figure A19: FTIR spectra of CuPd nanocrystals and pure ligands. Data were recorded and analyzed by Davide Derelli. CuPd nanocrystals were centrifuged and redispersed twice before measurement. The coinciding intense absorption bands indicate the presence of OlAm and OlAc ligands adsorbed on the surface of the CuPd nanocrystals.

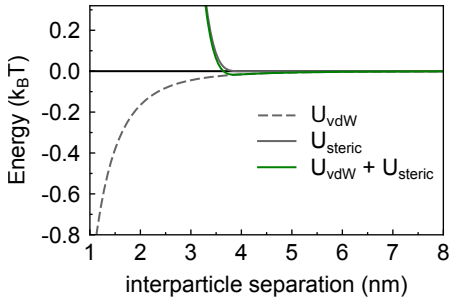

Figure A20: Estimation of the DLVO interaction potential of CuPd nanocrystals. The pairwise potential shows a minimum at an interparticle surface-to-surface separation of 3.9 nm with a depth of -0.02 k_BT. The main influence on the position and depth originates from the parameters chosen for the steric repulsion.

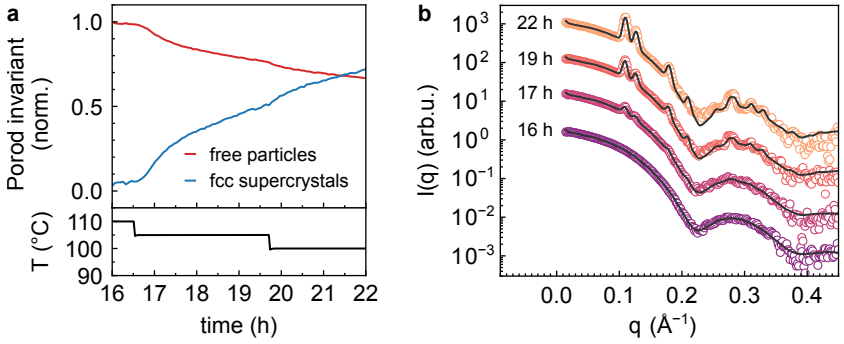

Figure A21: Evolution of CuPd fcc supercrystals in a laboratory in situ SAXS experiment. **a**, Porod invariants of a synthesis of CuPd supercrystals carried out in a laboratory SAXS setup. The temperature plateau for inducing the assembly is additionally shown. **b**, Selected in situ SAXS data from the synthesis shown in **a**, illustrating the direct assembly of free particles (16 h, 110 °C) into fcc supercrystals (22 h, 100 °C).

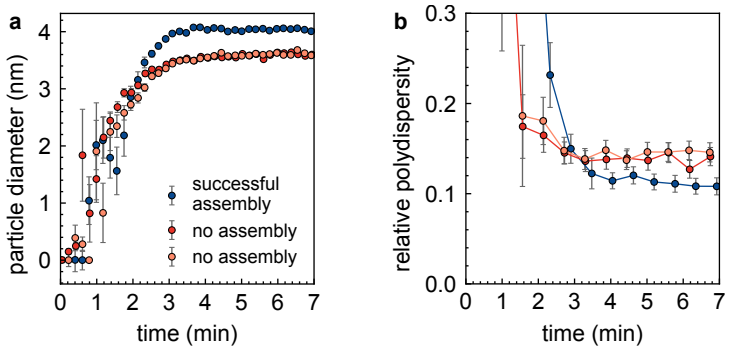

Figure A22: Effect of nanocrystal size and polydispersity on the supercrystal assembly. **a**, Particle diameter D obtained from SAXS fits of three individual in situ syntheses. Measurements were carried out with the laboratory SAXS setup (Table 3.6). A slight variation of initial growth rate and final particle diameter is observed, resulting from differences in heating and sealing of the in situ cell. Only the faster-growing, larger particles successfully assembled into supercrystals later. **b**, Corresponding relative polydispersity $\frac{\sigma_D}{D}$, legend as in **a**. Three consecutive data points are binned for clarity. Error bars indicate the standard deviation. Only the particles with lower polydispersity eventually formed an assembly ($\frac{\sigma_D}{D} = (11.2 \pm 0.7)\%$ compared to $(13.8 \pm 0.9)\%$ and $(14.6 \pm 0.6)\%$, respectively).

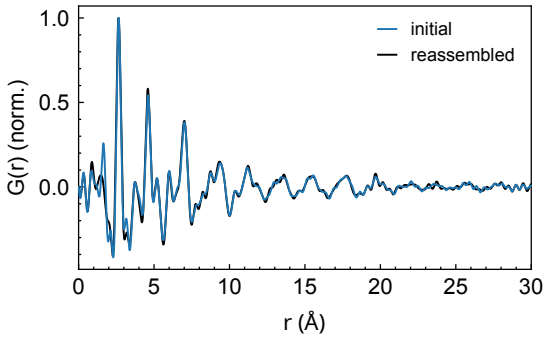

Figure A23: PDF of the nanocrystal cores before and after melting and reassembly. The curves are in very close agreement, showing that the nanocrystal cores are not altered by the melting and reassembly of the supercrystals. The differences are mainly at r smaller than the shortest interatomic distance in the metallic cores and are due to slightly different background subtraction. Data were processed by Davide Derelli.

A.8 CoO PDF and SAXS analysis

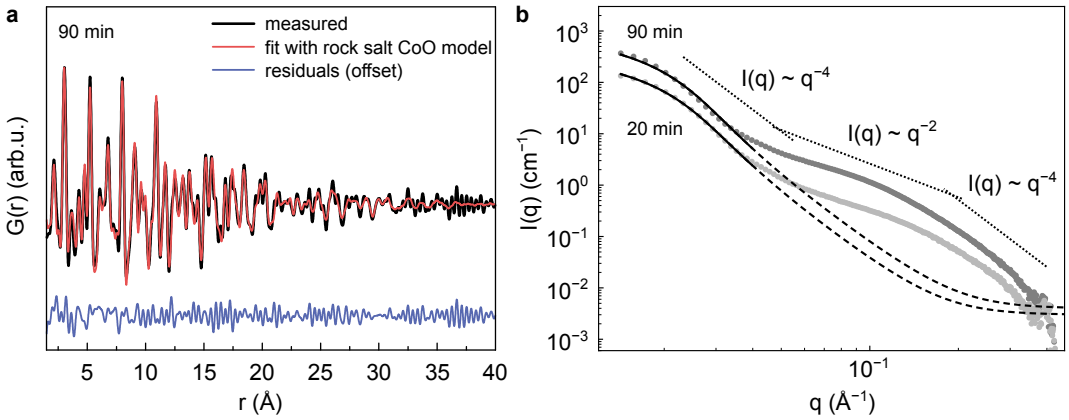

Figure A24: Exemplary PDF fit and laboratory SAXS fit of CoO assemblies. **a**, Measured $G(r)$ from an in situ synthesis at a reaction time of 90 min and fit with a model of rock salt CoO [429], $R_w = 0.233$. Data were analyzed by Cecilia Zito (UHH). **b**, Laboratory SAXS data of aliquots taken at 20 and 90 min reaction time, respectively, on absolute scale. Solid lines: Fitting range for the model of spherical assemblies. Dashed lines: Extension of the model to larger q, where the effects of the porous interior and rough surface dominate. Dotted lines: power laws as in Figure 4.45.

Table A17: Volume fractions of assemblies and concentrations of CoO obtained from laboratory SAXS data on absolute scale.

reaction time	**20 min**	**90 min**
volume fraction	$1.1 \cdot 10^{-4}$	$2.6 \cdot 10^{-4}$
concentration (mass)	0.74 mg/mL	1.65 mg/mL
concentration (amount)	$9.9 \cdot 10^{-3}$ mol/L	$2.2 \cdot 10^{-2}$ mol/L

Table A18: Densities and molar masses of materials.

chemical	**density (g/cm^3)**	**molar mass (g/mol)**
$CsPbBr_3$	4.55	579.82
Cu	8.96	63.546
Pd	12.02	106.42
CoO	6.45	74.93

A.9 Discussion, conclusion and outlook

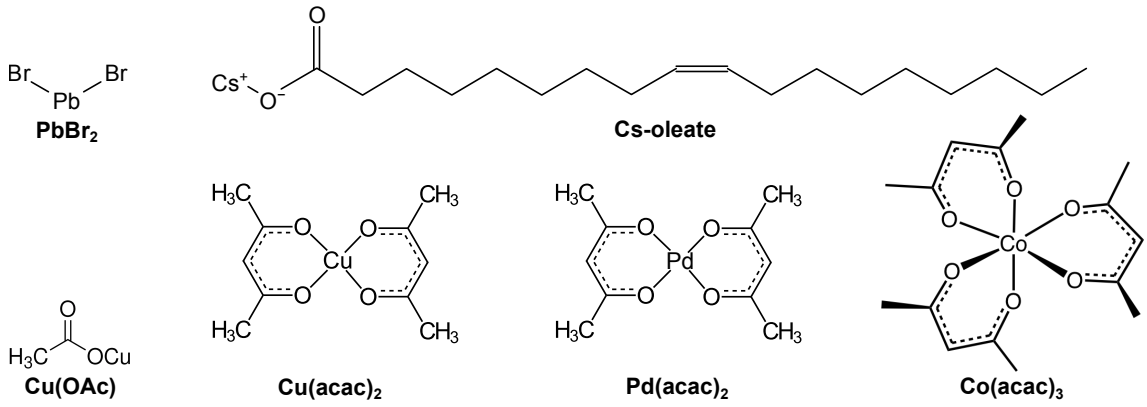

Figure A25: Simplified visualization of the structures of precursors used in this work. The precise local coordination by ligands and/or solvents in the actual reaction conditions is not shown. Note that $Co(acac)_3$ can exist as two enantiomers.

Table A19: Calculated and measured volume fractions of (intermediate) nanocrystals. The volume fractions are estimated from the precursor and solvent volumes and compared to measured values from SAXS data on absolute scale. Precursor and solvent amounts are given in Tables 3.1 and 3.4, molar masses and densities of the components in Table A18. *Calculated* values are based on molar concentrations (bold). They assume full precursor conversion, limited by the least abundant precursor. For LHP syntheses, c_0 denotes the default concentration. *Measured* values are based on the scale factor of SAXS data on absolute scale, which represents the volume fraction of particles (italic). The measured volume fraction of purified Cu nanospheres is approximately three times smaller than the calculated value. This deviation is due to the resuspension of the product in an arbitrary amount of solvent. The measured volume fraction of a CoO aliquot taken at 90 min is approximately five times lower than expected from a full precursor conversion. This is likely due to the assumption of the bulk CoO density in the SAXS analysis, which neglects the internal pores, and the incomplete fit of the SAXS model at large q values.

sample	**concentration (amount)**	**concentration (mass)**	**volume fraction**
LHP ($CsPbBr_3$) synthesis before antisolvent			
3ML NR (c_0)	$\mathbf{1.8 \cdot 10^{-3}}$ **mol/L**	1.04 mg/mL	$2.3 \cdot 10^{-4}$
2ML NPL (c_0)	$\mathbf{9.5 \cdot 10^{-4}}$ **mol/L**	0.55 mg/mL	$1.2 \cdot 10^{-4}$
LHP ($CsPbBr_3$) synthesis after antisolvent			
3ML NR (c_0)	$\mathbf{8.2 \cdot 10^{-4}}$ **mol/L**	0.48 mg/mL	$1.1 \cdot 10^{-4}$
2ML NPL (c_0)	$\mathbf{5.8 \cdot 10^{-4}}$ **mol/L**	0.34 mg/mL	$7.5 \cdot 10^{-5}$
Cu nanosphere synthesis	**0.1 mol/L**	6.35 mg/mL	$7.1 \cdot 10^{-4}$
purified Cu nanospheres (measured, Table A15)	0.035 mol/L	2.2 mg/mL	$\mathit{2.47 \cdot 10^{-4}}$
CuPd nanocrystal synthesis	**0.15 mol/L**	11.79 mg/mL	$1.2 \cdot 10^{-3}$
CoO nanoassembly synthesis	**0.1 mol/L**	7.49 mg/mL	$1.2 \cdot 10^{-3}$
CoO nanoassemblies (measured, Table A17)	0.022 mol/L	1.65 mg/mL	$\mathit{2.6 \cdot 10^{-4}}$

Table A20: Volume fractions of nanocrystals inside mesophases and assemblies. V_{cell} is the unit cell volume. "2D hex." indicates a 2D hexagonal, "lam." a lamellar assembly. V_{NC} is the nanocrystal volume including shell. V_{core} is the nanocrystal core volume. Core volumes for LHP synthesis are calculated from the lattice parameters assuming a cuboidal shape of the core. All other values assume a spherical shape. Uncertainties are 95% confidence intervals provided by the DREAM algorithm. Bold values are calculated as $V_{\mathrm{core}}/V_{\mathrm{cell}}$. Italic values are calculated as $\eta \frac{V_{\mathrm{core}}}{V_{\mathrm{effective}}}$. η and $V_{\mathrm{effective}}$ are the volume fraction and hard sphere volume in the structure factor, respectively (see Equation 2.25). (*) is calculated as $0.74 \frac{V_{\mathrm{core}}}{V_{\mathrm{effective}}}$, assuming an fcc packing in which spheres of $V_{\mathrm{effective}}$ are in direct contact.

sample	**lattice parameters**	$\mathbf{V_{cell}}$ **(nm^3)**	$\mathbf{V_{NC}}$ **(nm^3)**	$\mathbf{V_{core}}$ **(nm^3)**	**volume fraction of cores**
LHP ($CsPbBr_3$) synthesis after antisolvent					
3ML NR (c_0) initial	2D hex., $(4.8 \times 4.8 \times 10.5)\,\mathrm{nm}^3$	105	-	24	*0.23*
3ML NR (c_0) final	2D hex., $(4.9 \times 4.9 \times 13.5)\,\mathrm{nm}^3$	140	-	38	*0.27*
2ML NPL (c_0) initial	lam., $(4.4 \times 11 \times 11)\,\mathrm{nm}^3$	532	-	90	*0.17*
2ML NPL (c_0) final	lam., $(4.4 \times 12.5 \times 12.5)\,\mathrm{nm}^3$	688	-	126	*0.18*
Cu nanosphere synthesis initial	-	-	-	226	0.18 ± 0.03
Cu nanosphere synthesis final	-	-	-	813	0.42 ± 0.02
CuPd synthesis, SRO phase initial	-	-	380	141	**0.18**
CuPd synthesis, SRO phase final	-	-	220	141	**0.27**
CuPd synthesis, fcc supercrystal	10.24 nm	1074	199	141	0.52 (*)

Bibliography

[1] Montanarella, F. & Kovalenko, M. V. Three millennia of nanocrystals. *ACS Nano* **16**, 5085–5102 (2022). doi: 10.1021/acsnano.1c11159. (cited on pages 1, 5, 21, and 22).

[2] Protesescu, L. *et al.* Nanocrystals of cesium lead halide perovskites ($CsPbX_3$, X = Cl, Br, and I): novel optoelectronic materials showing bright emission with wide color gamut. *Nano Lett.* **15**, 3692–3696 (2015). doi: 10.1021/nl5048779. (cited on pages 1, 18, 19, 20, 21, and 95).

[3] Noguez, C. Surface plasmons on metal nanoparticles: The influence of shape and physical environment. *J. Phys. Chem. C* **111**, 3806–3819 (2007). doi: 10.1021/jp066539m. (cited on pages 1 and 22).

[4] Boles, M. A., Ling, D., Hyeon, T. & Talapin, D. V. The surface science of nanocrystals. *Nat. Mater.* **15**, 141–153 (2016). doi: 10.1038/nmat4526. (cited on page 1).

[5] Kagan, C. R., Lifshitz, E., Sargent, E. H. & Talapin, D. V. Building devices from colloidal quantum dots. *Science* **353**, aac5523 (2016). doi: 10.1126/science.aac5523. (cited on pages 1 and 25).

[6] Park, Y.-S., Roh, J., Diroll, B. T., Schaller, R. D. & Klimov, V. I. Colloidal quantum dot lasers. *Nat. Rev. Mater.* **6**, 382–401 (2021). doi: 10.1038/s41578-020-00274-9. (cited on page 1).

[7] Carey, G. H. *et al.* Colloidal quantum dot solar cells. *Chem. Rev.* **115**, 12732–12763 (2015). doi: 10.1021/acs.chemrev.5b00063. (cited on page 1).

[8] Fan, J. *et al.* Recent progress of quantum dots light-emitting diodes: Materials, device structures, and display applications. *Adv. Mater.* **36** (2024). doi: 10.1002/adma.202312948. (cited on page 1).

[9] Medintz, I. L., Uyeda, H. T., Goldman, E. R. & Mattoussi, H. Quantum dot bioconjugates for imaging, labelling and sensing. *Nat. Mater.* **4**, 435–446 (2005). doi: 10.1038/nmat1390. (cited on page 1).

[10] García de Arquer, F. P. *et al.* Semiconductor quantum dots: Technological progress and future challenges. *Science* **373** (2021). doi: 10.1126/science.aaz8541. (cited on page 1).

[11] Tao, A. R., Habas, S. & Yang, P. Shape control of colloidal metal nanocrystals. *Small* **4**, 310–325 (2008). doi: 10.1002/smll.200701295. (cited on pages 1, 5, and 7).

[12] Hens, Z. & De Roo, J. Atomically precise nanocrystals. *J. Am. Chem. Soc.* **142**, 15627–15637 (2020). doi: 10.1021/jacs.0c05082. (cited on pages 1 and 23).

[13] Sun, C., Jiang, Y., Zhang, L., Wei, K. & Yuan, M. Toward the controlled synthesis of lead halide perovskite nanocrystals. *ACS Nano* **17**, 17600–17609 (2023). doi: 10.1021/acsnano.3c05609. (cited on pages 1, 21, 72, 133, and 134).

[14] Nobel Prize Outreach. The Nobel Prize in Chemistry 2023. URL https://www.nobelprize.org/prizes/chemistry/2023/summary/. Accessed: March 11, 2025. (cited on page 1).

[15] LaMer, V. K. & Dinegar, R. H. Theory, production and mechanism of formation of monodispersed hydrosols. *J. Am. Chem. Soc.* **72**, 4847–4854 (1950). doi: 10.1021/ja01167a001. (cited on pages 1, 2, and 5).

[16] Turkevich, J. Colloidal gold. Part I: Historical and preparative aspects, morphology and structure. *Gold Bull.* **18**, 86–91 (1985). doi: 10.1007/bf03214690. (cited on pages 1 and 23).

[17] Murray, C. B., Norris, D. J. & Bawendi, M. G. Synthesis and characterization of nearly monodisperse CdE (E = sulfur, selenium, tellurium) semiconductor nanocrystallites. *J. Am. Chem. Soc.* **115**, 8706–8715 (1993). doi: 10.1021/ja00072a025. (cited on pages 1 and 37).

[18] Shi, Y. *et al.* Noble-metal nanocrystals with controlled shapes for catalytic and electrocatalytic applications. *Chem. Rev.* **121**, 649–735 (2020). doi: 10.1021/acs.chemrev.0c00454. (cited on pages 1, 22, 23, and 24).

[19] Kovalenko, M. V., Protesescu, L. & Bodnarchuk, M. I. Properties and potential optoelectronic applications of lead halide perovskite nanocrystals. *Science* **358**, 745–750 (2017). doi: 10.1126/science.aam7093. (cited on pages 1 and 17).

[20] Dey, A. *et al.* State of the art and prospects for halide perovskite nanocrystals. *ACS Nano* **15**, 10775–10981 (2021). doi: 10.1021/acsnano.0c08903. (cited on pages 1, 9, 17, 18, 19, 20, and 21).

[21] Ning, W. & Gao, F. Structural and functional diversity in lead-free halide perovskite materials. *Adv. Mater.* **31** (2019). doi: 10.1002/adma.201900326. (cited on page 1).

[22] Gawande, M. B. *et al.* Cu and Cu-based nanoparticles: Synthesis and applications in catalysis. *Chem. Rev.* **116**, 3722–3811 (2016). doi: 10.1021/acs.chemrev.5b00482. (cited on pages 1 and 23).

[23] Ferrando, R., Jellinek, J. & Johnston, R. L. Nanoalloys: From theory to applications of alloy clusters and nanoparticles. *Chem. Rev.* **108**, 845–910 (2008). doi: 10.1021/cr040090g. (cited on pages 1 and 24).

[24] Zhou, Z.-R., Liao, Z.-H. & Wang, F. Shape-controlled synthesis of one-dimensional cesium lead halide perovskite nanocrystals: methods and advances. *J. Mater. Chem. C* **11**, 3409–3427 (2023). doi: 10.1039/d2tc05211c. (cited on pages 1, 21, and 22).

[25] Otero-Martínez, C. *et al.* Colloidal metal-halide perovskite nanoplatelets: Thickness-controlled synthesis, properties, and application in light-emitting diodes. *Adv. Mater.* **34**, 2107105 (2022). doi: 10.1002/adma.202107105. (cited on pages 1, 8, 19, 21, 70, 71, and 86).

[26] Ye, J. *et al.* Direct linearly polarized electroluminescence from perovskite nanoplatelet superlattices. *Nat. Photon.* **18**, 586–594 (2024). doi: 10.1038/s41566-024-01398-y. (cited on pages 1, 21, 25, and 26).

[27] Boles, M. A., Engel, M. & Talapin, D. V. Self-assembly of colloidal nanocrystals: From intricate structures to functional materials. *Chem. Rev.* **116**, 11220–11289 (2016). doi: 10.1021/acs.chemrev.6b00196. (cited on pages 1, 2, 6, 9, 11, 12, 13, 25, 26, 27, and 135).

[28] Sugi, K. S., Maier, A. & Scheele, M. Emergent properties in supercrystals of atomically precise nanoclusters and colloidal nanocrystals. *Chem. Commun.* **58**, 6998–7017 (2022). doi: 10.1039/d2cc00778a. (cited on pages 1, 25, 26, and 135).

[29] Rainò, G. *et al.* Superfluorescence from lead halide perovskite quantum dot superlattices. *Nature* **563**, 671–675 (2018). doi: 10.1038/s41586-018-0683-0. (cited on pages 1, 20, 25, and 26).

[30] Choi, J.-H. *et al.* Exploiting the colloidal nanocrystal library to construct electronic devices. *Science* **352**, 205–208 (2016). doi: 10.1126/science.aad0371. (cited on pages 1, 24, and 25).

[31] Szychowski, B., Pelton, M. & Daniel, M.-C. Preparation and properties of plasmonic-excitonic nanoparticle assemblies. *Nanophotonics* **8**, 517–547 (2019). doi: 10.1515/nanoph-2018-0168. (cited on pages 1 and 26).

[32] Han, H. *et al.* Multiscale hierarchical structures from a nanocluster mesophase. *Nat. Mater.* **21**, 518–525 (2022). doi: 10.1038/s41563-022-01223-3. (cited on pages 1 and 27).

[33] Loiudice, A. & Buonsanti, R. Reaction intermediates in the synthesis of colloidal nanocrystals. *Nat. Synth.* **1**, 344–351 (2022). doi: 10.1038/s44160-022-00056-x. (cited on pages 1, 2, 6, 7, and 144).

[34] Akkerman, Q. A. *et al.* Controlling the nucleation and growth kinetics of lead halide perovskite quantum dots. *Science* **377**, 1406–1412 (2022). doi: 10.1126/science.abq3616. (cited on pages 2, 16, 20, 21, and 92).

[35] Kuno, M., Gushchina, I., Toso, S. & Trepalin, V. No one size fits all: Semiconductor nanocrystal sizing curves. *J. Phys. Chem. C* **126**, 11867–11874 (2022). doi: 10.1021/acs.jpcc.2c04734. (cited on pages 2, 20, and 143).

[36] Dahl, J. C., Wang, X., Huang, X., Chan, E. M. & Alivisatos, A. P. Elucidating the weakly reversible Cs–Pb–Br perovskite nanocrystal reaction network with high-throughput maps and transformations. *J. Am. Chem. Soc.* **142**, 11915–11926 (2020). doi: 10.1021/jacs.0c04997. (cited on pages 2 and 6).

[37] Koziej, D. Revealing complexity of nanoparticle synthesis in solution by in situ hard X-ray spectroscopy – today and beyond. *Chem. Mater.* **28**, 2478–2490 (2016). doi: 10.1021/acs.chemmater.6b00486. (cited on pages 2, 14, 45, and 46).

[38] Li, T., Senesi, A. J. & Lee, B. Small angle X-ray scattering for nanoparticle research. *Chem. Rev.* **116**, 11128–11180 (2016). doi: 10.1021/acs.chemrev.5b00690. (cited on pages 2, 14, 29, 30, 31, and 33).

[39] Terban, M. W. & Billinge, S. J. Structural analysis of molecular materials using the pair distribution function. *Chem. Rev.* **122**, 1208–1272 (2021). doi: 10.1021/acs.chemrev.1c00237. (cited on pages 2, 37, 39, and 40).

[40] Bertolotti, F., Moscheni, D., Guagliardi, A. & Masciocchi, N. When crystals go nano – the role of advanced X-ray total scattering methods in nanotechnology. *Eur. J. Inorg. Chem.* **2018**, 3789–3803 (2018). doi: 10.1002/ejic.201800534. (cited on pages 2 and 37).

[41] Reiss, H. The growth of uniform colloidal dispersions. *J. Chem. Phys.* **19**, 482–487 (1951). doi: 10.1063/1.1748251. (cited on pages 2 and 5).

[42] Jehannin, M., Rao, A. & Cölfen, H. New horizons of nonclassical crystallization. *J. Am. Chem. Soc.* **141**, 10120–10136 (2019). doi: 10.1021/jacs.9b01883. (cited on pages 2, 6, and 25).

[43] Lee, J., Yang, J., Kwon, S. G. & Hyeon, T. Nonclassical nucleation and growth of inorganic nanoparticles. *Nat. Rev. Mater.* **1**, 1–16 (2016). doi: 10.1038/natrevmats.2016.34. (cited on pages 2, 5, 6, and 7).

[44] Calvin, J. J., Brewer, A. S. & Alivisatos, A. P. The role of organic ligand shell structures in colloidal nanocrystal synthesis. *Nat. Synth.* **1**, 127–137 (2022). doi: 10.1038/s44160-022-00025-4. (cited on pages 2, 8, 12, and 17).

[45] Tutantsev, A. S. *et al.* New pigeonholing approach for selection of solvents relevant to lead halide perovskite processing. *J. Phys. Chem. C* **124**, 11117–11123 (2020). doi: 10.1021/acs.jpcc.0c03661. (cited on pages 2, 9, 90, and 91).

[46] Gholami, T. *et al.* A review on investigating the effect of solvent on the synthesis, morphology, shape and size of nanostructures. *Mater. Sci. Eng. B* **304**, 117370 (2024). doi: 10.1016/j.mseb.2024.117370. (cited on pages 2 and 9).

[47] Mahmood, A. U., Rizvi, M. H., Tracy, J. B. & Yingling, Y. G. Solvent effects in ligand stripping behavior of colloidal nanoparticles. *ACS Nano* **17**, 13319–13332 (2023). doi: 10.1021/acsnano.3c01313. (cited on pages 2, 17, 83, 87, 91, and 136).

[48] Xie, J. *et al.* Efficient interfacial synthesis strategy for perovskite $CsPbBr_3$ nanorods in the biphase solution. *Adv. Mater. Technologies* **7**, 2200131 (2022). doi: 10.1002/admt.202200131. (cited on pages 2, 9, and 21).

[49] Akkerman, Q. A. *et al.* Solution synthesis approach to colloidal cesium lead halide perovskite nanoplatelets with monolayer-level thickness control. *J. Am. Chem. Soc.* 1010–1016 (2016). doi: 10.1021/jacs.5b12124. (cited on pages 2 and 21).

[50] Gaponik, N., Talapin, D. V., Rogach, A. L., Eychmüller, A. & Weller, H. Efficient phase transfer of luminescent thiol-capped nanocrystals: from water to nonpolar organic solvents. *Nano Lett.* **2**, 803–806 (2002). doi: 10.1021/nl025662w. (cited on pages 2, 9, and 91).

[51] Talapin, D. V., Lee, J.-S., Kovalenko, M. V. & Shevchenko, E. V. Prospects of colloidal nanocrystals for electronic and optoelectronic applications. *Chem. Rev.* **110**, 389–458 (2010). doi: 10.1021/cr900137k. (cited on page 5).

[52] Reiss, P. *Semiconductor Nanocrystal Quantum Dots - Synthesis, Assembly, Spectroscopy and Applications*, chap. 2 (Springer Vienna, 2008). doi: 10.1007/978-3-211-75237-1. (cited on pages 5 and 9).

[53] Mozaffari, S. *et al.* The role of nanoparticle size and ligand coverage in size focusing of colloidal metal nanoparticles. *Nanoscale Adv.* **1**, 4052–4066 (2019). doi: 10.1039/c9na00348g. (cited on page 6).

[54] *The IUPAC Compendium of Chemical Terminology: The Gold Book* (International Union of Pure and Applied Chemistry (IUPAC), 2025). doi: 10.1351/goldbook. (cited on pages 6, 7, 10, 31, 60, and 63).

[55] De Yoreo, J. J. *et al.* Crystallization by particle attachment in synthetic, biogenic, and geologic environments. *Science* **349**, aaa6760 (2015). doi: 10.1126/science.aaa6760. (cited on pages 6, 7, and 25).

[56] Sturm (née Rosseeva), E. V. & Cölfen, H. Mesocrystals: structural and morphogenetic aspects. *Chem. Soc. Rev.* **45**, 5821–5833 (2016). doi: 10.1039/c6cs00208k. (cited on pages 6 and 13).

[57] Calcaterra, H. A. *et al.* Hints of growth mechanism left in supercrystals. *ACS Nano* **17**, 15999–16007 (2023). doi: 10.1021/acsnano.3c04365. (cited on pages 6 and 120).

[58] Salzmann, B. B., Van Der Sluijs, M. M., Soligno, G. & Vanmaekelbergh, D. Oriented attachment: from natural crystal growth to a materials engineering tool. *Acc. Chem. Res.* **54**, 787–797 (2021). doi: 10.1021/acs.accounts.0c00739. (cited on page 6).

[59] Wang, F., Richards, V. N., Shields, S. P. & Buhro, W. E. Kinetics and mechanisms of aggregative nanocrystal growth. *Chem. Mater.* **26**, 5–21 (2014). doi: 10.1021/cm402139r. (cited on pages 6 and 25).

[60] ten Wolde, P. R. & Frenkel, D. Enhancement of protein crystal nucleation by critical density fluctuations. *Science* 1975–1978 (1997). doi: 10.1126/science.277.5334.1975. (cited on pages 6 and

135).

[61] Zhang, F. *et al.* Charge-controlled metastable liquid–liquid phase separation in protein solutions as a universal pathway towards crystallization. *Soft Matter* **8**, 1313–1316 (2012). doi: 10.1039/c2Sm07008a. (cited on pages 6 and 135).

[62] Lee, S., Teich, E. G., Engel, M. & Glotzer, S. C. Entropic colloidal crystallization pathways via fluid–fluid transitions and multidimensional prenucleation motifs. *Proc. Natl. Acad. Sci. U.S.A.* **116**, 14843–14851 (2019). doi: 10.1073/pnas.1905929116. (cited on page 6).

[63] Tanner, C. P. N. *et al.* Enhancing nanocrystal superlattice self-assembly near a metastable liquid binodal. *ArXiv preprint* (2024). doi: 10.48550/arXiv.2404.16808. (cited on pages 6 and 135).

[64] Peng, Z. A. & Peng, X. Nearly monodisperse and shape-controlled CdSe nanocrystals via alternative routes: nucleation and growth. *J. Am. Chem. Soc.* **124**, 3343–3353 (2002). doi: 10.1021/ja0173167. (cited on page 6).

[65] Gary, D. C., Terban, M. W., Billinge, S. J. L. & Cossairt, B. M. Two-step nucleation and growth of inp quantum dots via magic-sized cluster intermediates. *Chem. Mater.* **27**, 1432–1441 (2015). doi: 10.1021/acs.chemmater.5b00286. (cited on page 6).

[66] Gebauer, D., Kellermeier, M., Gale, J. D., Bergström, L. & Cölfen, H. Pre-nucleation clusters as solute precursors in crystallisation. *Chem. Soc. Rev.* **43**, 2348–2371 (2014). doi: 10.1039/c3cs60451a. (cited on page 6).

[67] Busatto, S. & de Mello Donega, C. Magic-size semiconductor nanostructures: Where does the magic come from? *ACS Mater. Au* **2**, 237–249 (2022). doi: 10.1021/acsmaterialsau.1c00075. (cited on page 6).

[68] Pun, A. B., Mazzotti, S., Mule, A. S. & Norris, D. J. Understanding discrete growth in semiconductor nanocrystals: Nanoplatelets and magic-sized clusters. *Acc. Chem. Res.* **54**, 1545–1554 (2021). doi: 10.1021/acs.accounts.0c00859. (cited on page 6).

[69] Nevers, D. R. *et al.* Mesophase formation stabilizes high-purity magic-sized clusters. *J. Am. Chem. Soc.* **140**, 3652–3662 (2018). doi: 10.1021/jacs.7b12175. (cited on pages 6, 7, 14, 15, and 17).

[70] Mule, A. S. *et al.* Unraveling the growth mechanism of magic-sized semiconductor nanocrystals. *J. Am. Chem. Soc.* **143**, 2037–2048 (2021). doi: 10.1021/jacs.0c12185. (cited on page 6).

[71] Gromova, M. *et al.* Growth mechanism and surface state of $CuInS_2$ nanocrystals synthesized with dodecanethiol. *J. Am. Chem. Soc.* **139**, 15748–15759 (2017). doi: 10.1021/jacs.7b07401. (cited on pages 6 and 16).

[72] Abécassis, B. *et al.* Real-time in situ probing of high-temperature quantum dots solution synthesis. *Nano Lett.* **15**, 2620–2626 (2015). doi: 10.1021/acs.nanolett.5b00199. (cited on pages 6, 16, and 106).

[73] Liu, Y.-H., Wang, F., Wang, Y., Gibbons, P. C. & Buhro, W. E. Lamellar assembly of cadmium selenide nanoclusters into quantum belts. *J. Am. Chem. Soc.* **133**, 17005–17013 (2011). doi: 10.1021/ja206776g. (cited on page 7).

[74] van der Stam, W. *et al.* In situ probing of stack-templated growth of ultrathin $Cu_{2-x}S$ nanosheets. *Chem. Mater.* **28**, 6381–6389 (2016). doi: 10.1021/acs.chemmater.6b02787. (cited on pages 7, 16, 21, 86, 108, and 134).

[75] Jones, R. A. L. *Soft Condensed Matter*. Oxford Master Series in Physics (Oxford University Press, London, England, 2002). doi: 10.1088/0143-0807/23/6/703. (cited on pages 7 and 12).

[76] Cahn, J. W. On spinodal decomposition. *Acta Metallurgica* **9**, 795–801 (1961). doi: 10.1016/0001-6160(61)90182-1. (cited on page 7).

[77] Coropceanu, I. *et al.* Self-assembly of nanocrystals into strongly electronically coupled all-inorganic supercrystals. *Science* **375**, 1422–1426 (2022). doi: 10.1126/science.abm6753. (cited on pages 7, 13, 16, and 135).

[78] *International Tables for Crystallography: International Tables Online* (International Union of Crystallography). doi: 10.1107/97809553602060000001. (cited on pages 8 and 35).

[79] de Nijs, B. *et al.* Entropy-driven formation of large icosahedral colloidal clusters by spherical confinement. *Nat. Mater.* **14**, 56–60 (2014). doi: 10.1038/nmat4072. (cited on pages 8 and 131).

[80] Wulff, G. XXV. Zur Frage der Geschwindigkeit des Wachsthums und der Auflösung der Krystallflächen. *Zeitschrift für Kristallographie - Crystalline Materials* **34**, 449–530 (1901). doi: 10.1524/zkri.1901.34.1.449. (cited on page 8).

[81] Barmparis, G. D., Lodziana, Z., Lopez, N. & Remediakis, I. N. Nanoparticle shapes by using Wulff constructions and first-principles calculations. *Beilstein J. Nanotechnol.* **6**, 361–368 (2015). doi: 10.3762/bjnano.6.35. (cited on page 8).

[82] Yang, T.-H., Shi, Y., Janssen, A. & Xia, Y. Surface capping agents and their roles in shape-controlled synthesis of colloidal metal nanocrystals. *Angew. Chem. Int. Ed.* **59**, 15378–15401 (2020). doi: 10.1002/anie.201911135. (cited on page 8).

[83] Heuer-Jungemann, A. *et al.* The role of ligands in the chemical synthesis and applications of inorganic nanoparticles. *Chem. Rev.* **119**, 4819–4880 (2019). doi: 10.1021/acs.chemrev.8b00733. (cited on pages 8 and 9).

[84] Mourdikoudis, S. *et al.* Oleic acid/oleylamine ligand pair: a versatile combination in the synthesis of colloidal nanoparticles. *Nanoscale Horiz.* **7**, 941–1015 (2022). doi: 10.1039/d2nh00111j. (cited on pages 8 and 116).

[85] Marino, E., Kodger, T. E., Wegdam, G. H. & Schall, P. Revealing driving forces in quantum dot supercrystal assembly. *Adv. Mater.* **30** (2018). doi: 10.1002/adma.201803433. (cited on pages 9, 14, 16, 17, and 67).

[86] Weidman, M. C., Nguyen, Q., Smilgies, D.-M. & Tisdale, W. A. Impact of size dispersity, ligand coverage, and ligand length on the structure of PbS nanocrystal superlattices. *Chem. Mater.* **30**, 807–816 (2018). doi: acs.chemmater.7b04322. (cited on pages 9, 12, 16, 17, 67, and 116).

[87] Mourdikoudis, S. & Liz-Marzán, L. M. Oleylamine in nanoparticle synthesis. *Chem. Mater.* **25**, 1465–1476 (2013). doi: 10.1021/cm4000476. (cited on pages 9 and 67).

[88] Tanford, C. Micelle shape and size. *J. Phys. Chem.* **76**, 3020–3024 (1972). doi: 10.1021/j100665a018. (cited on pages 9, 109, and 136).

[89] Mantella, V., Castilla-Amorós, L. & Buonsanti, R. Shaping non-noble metal nanocrystals via colloidal chemistry. *Chem. Sci.* **11**, 11394–11403 (2020). doi: 10.1039/d0sc03663c. (cited on pages 9 and 23).

[90] Biacchi, A. J. & Schaak, R. E. The solvent matters: Kinetic versus thermodynamic shape control in the polyol synthesis of rhodium nanoparticles. *ACS Nano* **5**, 8089–8099 (2011). doi: 10.1021/nn2026758. (cited on page 9).

[91] Bautista-Quijano, J. R., Telschow, O., Paulus, F. & Vaynzof, Y. Solvent–antisolvent interactions in metal halide perovskites. *Chem. Commun.* **59**, 10588–10603 (2023). doi: 10.1039/d3cc02090h. (cited on page 9).

[92] Han, J. *et al.* Perovskite solar cells. *Nat. Rev. Methods Primers* **5** (2025). doi: 10.1038/s43586-024-00373-9. (cited on pages 9, 17, and 19).

[93] Demtröder, W. *Experimentalphysik 2 - Elektrizität und Optik.* Springer-Lehrbuch (Springer, Berlin, Germany, 2013), 6th edn. doi: 10.1007/978-3-662-55790-7. (cited on page 10).

[94] Debye, P. Polare Molekeln. *Leipzig: Hirzel* (1929). doi: 10.1002/ange.19300430814. (cited on page 10).

[95] Guggenheim, E. A. A proposed simplification in the procedure for computing electric dipole moments. *Trans. Faraday Soc.* **45**, 714 (1949). doi: 10.1039/tf9494500714. (cited on page 10).

[96] Dimroth, K., Reichardt, C., Siepmann, T. & Bohlmann, F. Über Pyridinium-N-phenol-betaine und ihre Verwendung zur Charakterisierung der Polarität von Lösungsmitteln. *Justus Liebigs Annalen der Chemie* **661**, 1–37 (1963). doi: 10.1002/jlac.19636610102. (cited on page 10).

[97] Hansen, C. M. *Hansen Solubility Parameters: A User's Handbook, Second Edition* (CRC Press, 2007). doi: 10.1201/9781420006834. (cited on page 10).

[98] Gutmann, V. Solvent effects on the reactivities of organometallic compounds. *Coord. Chem. Rev.* **18**, 225–255 (1976). doi: 10.1016/s0010-8545(00)82045-7. (cited on page 10).

[99] Hamill, J. C., Schwartz, J. & Loo, Y.-L. Influence of solvent coordination on hybrid organic–inorganic perovskite formation. *ACS Energy Lett.* **3**, 92–97 (2017). doi: 10.1021/acsenergylett.7b01057. (cited on page 10).

[100] O'Brien, M. N., Jones, M. R. & Mirkin, C. A. The nature and implications of uniformity in the hierarchical organization of nanomaterials. *Proc. Natl. Acad. Sci. U.S.A.* **113**, 11717–11725 (2016). doi: 10.1073/pnas.1605289113. (cited on pages 11, 12, and 17).

[101] Kang, Y. *et al.* Heterogeneous catalysts need not be so "heterogeneous": Monodisperse Pt nanocrystals by combining shape-controlled synthesis and purification by colloidal recrystallization.

J. Am. Chem. Soc. **135**, 2741–2747 (2013). doi: 10.1021/ja3116839. (cited on page 11).

[102] Israelachvili, J. N. *Intermolecular and surface forces* (Academic press, 2011). doi: 10.1016/C2009-0-21560-1. (cited on pages 11, 12, and 67).

[103] Wu, L. *et al.* High-temperature crystallization of nanocrystals into three-dimensional superlattices. *Nature* **548**, 197–201 (2017). doi: 10.1038/nature23308. (cited on pages 11, 14, 15, 16, 17, 66, 67, 118, and 119).

[104] Kim, J. U. & Matsen, M. W. Interaction between polymer-grafted particles. *Macromolecules* **41**, 4435–4443 (2008). doi: 10.1021/ma8002856. (cited on page 12).

[105] Salem, L. Attractive forces between long saturated chains at short distances. *J. Chem. Phys.* **37**, 2100–2113 (1962). doi: 10.1063/1.1733431. (cited on page 12).

[106] Goodfellow, B. W., Yu, Y., Bosoy, C. A., Smilgies, D.-M. & Korgel, B. A. The role of ligand packing frustration in body-centered cubic (bcc) superlattices of colloidal nanocrystals. *J. Phys. Chem. Letters* **6**, 2406–2412 (2015). doi: 10.1021/acs.jpclett.5b00946. (cited on page 12).

[107] Josten, E. *et al.* Superlattice growth and rearrangement during evaporation-induced nanoparticle self-assembly. *Sci. Rep.* **7**, 2802 (2017). doi: 10.1038/s41598-017-02121-4. (cited on pages 13 and 16).

[108] Dong, A., Chen, J., Vora, P. M., Kikkawa, J. M. & Murray, C. B. Binary nanocrystal superlattice membranes self-assembled at the liquid–air interface. *Nature* **466**, 474–477 (2010). doi: 10.1038/nature09188. (cited on page 13).

[109] Lokteva, I., Koof, M., Walther, M., Grübel, G. & Lehmkühler, F. Monitoring nanocrystal self-assembly in real time using in situ small-angle X-ray scattering. *Small* **15**, 1900438 (2019). doi: 10.1002/smll.201900438. (cited on pages 13 and 16).

[110] Momper, R. *et al.* Kinetic control over self-assembly of semiconductor nanoplatelets. *Nano Lett.* **20**, 4102–4110 (2020). doi: 10.1021/acs.nanolett.9b05270. (cited on page 13).

[111] Toso, S. *et al.* Multilayer diffraction reveals that colloidal superlattices approach the structural perfection of single crystals. *ACS Nano* **15**, 6243–6256 (2021). doi: 10.1021/acsnano.0c08929. (cited on page 13).

[112] Wei, W., Bai, F. & Fan, H. Oriented gold nanorod arrays: Self-assembly and optoelectronic applications. *Angew. Chem. Int. Ed.* **58**, 11956–11966 (2019). doi: 10.1002/anie.201902620. (cited on pages 13 and 26).

[113] Tanner, C. P. N. *et al.* In situ X-ray scattering reveals coarsening rates of superlattices self-assembled from electrostatically stabilized metal nanocrystals depend nonmonotonically on driving force. *ACS Nano* **18**, 5778–5789 (2024). doi: 10.1021/acsnano.3c12186. (cited on pages 13, 15, 16, 120, and 135).

[114] Baranov, D. *et al.* Assembly of colloidal semiconductor nanorods in solution by depletion attraction. *Nano Lett.* **10**, 743–749 (2010). doi: 10.1021/nl903946n. (cited on pages 13, 17, and 83).

[115] Talapin, D. V. *et al.* CdSe and CdSe/CdS nanorod solids. *J. Am. Chem. Soc.* **126**, 12984–12988 (2004). doi: 10.1021/ja046727v. (cited on page 14).

[116] Lv, Z.-P., Kapuscinski, M. & Bergström, L. Tunable assembly of truncated nanocubes by evaporation-driven poor-solvent enrichment. *Nat. Commun.* **10**, 4228 (2019). doi: 10.1038/s41467-019-12237-y. (cited on pages 14 and 16).

[117] Lee, B., Littrell, K., Sha, Y. & Shevchenko, E. V. Revealing the effects of the non-solvent on the ligand shell of nanoparticles and their crystallization. *J. Am. Chem. Soc.* **141**, 16651–16662 (2019). doi: 10.1021/jacs.9b06010. (cited on pages 14, 16, and 17).

[118] Marino, E., Rosen, D. J., Yang, S., Tsai, E. H. & Murray, C. B. Temperature-controlled reversible formation and phase transformation of 3D nanocrystal superlattices through in situ small-angle X-ray scattering. *Nano Lett.* (2023). doi: 10.1021/acs.nanolett.3c00299. (cited on pages 14, 16, and 135).

[119] Yu, Y. *et al.* Nanocrystal superlattices that exhibit improved order on heating: an example of inverse melting? *Faraday Discuss.* **181**, 181–192 (2015). doi: 10.1039/c5fd00006h. (cited on pages 14 and 135).

[120] Yee, D. W., Lee, M. S., An, J. & Macfarlane, R. J. Reversible diffusionless phase transitions in 3D nanoparticle superlattices. *J. Am. Chem. Soc.* **145**, 6051–6056 (2023). doi: 10.1021/jacs.3c01286. (cited on pages 14 and 16).

[121] Nakagawa, F. *et al.* In situ control of crystallinity of 3D colloidal crystals by tuning the growth kinetics of nanoparticle building blocks. *J. Am. Chem. Soc.* **144**, 5871–5877 (2022). doi: 10.1021/jacs.1c12456. (cited on pages 14, 16, and 17).

[122] Abécassis, B., Testard, F. & Spalla, O. Gold nanoparticle superlattice crystallization probed in situ. *Phys. Rev. Lett.* **100**, 115504 (2008). doi: 10.1103/PhysRevLett.100.115504. (cited on pages 14 and 16).

[123] Montanarella, F. *et al.* Growth and self-assembly of $CsPbBr_3$ nanocrystals in the TOPO/$PbBr_2$ synthesis as seen with X-ray scattering. *Nano Lett.* **23**, 667–676 (2023). doi: 10.1021/acs.nanolett.2c04532. (cited on pages 14, 16, 17, and 21).

[124] Pokratath, R. *et al.* An amorphous phase precedes crystallization: Unraveling the colloidal synthesis of zirconium oxide nanocrystals. *ACS Nano* **17**, 8796–8806 (2023). doi: 10.1021/acsnano.3c02149. (cited on pages 14 and 15).

[125] Udayabhaskararao, T., Kazes, M., Houben, L., Lin, H. & Oron, D. Nucleation, growth, and structural transformations of perovskite nanocrystals. *Chem. Mater.* **29**, 1302–1308 (2017). doi: 10.1021/acs.chemmater.6b04841. (cited on pages 14, 22, and 134).

[126] Mandal, P., Roy, A., Mannar, S. & Viswanatha, R. Growth mechanistic insights into perovskite nanocrystals: dimensional growth. *Nanoscale Adv.* **2**, 5305–5311 (2020). doi: 10.1039/d0na00732c. (cited on page 14).

[127] Moral, R. F. *et al.* Self-assembly of perovskite nanoplates in colloidal suspensions. *Materials Horizons* **10**, 5822–5834 (2023). doi: 10.1039/d3mh01401k. (cited on pages 14 and 134).

[128] Jeppesen, H. S., Nielsen, I. G., Kondrup, J. C., Just, J. & Lock, N. LiquidReactionCell – a versatile setup for in situ synchrotron studies of compounds in liquid suspension and solution. *CrystEngComm* **25**, 751–760 (2023). doi: 10.1039/d2ce01374f. (cited on page 15).

[129] Siliqi, D. *et al.* Formation of calcium phosphate nanoparticles in the presence of carboxylate molecules: a time-resolved in situ synchrotron SAXS and WAXS study. *CrystEngComm* **25**, 550–559 (2023). doi: 10.1039/d2ce01227h. (cited on page 14).

[130] Montanarella, F. *et al.* Crystallization of nanocrystals in spherical confinement probed by in situ X-ray scattering. *Nano Lett.* **18**, 3675–3681 (2018). doi: 10.1021/acs.nanolett.8b00809. (cited on pages 14, 16, 133, and 139).

[131] Marino, E. *et al.* Crystallization of binary nanocrystal superlattices and the relevance of short-range attraction. *Nat. Synth.* **3**, 111–122 (2023). doi: 10.1038/s44160-023-00407-2. (cited on pages 14, 16, and 135).

[132] Lassenberger, A. *et al.* Monodisperse iron oxide nanoparticles by thermal decomposition: Elucidating particle formation by second-resolved in situ small-angle X-ray scattering. *Chem. Mater.* **29**, 4511–4522 (2017). doi: 10.1021/acs.chemmater.7b01207. (cited on page 14).

[133] Lignos, I., Maceiczyk, R. & deMello, A. J. Microfluidic technology: Uncovering the mechanisms of nanocrystal nucleation and growth. *Acc. Chem. Res.* **50**, 1248–1257 (2017). doi: 10.1021/acs.accounts.7b00088. (cited on pages 14, 139, and 144).

[134] Yaghmur, A. & Hamad, I. Microfluidic nanomaterial synthesis and in situ SAXS, WAXS, or SANS characterization: Manipulation of size characteristics and online elucidation of dynamic structural transitions. *Molecules* **27**, 4602 (2022). doi: 10.3390/molecules27144602. (cited on pages 14, 138, and 139).

[135] Greenberg, M. W., Lin, C.-H., Chodankar, S. & Ghose, S. K. In situ synchrotron X-ray total scattering measurements and analysis of colloidal $CsPbX_3$ nanocrystals during flow synthesis. *J. Synchrotron Rad.* **30** (2023). doi: 10.1107/s1600577523007300. (cited on page 14).

[136] Mathiesen, J. K. *et al.* Simple setup miniaturization with multiple benefits for green chemistry in nanoparticle synthesis. *ACS Omega* **7**, 4714–4721 (2022). doi: 10.1021/acsomega.2c00030. (cited on page 15).

[137] Czajka, A. & Armes, S. P. Time-resolved small-angle X-ray scattering studies during aqueous emulsion polymerization. *J. Am. Chem. Soc.* **143**, 1474–1484 (2021). doi: 10.1021/jacs.0c11183. (cited on page 15).

[138] Roelsgaard, M. *et al.* A reactor for time-resolved X-ray studies of nucleation and growth during solvothermal synthesis. *J. Appl. Cryst.* **56**, 581–588 (2023). doi: 10.1107/s1600576723002339. (cited on page 15).

[139] Sanchez Monserrate, B. A., Grenier, A., Chupas, P. J. & Chapman, K. W. A high-temperature sample changer for parallelized in situ X-ray studies to efficiently explore reaction space. *J. Appl. Cryst.* **56**, 1732–1738 (2023). doi: 10.1107/s160057672300907x. (cited on page 15).

[140] van der Bok, J. C. *et al.* In situ optical and X-ray spectroscopy reveals evolution toward mature CdSe nanoplatelets by synergetic action of myristate and acetate ligands. *J. Am. Chem. Soc.* **144**, 8096–8105 (2022). doi: 10.1021/jacs.2c00423. (cited on pages 15 and 86).

[141] Prins, P. T. *et al.* Extended nucleation and superfocusing in colloidal semiconductor nanocrystal synthesis. *Nano Lett.* **21**, 2487–2496 (2021). doi: 10.1021/acs.nanolett.0c04813. (cited on pages 15 and 16).

[142] Just, J. *et al.* Insights into nucleation and growth of colloidal quaternary nanocrystals by multimodal X-ray analysis. *ACS Nano* **15**, 6439–6447 (2021). doi: 10.1021/acsnano.0c08617. (cited on pages 15, 16, and 138).

[143] Qiao, Z. *et al.* In situ real-time observation of formation and self-assembly of perovskite nanocrystals at high temperature. *Nano Lett.* **23**, 10788–10795 (2023). doi: 10.1021/acs.nanolett.3c02908. (cited on pages 15, 16, 17, 18, 21, and 134).

[144] Mantella, V. *et al.* Polymer lamellae as reaction intermediates in the formation of copper nanospheres as evidenced by in situ X-ray studies. *Angew. Chem. Int. Ed.* **59**, 11627–11633 (2020). doi: 10.1002/anie.202004081. (cited on pages 15, 63, 103, 104, 106, 107, and 108).

[145] Pankhurst, J. R. *et al.* Copper phosphonate lamella intermediates control the shape of colloidal copper nanocrystals. *J. Am. Chem. Soc.* **144**, 12261–12271 (2022). doi: 10.1021/jacs.2c03489. (cited on pages 15, 23, 104, 106, and 108).

[146] Wu, L. *et al.* Tuning precursor reactivity toward nanometer-size control in palladium nanoparticles studied by in situ small angle X-ray scattering. *Chem. Mater.* **30**, 1127–1135 (2018). doi: 10.1021/acs.chemmater.7b05186. (cited on page 16).

[147] Abécassis, B. *et al.* Persistent nucleation and size dependent attachment kinetics produce monodisperse PbS nanocrystals. *Chem. Sci.* **13**, 4977–4983 (2022). doi: 10.1039/d1sc06134h. (cited on page 16).

[148] Mozaffari, S. *et al.* Colloidal nanoparticle size control: experimental and kinetic modeling investigation of the ligand–metal binding role in controlling the nucleation and growth kinetics. *Nanoscale* **9**, 13772–13785 (2017). doi: 10.1039/c7nr04101b. (cited on page 16).

[149] Watzky, M. A. & Finke, R. G. Transition metal nanocluster formation kinetic and mechanistic studies. A new mechanism when hydrogen is the reductant: Slow, continuous nucleation and fast autocatalytic surface growth. *J. Am. Chem. Soc.* **119**, 10382–10400 (1997). doi: 10.1021/ja9705102. (cited on page 16).

[150] Avrami, M. Kinetics of phase change. I General theory. *J. Chem. Phys.* **7**, 1103–1112 (1939). doi: 10.1063/1.1750380. (cited on page 16).

[151] Gualtieri, A. F. Synthesis of sodium zeolites from a natural halloysite. *Phys. Chem. Miner.* **28**, 719–728 (2001). doi: 10.1007/s002690100197. (cited on page 16).

[152] Kapuscinski, M. *et al.* Temporal evolution of superlattice contraction and defect-induced strain anisotropy in mesocrystals during nanocube self-assembly. *ACS Nano* **14**, 5337–5347 (2020). doi: 10.1021/acsnano.9b07820. (cited on page 16).

[153] Castro, N. *et al.* Insights into the formation mechanism of CdSe nanoplatelets using in situ X-ray scattering. *Nano Lett.* **19**, 6466–6474 (2019). doi: 10.1021/acs.nanolett.9b02687. (cited on pages 16 and 21).

[154] Hubert, F. *et al.* Growth and overgrowth of concentrated gold nanorods: Time resolved SAXS and XANES. *Crystal Growth & Design* **12**, 1548–1555 (2012). doi: 10.1021/cg2016116. (cited on page 16).

[155] Kwon, S. G. *et al.* Heterogeneous nucleation and shape transformation of multicomponent metallic nanostructures. *Nat. Mater.* **14**, 215–223 (2014). doi: 10.1038/nmat4115. (cited on page 16).

[156] Özkan, E. *et al.* Peering into the formation of cerium oxide colloidal particles in solution by in situ small-angle X-ray scattering. *Langmuir* **36**, 9175–9190 (2020). doi: 10.1021/acs.langmuir.0c01463. (cited on page 16).

[157] Leffler, V., Ehlert, S., Forster, B., Dulle, M. & Förster, S. Nanoparticle heat-up synthesis: In situ X-ray diffraction and extension from classical to nonclassical nucleation and growth theory. *ACS Nano* **15**, 840–856 (2021). doi: 10.1021/acsnano.0c07359. (cited on page 16).

[158] Jensen, G. V. *et al.* Anisotropic crystal growth kinetics of anatase TiO_2 nanoparticles synthesized in a nonaqueous medium. *Chem. Mater.* **22**, 6044–6055 (2010). doi: 10.1021/cm100469y. (cited on page 16).

[159] Anker, A. S. *et al.* Structural changes during the growth of atomically precise metal oxido nanoclusters from combined pair distribution function and small-angle X-ray scattering analysis. *Angew. Chem. Int. Ed.* **60**, 20407–20416 (2021). doi: 10.1002/anie.202103641. (cited on pages 16 and 141).

[160] Mathiesen, J. K. *et al.* Chemical insights into the formation of colloidal iridium nanoparticles from in situ X-ray total scattering: Influence of precursors and cations on the reaction pathway. *J. Am. Chem. Soc.* **145**, 1769–1782 (2023). doi: 10.1021/jacs.2c10814. (cited on page 16).

[161] Ramamoorthy, R. K. *et al.* The role of pre-nucleation clusters in the crystallization of gold nanoparticles. *Nanoscale* **12**, 16173–16188 (2020). doi: 10.1039/d0nr03486j. (cited on pages 16 and 77).

[162] Mathiesen, J. K. *et al.* Breaking with the principles of coreduction to form stoichiometric intermetallic PdCu nanoparticles. *Small Methods* **6**, 2200420 (2022). doi: 10.1002/smtd.202200420. (cited on pages 16, 24, and 132).

[163] Huang, X. *et al.* In situ constructing the kinetic roadmap of octahedral nanocrystal assembly toward controlled superlattice fabrication. *J. Am. Chem. Soc.* **143**, 4234–4243 (2021). doi: 10.1021/jacs.0c12087. (cited on page 16).

[164] Lokteva, I. *et al.* Real-time X-ray scattering discovers rich phase behavior in PbS nanocrystal superlattices during in situ assembly. *Chem. Mater.* **33**, 6553–6563 (2021). doi: 10.1021/acs.chemmater.1c02159. (cited on page 16).

[165] Winslow, S. W., Swan, J. W. & Tisdale, W. A. The importance of unbound ligand in nanocrystal superlattice formation. *J. Am. Chem. Soc.* **142**, 9675–9685 (2020). doi: 10.1021/jacs.0c01809. (cited on page 17).

[166] Mondal, R. & Kumaraswamy, G. Materials prepared by freezing-induced self-assembly of dispersed solutes: A review. *Materials Advances* **3**, 3041–3054 (2022). doi: 10.1039/d1ma01017d. (cited on pages 17 and 136).

[167] Chakhmouradian, A. R. & Woodward, P. M. Celebrating 175 years of perovskite research: a tribute to Roger H. Mitchell. *Phys. Chem. Miner.* **41**, 387–391 (2014). doi: 10.1007/s00269-014-0678-9. (cited on page 17).

[168] Stoumpos, C. C. *et al.* Crystal growth of the perovskite semiconductor $CsPbBr_3$: A new material for high-energy radiation detection. *Crystal growth & design* **13**, 2722–2727 (2013). doi: 10.1021/cg400645t. (cited on pages 18, 19, and 73).

[169] Tao, S. *et al.* Absolute energy level positions in tin- and lead-based halide perovskites. *Nat. Commun.* **10**, 2560 (2019). doi: 10.1038/s41467-019-10468-7. (cited on pages 18 and 19).

[170] Wells, H. L. Über die Cäsium- und Kalium-Bleihalogenide. *Zeitschrift für anorganische Chemie* **3**, 195–210 (1893). doi: 10.1002/zaac.18930030124. (cited on page 17).

[171] Kojima, A., Teshima, K., Shirai, Y. & Miyasaka, T. Organometal halide perovskites as visible-light sensitizers for photovoltaic cells. *J. Am. Chem. Soc.* **131**, 6050–6051 (2009). doi: 10.1021/ja809598r. (cited on page 17).

[172] Era, M., Morimoto, S., Tsutsui, T. & Saito, S. Organic-inorganic heterostructure electroluminescent device using a layered perovskite semiconductor $(C_6H_5C_2H_4NH_3)_2PbI_4$. *Appl. Phys. Lett.* **65**, 676–678 (1994). doi: 10.1063/1.112265. (cited on page 17).

[173] Fakharuddin, A. *et al.* Perovskite light-emitting diodes. *Nat. Electron.* **5**, 203–216 (2022). doi: 10.1038/s41928-022-00745-7. (cited on page 17).

[174] Wan, Q. *et al.* Ultrathin light-emitting diodes with external efficiency over 26% based on resurfaced perovskite nanocrystals. *ACS Energy Lett.* **8**, 927–934 (2023). doi: 10.1021/acsenergylett.2c02802. (cited on page 17).

[175] Sutherland, B. R. & Sargent, E. H. Perovskite photonic sources. *Nat. Photon.* **10**, 295–302 (2016). doi: 10.1038/nphoton.2016.62. (cited on page 17).

[176] Chen, Q. *et al.* All-inorganic perovskite nanocrystal scintillators. *Nature* **561**, 88–93 (2018). doi: 10.1038/s41586-018-0451-1. (cited on page 18).

[177] Becker, M. A. *et al.* Bright triplet excitons in caesium lead halide perovskites. *Nature* **553**, 189–193 (2018). doi: 10.1038/nature25147. (cited on page 18).

[178] Almutlaq, J. *et al.* Engineering colloidal semiconductor nanocrystals for quantum information processing. *Nat. Nanotechnol.* **19**, 1091–1100 (2024). doi: 10.1038/s41565-024-01606-4. (cited on pages 18 and 26).

[179] Yazdani, N. *et al.* Coupling to octahedral tilts in halide perovskite nanocrystals induces phonon-mediated attractive interactions between excitons. *Nature Physics* **20**, 47–53 (2024). doi: 10.1038/s41567-023-02253-7. (cited on page 18).

[180] Gramlich, M., Lampe, C., Drewniok, J. & Urban, A. S. How exciton–phonon coupling impacts photoluminescence in halide perovskite nanoplatelets. *J. Phys. Chem. Letters* **12**, 11371–11377 (2021). doi: 10.1021/acs.jpclett.1c03437. (cited on page 18).

[181] Xu, J. *et al.* Halide perovskites for nonlinear optics. *Adv. Mater.* **32**, 1806736 (2020). doi: 10.1002/adma.201806736. (cited on page 18).

[182] Goldschmidt, V. M. Die Gesetze der Krystallochemie. *Naturwissenschaften* **14**, 477–485 (1926). doi: 10.1007/bf01507527. (cited on page 18).

[183] Travis, W., Glover, E., Bronstein, H., Scanlon, D. & Palgrave, R. On the application of the tolerance factor to inorganic and hybrid halide perovskites: a revised system. *Chem. Sci.* **7**, 4548–4556 (2016). doi: 10.1039/c5sc04845a. (cited on page 18).

[184] Rodová, M., Brožek, J., Knížek, K. & Nitsch, K. Phase transitions in ternary caesium lead bromide. *J. Therm. Anal. Calorim.* **71**, 667–673 (2003). doi: 10.1023/a:1022836800820. (cited on page 18).

[185] Svirskas, Š. *et al.* Phase transitions, screening and dielectric response of $CsPbBr_3$. *J. Mater. Chem. A* **8**, 14015–14022 (2020). doi: 10.1039/d0ta04155f. (cited on page 18).

[186] Cottingham, P. & Brutchey, R. L. On the crystal structure of colloidally prepared $CsPbBr_3$ quantum dots. *Chem. Commun.* **52**, 5246–5249 (2016). doi: 10.1039/c6cc01088a. (cited on pages 18, 100, and 156).

[187] Bertolotti, F. *et al.* Crystal structure, morphology, and surface termination of cyan-emissive, six-monolayers-thick $CsPbBr_3$ nanoplatelets from X-ray total scattering. *ACS Nano* **13**, 14294–14307 (2019). doi: 10.1021/acsnano.9b07626. (cited on pages 18, 21, and 142).

[188] Zhang, B. *et al.* Stable $CsPbBr_3$ nanoclusters feature a disk-like shape and a distorted orthorhombic structure. *J. Am. Chem. Soc.* **144**, 5059–5066 (2022). doi: 10.1021/jacs.1c13544. (cited on pages 18, 98, and 143).

[189] Bertolotti, F. *et al.* Coherent nanotwins and dynamic disorder in cesium lead halide perovskite nanocrystals. *ACS Nano* **11**, 3819–3831 (2017). doi: 10.1021/acsnano.7b00017. (cited on pages 18, 92, and 142).

[190] Trots, D. & Myagkota, S. High-temperature structural evolution of caesium and rubidium triiodoplumbates. *Journal of Physics and Chemistry of Solids* **69**, 2520–2526 (2008). doi: 10.1016/j.jpcs.2008.05.007. (cited on pages 18 and 161).

[191] Sutton, R. J. *et al.* Cubic or orthorhombic? Revealing the crystal structure of metastable black-phase $CsPbI_3$ by theory and experiment. *ACS Energy Lett.* **3**, 1787–1794 (2018). doi: 10.1021/acsenergylett.8b00672. (cited on page 18).

[192] Glazer, A. M. The classification of tilted octahedra in perovskites. *Acta Cryst. B* **28**, 3384–3392 (1972). doi: 10.1107/s0567740872007976. (cited on page 18).

[193] Skjærvø, S. H., Karlsen, M. A., Comin, R. & Billinge, S. J. L. Refining perovskite structures to pair distribution function data using collective Glazer modes as a basis. *IUCrJ* **9**, 705–712 (2022). doi: 10.1107/s2052252522007680. (cited on page 18).

[194] Bertolotti, F. *et al.* Size- and temperature-dependent lattice anisotropy and structural distortion in $CsPbBr_3$ quantum dots by reciprocal space X-ray total scattering analysis. *Small Structures* **5**, 2300264 (2024). doi: 10.1002/sstr.202300264. (cited on pages 18, 37, and 99).

[195] Wen, J.-R., Rodriguez Ortiz, F. A., Champ, A. & Sheldon, M. T. Kinetic control for continuously tunable lattice parameters, size, and composition during $CsPbX_3$ (X= Cl, Br, I) nanorod synthesis. *ACS Nano* **16**, 8318–8328 (2022). doi: 10.1021/acsnano.2c02474. (cited on pages 18, 22, and 99).

[196] Akkerman, Q. A. & Manna, L. What defines a halide perovskite? *ACS Energy Lett.* **5**, 604–610 (2020). doi: 10.1021/acsenergylett.0c00039. (cited on page 18).

[197] Wen, J.-R. *et al.* Chemical availability of bromide dictates $CsPbBr_3$ nanocrystal growth. *Chem. Mater.* **31**, 8551–8557 (2019). doi: 10.1021/acs.chemmater.9b03709. (cited on pages 18, 22, and 73).

[198] Mosquera-Lois, I. *et al.* Multifaceted nature of defect tolerance in halide perovskites and emerging semiconductors. *Nat. Rev. Chem.* **9**, 287–304 (2025). doi: 10.1038/s41570-025-00702-w. (cited on page 19).

[199] Shamsi, J., Urban, A. S., Imran, M., De Trizio, L. & Manna, L. Metal halide perovskite nanocrystals: Synthesis, post-synthesis modifications, and their optical properties. *Chem. Rev.* **119**, 3296–3348 (2019). doi: 10.1021/acs.chemrev.8b00644. (cited on pages 19 and 21).

[200] Bohn, B. J. *et al.* Boosting tunable blue luminescence of halide perovskite nanoplatelets through postsynthetic surface trap repair. *Nano Lett.* **18**, 5231–5238 (2018). doi: 10.1021/acs.nanolett.8b02190. (cited on pages 19, 22, 49, 50, 70, 72, 86, and 94).

[201] Shannon, R. D. Revised effective ionic radii and systematic studies of interatomic distances in halides and chalcogenides. *Acta Cryst. A* **32**, 751–767 (1976). doi: 10.1107/s0567739476001551. (cited on page 19).

[202] Lai, M. *et al.* Intrinsic anion diffusivity in lead halide perovskites is facilitated by a soft lattice. *Proc. Natl. Acad. Sci. U.S.A.* **115**, 11929–11934 (2018). doi: 10.1073/pnas.1812718115. (cited on pages 19 and 101).

[203] Nedelcu, G. *et al.* Fast anion-exchange in highly luminescent nanocrystals of cesium lead halide perovskites ($CsPbX_3$, X= Cl, Br, I). *Nano Lett.* **15**, 5635–5640 (2015). doi: 10.1021/acs.nanolett.5b02404. (cited on page 19).

[204] Vegard, L. Die Konstitution der Mischkristalle und die Raumfüllung der Atome. *Zeitschrift für Physik* **5**, 17–26 (1921). doi: 10.1007/bf01349680. (cited on page 19).

[205] Fox, A. *Optical Properties of Solids.* Oxford master series in condensed matter physics (Oxford University Press, 2001). doi: 10.1119/1.1691372. (cited on pages 19, 20, 43, and 44).

[206] Caicedo-Dávila, S. *et al.* Effects of quantum and dielectric confinement on the emission of Cs-Pb-Br composites. *Adv. Funct. Mater.* **33**, 2305240 (2023). doi: 10.1002/adfm.202305240. (cited on page 19).

[207] Alivisatos, A. P. Semiconductor clusters, nanocrystals, and quantum dots. *Science* **271**, 933–937 (1996). doi: 10.1126/science.271.5251.933. (cited on page 19).

[208] Weidman, M. C., Goodman, A. J. & Tisdale, W. A. Colloidal halide perovskite nanoplatelets: An exciting new class of semiconductor nanomaterials. *Chem. Mater.* **29**, 5019–5030 (2017). doi: 10.1021/acs.chemmater.7b01384. (cited on page 20).

[209] Zhang, D. *et al.* Ultrathin colloidal cesium lead halide perovskite nanowires. *J. Am. Chem. Soc.* **138**, 13155–13158 (2016). doi: 10.1021/jacs.6b08373. (cited on pages 20 and 21).

[210] Docampo, P. & Bein, T. A long-term view on perovskite optoelectronics. *Acc. Chem. Res.* **49**, 339–346 (2016). doi: 10.1021/acs.accounts.5b00465. (cited on page 20).

[211] Fu, W. *et al.* Stability of perovskite materials and devices. *Materials Today* **58**, 275–296 (2022). doi: 10.1016/j.mattod.2022.06.020. (cited on page 20).

[212] Knight, A. J. *et al.* Halide segregation in mixed-halide perovskites: Influence of A-site cations. *ACS Energy Lett.* **6**, 799–808 (2021). doi: 10.1021/acsenergylett.0c02475. (cited on pages 20 and 101).

[213] Fiuza-Maneiro, N. *et al.* Ligand chemistry of inorganic lead halide perovskite nanocrystals. *ACS Energy Lett.* **8**, 1152–1191 (2023). doi: 10.1021/acsenergylett.2c02363. (cited on pages 21 and 94).

[214] Cherniukh, I. *et al.* Structural diversity in multicomponent nanocrystal superlattices comprising lead halide perovskite nanocubes. *ACS Nano* **16**, 7210–7232 (2022). doi: 10.1021/acsnano.1c10702. (cited on page 21).

[215] Boehme, S. C. *et al.* Strongly confined $CsPbBr_3$ quantum dots as quantum emitters and building blocks for rhombic superlattices. *ACS Nano* **17**, 2089–2100 (2023). doi: 10.1021/acsnano.2c07677. (cited on page 21).

[216] Bekenstein, Y., Koscher, B. A., Eaton, S. W., Yang, P. & Alivisatos, A. P. Highly luminescent colloidal nanoplates of perovskite cesium lead halide and their oriented assemblies. *J. Am. Chem. Soc.* **137**, 16008–16011 (2015). doi: 10.1021/jacs.5b11199. (cited on pages 21 and 86).

[217] Jurow, M. J. *et al.* Manipulating the transition dipole moment of $CsPbBr_3$ perovskite nanocrystals for superior optical properties. *Nano Lett.* **19**, 2489–2496 (2019). doi: 10.1021/acs.nanolett.9b00122. (cited on page 21).

[218] Diroll, B. T., Banerjee, P. & Shevchenko, E. V. Optical anisotropy of $CsPbBr_3$ perovskite nanoplatelets. *Nano Converg.* **10** (2023). doi: 10.1186/s40580-023-00367-5. (cited on page 21).

[219] Wang, Y. *et al.* Reversible transformation between $CsPbBr_3$ perovskite nanowires and nanorods with polarized optoelectronic properties. *Adv. Funct. Mater.* **31**, 2011251 (2021). doi: 10.1002/adfm.202011251. (cited on page 21).

[220] Krajewska, C. J. *et al.* Controlled assembly and anomalous thermal expansion of ultrathin cesium lead bromide nanoplatelets. *Nano Lett.* **23**, 2148–2157 (2023). doi: 10.1021/acs.nanolett.2c04526. (cited on page 21).

[221] Scott, R. *et al.* Directed emission of CdSe nanoplatelets originating from strongly anisotropic 2D electronic structure. *Nat. Nanotechnol.* **12**, 1155–1160 (2017). doi: 10.1038/nnano.2017.177. (cited on page 21).

[222] Seth, S. & Samanta, A. A facile methodology for engineering the morphology of $CsPbX_3$ perovskite nanocrystals under ambient condition. *Sci. Rep.* **6** (2016). doi: 10.1038/srep37693. (cited on page 21).

[223] Sun, S., Yuan, D., Xu, Y., Wang, A. & Deng, Z. Ligand-mediated synthesis of shape-controlled cesium lead halide perovskite nanocrystals via reprecipitation process at room temperature. *ACS Nano* **10**, 3648–3657 (2016). doi: 10.1021/acsnano.5b08193. (cited on pages 21 and 22).

[224] Zhang, X. *et al.* Water-assisted size and shape control of $CsPbBr_3$ perovskite nanocrystals. *Angew. Chem. Int. Ed.* **57**, 3337–3342 (2018). doi: 10.1002/anie.201710869. (cited on page 21).

[225] Yang, H. *et al.* Slowing down for growth mechanism and speeding up for performance optimization based on single ligand passivated $CsPbBr_3$ nanoplatelets. *Adv. Opt. Mater.* **10**, 2200683 (2022). doi: 10.1002/adom.202200683. (cited on pages 21 and 133).

[226] Sichert, J. A. *et al.* Quantum size effect in organometal halide perovskite nanoplatelets. *Nano Lett.* **15**, 6521–6527 (2015). doi: 10.1021/acs.nanolett.5b02985. (cited on page 22).

[227] Zhu, H. *et al.* One-dimensional highly-confined $CsPbBr_3$ nanorods with enhanced stability: Synthesis and spectroscopy. *Nano Lett.* **22**, 8355–8362 (2022). doi: 10.1021/acs.nanolett.2c03458. (cited on page 22).

[228] He, L., Pan, S., Lin, Z. & Peng, J. Rapid route to polar solvent-directed growth of perovskite nanowires. *ACS Appl. Nano Mater.* **2**, 7910–7915 (2019). doi: 10.1021/acsanm.9b01922. (cited on page 22).

[229] Zhao, Q. *et al.* Shape-controlled synthesis of $CsPbBr_3$ nanorods with bright pure blue emission and high stability. *J. Mater. Chem. C* **12**, 4234–4242 (2024). doi: 10.1039/d3tc04681h. (cited on page 22).

[230] Xu, Y. *et al.* Synthesis of ultrasmall $CsPbBr_3$ nanoclusters and their transformation to highly deep-blue-emitting nanoribbons at room temperature. *Nanoscale* **9**, 17248–17253 (2017). doi: 10.1039/c7nr06959f. (cited on page 22).

[231] Su, S. *et al.* Stable and highly efficient blue-emitting $CsPbBr_3$ perovskite nanomaterials via kinetic-controlled growth. *Chemical Engineering Journal* **419**, 129612 (2021). doi: 10.1016/j.cej.2021.129612. (cited on page 22).

[232] Peng, L., Dutta, A., Xie, R., Yang, W. & Pradhan, N. Dot–wire–platelet–cube: Step growth and structural transformations in $CsPbBr_3$ perovskite nanocrystals. *ACS Energy Lett.* **3**, 2014–2020 (2018). doi: 10.1021/acsenergylett.8b01037. (cited on page 22).

[233] Leng, J. *et al.* Thermodynamic control in the synthesis of quantum-confined blue-emitting $CsPbBr_3$ perovskite nanostrips. *J. Phys. Chem. Letters* **11**, 2036–2043 (2020). doi: 10.1021/acs.jpclett.9b03873. (cited on page 22).

[234] Lampe, C. *et al.* Rapid data-efficient optimization of perovskite nanocrystal syntheses through machine learning algorithm fusion. *Adv. Mater.* **35**, 2208772 (2023). doi: 10.1002/adma.202208772. (cited on pages 22, 49, 71, and 140).

[235] Lampe, C. *Challenges for perovskite nanocrystals and how to overcome them.* Ph.D. thesis, LMU Munich (2022). doi: 10.5282/edoc.30332. (cited on pages 22, 94, 95, and 98).

[236] Saha, K., Agasti, S. S., Kim, C., Li, X. & Rotello, V. M. Gold nanoparticles in chemical and biological sensing. *Chem. Rev.* **112**, 2739–2779 (2012). doi: 10.1021/cr2001178. (cited on page 22).

[237] Atwater, H. A. & Polman, A. Plasmonics for improved photovoltaic devices. *Nat. Mater.* **9**, 205–213 (2010). doi: 10.1038/nmat2629. (cited on page 22).

[238] Camargo, P. H. & Cortés, E. *Plasmonic catalysis: from fundamentals to applications* (John Wiley & Sons, 2021). doi: 10.1002/9783527826971. (cited on page 22).

[239] Che, M. Nobel Prize in chemistry 1912 to Sabatier: Organic chemistry or catalysis? *Catal. Today* **218–219**, 162–171 (2013). doi: 10.1016/j.cattod.2013.07.006. (cited on page 23).

[240] Witte, P. T. *et al.* BASF NanoSelect™ technology: Innovative supported Pd-and Pt-based catalysts for selective hydrogenation reactions. *Top. Catal.* **55**, 505–511 (2012). doi: 10.1007/s11244-012-9818-y. (cited on page 23).

[241] Reske, R., Mistry, H., Behafarid, F., Roldan Cuenya, B. & Strasser, P. Particle size effects in the catalytic electroreduction of CO_2 on Cu nanoparticles. *J. Am. Chem. Soc.* **136**, 6978–6986 (2014). doi: 10.1021/ja500328k. (cited on page 23).

[242] Kang, Y. *et al.* Effect of crystal facets in plasmonic catalysis. *Nat. Commun.* **15**, 3923 (2024). doi: 10.1038/s41467-024-47994-y. (cited on page 23).

[243] Kuhl, K. P., Cave, E. R., Abram, D. N. & Jaramillo, T. F. New insights into the electrochemical reduction of carbon dioxide on metallic copper surfaces. *Energy & Environmental Science* **5**, 7050 (2012). doi: 10.1039/c2ee21234j. (cited on page 23).

[244] Loiudice, A. *et al.* Tailoring copper nanocrystals towards C_2 products in electrochemical CO_2 reduction. *Angew. Chem. Int. Ed.* **55**, 5789–5792 (2016). doi: 10.1002/anie.201601582. (cited on page 23).

[245] Ma, M., Djanashvili, K. & Smith, W. A. Controllable hydrocarbon formation from the electrochemical reduction of CO_2 over Cu nanowire arrays. *Angew. Chem. Int. Ed.* **55**, 6680–6684 (2016). doi: 10.1002/anie.201601282. (cited on page 23).

[246] Li, Y. *et al.* Structure-sensitive CO_2 electroreduction to hydrocarbons on ultrathin 5-fold twinned copper nanowires. *Nano Lett.* **17**, 1312–1317 (2017). doi: 10.1021/acs.nanolett.6b05287. (cited on page 23).

[247] Jana, N. R., Gearheart, L. & Murphy, C. J. Wet chemical synthesis of high aspect ratio cylindrical gold nanorods. *J. Phys. Chem. B* **105**, 4065–4067 (2001). doi: 10.1021/jp0107964. (cited on page 23).

[248] Xia, Y., Gilroy, K. D., Peng, H.-C. & Xia, X. Seed-mediated growth of colloidal metal nanocrystals. *Angew. Chem. Int. Ed.* **56**, 60–95 (2017). doi: 10.1002/anie.201604731. (cited on page 23).

[249] Strach, M. *et al.* Insights into reaction intermediates to predict synthetic pathways for shape-controlled metal nanocrystals. *J. Am. Chem. Soc.* **141**, 16312–16322 (2019). doi: 10.1021/jacs.9b06267. (cited on page 23).

[250] Rodrigues, T. S. *et al.* Synthesis of colloidal metal nanocrystals: A comprehensive review on the reductants. *Chemistry – A European Journal* **24**, 16944–16963 (2018). doi: 10.1002/chem.201802194. (cited on page 23).

[251] Jin, R., Zeng, C., Zhou, M. & Chen, Y. Atomically precise colloidal metal nanoclusters and nanoparticles: Fundamentals and opportunities. *Chem. Rev.* **116**, 10346–10413 (2016). doi: 10.1021/acs.chemrev.5b00703. (cited on page 23).

[252] Kang, X. *et al.* Reversible nanocluster structure transformation between face-centered cubic and icosahedral isomers. *Chem. Sci.* **10**, 8685–8693 (2019). doi: 10.1039/c9sc02667c. (cited on page 23).

[253] Huang, J., Mensi, M., Oveisi, E., Mantella, V. & Buonsanti, R. Structural sensitivities in bimetallic catalysts for electrochemical CO_2 reduction revealed by Ag–Cu nanodimers. *J. Am. Chem. Soc.* **141**, 2490–2499 (2019). doi: 10.1021/jacs.8b12381. (cited on page 23).

[254] Zaza, L., Rossi, K. & Buonsanti, R. Well-defined copper-based nanocatalysts for selective electrochemical reduction of CO_2 to C_2 products. *ACS Energy Lett.* **7**, 1284–1291 (2022). doi: 10.1021/acsenergylett.2c00035. (cited on pages 23 and 24).

[255] Li, J. & Sun, S. Intermetallic nanoparticles: Synthetic control and their enhanced electrocatalysis. *Acc. Chem. Res.* **52**, 2015–2025 (2019). doi: 10.1021/acs.accounts.9b00172. (cited on page 23).

[256] Ma, S. *et al.* Electroreduction of carbon dioxide to hydrocarbons using bimetallic Cu–Pd catalysts with different mixing patterns. *J. Am. Chem. Soc.* **139**, 47–50 (2016). doi: 10.1021/jacs.6b10740. (cited on page 24).

[257] Zhang, S. *et al.* Polymer-supported CuPd nanoalloy as a synergistic catalyst for electrocatalytic reduction of carbon dioxide to methane. *Proc. Natl. Acad. Sci. U.S.A.* **112**, 15809–15814 (2015). doi: 10.1073/pnas.1522496112. (cited on page 24).

[258] Bai, S. *et al.* Highly active and selective hydrogenation of CO_2 to ethanol by ordered Pd–Cu nanoparticles. *J. Am. Chem. Soc.* **139**, 6827–6830 (2017). doi: 10.1021/jacs.7b03101. (cited on

page 24).

[259] Rodríguez, J. A. & Fernández-García, M. *Synthesis, properties, and applications of oxide nanomaterials* (John Wiley & Sons, 2007). doi: 10.1002/0470108975. (cited on page 24).

[260] Gross, R., Marx, A. & Einzel, D. *Festkörperphysik. Aufgaben und Lösungen* (Walter de Gruyter, 2013). doi: 10.1524/9783110358704. (cited on pages 24 and 29).

[261] Lloyd, L. *Handbook of Industrial Catalysts* (Springer US, 2011). doi: 10.1007/978-0-387-49962-8. (cited on page 24).

[262] Winter, M. & Brodd, R. J. What are batteries, fuel cells, and supercapacitors? *Chem. Rev.* **104**, 4245–4270 (2004). doi: 10.1021/cr020730k. (cited on pages 24 and 25).

[263] Welborn, S. S. & Detsi, E. Small-angle X-ray scattering of nanoporous materials. *Nanoscale Horiz.* **5**, 12–24 (2020). doi: 10.1039/c9nh00347a. (cited on pages 24, 31, 33, and 106).

[264] Newman, J. & Tiedemann, W. Porous-electrode theory with battery applications. *AIChE Journal* **21**, 25–41 (1975). doi: 10.1002/aic.690210103. (cited on page 25).

[265] Zhang, H., Yu, X. & Braun, P. V. Three-dimensional bicontinuous ultrafast-charge and-discharge bulk battery electrodes. *Nat. Nanotechnol.* **6**, 277–281 (2011). doi: 10.1038/nnano.2011.38. (cited on page 25).

[266] Teixidor, G. T., Park, B., Mukherjee, P., Kang, Q. & Madou, M. Modeling fractal electrodes for Li-ion batteries. *Electrochim. Acta* **54**, 5928–5936 (2009). doi: 10.1016/j.electacta.2009.05.060. (cited on page 25).

[267] George, J. M., Antony, A. & Mathew, B. Metal oxide nanoparticles in electrochemical sensing and biosensing: a review. *Microchim. Acta* **185** (2018). doi: 10.1007/s00604-018-2894-3. (cited on page 25).

[268] Niederberger, M. Multiscale nanoparticle assembly: From particulate precise manufacturing to colloidal processing. *Adv. Funct. Mater.* **27** (2017). doi: 10.1002/adfm.201703647. (cited on page 25).

[269] Nam, K. M. *et al.* Single-crystalline hollow face-centered-cubic cobalt nanoparticles from solid face-centered-cubic cobalt oxide nanoparticles. *Angew. Chem. Int. Ed.* **47**, 9504–9508 (2008). doi: 10.1002/anie.200803048. (cited on page 25).

[270] Grote, L. *et al.* Imaging Cu_2O nanocube hollowing in solution by quantitative in situ X-ray ptychography. *Nat. Commun.* **13**, 4971 (2022). doi: 10.1038/s41467-022-32373-2. (cited on pages 25 and 138).

[271] Mei, J., Liao, T., Ayoko, G. A., Bell, J. & Sun, Z. Cobalt oxide-based nanoarchitectures for electrochemical energy applications. *Prog. Mater. Sci.* **103**, 596–677 (2019). doi: 10.1016/j.pmatsci.2019.03.001. (cited on page 25).

[272] Drasovean, R., Condurache-Bota, S. *et al.* Structural characterization and optical properties of Co_3O_4 and CoO films. *Journal of Optoelectronics and Adv. Mater.* **11**, 2141–2144 (2009). URL https://joam.inoe.ro/articles/structural-characterization-and-optical-properties-of-co3o4-and-coo-films/fulltext. (cited on page 25).

[273] Jiang, Z.-J. & Jiang, Z. Interaction induced high catalytic activities of CoO nanoparticles grown on nitrogen-doped hollow graphene microspheres for oxygen reduction and evolution reactions. *Sci. Rep.* **6**, 27081 (2016). doi: 10.1038/srep27081. (cited on page 25).

[274] Liao, L. *et al.* Efficient solar water-splitting using a nanocrystalline CoO photocatalyst. *Nat. Nanotechnol.* **9**, 69–73 (2014). doi: 10.1038/nnano.2013.272. (cited on page 25).

[275] Sievers, G. W. *et al.* Self-supported Pt–CoO networks combining high specific activity with high surface area for oxygen reduction. *Nat. Mater.* **20**, 208–213 (2021). doi: 10.1038/s41563-020-0775-8. (cited on page 25).

[276] Budiyanto, E. & Tüysüz, H. Cobalt oxide nanowires with controllable diameters and crystal structures for the oxygen evolution reaction. *Eur. J. Inorg. Chem.* **2022**, e202200065 (2022). doi: 10.1002/ejic.202200065. (cited on page 25).

[277] Kong, F.-C., Li, Y.-F., Shang, C. & Liu, Z.-P. Stability and phase transition of cobalt oxide phases by machine learning global potential energy surface. *J. Phys. Chem. C* **123**, 17539–17547 (2019). doi: 10.1021/acs.jpcc.9b02842. (cited on page 25).

[278] Jang, K. Y., Ahn, S. J., Kwon, J.-H., Nam, K. M. & Kim, Y. H. Novel route from a wurtzite to a rock-salt structure in CoO nanocrystals: in situ transmission electron microscopy study. *J. Phys.*

Chem. C **123**, 10689–10694 (2019). doi: 10.1021/acs.jpcc.9b01548. (cited on page 25).

[279] He, X. *et al.* Phase-and size-dependent optical and magnetic properties of CoO nanoparticles. *J. Phys. Chem. C* **119**, 9550–9559 (2015). doi: 10.1021/jp5127909. (cited on pages 25 and 134).

[280] Li, Y. *et al.* Morphology-dominant microwave absorption enhancement and electron tomography characterization of CoO self-assembly 3D nano-flowers. *J. Mater. Chem. C* **2**, 5216–5222 (2014). doi: 10.1039/c4tc00739e. (cited on page 25).

[281] Staniuk, M. *et al.* Puzzling mechanism behind a simple synthesis of cobalt and cobalt oxide nanoparticles: In situ synchrotron X-ray absorption and diffraction studies. *Chem. Mater.* **26**, 2086–2094 (2014). doi: 10.1021/cm500090r. (cited on pages 25, 52, and 138).

[282] Chen, Z., Xu, A., Zhang, Y. & Gu, N. Preparation of NiO and CoO nanoparticles using m^{2+}-oleate (m = ni, co) as precursor. *Curr. Appl. Phys.* **10**, 967–970 (2010). doi: 10.1016/j.cap.2009.11.083. (cited on page 25).

[283] Koziej, D. *et al.* Interplay between size and crystal structure of molybdenum dioxide nanoparticles – synthesis, growth mechanism, and electrochemical performance. *Small* **7**, 377–387 (2011). doi: 10.1002/smll.201001606. (cited on page 25).

[284] Niederberger, M., Garnweitner, G., Ba, J., Polleux, J. & Pinna, N. Nonaqueous synthesis, assembly and formation mechanisms of metal oxide nanocrystals. *Int. J. Nanotechnol.* **4**, 263–281 (2007). doi: 10.1504/ijnt.2007.013473. (cited on page 25).

[285] Lak, A. *et al.* The dissociation rate of acetylacetonate ligands governs the size of ferrimagnetic zinc ferrite nanocubes. *ACS Appl. Mater. Interfaces* **12**, 217–226 (2019). doi: 10.1021/acsami.9b17714. (cited on page 25).

[286] Hadjimichael, M. *et al.* Metal–ferroelectric supercrystals with periodically curved metallic layers. *Nat. Mater.* **20**, 495–502 (2021). doi: 10.1038/s41563-020-00864-6. (cited on page 25).

[287] Baek, W. *et al.* Highly luminescent and catalytically active suprastructures of magic-sized semiconductor nanoclusters. *Nat. Mater.* **20**, 650–657 (2021). doi: 10.1038/s41563-020-00880-6. (cited on page 25).

[288] Li, J. *et al.* Nanoparticle superlattices as efficient bifunctional electrocatalysts for water splitting. *J. Am. Chem. Soc.* **137**, 14305–14312 (2015). doi: 10.1021/jacs.5b07756. (cited on page 25).

[289] Cherniukh, I. *et al.* Perovskite-type superlattices from lead halide perovskite nanocubes. *Nature* **593**, 535–542 (2021). doi: 10.1038/s41586-021-03492-5. (cited on pages 25 and 26).

[290] Goubet, N. & Pileni, M. P. Analogy between atoms in a nanocrystal and nanocrystals in a supracrystal: Is it real or just a highly probable speculation? *J. Phys. Chem. Letters* **2**, 1024–1031 (2011). doi: 10.1021/jz200134x. (cited on page 25).

[291] Kagan, C. R. & Murray, C. B. Charge transport in strongly coupled quantum dot solids. *Nat. Nanotechnol.* **10**, 1013–1026 (2015). doi: 10.1038/nnano.2015.247. (cited on pages 25 and 26).

[292] Russ, B. & Eisler, C. N. The future of quantum technologies: superfluorescence from solution-processed, tunable materials. *Nanophotonics* **13**, 1943–1951 (2024). doi: 10.1515/nanoph-2023-0919. (cited on page 26).

[293] Liu, Y. *et al.* Dependence of carrier mobility on nanocrystal size and ligand length in PbSe nanocrystal solids. *Nano Lett.* **10**, 1960–1969 (2010). doi: 10.1021/nl101284k. (cited on page 26).

[294] Diroll, B. T., Greybush, N. J., Kagan, C. R. & Murray, C. B. Smectic nanorod superlattices assembled on liquid subphases: Structure, orientation, defects, and optical polarization. *Chem. Mater.* **27**, 2998–3008 (2015). doi: 10.1021/acs.chemmater.5b00355. (cited on page 26).

[295] Tao, A. R., Ceperley, D. P., Sinsermsuksakul, P., Neureuther, A. R. & Yang, P. Self-organized silver nanoparticles for three-dimensional plasmonic crystals. *Nano Lett.* **8**, 4033–4038 (2008). doi: 10.1021/nl802877h. (cited on page 26).

[296] Ye, X., Chen, J., Diroll, B. T. & Murray, C. B. Tunable plasmonic coupling in self-assembled binary nanocrystal superlattices studied by correlated optical microspectrophotometry and electron microscopy. *Nano Lett.* **13**, 1291–1297 (2013). doi: 10.1021/nl400052w. (cited on page 26).

[297] Davis, T. J., Gómez, D. E. & Roberts, A. Plasmonic circuits for manipulating optical information. *Nanophotonics* **6**, 543–559 (2016). doi: 10.1515/nanoph-2016-0131. (cited on page 26).

[298] Sekh, T. V. *et al.* All-perovskite multicomponent nanocrystal superlattices. *ACS Nano* **18**, 8423–8436 (2024). doi: 10.1021/acsnano.3c13062. (cited on page 26).

[299] Kang, Y. *et al.* Engineering catalytic contacts and thermal stability: Gold/iron oxide binary nanocrystal superlattices for CO oxidation. *J. Am. Chem. Soc.* **135**, 1499–1505 (2013). doi: 10.1021/ja310427u. (cited on page 27).

[300] Treml, B. E., Lukose, B., Clancy, P., Smilgies, D.-M. & Hanrath, T. Connecting the particles in the box – controlled fusion of hexamer nanocrystal clusters within an AB_6 binary nanocrystal superlattice. *Sci. Rep.* **4** (2014). doi: 10.1038/srep06731. (cited on page 27).

[301] Green, E., Fullwood, E., Selden, J. & Zharov, I. Functional membranes via nanoparticle self-assembly. *Chem. Commun.* **51**, 7770–7780 (2015). doi: 10.1039/c5cc01388g. (cited on page 27).

[302] Jiao, Y. *et al.* Fabrication of three-dimensionally interconnected nanoparticle superlattices and their lithium-ion storage properties. *Nat. Commun.* **6**, 6420 (2015). doi: 10.1038/ncomms7420. (cited on page 27).

[303] Zhang, H., Kinnear, C. & Mulvaney, P. Fabrication of single-nanocrystal arrays. *Adv. Mater.* **32**, 1904551 (2020). doi: 10.1002/adma.201904551. (cited on page 27).

[304] Podsiadlo, P. *et al.* The role of order, nanocrystal size, and capping ligands in the collective mechanical response of three-dimensional nanocrystal solids. *J. Am. Chem. Soc.* **132**, 8953–8960 (2010). doi: 10.1021/ja100464a. (cited on page 27).

[305] Courty, A., Mermet, A., Albouy, P. A., Duval, E. & Pileni, M. P. Vibrational coherence of self-organized silver nanocrystals in f.c.c. supra-crystals. *Nat. Mater.* **4**, 395–398 (2005). doi: 10.1038/nmat1366. (cited on page 27).

[306] Dreyer, A. *et al.* Organically linked iron oxide nanoparticle supercrystals with exceptional isotropic mechanical properties. *Nat. Mater.* **15**, 522–528 (2016). doi: 10.1038/nmat4553. (cited on pages 27 and 135).

[307] Begley, M. R., Gianola, D. S. & Ray, T. R. Bridging functional nanocomposites to robust macroscale devices. *Science* **364**, eaav4299 (2019). doi: 10.1126/science.aav4299. (cited on page 27).

[308] Als-Nielsen, J. & McMorrow, D. *Elements of modern X-ray physics* (John Wiley & Sons, 2011). doi: 10.1002/9781119998365. (cited on pages 27, 28, 29, 36, 38, 41, 61, and 62).

[309] Liss, K.-D., Bartels, A., Schreyer, A. & Clemens, H. High-energy X-rays: a tool for advanced bulk investigations in materials science and physics. *Textures and Microstructures* **35**, 219–252 (2003). doi: 10.1080/07303300310001634952. (cited on pages 27 and 41).

[310] Bertram, F., Gutowski, O., Patommel, J., Schroer, C. & Ruett, U. 1D silicon refractive lenses for surface scattering with high energy X-rays. In *AIP Conference Proceedings*, vol. 1741 (AIP Publishing, 2016). doi: 10.1063/1.4952875. (cited on pages 27, 41, 53, 55, 56, 63, and 111).

[311] Warren, B. E. *X-ray Diffraction* (Dover Publication, 1990). doi: 10.1107/S0567739471000445. (cited on pages 27 and 36).

[312] Galli, S. X-ray Crystallography: One Century of Nobel Prizes. *J. Chem. Educ.* **91**, 2009–2012 (2014). doi: 10.1021/ed500343x. (cited on page 27).

[313] Chantler, C. *et al.* X-ray form factor, attenuation and scattering tables (version 2.1) (2005). URL https://physics.nist.gov/PhysRefData/FFast/html/form.html. National Institute of Standards and Technology, Gaithersburg, MD. Accessed: April 2, 2025. (cited on pages 28 and 62).

[314] Hahn, T. & Klapper, H. *Crystallographic and noncrystallographic point groups*, 762–803 (International Union of Crystallography, 2006). doi: 10.1107/97809553602060000520. (cited on page 29).

[315] de Jeu, W. H. *Basic X-ray scattering for soft matter* (Oxford University Press, London, England, 2016). doi: 10.1080/00107514.2017.1330286. (cited on pages 29, 33, 41, and 84).

[316] Haas, S., Sun, X., Conceição, A., Horbach, J. & Pfeffer, S. The new small-angle X-ray scattering beamline for materials research at PETRA III: SAXSMAT beamline P62. *J. Synchrotron Rad.* **30**, 1156–1167 (2023). doi: 10.1107/s1600577523008603. (cited on pages 29, 41, 53, 55, and 138).

[317] Glatter, O. & Kratky, O. *Small-Angle X-ray Scattering* (Academic Press, London, 1982). doi: 10.1002/actp.1985.010360520. (cited on pages 31, 32, 33, 41, and 128).

[318] Svergun, D. & Stuhrmann, H. New developments in direct shape determination from small-angle scattering. 1. Theory and model calculations. *Acta Cryst. A* **47**, 736–744 (1991). doi: 10.1107/s0108767391006414. (cited on page 31).

[319] Svergun, D. I. Restoring low resolution structure of biological macromolecules from solution scattering using simulated annealing. *Biophys. J.* **76**, 2879–2886 (1999). doi: 10.1016/s0006-3495(99)77443-6. (cited on page 31).

[320] Maes, J. *et al.* Size and concentration determination of colloidal nanocrystals by small-angle X-ray scattering. *Chem. Mater.* **30**, 3952–3962 (2018). doi: 10.1021/acs.chemmater.8b00903. (cited on page 31).

[321] Kotlarchyk, M. & Chen, S.-H. Analysis of small angle neutron scattering spectra from polydisperse interacting colloids. *J. Chem. Phys.* **79**, 2461–2469 (1983). doi: 10.1063/1.446055. (cited on pages 32 and 34).

[322] Percus, J. K. & Yevick, G. J. Analysis of classical statistical mechanics by means of collective coordinates. *Phys. Rev.* **110**, 1 (1958). doi: 10.1103/PhysRev.110.1. (cited on page 32).

[323] Debye, P. & Bueche, A. Scattering by an inhomogeneous solid. *J. Appl. Phys.* **20**, 518–525 (1949). doi: 10.1063/1.1698419. (cited on page 33).

[324] Debye, P., Anderson, H. & Brumberger, H. Scattering by an inhomogeneous solid. II. The correlation function and its application. *J. Appl. Phys.* **28**, 679–683 (1957). doi: 10.1063/1.1722830. (cited on page 33).

[325] Martin, J. E. & Hurd, A. J. Scattering from fractals. *J. Appl. Cryst.* **20**, 61–78 (1987). doi: 10.1107/s0021889887087107. (cited on page 33).

[326] Mildner, D. & Hall, P. Small-angle scattering from porous solids with fractal geometry. *J. Phys. D: Appl. Phys.* **19**, 1535 (1986). doi: 10.1088/0022-3727/19/8/021. (cited on pages 33 and 129).

[327] Beaucage, G. Small-angle scattering from polymeric mass fractals of arbitrary mass-fractal dimension. *J. Appl. Cryst.* **29**, 134–146 (1996). doi: 10.1107/s0021889895011605. (cited on pages 33 and 105).

[328] Seddon, J. M. & Cevc, G. Lipid polymorphism: Structure and stability of lyotropic mesophases of phospholipids. In *Phospholipids handbook*, 402–454 (CRC Press, 2018). doi: 10.1201/9780203743577. (cited on pages 33 and 92).

[329] Förster, S. *et al.* Scattering curves of ordered mesoscopic materials. *J. Phys. Chem. B* **109**, 1347–1360 (2005). doi: 10.1021/jp0467494. (cited on page 34).

[330] Yager, K. G., Zhang, Y., Lu, F. & Gang, O. Periodic lattices of arbitrary nano-objects: modeling and applications for self-assembled systems. *J. Appl. Cryst.* **47**, 118–129 (2014). doi: 10.1107/s160057671302832x. (cited on page 34).

[331] Doucet, M. *et al.* Sasview Zenodo. (2022). doi: 10.5281/zenodo.7581378. (cited on pages 34, 56, 58, 59, 60, 62, and 63).

[332] Kohlbrecher, J. & Breßler, I. Updates in SASfit for fitting analytical expressions and numerical models to small-angle scattering patterns. *J. Appl. Cryst.* **55**, 1677–1688 (2022). doi: 10.1107/s1600576722009037. (cited on page 34).

[333] Biehl, R. Jscatter, a program for evaluation and analysis of experimental data. *PLoS One* **14**, e0218789 (2019). doi: 10.1371/journal.pone.0218789. (cited on page 34).

[334] Breßler, I., Pauw, B. R. & Thünemann, A. McSAS: software for the retrieval of model parameter distributions from scattering patterns. *J. Appl. Cryst.* **48**, 962–969 (2015). doi: 10.1107/s1600576715007347. (cited on page 34).

[335] Ilavsky, J. & Jemian, P. R. Irena: tool suite for modeling and analysis of small-angle scattering. *J. Appl. Cryst.* **42**, 347–353 (2009). doi: 10.1107/s0021889809002222. (cited on page 34).

[336] Manalastas-Cantos, K. *et al.* ATSAS 3.0: expanded functionality and new tools for small-angle scattering data analysis. *J. Appl. Cryst.* **54**, 343–355 (2021). doi: 10.1107/s1600576720013412. (cited on pages 34 and 56).

[337] Storn, R. & Price, K. Differential evolution – a simple and efficient heuristic for global optimization over continuous spaces. *J. Glob. Optim.* **11**, 341–359 (1997). doi: 10.1023/a:1008202821328. (cited on page 34).

[338] Vrugt, J. A. *et al.* Accelerating Markov chain Monte Carlo simulation by differential evolution with self-adaptive randomized subspace sampling. *Int. J. Nonlinear Sci. Numer. Simul.* **10**, 273–290 (2009). doi: 10.1515/IJNSNS.2009.10.3.273. (cited on page 34).

[339] Gražulis, S. *et al.* Crystallography open database – an open-access collection of crystal structures. *J. Appl. Cryst.* **42**, 726–729 (2009). doi: 10.1107/s0021889809016690. (cited on pages 35, 112, 149,

and 161).

[340] Jain, A. *et al.* Commentary: The materials project: A materials genome approach to accelerating materials innovation. *APL Mater.* **1** (2013). doi: 10.1063/1.4812323. (cited on pages 35 and 161).

[341] Kaduk, J. A. *et al.* Powder diffraction. *Nat. Rev. Methods Primers* **1**, 1–22 (2021). doi: 10.1038/s43586-021-00074-7. (cited on pages 36 and 41).

[342] Zhao, J. *et al.* Great disparity in photoluminesence quantum yields of colloidal $CsPbBr_3$ nanocrystals with varied shape: The effect of crystal lattice strain. *J. Phys. Chem. Letters* **8**, 3115–3121 (2017). doi: 10.1021/acs.jpclett.7b01083. (cited on page 37).

[343] Scherrer, P. Bestimmung der Größe und der inneren Struktur von Kolloidteilchen mittels Röntgenstrahlen. *Nachrichten von der Gesellschaft der Wissenschaften zu Göttingen, Mathematisch-Physikalische Klasse* **1918**, 98–100 (1918). URL http://eudml.org/doc/59018. (cited on page 37).

[344] Williamson, G. & Hall, W. X-ray line broadening from filed aluminium and wolfram. *Acta Metallurgica* **1**, 22–31 (1953). doi: 10.1016/0001-6160(53)90006-6. (cited on page 37).

[345] Black, D. R. *et al.* Certification of standard reference material 660c for powder diffraction. *Powder Diffraction* **35**, 17–22 (2020). doi: 10.1017/s0885715620000068. (cited on page 37).

[346] Egami, T. & Billinge, S. J. *Underneath the Bragg peaks: structural analysis of complex materials*, vol. 16 (Elsevier, 2003). doi: 10.1016/S1369-7021(03)00635-7. (cited on pages 37, 38, and 142).

[347] Cernuto, G., Masciocchi, N., Cervellino, A., Colonna, G. M. & Guagliardi, A. Size and shape dependence of the photocatalytic activity of TiO_2 nanocrystals: A total scattering Debye function study. *J. Am. Chem. Soc.* **133**, 3114–3119 (2011). doi: 10.1021/ja110225n. (cited on page 37).

[348] Neder, R. B. & Korsunskiy, V. I. Structure of nanoparticles from powder diffraction data using the pair distribution function. *J. Phys. Condens. Matter* **17**, S125 (2005). doi: 10.1088/0953-8984/17/5/013. (cited on page 37).

[349] Christiansen, T. L., Cooper, S. R. & Jensen, K. M. There's no place like real-space: elucidating size-dependent atomic structure of nanomaterials using pair distribution function analysis. *Nanoscale Adv.* **2**, 2234–2254 (2020). doi: 10.1039/d0na00120a. (cited on page 37).

[350] Debye, P. Dispersion of Röntgen rays. *Ann. Phys* **46**, 21 (1915). (cited on page 37).

[351] Peterson, P. F., Olds, D., McDonnell, M. T. & Page, K. Illustrated formalisms for total scattering data: a guide for new practitioners. *J. Appl. Cryst.* **54**, 317–332 (2021). doi: 10.1107/S1600576720015630. (cited on pages 37, 39, and 141).

[352] Cervellino, A., Giannini, C. & Guagliardi, A. On the efficient evaluation of Fourier patterns for nanoparticles and clusters. *J. Comput. Chem.* **27**, 995–1008 (2006). doi: 10.1002/jcc.20407. (cited on page 38).

[353] Juhás, P., Davis, T., Farrow, C. L. & Billinge, S. J. PDFgetX3: a rapid and highly automatable program for processing powder diffraction data into total scattering pair distribution functions. *J. Appl. Cryst.* **46**, 560–566 (2013). doi: 10.1107/s0021889813005190. (cited on pages 39, 63, and 64).

[354] Chupas, P. J. *et al.* Rapid-acquisition pair distribution function (RA-PDF) analysis. *J. Appl. Cryst.* **36**, 1342–1347 (2003). doi: 10.1107/s0021889803017564. (cited on page 40).

[355] Farrow, C. *et al.* PDFfit2 and PDFgui: computer programs for studying nanostructure in crystals. *J. Phys. Condens. Matter* **19**, 335219 (2007). doi: 10.1088/0953-8984/19/33/335219. (cited on page 40).

[356] Banerjee, S. *et al.* Cluster-mining: an approach for determining core structures of metallic nanoparticles from atomic pair distribution function data. *Acta Cryst. A: Foundations and Advances* **76**, 24–31 (2020). doi: 10.1107/S2053273319013214. (cited on pages 40, 113, and 141).

[357] Dengo, N., Masciocchi, N., Cervellino, A., Guagliardi, A. & Bertolotti, F. Effects of structural and microstructural features on the total scattering pattern of nanocrystalline materials. *Nanomaterials* **12**, 1252 (2022). doi: 10.3390/nano12081252. (cited on page 40).

[358] The Incoatec Microfocus Source for XRD-Applications. https://www.incoatec.de/files/downloads/poster/IDO-P21-013A-xs.pdf. Accessed: May 26, 2025. (cited on page 41).

[359] Buffet, A. *et al.* P03, the microfocus and nanofocus X-ray scattering (MiNaXS) beamline of the PETRA III storage ring: the microfocus endstation. *J. Synchrotron Rad.* **19**, 647–653 (2012). doi: 10.1107/s0909049512016895. (cited on pages 41, 55, 63, and 128).

[360] v. Zimmermann, M. *et al.* P21.1 at PETRA III – a high-energy X-ray diffraction beamline for physics and chemistry. *J. Synchrotron Rad.* **32**, 802–814 (2025). doi: 10.1107/s1600577525002826. (cited on pages 41, 42, 55, 64, and 126).

[361] Raimondi, P. *et al.* The Extremely Brilliant Source storage ring of the European Synchrotron Radiation Facility. *Commun. Phys.* **6**, 82 (2023). doi: 10.1038/s42005-023-01195-z. (cited on pages 41 and 137).

[362] Seltzer, S. XCOM-photon cross sections database, NIST standard reference database 8 (1987). doi: 10.18434/t48g6x. (cited on page 42).

[363] Pilatus 3R 300K technical specifications. https://media.dectris.com/TechnicalSpecification-PILATUS3-R-300K-v1.2.0.pdf. Accessed: May 28, 2024. (cited on pages 42, 55, and 138).

[364] Donath, T. *et al.* Enhancing high-energy powder X-ray diffraction applications using a PILATUS4 CdTe detector. *J. Synchrotron Rad.* **32**, 378–384 (2025). doi: 10.1107/S1600577525000566. (cited on pages 42 and 138).

[365] Varex 4343CT technical specifications. https://www.vareximaging.com/wp-content/uploads/2022/01/XRD-4343CT_118914-1.pdf. Accessed: May 28, 2024. (cited on pages 42 and 55).

[366] Pauw, B. R. Everything SAXS: small-angle scattering pattern collection and correction. *J. Phys. Condens. Matter* **25**, 383201 (2013). doi: 10.1088/0953-8984/25/38/383201. (cited on pages 42 and 43).

[367] Baron, A. Q. & Ishikawa, D. Background rates in several hard X-ray photon counting pixel array detectors. *Nucl. Instrum. Methods Phys. Res. A* **1049**, 168101 (2023). doi: 10.1016/j.nima.2023.168101. (cited on page 42).

[368] Lakowicz, J. R. *Principles of fluorescence spectroscopy* (Springer, New York, NY, 2006), 3rd edn. doi: 10.1007/978-0-387-46312-4. (cited on pages 43 and 44).

[369] Ocean Optics Flame Miniature Spectrometer User Manual. https://www.oceanoptics.com/wp-content/uploads/2024/12/Flame-User-Manual.pdf. Accessed: May 26, 2025. (cited on pages 43 and 54).

[370] Carter, C. B. & Williams, D. B. *Transmission electron microscopy: Diffraction, imaging, and spectrometry* (Springer, 2016). doi: 10.1007/978-0-387-76501-3. (cited on pages 44 and 45).

[371] Goldstein, J. I. *et al. Scanning Electron Microscopy and X-Ray Microanalysis* (Springer, 2018), 4th edn. doi: 10.1007/978-1-4939-6676-9. (cited on page 45).

[372] Cutsail III, G. E. & DeBeer, S. Challenges and opportunities for applications of advanced X-ray spectroscopy in catalysis research. *ACS Catalysis* **12**, 5864–5886 (2022). doi: 10.1021/acscatal.2c01016. (cited on page 45).

[373] van Bokhoven, J. A. & Lamberti, C. *X-ray absorption and X-ray emission spectroscopy* (John Wiley & Sons, Nashville, TN, 2016). doi: 10.1002/9781118844243. (cited on page 46).

[374] De Juan, A., Jaumot, J. & Tauler, R. Multivariate curve resolution (MCR). Solving the mixture analysis problem. *Anal. Methods.* **6**, 4964–4976 (2014). doi: 10.1039/c4ay00571f. (cited on pages 46, 66, and 143).

[375] Smith, B. C. *Fundamentals of Fourier transform infrared spectroscopy, second edition* (CRC Press, Boca Raton, FL, 2009), 2nd edn. doi: 10.1201/b10777. (cited on page 47).

[376] Hung, L.-I., Tsung, C.-K., Huang, W. & Yang, P. Room-temperature formation of hollow Cu_2O nanoparticles. *Adv. Mater.* **22**, 1910–1914 (2010). doi: 10.1002/adma.200903947. (cited on page 50).

[377] Grote, L. *et al.* X-ray studies bridge the molecular and macro length scales during the emergence of CoO assemblies. *Nat. Commun.* **12**, 4429 (2021). doi: 10.1038/s41467-021-24557-z. (cited on pages 52, 64, 125, 126, 127, 128, 129, and 130).

[378] Bruetzel, L. K. *et al.* A Mo-anode-based in-house source for small-angle X-ray scattering measurements of biological macromolecules. *Rev. Sci. Instrum.* **87**, 025103 (2016). doi: 10.1063/1.4940936. (cited on pages 53, 55, and 56).

[379] Frank, K. *et al.* Antisolvent controls the shape and size of anisotropic lead halide perovskite nanocrystals. *Nat. Commun.* **15**, 8952 (2024). doi: 10.1038/s41467-024-53221-5. (cited on pages 53, 69, 70, 71, 72, 73, 74, 75, 76, 78, 79, 80, 81, 82, 85, 87, 88, 90, and 94).

[380] 1512 CMOS flat panel detector. https://www.vareximaging.com/wp-content/uploads/2022/01/1512-CMOS-Medical-149127-000_PDS.pdf. Accessed: June 16, 2025. (cited on page 55).

[381] Kieffer, J., Valls, V., Blanc, N. & Hennig, C. New tools for calibrating diffraction setups. *J. Synchrotron Rad.* **27**, 558–566 (2020). doi: 10.1107/s1600577520000776. (cited on pages 56, 58, 59, 63, and 64).

[382] Frank, K. *et al.* Data for: Antisolvent controls the shape and size of anisotropic lead halide perovskite nanocrystals (2024). doi: 10.57970/nb26d-cak63, URL https://doi.org/10.57970/nb26d-cak63. (cited on page 56).

[383] Newville, M. *et al.* lmfit version 1.2.2 Zenodo. (2023). doi: 10.5281/zenodo.8145703, URL https://doi.org/10.5281/zenodo.8145703. (cited on page 59).

[384] Harris, C. R. *et al.* Array programming with NumPy. *Nature* **585**, 357–362 (2020). doi: 10.1038/s41586-020-2649-2. (cited on page 59).

[385] Virtanen, P. *et al.* SciPy 1.0: Fundamental Algorithms for Scientific Computing in Python. *Nature Methods* **17**, 261–272 (2020). doi: 10.1038/s41592-019-0686-2. (cited on page 59).

[386] Kluyver, T. *et al.* Jupyter notebooks – a publishing format for reproducible computational workflows. In Loizides, F. & Schmidt, B. (eds.) *Positioning and Power in Academic Publishing: Players, Agents and Agendas*, 87–90 (IOS Press, Netherlands, 2016). doi: 10.3233/978-1-61499-649-1-87. (cited on page 59).

[387] Larsen, A. H. *et al.* The atomic simulation environment – a python library for working with atoms. *J. Phys. Condens. Matter* **29**, 273002 (2017). doi: 10.1088/1361-648x/aa680e. (cited on pages 61, 64, and 142).

[388] Ilavsky, J. Nika: software for two-dimensional data reduction. *J. Appl. Cryst.* **45**, 324–328 (2012). doi: 10.1107/s0021889812004037. (cited on page 63).

[389] Juhás, P., Farrow, C., Yang, X., Knox, K. & Billinge, S. Complex modeling: a strategy and software program for combining multiple information sources to solve ill posed structure and nanostructure inverse problems. *Acta Cryst. A: Foundations and Advances* **71**, 562–568 (2015). doi: 10.1107/s2053273315014473. (cited on pages 63, 64, and 141).

[390] van Beek, W., Safonova, O. V., Wiker, G. & Emerich, H. SNBL, a dedicated beamline for combined in situ X-ray diffraction, X-ray absorption and Raman scattering experiments. *Phase Transitions* **84**, 726–732 (2011). doi: 10.1080/01411594.2010.549944. (cited on pages 63 and 66).

[391] Hammersley, A. P. FIT2D: a multi-purpose data reduction, analysis and visualization program. *J. Appl. Cryst.* **49**, 646–652 (2016). doi: 10.1107/s1600576716000455. (cited on page 64).

[392] Derelli, D. *et al.* Direct synthesis of CuPd icosahedra supercrystals studied by in situ X-ray scattering. *Small* **20**, 2311714 (2024). doi: 10.1002/smll.202311714. (cited on pages 64, 110, 111, 112, 113, 114, 115, 117, 118, and 120).

[393] Macrae, C. F. *et al.* Mercury 4.0: From visualization to analysis, design and prediction. *J. Appl. Cryst.* **53**, 226–235 (2020). doi: 10.1107/s1600576719014092. (cited on page 64).

[394] Momma, K. & Izumi, F. VESTA 3 for three-dimensional visualization of crystal, volumetric and morphology data. *J. Appl. Cryst.* **44**, 1272–1276 (2011). doi: 10.1107/s0021889811038970. (cited on pages 64 and 161).

[395] Glatzel, P. *et al.* The five-analyzer point-to-point scanning crystal spectrometer at ESRF ID26. *J. Synchrotron Rad.* **28**, 362–371 (2021). doi: 10.1107/s1600577520015416. (cited on page 66).

[396] Solé, V., Papillon, E., Cotte, M., Walter, P. & Susini, J. A multiplatform code for the analysis of energy-dispersive X-ray fluorescence spectra. *Spectrochim. Acta Part B At. Spectrosc.* **62**, 63–68 (2007). doi: 10.1016/j.sab.2006.12.002. (cited on page 66).

[397] Glicksman, M. *Plasmas in Solids*, 275–427 (Elsevier, 1971). doi: 10.1016/s0081-1947(08)60493-2. (cited on page 67).

[398] Imran, M. *et al.* Colloidal synthesis of strongly fluorescent $CsPbBr_3$ nanowires with width tunable down to the quantum confinement regime. *Chem. Mater.* **28**, 6450–6454 (2016). doi: 10.1021/acs.chemmater.6b03081. (cited on page 71).

[399] Socie, E., Vale, B. R. C., Terpstra, A. T., Schiavon, M. A. & Moser, J.-E. Resonant band-edge emissive states in strongly confined $CsPbBr_3$ perovskite nanoplatets. *J. Phys. Chem. C* **125**, 14317–14325 (2021). doi: 10.1021/acs.jpcc.1c01353. (cited on page 72).

[400] Dang, Z. *et al.* In situ transmission electron microscopy study of electron beam-induced transformations in colloidal cesium lead halide perovskite nanocrystals. *ACS Nano* **11**, 2124–2132 (2017). doi: 10.1021/acsnano.6b08324. (cited on page 72).

[401] Loubat, A. *et al.* Ultrathin gold nanowires: soft-templating versus liquid phase synthesis, a quantitative study. *J. Phys. Chem. C* **119**, 4422–4430 (2015). doi: 10.1021/acs.jpcc.5b00242. (cited on page 73).

[402] Dahl, J. C. *et al.* Precursor chemistry of lead bromide perovskite nanocrystals. *ACS Nano* **18**, 22208–22219 (2024). doi: 10.1021/acsnano.4c05761. (cited on pages 77, 132, and 139).

[403] Vickers, E. T. *et al.* Interplay between perovskite magic-sized clusters and amino lead halide molecular clusters. *Research* **2021** (2021). doi: 10.34133/2021/6047971. (cited on page 77).

[404] Shargaieva, O., Kuske, L., Rappich, J., Unger, E. & Nickel, N. H. Building blocks of hybrid perovskites: A photoluminescence study of lead-iodide solution species. *ChemPhysChem* **21**, 2327–2333 (2020). doi: 10.1002/cphc.202000479. (cited on pages 77 and 132).

[405] Lu, C. *et al.* Cesium oleate precursor preparation for lead halide perovskite nanocrystal synthesis: The influence of excess oleic acid on achieving solubility, conversion, and reproducibility. *Chem. Mater.* **31**, 62–67 (2018). doi: 10.1021/acs.chemmater.8b04876. (cited on page 77).

[406] Jana, S. *et al.* Stacking and colloidal stability of CdSe nanoplatelets. *Langmuir* **31**, 10532–10539 (2015). doi: 10.1021/acs.langmuir.5b02152. (cited on pages 83 and 88).

[407] Sun, Y. *et al.* Research on the influence of polar solvents on $CsPbBr_3$ perovskite QDs. *RSC Adv.* **11**, 27333–27337 (2021). doi: 10.1039/d1ra04485k. (cited on page 87).

[408] Yang, Y., Gao, F., Gao, S. & Wei, S.-H. Origin of the stability of two-dimensional perovskites: a first-principles study. *J. Mater. Chem. A* **6**, 14949–14955 (2018). doi: 10.1039/c8ta01496e. (cited on page 88).

[409] Burlakov, V. M., Hassan, Y., Danaie, M., Snaith, H. J. & Goriely, A. Competitive nucleation mechanism for $CsPbBr_3$ perovskite nanoplatelet growth. *J. Phys. Chem. Letters* **11**, 6535–6543 (2020). doi: 10.1021/acs.jpclett.0c01794. (cited on page 88).

[410] Riedinger, A. *et al.* An intrinsic growth instability in isotropic materials leads to quasi-two-dimensional nanoplatelets. *Nat. Mater.* **16**, 743–748 (2017). doi: 10.1038/nmat4889. (cited on page 88).

[411] Petersen, N., Girard, M., Riedinger, A. & Valsson, O. The crucial role of solvation forces in the steric stabilization of nanoplatelets. *Nano Lett.* **22**, 9847–9853 (2022). doi: 10.1021/acs.nanolett.2c02848. (cited on page 89).

[412] Antanovich, A., Prudnikau, A., Matsukovich, A., Achtstein, A. & Artemyev, M. Self-assembly of CdSe nanoplatelets into stacks of controlled size induced by ligand exchange. *J. Phys. Chem. C* **120**, 5764–5775 (2016). doi: 10.1021/acs.jpcc.5b12139. (cited on pages 89 and 119).

[413] Morad, V. *et al.* Designer phospholipid capping ligands for soft metal halide nanocrystals. *Nature* **626**, 542–548 (2024). doi: 10.1038/s41586-023-06932-6. (cited on page 92).

[414] Worku, M. *et al.* Hollow metal halide perovskite nanocrystals with efficient blue emissions. *Sci. Adv.* **6**, eaaz5961 (2020). doi: 10.1126/sciadv.aaz5961. (cited on page 92).

[415] Pradhan, N. Do halide perovskites prefer a specific direction for forming one-dimensional nanostructures? *ACS Energy Lett.* **7**, 150–153 (2021). doi: 10.1021/acsenergylett.1c02235. (cited on page 92).

[416] Zhang, J. *et al.* Highly luminescent and stable $CsPbI_3$ perovskite nanocrystals with sodium dodecyl sulfate ligand passivation for red-light-emitting diodes. *J. Phys. Chem. Letters* **12**, 2437–2443 (2021). doi: 10.1021/acs.jpclett.1c00008. (cited on page 95).

[417] Huang, H. *et al.* Spontaneous crystallization of perovskite nanocrystals in nonpolar organic solvents: A versatile approach for their shape-controlled synthesis. *Angew. Chem. Int. Ed.* **58**, 16558–16562 (2019). doi: 10.1002/anie.201906862. (cited on page 95).

[418] Xie, M., Zhu, Y., Wang, R. & Tian, J. High efficiency and narrow emission band pure-red perovskite colloidal quantum wells. *J. Phys. Chem. Letters* **12**, 10735–10741 (2021). doi: 10.1021/acs.jpclett.1c03244. (cited on page 95).

[419] Ma, Z. *et al.* $CsPb(Br/I)_3$ perovskite nanocrystals for hybrid GaN-based high-bandwidth white light-emitting diodes. *ACS Appl. Nano Mater.* **4**, 8383–8389 (2021). doi: 10.1021/acsanm.1c01604. (cited on page 100).

[420] Nam, Y. *et al.* Negligible bowing effect of bandgap and lattice constant in a variety of compositions using large tilt distortion in a cesium–lead mixed-halide system. *Adv. Opt. Mater.* **11**, 2300682 (2023). doi: 10.1002/adom.202300682. (cited on page 100).

[421] Lehmann, F. *et al.* The phase diagram of a mixed halide (Br, I) hybrid perovskite obtained by synchrotron X-ray diffraction. *RSC Adv.* **9**, 11151–11159 (2019). doi: 10.1039/c8ra09398a. (cited on page 100).

[422] Vinçon, I., Barfüßer, A., Feldmann, J. & Akkerman, Q. A. Quantum dot metal salt interactions unraveled by the sphere of action model. *J. Am. Chem. Soc.* **145**, 14395–14403 (2023). doi: 10.1021/jacs.3c03582. (cited on page 102).

[423] Calvin, J., Sedlak, A., Brewer, A., Kaufman, T. & Alivisatos, P. Quantum dot size dependence on ligand exchange driving forces and insights into the structure of the solvated ligand shell. *ChemRxiv preprint* (2024). doi: 10.26434/chemrxiv-2024-nlpsf. (cited on page 102).

[424] Park, J. *et al.* Air-stable cesium lead bromide perovskite nanocrystals via post-synthetic treatment with oleylammonium bromides. *New J. Chem.* **46**, 19514–19522 (2022). doi: 10.1039/d2nj03057h. (cited on page 102).

[425] Derelli, D. *Investigating Nanostructured Materials by Multi-modal in situ X-ray Methods.* Ph.D. thesis, University of Hamburg (2024). URL https://ediss.sub.uni-hamburg.de/handle/ediss/10963. (cited on page 112).

[426] Jeong, A. *et al.* Colloidal dispersions of sterically and electrostatically stabilized PbS quantum dots: Structure factors, second virial coefficients, and film-forming properties. *ACS Nano* **18**, 33864–33874 (2024). doi: 10.1021/acsnano.4c06033. (cited on page 122).

[427] von Chrzanowski, L. S., Lutz, M. & Spek, A. L. α-tris (2, 4-pentanedionato-κ2o, o$\prime$) cobalt (III) at 240, 210, 180, 150 and 110 K. *Acta Cryst. C* **63**, m283–m288 (2007). doi: 10.1107/s0108270107022950. (cited on page 127).

[428] Radon, M., Srebro, M. & Broclawik, E. Conformational stability and spin states of cobalt (II) acetylacetonate: CASPT2 and DFT study. *J. Chem. Theory Comput.* **5**, 1237–1244 (2009). doi: 10.1021/ct800571y. (cited on page 127).

[429] Sasaki, S., Fujino, K. & Takéuchi, Y. X-ray determination of electron-density distributions in oxides, MgO, MnO, CoO, and NiO, and atomic scattering factors of their constituent atoms. *Proc. Jpn. Acad. B: Phys. Biol. Sci.* **55**, 43–48 (1979). doi: 10.2183/pjab.55.43. (cited on pages 127 and 168).

[430] Damasceno, P. F., Engel, M. & Glotzer, S. C. Predictive self-assembly of polyhedra into complex structures. *Science* **337**, 453–457 (2012). doi: 10.1126/science.1220869. (cited on pages 130 and 143).

[431] Kansal, A. R., Torquato, S. & Stillinger, F. H. Computer generation of dense polydisperse sphere packings. *J. Chem. Phys.* **117**, 8212–8218 (2002). doi: 10.1063/1.1511510. (cited on page 130).

[432] Broge, N. L. N. *et al.* Exploration of anion effects in solvothermal synthesis using in situ X-ray diffraction. *Phys. Chem. Chem. Phys.* **26**, 12121–12132 (2024). doi: 10.1039/d4cp00541d. (cited on page 132).

[433] Staniuk, M., Rechberger, F., Tervoort, E. & Niederberger, M. Adapting the concepts of nonaqueous sol–gel chemistry to metals: synthesis and formation mechanism of palladium and palladium–copper nanoparticles in benzyl alcohol. *J. Sol-Gel Sci. Technol.* **95**, 573–586 (2020). doi: 10.1007/s10971-020-05278-z. (cited on pages 132 and 136).

[434] Win, A. A., Chou, K.-C., Zeitz, D. C., Todd, C. & Zhang, J. Z. Origin of the near 400 nm absorption and emission band in the synthesis of cesium lead bromide nanostructures: metal halide molecular clusters rather than perovskite magic-sized clusters. *J. Phys. Chem. Lett.* **14**, 116–121 (2022). doi: 10.1021/acs.jpclett.2c03734. (cited on page 132).

[435] Dahl, J. C. *et al.* Scientific machine learning of 2D perovskite nanosheet formation. *J. Am. Chem. Soc.* **145**, 23076–23087 (2023). doi: 10.1021/jacs.3c05984. (cited on pages 132, 139, and 140).

[436] DuBose, J. T., Christy, A., Chakkamalayath, J. & Kamat, P. V. Transformation of perovskite nanoplatelets to large nanostructures driven by solvent polarity. *ACS Materials Letters* **4**, 93–101 (2021). doi: 10.1021/acsmaterialslett.1c00663. (cited on page 134).

[437] Noro, M. G. & Frenkel, D. Extended corresponding-states behavior for particles with variable range attractions. *J. Chem. Phys.* **113**, 2941–2944 (2000). doi: 10.1063/1.1288684. (cited on page 135).

[438] Saez Cabezas, C. A. *et al.* Gelation of plasmonic metal oxide nanocrystals by polymer-induced depletion attractions. *Proc. Natl. Acad. Sci. U.S.A.* **115**, 8925–8930 (2018). doi: 10.1073/pnas.1806927115. (cited on page 135).

[439] Sandhyarani, N., Antony, M. P., Selvam, G. P. & Pradeep, T. Melting of monolayer protected cluster superlattices. *J. Chem. Phys.* **113**, 9794–9803 (2000). doi: 10.1063/1.1322029. (cited on pages 135 and 136).

[440] Chen, L. B., Chow, M. K., Ackerson, B. J. & Zukoski, C. F. Rheological and microstructural transitions in colloidal crystals. *Langmuir* **10**, 2817–2829 (1994). doi: 10.1021/la00020a052. (cited on page 135).

[441] Dey, J. *et al.* Spontaneous formation of highly stable nanoparticle supercrystals driven by a covalent bonding interaction. *Nano Lett.* **21**, 258–264 (2020). doi: 10.1021/acs.nanolett.0c03616. (cited on page 135).

[442] Plunkett, A. *et al.* Strengthening engineered nanocrystal three-dimensional superlattices via ligand conformation and reactivity. *ACS Nano* **16**, 11692–11707 (2022). doi: 10.1021/acsnano.2c01332. (cited on page 135).

[443] Wang, S. *et al.* A general approach to stabilize nanocrystal superlattices by covalently bonded ligands. *ACS Nano* **17**, 2792–2801 (2023). doi: 10.1021/acsnano.2c11077. (cited on page 135).

[444] Liu, Z., Kooijman, H., Spek, A. L. & Bouwman, E. New manganese-based catalyst systems for alkyd paint drying. *Progress in Organic Coatings* **60**, 343–349 (2007). doi: 10.1016/j.porgcoat.2007.08.003. (cited on page 136).

[445] Xia, Y., Xiong, Y., Lim, B. & Skrabalak, S. E. Shape-controlled synthesis of metal nanocrystals: simple chemistry meets complex physics? *Angew. Chem. Int. Ed.* **48**, 60–103 (2009). doi: 10.1002/anie.200802248. (cited on page 136).

[446] Widmer-Cooper, A. & Geissler, P. Orientational ordering of passivating ligands on CdS nanorods in solution generates strong rod–rod interactions. *Nano Lett.* **14**, 57–65 (2013). doi: 10.1021/nl403067p. (cited on page 136).

[447] Vitale, S. A. & Katz, J. L. Liquid droplet dispersions formed by homogeneous liquid–liquid nucleation: "The Ouzo Effect". *Langmuir* **19**, 4105–4110 (2003). doi: 10.1021/la026842o. (cited on page 136).

[448] Prévost, S. *et al.* Spontaneous ouzo emulsions coexist with pre-ouzo ultraflexible microemulsions. *Langmuir* **37**, 3817–3827 (2021). doi: 10.1021/acs.langmuir.0c02935. (cited on page 136).

[449] Monego, D. *et al.* When like destabilizes like: Inverted solvent effects in apolar nanoparticle dispersions. *ACS Nano* **14**, 5278–5287 (2020). doi: 10.1021/acsnano.9b03552. (cited on page 137).

[450] Hasan, M. R. *et al.* The colloidal stability of apolar nanoparticles in solvent mixtures. *ACS Nano* **17**, 9302–9312 (2023). doi: 10.1021/acsnano.3c00812. (cited on page 137).

[451] Zhang, Q., Diao, F. & Wang, Y. The role of antisolvents with different functional groups in the formation of Cs_4PbBr_6 and $CsPbBr_3$ particles. *Inorganic Chemistry* **63**, 1562–1574 (2024). doi: 10.1021/acs.inorgchem.3c03398. (cited on page 137).

[452] Schroer, C. G. *et al.* The synchrotron radiation source PETRA III and its future ultra-low-emittance upgrade PETRA IV. *Eur. Phys. J. Plus* **137** (2022). doi: 10.1140/epjp/s13360-022-03517-6. (cited on page 137).

[453] Matsumoto, Y. *et al.* An arrayed-window microfluidic device for observation of mixed nanoparticles with an X-ray free-electron laser. *Opt. Rev.* **29**, 7–12 (2022). doi: 10.1007/s10043-021-00716-x. (cited on page 138).

[454] Sapnik, A. F. *et al.* High-quality ultra-fast total scattering and pair distribution function data using an X-ray free-electron laser. *IUCrJ* **12** (2025). doi: 10.1107/s205225252500538x. (cited on pages 138 and 139).

[455] Ober, M. *Photoswitching of lipids and silicification of DNA origami objects probed by small-angle X-ray scattering.* Ph.D. thesis, LMU Munich (2022). doi: 10.5282/edoc.29919. (cited on page 138).

[456] Garman, E. F. & Weik, M. X-ray radiation damage to biological samples: recent progress. *J. Synchrotron Rad.* **26**, 907–911 (2019). doi: 10.1107/s1600577519009408. (cited on page 138).

[457] Eiger X 1M technical specifications. https://media.dectris.com/TechnicalSpecifications_EIGER_X_1M_rMCm8U0.pdf. Accessed: January 19, 2025. (cited on page 138).

[458] Pithan, L. *et al.* Closing the loop: autonomous experiments enabled by machine-learning-based online data analysis in synchrotron beamline environments. *J. Synchrotron Rad.* **30**, 1064–1075 (2023). doi: 10.1107/s160057752300749x. (cited on page 139).

[459] Burian, M. *et al.* Picosecond pump–probe X-ray scattering at the Elettra SAXS beamline. *J. Synchrotron Rad.* **27**, 51–59 (2020). doi: 10.1107/s1600577519015728. (cited on page 139).

[460] Abdel-Latif, K., Bateni, F., Crouse, S. & Abolhasani, M. Flow synthesis of metal halide perovskite quantum dots: From rapid parameter space mapping to AI-guided modular manufacturing. *Matter* **3**, 1053–1086 (2020). doi: 10.1016/j.matt.2020.07.024. (cited on page 139).

[461] Polte, J. *et al.* Nucleation and growth of gold nanoparticles studied via in situ small angle X-ray scattering at millisecond time resolution. *ACS Nano* **4**, 1076–1082 (2010). doi: 10.1021/nn901499c. (cited on page 139).

[462] Probst, J. *et al.* In situ X-ray absorption spectroscopy and droplet-based microfluidics: An analysis of calcium carbonate precipitation. *ACS Meas. Sci. Au* **1**, 27–34 (2021). doi: 10.1021/acsmeasuresciau.1c00005. (cited on page 139).

[463] Lignos, I. *et al.* Unveiling the shape evolution and halide-ion-segregation in blue-emitting formamidinium lead halide perovskite nanocrystals using an automated microfluidic platform. *Nano Lett.* **18**, 1246–1252 (2018). doi: 10.1021/acs.nanolett.7b04838. (cited on page 139).

[464] Abolhasani, M. & Kumacheva, E. The rise of self-driving labs in chemical and materials sciences. *Nat. Synth.* **2**, 483–492 (2023). doi: 10.1038/s44160-022-00231-0. (cited on page 140).

[465] Williamson, E. M., Sun, Z., Mora-Tamez, L. & Brutchey, R. L. Design of experiments for nanocrystal syntheses: A how-to guide for proper implementation. *Chem. Mater.* **34**, 9823–9835 (2022). doi: 10.1021/acs.chemmater.2c02924. (cited on page 140).

[466] Urban, A. *et al.* Synthesizer: Machine learning-guided perovskite nanocrystal optimization. *Researchsquare preprint* (2025). doi: 10.21203/rs.3.rs-6411699/v1. (cited on page 140).

[467] Zaza, L., Ranković, B., Schwaller, P. & Buonsanti, R. A holistic data-driven approach to synthesis predictions of colloidal nanocrystal shapes. *J. Am. Chem. Soc.* **147**, 6116–6125 (2025). doi: 10.1021/jacs.4c17283. (cited on page 140).

[468] Svergun, D., Barberato, C. & Koch, M. H. J. CRYSOL – a program to evaluate X-ray solution scattering of biological macromolecules from atomic coordinates. *J. Appl. Cryst.* **28**, 768–773 (1995). doi: 10.1107/s0021889895007047. (cited on page 141).

[469] Trewhella, J., Vachette, P. & Larsen, A. H. Benchmarking predictive methods for small-angle X-ray scattering from atomic coordinates of proteins using maximum likelihood consensus data. *IUCrJ* **11**, 762–779 (2024). doi: 10.1107/s205225252400486x. (cited on page 141).

[470] Thompson, N. B., Mulfort, K. L. & Tiede, D. M. Toward a quantitative description of solvation structure: a framework for differential solution scattering measurements. *IUCrJ* **11**, 423–433 (2024). doi: 10.1107/s2052252524003282. (cited on page 141).

[471] Thomae, S. L. *et al.* Pushing data quality for laboratory pair distribution function experiments. *Rev. Sci. Instrum.* **90**, 043905 (2019). doi: 10.1063/1.5093714. (cited on page 141).

[472] Calvin, J. J., Kaufman, T. M., Sedlak, A. B., Crook, M. F. & Alivisatos, A. P. Observation of ordered organic capping ligands on semiconducting quantum dots via powder X-ray diffraction. *Nat. Commun.* **12**, 2663 (2021). doi: 10.1038/s41467-021-22947-x. (cited on page 142).

[473] Skinner, L. B. *et al.* Benchmark oxygen-oxygen pair-distribution function of ambient water from X-ray diffraction measurements with a wide Q-range. *J. Chem. Phys.* **138**, 074506 (2013). doi: 10.1063/1.4790861. (cited on page 142).

[474] Tomšič, M., Jamnik, A., Fritz-Popovski, G., Glatter, O. & Vlček, L. Structural properties of pure simple alcohols from ethanol, propanol, butanol, pentanol, to hexanol: Comparing Monte Carlo simulations with experimental SAXS data. *J. Phys. Chem. B* **111**, 1738–1751 (2007). doi: 10.1021/jp066139z. (cited on page 142).

[475] Beneduce, C. *et al.* Falsifiability test for classical nucleation theory. *Phys. Rev. Lett.* **134**, 148201 (2025). doi: 10.1103/PhysRevLett.134.148201. (cited on page 142).

[476] Johansen, F. L. *et al.* A GPU-accelerated open-source python package for calculating powder diffraction, small-angle-, and total scattering with the Debye scattering equation. *J. Open Source Softw.* 6024 (2024). (cited on page 142).

[477] Beyer, J., Kato, K. & Brummerstedt Iversen, B. Synchrotron total-scattering data applicable to dual-space structural analysis. *IUCrJ* **8**, 387–394 (2021). doi: 10.1107/s2052252521001664. (cited

on page 142).

[478] Monge, N., Deschamps, A. & Amini, M.-R. Automated selection of nanoparticle models for small-angle X-ray scattering data analysis using machine learning. *Acta Cryst. A* **80**, 202–212 (2024). doi: 10.1107/s2053273324000950. (cited on page 143).

[479] Paporakis, S. *et al.* Automation of liquid crystal phase analysis for SAXS, including the rapid production of novel phase diagrams for SDS–water–PIL systems. *J. Chem. Phys.* **158**, 014902 (2023). doi: 10.1063/5.0122516. (cited on page 143).

[480] Pauw, B. R. *et al.* The human factor: results of a small-angle scattering data analysis round robin. *J. Appl. Cryst.* **56**, 1618–1629 (2023). doi: 10.1107/s1600576723008324. (cited on page 143).

[481] Prehal, C. *et al.* On the nanoscale structural evolution of solid discharge products in lithium-sulfur batteries using operando scattering. *Nat. Commun.* **13**, 6326 (2022). doi: 10.1038/s41467-022-33931-4. (cited on pages 143 and 144).

[482] Röding, M., Tomaszewski, P., Yu, S., Borg, M. & Rönnols, J. Machine learning-accelerated small-angle X-ray scattering analysis of disordered two- and three-phase materials. *Front. Mater.* **9** (2022). doi: 10.3389/fmats.2022.956839. (cited on page 143).

[483] Tejero-Cantero, Á. *et al.* sbi: A toolkit for simulation-based inference. *J. Open Source Softw.* **5**, 2505 (2020). doi: 10.21105/joss.02505. (cited on page 143).

[484] von Mentlen, J.-M. *et al.* Exploring multiphase conversion pathways in Li-S batteries through cryo-TEM and ML-assisted operando neutron scattering. *Researchsquare preprint* (2024). doi: 10.21203/rs.3.rs-5689820. (cited on page 143).

[485] Starostin, V. *et al.* Fast and reliable probabilistic reflectometry inversion with prior-amortized neural posterior estimation. *Sci. Adv.* **11**, eadr9668 (2025). doi: 10.1126/sciadv.adr9668. (cited on page 143).

[486] Anker, A. S. *et al.* Extracting structural motifs from pair distribution function data of nanostructures using explainable machine learning. *npj Comput. Mater.* **8**, 213 (2022). doi: 10.1038/s41524-022-00896-3. (cited on page 143).

[487] Klemeyer, L. *et al.* Spatially resolved in situ X-ray absorption spectroscopy studies of ZnS nanoparticle synthesis at the water–toluene interface. *ACS Nano* **19**, 25710–25719 (2025). doi: 10.1021/acsnano.5c02875. (cited on page 144).

[488] Magnussen, O. M. *et al.* In situ and operando X-ray scattering methods in electrochemistry and electrocatalysis. *Chem. Rev.* **124**, 629–721 (2024). doi: 10.1021/acs.chemrev.3c00331. (cited on page 144).

[489] de Ruiter, J. *et al.* Multiscale X-ray scattering elucidates activation and deactivation of oxide-derived copper electrocatalysts for CO_2 reduction. *Nat. Commun.* **16**, 373 (2025). doi: 10.1038/s41467-024-55742-5. (cited on page 144).

[490] Huang, J. *et al.* Potential-induced nanoclustering of metallic catalysts during electrochemical CO_2 reduction. *Nat. Commun.* **9**, 3117 (2018). doi: 10.1038/s41467-018-05544-3. (cited on page 144).

[491] Derelli, D. *et al.* Photodegradation of $CuBi_2O_4$ films evidenced by fast formation of metallic Bi using operando surface-sensitive X-ray scattering. *Angew. Chem. Int. Ed.* **62**, e202307948 (2023). doi: 10.1002/anie.202307948. (cited on page 144).

[492] Bogar, M. *et al.* Interplay among dealloying, ostwald ripening, and coalescence in $Pt_X Ni_{100-X}$ bimetallic alloys under fuel-cell-related conditions. *ACS catalysis* **11**, 11360–11370 (2021). doi: 10.1021/acscatal.1c01111. (cited on page 144).

[493] Asset, T. *et al.* Disentangling the degradation pathways of highly defective PtNi/C nanostructures – an operando wide and small angle X-ray scattering study. *ACS Catalysis* **9**, 160–167 (2018). doi: 10.1021/acscatal.8b02665. (cited on page 144).

[494] Henke, B. L., Gullikson, E. M. & Davis, J. C. X-ray interactions: photoabsorption, scattering, transmission, and reflection at E = 50–30,000 eV, Z = 1–92. *Atomic data and nuclear data tables* **54**, 181–342 (1993). doi: 10.1006/adnd.1993.1013, URL https://henke.lbl.gov/optical_constants/. (cited on page 149).

[495] Orthaber, D., Bergmann, A. & Glatter, O. SAXS experiments on absolute scale with Kratky systems using water as a secondary standard. *J. Appl. Cryst.* **33**, 218–225 (2000). doi: 10.1107/s0021889899015216. (cited on page 149).

List of figures

List of tables

List of abbreviations

acac acetylacetonate

ADF-STEM annular dark field scanning transmission electron microscopy

AI artificial intelligence

arb.u. arbitrary units

ATR attenuated total reflection

BnOH benzyl alcohol

CCD charge-coupled device

COD crystallography open database

DESY Deutsches Elektronen-Synchrotron

DFT density functional theory

DLS dynamic light scattering

DOE design of experiments

DLVO Derjaguin, Landau, Verwey, Overbeek

DREAM differential evolution adaptive Metropolis

DSE Debye scattering equation

EDX energy-dispersive X-ray spectroscopy

ESRF European Synchrotron Radiation Facility

EPFL École Polytechnique Fédérale de Lausanne

fcc face-centered cubic

FFT fast Fourier transform

FKM fluorine kautschuk material

FTIR Fourier transform infrared spectroscopy

GPU graphics processing unit

hcp hexagonal close packed

HERFD-XANES high energy resolution fluorescence-detected X-ray absorption near edge spectroscopy

HRTEM high resolution transmission electron microscopy

JMAK Johnson, Mehl, Avrami, Kolmogorov

LARP ligand-assisted reprecipitation process

LED light-emitting diode

LHP lead halide perovskite

LMU Ludwig-Maximilians-Universität München

MCR-ALS multivariate curve resolution by alternating least-squares

ML monolayer

mp materials project

NMR nuclear magnetic resonance

NPL nanoplatelet

NR nanorod

ODE 1-octadecene

OlAc oleic acid

OlAm oleylamine

PD polydispersity

PDF pair distribution function (used for TS data)

PDDF pair distance distribution function (used for SAXS data)

PEEK polyether ether ketone

PL photoluminescence

PLQY photoluminescence quantum yield

RDF radial distribution function

SAXS small-angle X-ray scattering

SDD sample-to-detector distance

SEM scanning electron microscopy

SLD scattering length density

SRO short-range ordered

TDPA tetradecylphosphonic acid

TEM transmission electron microscopy

TOA trioctylamine

TS total scattering

UHH University of Hamburg

UV/vis ultraviolet-visible spectroscopy

vdW van der Waals

WAXS wide-angle X-ray scattering

XANES X-ray absorption near-edge structure

List of publications and conference presentations

Scientific publications of results presented in this work
(*) denotes equal contribution

- **Frank, K.** (*), Henke, N. A. (*), Lampe, C., Lorenzen, T., März, B., Sun, X., Haas, S., Gutowski, O., Dippel, A.-C., Mayer, V., Müller-Caspary, K., Urban, A. S., and Nickel, B. Antisolvent controls the shape and size of anisotropic lead halide perovskite nanocrystals. *Nat. Commun.* 15, 8952 (2024). doi: 10.1038/s41467-024-53221-5
- Derelli, D. (*), **Frank, K.** (*), Grote, L., Mancini, F., Dippel, A.-C., Gutowski, O., Nickel, B., and Koziej, D. Direct Synthesis of CuPd Icosahedra Supercrystals Studied by In Situ X-ray Scattering. *Small*, 2311714 (2024). doi: 10.1002/smll.202311714
- Mantella, V. (*), Strach, M. (*), **Frank, K.**, Pankhurst, J. R., Stoian, D., Gadiyar, C., Nickel, B. and Buonsanti, R. Polymer Lamellae as Reaction Intermediates in the Formation of Copper Nanospheres as Evidenced by In Situ X-ray Studies. *Angew. Chem. Int. Ed.* 59, 11627–11633 (2020). doi: 10.1002/anie.202004081
- Grote, L. (*), Zito, C. A. (*), **Frank, K.** (*), Dippel, A. C., Reisbeck, P., Pitala, K., Kvashnina, K. O., Bauters, S., Detlefs, B., Ivashko, O., Pandit, P., Rebber, M., Harouna-Mayer, S., Nickel, B., and Koziej, D. X-ray studies bridge the molecular and macro length scales during the emergence of CoO assemblies. *Nat. Commun.* 12, 4429 (2021). doi: 10.1038/s41467-021-24557-z

Other publications

- Bootz, P., **Frank, K.**, Eichhorn, J., Döblinger, M., Bagaria, T., Nickel, B., Feldmann, J., and Debnath, B. S-Scheme Interface Between K–C_3N_4 and $FePS_3$ Fosters Photocatalytic H_2 Evolution. *ACS Appl. Mater. Interfaces*, 16, 65610–65619 (2024). doi: 10.1021/acsami.4c15236
- Kang, Y., João, S. M., Lin, R., Zhu, L., Fu, J., Cheong, W.-C., Lee, S., **Frank, K.**, Nickel, B., Liu, M, Lischner, J., and Cortés, E. Effect of crystal facets in plasmonic catalysis. *Nat. Commun.* 15, 3923 (2023). doi: 10.1038/s41467-024-47994-y
- Derelli D., Caddeo, F., **Frank, K.**, Krötzsch, K., Ewerhardt, P., Krüger, M., Nickel, B., and Koziej, D. Photodegradation of $CuBi_2O_4$ Films Evidenced by Fast Formation of Metallic Bi using Operando Surface-sensitive X-ray Scattering. *Angew. Chem. Int. Ed.* 62, e202307948 (2023). doi: 10.1002/anie.202307948
- Martin, S., Henke, N. A., Lampe, C., Döblinger, M., **Frank, K.**, Ganswindt, P., Nickel, B. and Urban, A. S. Fine-Tuning Blue-Emitting Halide Perovskite Nanocrystals. *Adv. Opt. Mater.* 2301009 (2023). doi: 10.1002/adom.202301009
- Philipp, J., Dabkowska, A., Reiser, A., **Frank, K.**, Krzysztoń, R., Brummer, C., Nickel, B., Blanchet, C. E., Sudarsan, A., Ibrahim, M., Johansson, S., Skantze, P., Skantze, U., Östman, S., Johansson, M., Henderson, N., Elvevold, K., Smedsrød, B., Schwierz, N., Lindfors, L., and Rädler, J. O. pH-dependent structural transitions in cationic ionizable lipid mesophases are critical for lipid nanoparticle function. *Proc. Natl. Acad. Sci. U.S.A.*, 120, e2310491120 (2023). doi: 10.1073/pnas.2310491120
- Pauw, B. R., Smales, G.J., ..., **Frank, K.**, ..., and Wuttke, J. The human factor: results of a small-angle scattering data analysis round robin. *J. Appl. Cryst.* 56, 1618–1629 (2023). doi: 10.1107/S1600576723008324

- Treber, F., **Frank, K.**, Nickel, B., Lampe, C., and Urban, A. S. Lead-Free, Luminescent Perovskite Nanocrystals Obtained through Ambient Condition Synthesis. *Small* 19, 2300525 (2023). doi: 10.1002/smll.202300525
- Armer, M., Dörflinger, P., Weis, A., Büchner, C., Gottscholl, A., Höcker, J., **Frank, K.**, Nusser, L., Sirtl, M. T., Nickel. B., Bein, T., and Dyakonov, V. Low Temperature Optical Properties of Novel Lead-Free $Cs_2NaFeCl_6$ Perovskite Single Crystals. *Adv. Photonics Res.* 4, 2300017 (2023). doi: 10.1002/adpr.202300017
- Lehner, L. E., Demchyshyn, S., **Frank, K.**, Minenkov, A., Kubicki, D. J., Sun, H., Hailegnaw, B., Putz, C., Mayr, F., Cobet, M., Hesser, G., Schöfberger, W., Sariciftci, N. S., Scharber, M. C., Nickel, B., and Kaltenbrunner, M. Elucidating the Origins of High Preferential Crystal Orientation in Quasi-2D Perovskite Solar Cells (2022). *Adv. Mater.* 35, 2208061. doi: 10.1002/adma.202208061
- Xue, Q., Lampe, C., Naujoks, T., **Frank, K.**, Gramlich, M., Schoger, M., Vanderlinden, W., Reisbeck, P., Nickel, B., Brütting, W., Urban, A. S. Doubly Stabilized Perovskite Nanocrystal Luminescence Downconverters. *Adv. Opt. Mater.* 10, 2102791 (2022). doi: 10.1002/adom.202102791
- Rieger, S., Schönweitz, S., **Frank, K.**, Fürmann, T., Kerschbaumer, N. M., Steidl, V., Fang, J., Döblinger, M., Nickel, B., Stolarczyk, J. K., and Feldmann J. Anisotropic polarons and self-trapping in bismuth oxyiodide (BiOI) nanoplatelets, *under review at ACS Nano* (2022).

Contributions to conferences and workshops

- 12^{th} Soltech Conference, poster: In-situ SAXS to understand growth and self-assembly of lead halide perovskite and CuPd alloy nanoparticles, Würzburg, Germany, October 2023
- CeNS/SFB1032 Workshop, poster: In-situ SAXS to understand growth and self-assembly of lead halide perovskite and CuPd alloy nanoparticles, Venice, Italy, September 2023
- CeNS Science rocks, informal scientific talks for PhD students, talk: Keeping it real: another perspective on diffraction of nanoparticles, Munich, Germany, May 2023
- DPG Spring Meeting, talk: Unraveling the synthesis of halide perovskite nanoplatelets by SAXS, Dresden, Germany, March 2023
- 11^{th} Soltech Conference, talk and poster: In situ SAXS and total scattering to understand nanoparticle growth and self-assembly, Munich, Germany, October 2022
- DPG Autumn Meeting, talk: In situ small-angle X-ray scattering and total scattering to study CuPd nanoparticle growth and self-assembly, Regensburg, Germany, September 2022
- RÅC Summer School, poster: Combining in situ SAXS and total scattering to understand nanoparticle growth and self-assembly, Varberg, Sweden, August 2022
- Condensed Matter Physics and Chemistry (CMPC) meeting, talk: Simultaneous in situ SAXS and PDF to unveil transformations at the nanoscale, online, June 2021
- Soltech Keylab Workshop, talk: Nonclassical nanoparticle nucleation revealed by in-situ SAXS, online, October 2020
- DESY GISAXS workshop, poster: Photocatalytic nanomaterials studied by (GI)SAXS, Hamburg, Germany, November 2019
- CeNS/SFB1032 Workshop, poster: Photocatalytic nanomaterials studied with high-energy X-rays, Venice, Italy, September 2019

Acknowledgments

First of all I want to thank you, **Bert Nickel**, for giving me the opportunity to do a PhD under your supervision. You have supported me as a mentor starting from my time as a bachelor student, during my master thesis and my PhD journey. You gave me a lot of freedom to explore my own ideas and offered me great and fitting opportunities, valuable advice during our many meetings, and a helping hand for our joint beamtimes. I really enjoy our scientific discussions and I am thankful for your constructive criticism, dedication, and the inspiration you bring to the group.

Dorota Koziej, thank you for being my "second supervisor" in the LUCENT project. Considering our long-standing and fruitful collaboration, which goes far beyond what is shown in this thesis, we sadly did not meet often in person. Our almost weekly Zoom calls and mail exchanges were, nevertheless, very enjoyable and productive. Thank you for your trust, for sharing your ideas with us and pushing the project forward despite the geographical distance and Corona times.

Alexander Urban, I am very thankful that you agreed to be the second referee for my thesis. Our collaboration goes back to the very beginning of my PhD and some of the most rewarding projects resulted from it. Your enthusiasm and your constructive and critical input made the countless paper discussions very productive and inspiring.

Joachim Rädler, I am thankful that you created such a welcoming atmosphere at your chair, that you share your ideas about the big picture and your experience with your team, and I appreciate your advice.

Davide Derelli, as co-PhD students in the LUCENT project we have fought through many beamtimes, data analyses and paper drafts together and successfully mastered all these challenges. Thank you for your ideas which defined the fundamental directions within LUCENT, for your constant dedication and support.

Carola Lampe, we've started the second big experiment of LUCENT which culminated in this thesis, and had a great collaboration around many other topics. I really enjoyed our beamtimes, the hours of planning and the following discussions, which turned out to lay the foundation for some really cool results.

Nina Henke, little did we know that when you followed in Caro's footsteps, we would end up rewriting the story of nanorods and nanoplatelets over and over again. You had excellent answers to all my urgent questions. Thank you for your patience with the many experiments and for your great input going into analyses, edits and revisions. They made the work on this chapter very enjoyable and successful.

Quinten Akkerman, you gave very valuable feedback to our manuscript draft which helped us go forward. Working with you also on other projects and learning from your experience and critical thinking has been a pleasure. **Lukas Grote**, the project with you was a great start to the Munich-Hamburg collaboration and I am really thankful for your well-thought-out and professional input.

Ann-Christin Dippel, **Olof Gutowski**, **Xiao Sun**, **Sylvio Haas**, **Marina Sturm**, **Soham Banerjee**, **Oleh Ivashko** it is wonderful to have such committed collaborators at the DESY beamlines. You went above and beyond before, during, and after our experiments to put our ideas into practice and helped us wrangle with the data so that they are analyzed to the highest standard. Your contribution to the experiments is truly essential.

Sani Harouna-Mayer, **Tjark Gröne**, **Francesco Caddeo**, **Lars Klemeyer**, **Cecilia Zito** and the whole **Koziej group**, thank you for sharing your ideas and feedback with me, for selflessly working at the beamtimes and committing to our joint projects with great dedication.

Valeria Mantella, even before the LUCENT project gained traction you were already sharing all your in situ synthesis knowledge with me. I really enjoyed your visits which were packed with

experiments. We got great results in short time and overcame some major setbacks. **Raffaella Buonsanti**, thank you for driving this project with enthusiasm and curiosity. You contributed your profound knowledge and pushed us forward. This inspired me for all the further experiments. **Michal Strach**, thank you for trusting me with the very first in situ cell. **Tizian Lorenzen**, **Benjamin März** and **Knut Müller-Caspary**, thank you for recording nice STEM images for the perovskite nanocrystal project.

Jürgen Aust, **Thomas Großhauser** and the team from the workshop, **Rudolf Klinger** and the team from the glass workshop, and their colleagues at UHH and DESY, thank you for making our setups and sample environments work and for your valuable input how to design and manufacture things.

The whole **Urban group**, it has always been fun stopping by or meeting in our lab for some nice discussions, food and drinks, or for building a PhD hat. **Lukas Lehner**, **Stepan Demchyshyn** and **Martin Kaltenbrunner**, thank you for including me in your project, which unfortunately did not make it in this thesis. I'm glad that Bert's long standing and professional collaboration with your group continues. **Sebastian Rieger**, **Philipp Bootz**, **Bharati Debnath**, **Julian Mann**, **Jochen Feldmann**, **Yicui Kang**, **Emiliano Cortés**, thank you for sharing your research topics and samples with me, giving me the opportunity to contribute a little and learn more about energy materials (not only perovskites). I am thankful for the **CeNS** and **Soltech** research networks for hosting talks with excellent speakers and inspiring retreats. **Lisa Schraut-May** and **Jens Pflaum**, it has been great to work out the tricks of single crystal experiments with you. **Saeid Alirezazadeh** and **Stefan Kowarik**, thank you for the fruitful discussions about the cosmic background.

A heartfelt thank you goes to the entire Nickel group: **Martina Ober**, thanks for listening and giving great feedback all throughout my master and PhD times. **Batu Kalkan**, **Veronika Reisner**, **Julian Höcker**, **Katya Kostyurina**, **Theresa Kammerbauer**, the master and bachelor students **Patrick Reisbeck**, **Benedikt Bichler**, **Matthias Lösche**, **Benjamin Ajanović**, **Pia Alexander**, **Tianyi Cao**, **Matthias Süß**, **Lukas Rescher**, **Mario Alvarado**. You made working in the group a real pleasure. Not only did you create a welcoming and inspiring atmosphere to exchange ideas and results, you also contributed your part to many of the setups and results shown in this thesis.

Gerlinde Schwake, **Susanne Kempter** and **Charlott Leu**, thanks for being so kind and supportive and for making the chair run. My former office mates, **Sophia Schaffer**, **Anita Reiser**, **Julian Philipp**, **Johannes Heyn**, **Emily Brieger**, **Agathe Jouneau**, **Gregor Posnjak** and all the members of the Rädler chair, thanks a lot for being around and making me feel part of the group. You are great company for "being in science together", as well as for taking a break from it from time to time.

Thank you, **Nina**, **Sani**, **Katya** and **Gerlinde** for proofreading parts of this thesis.

Finally, I want to thank **my parents** for always believing in me and supporting me.